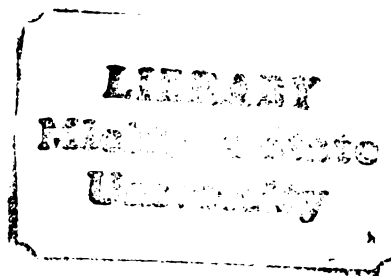


THESIS
C.1



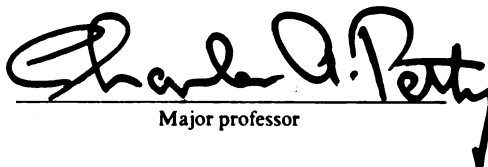
This is to certify that the
dissertation entitled
MEAN VELOCITY MEASUREMENTS IN A
3"-HYDROCYCLONE USING LASER
DOPPLER ANEMOMETRY

presented by

Bahram Dabir

has been accepted towards fulfillment
of the requirements for

Ph.D. degree in Chemical Engineering


Major professor

Date 2-26-83



RETURNING MATERIALS:
Place in book drop to
remove this checkout from
your record. FINES will
be charged if book is
returned after the date
stamped below.

ROOM USE ONLY

DO NOT CIRCULATE

MEAN VELOCITY MEASUREMENTS IN A
3"-HYDROCYCLONE USING LASER
DOPPLER ANEMOMETRY

BY

Bahram Dabir

A DISSERTATION

Submitted to
Michigan State University
in partial fulfillment of the requirements
for the degree of

DOCTOR OF PHILOSOPHY

Department of Chemical Engineering

1983

ABSTRACT

MEAN VELOCITY MEASUREMENTS IN A 3"-HYDROCYCLONE USING LASER DOPPLER ANEMOMETRY

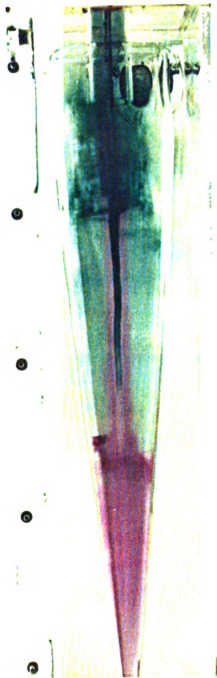
By

Bahram Dabir

Within the class of inertial separators, the hydrocyclone is especially noteworthy because of its simplicity of operation and its many diverse applications. Although a good qualitative understanding of solid-liquid separations in hydrocyclones is presently available, the relative importance of the various secondary motions on the separation efficiency of a hydrocyclone has not been quantitatively considered.

In the absence of a particulate phase and an air core, a quantitative study of the axial and tangential components of the mean velocity in a glass 3"-hydrocyclone using laser doppler anemometry has revealed multiple reverse flows in the vortex core. Flow visualization by dye injection shows that these flows are coherent over a significant portion of the hydrocyclone and that little radial mixing occurs between these secondary flows and the outer helical flow, although the Reynolds number based on the entrance diameter and feed flow rate exceeded 10,000. Several different vortex finder designs were studied, including one which satisfies standard optimal scaling rules. It was discovered that a 2:1 contraction in the vortex finder

causes four distinct simultaneous countercurrent flows in the conical section of the hydrocyclone. Moreover, for low backpressure operation (< 2 psig), a recirculation zone was detected in the upper part of the hydrocyclone with as many as six reverse flows. For some hydrocyclone designs and operating conditions, a jet-like flow on the axis occurs from the apex region to the vortex finder. This phenomenon partially explains why the design criteria of Rietema are optimal. The measured tangential velocity profiles were independent of axial location, and showed a characteristic "forced" and "free" vortex behavior in the inner and outer regions, respectively. The addition of 100 wppm Separan AP-30 decreased the tangential velocity and reduced the magnitude of the reverse flows in the core region. For the hydrocyclone studied, a split ratio from zero to infinity and a feed rate from 150-500 cm^2/sec have little effect on the vortex diameter (≈ 3 mm) and the conical locus of zero axial velocity in the outer flow domain.



Mixing Patterns in a 3"-Hydrocyclone

To my family

ACKNOWLEDGMENTS

I wish to express my deepest gratitude to Dr. C.A. Petty for his guidance and assistance throughout this study and in preparation of this manuscript.

I also wish to thank Professors R.E. Falco, J.D. Schuur, and P.E. Wood for their ideas, guidance, and assistance during the author's graduate studies. Special thanks are also given to Professor D.R. Woods of McMaster University who kindly loaned us his 3"-hydrocyclone for this study. The interest in this research by Dr. C.A. Willus of Dorr-Oliver, Inc. is also appreciated.

This research was supported by the National Science Foundation under grant NSF 71-1642 and by the Division of Engineering Research at Michigan State University. This assistance is warmly acknowledged.

Finally, I would like to thank my friend Dr. Manochehr Hessary for his help and moral support.

TABLE OF CONTENTS

	Page
LIST OF TABLES	vii
LIST OF FIGURES	viii
 CHAPTER	
1. INTRODUCTION	1
1.1. The Physical Problem	1
1.2. Background	5
1.2.1. Confined vortex flows	6
1.2.2. Previous velocity measurements in hydrocyclones	18
1.2.3. Effect of polymer additives on secondary flows	23
1.3. Objectives and Scope of This Research	25
2. EXPERIMENTAL APPARATUS AND PROCEDURES	34
2.1. Flow Loop	34
2.2. The Hydrocyclone	39
2.3. The Laser-Doppler System	45
2.4. Alignment Procedure for the Laser Doppler Anemometer	47
2.5. Procedure for Obtaining Good Doppler Signals . .	55
2.6. Data Analysis and Consistency Checks	59
3. FLOW VISUALIZATION STUDIES	65

	Page
CHAPTER	
4. VELOCITY MEASUREMENTS IN A 3"-HYDROCYCLONE WITH A 2:1 CONTRACTION IN THE VORTEX FINDER	76
4.1. Axial and Tangential Profiles	76
4.2. The Effect of Split Ratio on the Velocity Profiles	85
4.3. The Effect of Reynolds Number and Backpressure on the Velocity Profiles	91
4.4. The Effect of Separan AP-30 on the Velocity Profiles	96
5. VELOCITY MEASUREMENTS FOR DIFFERENT VORTEX FINDER CONFIGURATIONS	100
5.1. Rietema's "Optimal" Design	100
5.2. Equal Overflow and Underflow Areas	116
5.3. The Effect of Vortex Finder Design on Flow Reversals	125
6. DISCUSSION AND CONCLUSIONS	132
6.1. Summary Discussion of Results	132
6.2. Conclusions Based on this Research	136
6.3. Indirect Conclusions Suggested by the Results of this Research	141
7. RECOMMENDATION FOR FURTHER RESEARCH	148
7.1. Experiments Needed to Complete This Study	148
7.2. Problems Which Would Provide New Fundamental Understanding	150
7.3. Problems Which Could Lead to New Applications	151

APPENDIX

A.	APPLICATION OF LASER DOPPLER ANEMOMETRY TO VELOCITY MEASUREMENTS IN A HYDROCYCLONE	154
A.1.	Basic Principles	154
A.2.	Frequency Shifting	169
A.3.	Corrections Due to Refraction Phenomena	170
A.3.1.	The cylindrical section	172
A.3.2.	The conical section	181
A.4.	Additional Remarks on Experimental Apparatus	193
A.4.1.	Light source	193
A.4.2.	Optical components	194
A.4.3.	Data processing	197
A.5.	Example Problem: Laminar Flow in a Circular Tube	201
A.6.	Example Problem: Axial and Tangential Velocity Profiles in a Hydrocyclone	204
B.	DRAG REDUCTION CHARACTERISTICS OF SEPARAN AP-30	208
B.1.	Viscosity Measurements	208
B.2.	Drag Reduction Results	213
C.	FLOW CHARACTERISTICS FOR THE 3"-HYDROCYCLONE	218
D.	DATA FOR THE 3"-HYDROCYCLONE WHICH SATISFIES RIETEMA'S DESIGN CRITERIA	225
	LIST OF REFERENCES	242

LIST OF TABLES

TABLE	Page
1.1. Summary of problems studied for this research	26
1.2. Velocity profiles measured in the hydrocyclone with a 2:1 contraction in the vortex finder	29
1.3. Velocity profiles measured in the hydrocyclone with a 2:1 contraction in the vortex finder for 100 wppm Separan AP-30	30
1.4. Velocity profiles measured in the hydrocyclone which satisfy Rietema's optimal design criteria	31
1.5. Velocity profiles measured in the hydrocyclone with equal overflow and underflow areas	32
1.6. Velocity profiles measured in the hydrocyclone for other vortex finder geometries	32
2.1. Components of the TSI laser doppler anemometer used in this study	48
3.1. Scope of flow visualization studies	66
5.1. Change in flow topology with average circulation . . .	109
A.1. Mean axial velocity data measured in the hydrocyclone which satisfies Rietema's optimal design criteria . . .	205
A.2. Mean tangential velocity data measured in the hydrocyclone which satisfies Rietema's optimal design criteria	207
C.1. Values of exponent 'm' for various size hydrocyclones	222
D.1. Mean velocity data measured in the hydrocyclone which satisfy Rietema's optimal design criteria	226

LIST OF FIGURES

FIGURE	Page
1.1. Main flow structures in a hydrocyclone	2
1.2. Flow reversal observed by Nuttal [1953] for swirling flow in a circular pipe	8
1.3. Secondary flows in the core region and on the boundaries in confined vortex flow (from Rosenzweig et al., 1962)	14
2.1. Flow loop (nominal lengths given in cm)	35
2.2. Flow loop for polymer studies	37
2.3. Dimensions of the hydrocyclone used in this study (nominal lengths given in mm)	40
2.4. Side and front view of the test section	41
2.5. Vortex finder configurations studied (all dimensions given in mm)	42
2.6. Schematic diagram of test section for laser doppler and flow visualization setting	44
2.7. Schematic of laser doppler anemometer for forward mode of operation	46
2.8. Shifted and unshifted beam location as seen on the alignment mask	50
2.9. Projection of beams to check the crossing of the beams	52
2.10. Test section set-up to locate center of the hydrocyclone	54
2.11a-b Typical doppler signals obtained from the signal processor	56
2.11c-d Typical doppler signals obtained from the signal processor	58

FIGURE	Page
2.12. Output of the photomultiplier tube when the beam crossing intersects the hydrocyclone wall	60
2.13. Instantaneous axial velocity in the hydrocyclone (illustrative purposes only)	61
2.14. Symmetry and Reproducibility of velocity profiles . .	63
3.1. Flow visualization of the core region for Series I . .	67
3.2. Flow visualization of composite flows in the core region for $Q_0/Q_u = 4.0$ (Series I)	69
3.3. Flow patterns observed in the 3"-hydrocyclone using dye injection	72
3.4. Flow visualization of the core region for Series II and III	73
3.5. Composite results of flow visualization study for Series II and III	75
4.1. Mean axial velocity profiles for $Q_0/Q_u = 4$ and $Re_F \approx 30,000$	77
4.2. Mean tangential velocity profiles for $Q_0/Q_u = 4$ and $Re_F \approx 30,000$	79
4.3. Deviation from free vortex flow in the outer region for a split ratio of 4 and an inlet Reynolds number of 30,000	80
4.4. Mean axial and tangential velocity profiles at $z = 32$ cm for $Q_0/Q_u = 4$ and $Re_F \approx 30,000$ (o, □ present study; ●, ■ Knowles, 1971)	82
4.5. Average radial velocity profiles for $Q_0/Q_u = 4$ and $Re_F \approx 30,000$	84
4.6. The effect of split ratio on $\langle u_z \rangle$ at $z = 32$ cm and $Re_F \approx 30,000$	86
4.7. The effect of split ratio on $\langle u_\theta \rangle$ at $z = 32$ cm and $Re_F \approx 30,000$	87
4.8. Mean axial velocity profiles for $Q_0/Q_u = 0.25$ and $Re_F \approx 30,000$	89

FIGURE	Page
4.9. The effect of Reynolds number and back pressure on $\langle u_z \rangle$ for $Q_0/Q_u = 4$ at $z = 30$ cm	92
4.10. The effect of Reynolds number and back pressure on $\langle u_\theta \rangle$ for $Q_0/Q_u = 4$ at 20 cm	93
4.11. The effect of low back pressure on flow reversals for $Q_0/Q_u = 4$ and $Re_F \approx 30,000$ at $z = 32$ cm	95
4.12. Mean axial velocity profiles for 100 wppm Separan AP-30 with $Q_0/Q_u = 4$ and $Re_F \approx 24,300$ ($Q_F \approx 500$ cm ² /sec, $T = 12^\circ\text{C}$)	97
4.13. Mean tangential velocity profiles for 100 wppm Separan AP-30 with $Q_0/Q_u = 4$ and $Re_F \approx 24,300$ ($Q_F \approx 500$ cm ³ /sec, $T = 12^\circ\text{C}$)	98
5.1. The effect of split ratio on $\langle u_z \rangle$ for $Re_F \approx 24,200$ at $z = 20$ cm	101
5.2. The effect of split ratio on $\langle u_\theta \rangle$ for $Re_F \approx 24,200$ at $z = 20$ cm	102
5.3. The effect of Reynolds number on $\langle u_z \rangle$ for $Q_0/Q_u = 4$ at $z = 20$ cm	105
5.4. The effect of Reynolds number on $\langle u_\theta \rangle$ for $Q_0/Q_u = 4$ at $z = 20$ cm	106
5.5. Mean axial velocity profiles for $Q_0/Q_u = 0.25$ and $Re_F \approx 24,200$	110
5.6. Mean tangential velocity profiles for $Q_0/Q_u = 0.25$ and $Re_F \approx 24,200$	111
5.7. Mean axial velocity profiles for $Q_0/Q_u = 4$ and $Re_F \approx 24,300$	112
5.8. Mean tangential velocity profiles for $Q_0/Q_u = 4$ and $Re_F \approx 24,300$	113
5.9. Mean axial velocity profiles for $Q_0/Q_u = \infty$ and $Re_F \approx 24,100$	114
5.10. Mean tangential velocity profiles for $Q_0/Q_u = \infty$ and $Re_F \approx 24,100$	115

FIGURE	Page
5.11. Average radial velocity profiles for $Q_0/Q_u = 4$ and $Re_F \approx 24,300$	117
5.12. Mean axial velocity profiles for $Q_0/Q_u = 0.25$ and $Re_F \approx 24,300$	118
5.13. Mean axial velocity profiles for $Q_0/Q_u = 4$ and $Re_F \approx 24,300$	119
5.14. Mean axial velocity profiles for $Q_0/Q_u = \infty$ and $Re_F \approx 24,300$	120
5.15. The effect of split ratio on $\langle u_\theta \rangle$ for $Re_F \approx 24,300$ at $z = 32$ cm	122
5.16. The effect of Reynolds number on $\langle u_z \rangle$ for $Q_0/Q_u = 4$ at $z = 20$ cm	123
5.17. The effect of Reynolds number on $\langle u_\theta \rangle$ for $Q_0/Q_u = 4$ at $z = 30$ cm	124
5.18. The effect of the degree of contraction in the vortex finder on $\langle u_z \rangle$ for $Q_0/Q_u = 4$ and $Re_F \approx 24,300$ at $z = 32$ cm	126
5.19. The effect of the degree of contraction on $\langle u_z \rangle$ for $Q_0/Q_u = 4$ and $Re_F \approx 24,300$ at $z = 32$ cm	127
5.20. The effect of the degree of contraction on $\langle u_z \rangle$ for $Q_0/Q_u = \infty$ and $Re_F \approx 24,300$ at $z = 32$ cm	128
5.21. The effect of vortex finder configuration on $\langle u_\theta \rangle$ for $Q_0/Q_u = 4$ at $z = 32$ cm	129
5.22. The effect of vortex finder configuration on $\langle u_z \rangle$ for $Q_0/Q_u = 4$ at $z = 32$ cm	131
6.1. The effect of polymer (100 wppm Separan AP-30) on $\langle u_z \rangle$ for $Q_0/Q_u = 4$ and $Re_F \approx 24,300$	138
6.2. Mean axial velocity profiles for $Q_0/Q_u = 4$, $Re_F \approx 24,300$, and at $z = 2$ cm	140
7.1. Formation of oil core in a hydrocyclone with a contraction	153
A.I. Dual beam mode	157

FIGURE	Page
A.2. Vector diagram of light propagation	158
A.3. Cross section of two beams from the same source . . .	162
A.4. The coordinate system used for a fringe system	164
A.5. Beam intersection region in the real fringe system. The inner ellipse represents Eq. (A.17) and the outer ellipse is the locus of points at which the signal falls to e^{-2} of its maximum	167
A.6. Typical signal from the photodetector	168
A.7. Refraction of laser beams during axial velocity mea- surement in the cylindrical section	173
A.8. Refraction of laser beams during tangential velocity measurements in the cylindrical section	177
A.9. Refraction corrections for the cylindrical section . .	182
A.10. Refraction of laser beams during axial velocity mea- surements in the conical section	183
A.11. Geometry of test ring for LDA measurements of parabolic profiles	202
A.12. Mean velocity profile for fully developed laminar flow in a circular tube	203
B.1. Chemical structure of Separan AP-30, a co-polymer of polyacrylamide and polyacrylic acid	209
B.2. The effect of polymer concentration on the apparent viscosity of aqueous AP-30 mixtures at different temperatures	211
B.3. The effect of polymer concentration and PH on the apparent viscosity of aqueous AP-30 mixture	212
B.4. The effect of PH on drag reduction characteristic of Separan AP-30 (100 wppm)	215
B.5. The effect of shear on the % drag reduction for 100 wppm Separan AP-30	217
C.1. Operating characteristics of a 3"-hydrocyclone for $Q_0/Q_u = 0.25$	219

FIGURE	Page
C.2. Operating characteristics of a 3"-hydrocyclone for $Q_0/Q_u = 4$	220
C.3. Operating characteristic of a 3"-hydrocyclone for $Q_0/Q_u = \infty$	221
C.4. Effect of inlet pressure on the Q_0/Q_u of a 3"- hydrocyclone with a 2:1 contraction above the vortex finder	224

CHAPTER 1

INTRODUCTION

1.1. The Physical Problem

Solids dispersed in a continuous fluid phase can be separated by several complementary methods which exploit different fundamental principles. Within the class of inertial separators, the hydrocyclone is especially noteworthy because of its simplicity of operation and its many diverse applications. In a hydrocyclone a centrifugal force field is created by the swirling motion of a continuous fluid phase. One of the main flow features in all hydrocyclones (see Figure 1.1) is the occurrence of a downward helical flow in the outer region and an upward helical flow in the core. Solids having a larger density than the fluid migrate to the outer boundary layer and are removed with the underflow fluid; however, some solids short-circuit to the overflow in a boundary layer which runs across the roof of the hydrocyclone to the vortex finder. This inward radial flow is caused by a pressure gradient induced by the tangential flow. Other secondary flows occur in hydrocyclones as amply illustrated by the frontespiece of this dissertation and the results of a flow visualization study summarized in Chapter 3.

The basic ideas currently being used to design hydrocyclones can be traced to the pioneering studies of Kelsall [1952], Bradley and Pulling [1959], and Rietema [1961a-d]. An excellent summary

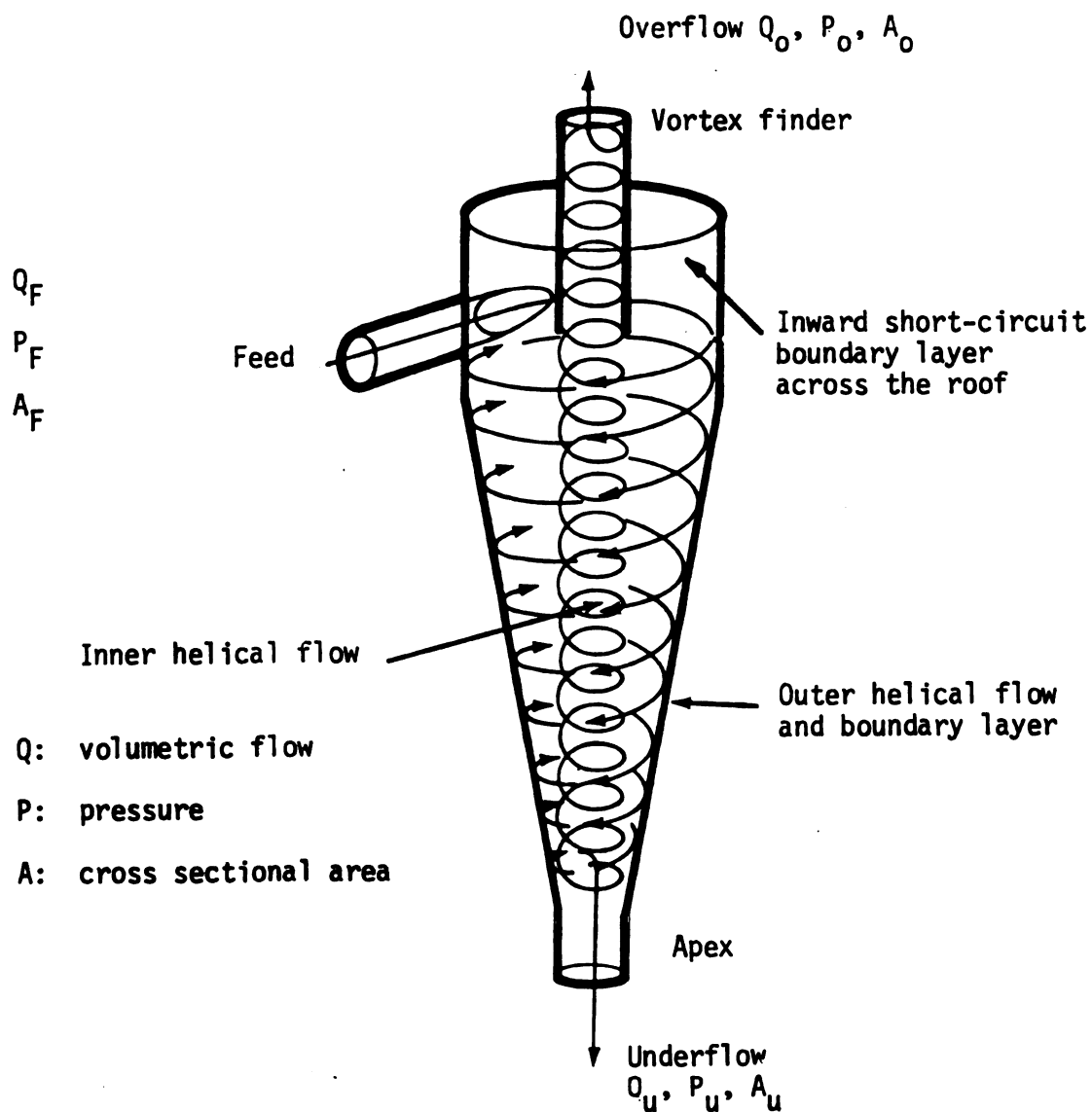


Figure 1.1. Main flow structures in a hydrocyclone.

and analysis of these and other works can be found in Bradley [1965]. Poole and Doyle [1968] and, more recently, Svarovsky [1977] also give good, but brief, reviews of design strategies. Also see Rietema and Verver [1961]. The work of Rietema has led to the general acceptance of an "optimal" design for hydrocyclones. The geometric proportions of the 3"-hydrocyclone used in this study satisfy his criteria. Presumably, such a design minimizes the adverse effects of turbulent mixing on separation efficiency.

Most hydrocyclones are presently designed based on experience rather than fundamental principles. The basic interactions between the outer swirling flows and the boundary layer flows have not been exploited systematically. The separation efficiency is certainly affected by multiple recirculation zones and flow reversals on the core axis, yet quantitative understanding of these and other phenomena is still lacking. Perhaps a better understanding would provide some clues as to why highly efficient hydrocyclones for small particle separations cannot be scaled-up.

Although the interactions between the various mixing patterns within a hydrocyclone can be influenced significantly by changing geometric scales, another and potentially more flexible possibility exists. For instance, it is widely known (see, especially, Metzner et al., 1969; and Virk, 1975) that small amounts of a high molecular weight polymer can have a dramatic effect on certain turbulent and non-turbulent flow structures of a Newtonian fluid. This suggests *that* certain combinations of hydrocyclone geometry and fluid

rheology may also improve the performance of hydrocyclones. The feasibility of this idea in a 3"-hydrocyclone partially motivated this research. Some initial findings are given in Section 4.4.

Several years ago, a preliminary study was initiated in our laboratory to determine if the efficiency of a 10 mm hydrocyclone could be affected by adding a drag reducing polymer to the feed stream. The results of this study (see Dabir et al., 1980) confirmed the earlier discovery by Wallace [1980] that the addition of a small amount of Separan AP-30 to a 2 wt. % water-clay suspension of $\approx 1\mu$ size particles results in significant changes in the separation efficiency. Depending on the specific details of how the polymer-water-clay mixtures were prepared, increases or decreases in efficiency by as much as 70% were observed. Thomas [1982] has recently completed another study which basically verifies this paradoxical mixing effect (also see Wallace et al., 1980).

Because of the complex nature of the flow patterns within a hydrocyclone, it would be premature to propose a mechanism for the foregoing phenomenon without a quantitative study of the mean velocity field with and without polymer additive. Furthermore, the distinct possibility that Separan AP-30 could also promote stable flocculation of clay particles in a high shear field makes any indirect conclusions to the contrary speculative. Mean velocity measurements using a laser-doppler technique even without polymer additives should provide new information regarding internal flow patterns in hydrocyclones. Earlier measurements are still incomplete

and contradictory, so a complete set of velocity data would be welcomed. Chapters 4 and 5 summarize the behavior of the tangential and axial components of the mean velocity in a 3"-hydrocyclone over a wide range of operating conditions.

1.2. Background

Swirling flows have numerous applied applications and the hydrocyclone is only one of many practical devices which exploit the unique features of confined vortex flows. In what follows, a brief review of some flow phenomena characteristic of confined vortex flows relevant to the performance of hydrocyclones is developed (Section 1.2.1). The more fundamental aspects of rotating flows in general are lucidly presented by Greenspan [1968] in his now classical monograph on the topic. Lewellen [1971] gives an excellent discussion of the relevant fluid mechanics related to several important applications including the cyclone separator and advanced nuclear rocket concepts using vortex confinement.

In Section 1.2.2, previous quantitative studies of swirling flows are examined with an emphasis on those specific areas where detailed knowledge is lacking or where inconclusive results need additional clarification. The known effects of polymer additives on flow structures are reviewed briefly in Section 1.2.3. From this discussion, we anticipate that Separan AP-30 could alter some of the secondary flow patterns illustrated in Figure 1.1.

1.2.1. Confined vortex flows

Several fundamental properties of confined vortex flows are worth noting. First, because the swirl velocity is large, the mean radial pressure distribution is primarily determined by the centrifugal force field per unit volume (i.e., $\rho \langle u_\theta \rangle^2 / r$). Thus,

$$\frac{\partial \langle p \rangle}{\partial r} \approx \rho \frac{\langle u_\theta \rangle^2}{r} . \quad (1.1)$$

Furthermore, in rotational flows there is a strong tendency toward two dimensional behavior (see p. 2 in Greenspan, 1968). Within the hydrocyclone, this translates into the important observation that the flow field quickly becomes axisymmetric, even if the fluid is introduced asymmetrically as shown in Figure 1.1. Moreover, the tangential component of the velocity to a good approximation is independent of both the θ - and the z -coordinate directions. Of course, this feature is altered dramatically near the boundaries of the hydrocyclone, especially deep in the apex region.

The important qualitative conclusion from the foregoing discussion is that the axial variation of the pressure is determined largely by the secondary flows within the central core region and within the boundary layer on the cone wall. The radial distribution of $\langle p \rangle$ between the inner vortex core and the outer boundary layer is determined basically by the swirling velocity of the primary flow. If the primary flow tries to conserve the axial component of angular momentum, then $r \langle u_\theta \rangle = \text{constant}$ and the pressure decreases rapidly from the outer to the inner region of the flow field. Indeed,

the inner core pressure could become subatmospheric causing an air core to be sucked into the hydrocyclone through the apex or vortex finder. This phenomenon is well known for hydrocyclones and is clearly documented in the early flow visualization study of Bradley and Pulling [1959]. A similar entrainment of external fluid also occurs for gas cyclones (see Ter Linden, 1949; and Stairmand, 1951). This is a general phenomenon of rotating flows caused by a pressure distribution satisfying, in part, Eq. (1.1).

In a comprehensive experimental study of flow reversal in a cylindrical vortex chamber closed at one end, Donaldson and Snedeker [1962] showed that entrainment of surrounding fluid was primarily governed by the relative magnitudes of a characteristic swirl velocity and a characteristic radial velocity. Transition from a single celled vortex structure (no entrainment) to a two-celled structure (entrainment) occurred when the swirl component was approximately three times larger than the radial component.

Nuttal [1953] showed that reverse flows are also characteristic of swirling flows in circular pipes. For Reynolds numbers in the range 1×10^4 to 3×10^4 , the three types of flow patterns illustrated in Figure 1.2 were observed. Transition from a one-celled to a two- and, finally, a three-celled vortex structure occurs as the swirl component of the velocity increases. Nuttal [1953] gave no explanation for this phenomenon but, as clearly discussed by Donaldson and Snedeker [1962], the basic underlying physical effect is contained in Eq. (1.1).

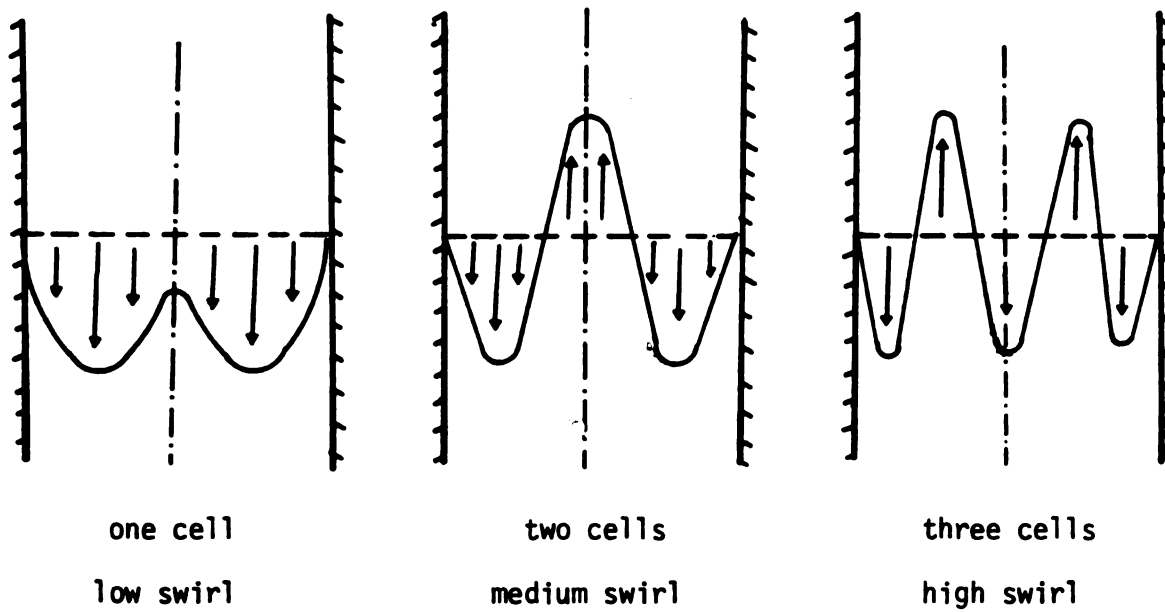


Figure 1.2. Flow reversal observed by Nuttal [1953] for swirling flow in a circular pipe.

Binnie [1957] also investigated the nature of the flow patterns when swirling water passes through a long, circular tube. Several different vortex chambers were studied at low Reynolds numbers (≤ 300). Transition from a single-celled vortex structure to a three-celled structure depends on the Reynolds number and the ratio of swirl to axial flow. For fixed Re, reverse flow was induced by increasing the swirl component of the flow. Nissan and Bresan [1961] examined some of the underlying factors governing flow reversals at high Reynolds numbers in cylinders by measuring pressure and velocity profiles. Because of the appearance of a large stationary bubble on the core axis, they also concluded that a three-celled structure was possible at high Reynolds numbers.

Escudier et al. [1980] studied confined turbulent vortex flows by using a laser doppler anemometer and a flow visualization technique. They showed that the size of the exit hole affects the location and magnitude of the swirl velocity and, thereby, the number of flow reversals possible. For the conditions studied, transition from a two-celled structure to a three-celled structure occurs as the exit hole diameter to vortex chamber diameter increases. The critical ratio was about two.

Binnie and Teare [1956] showed that reverse flows were not limited to cylinders by observing a two-celled vortex structure at very high swirl velocities for flow through a conical nozzle; a three-celled structure was not reported. In cyclone separators, Ter Linden [1949], Kelsall [1953], and Ohasi and Maeda [1958] all

obtained velocity measurements showing a core flow in the opposite direction to the flow along the conical wall. Kelsall [1953] noted that under certain conditions a three-celled vortex structure was possible at high inlet Reynolds numbers within a 3"-hydrocyclone. Smith [1962] also demonstrated multiple cell phenomena (as many as three) in a gas cyclone separator.

Exact solutions to the Navier-Stokes equation exist which show multiple cell behavior (see, esp., Donaldson, 1956; Sullivan, 1959; and Donaldson and Sullivan, 1960). Unfortunately, because important physical effects due to the boundaries have been neglected, these solutions do not provide a quantitative basis for understanding flow reversals; however, some insight from the Navier-Stokes equation does follow by making the equation dimensionless (see, esp., p. 7 in Greenspan, 1968). Basically, two characteristic velocity scales can be identified in confined vortex flows: one related to the swirl component of the velocity and the other to either the radial or the axial flow.

For hydrocyclone applications, a characteristic swirl velocity is simply the feed volumetric flow rate divided by the cross sectional area of the inlet (see Figure 1.1):

$$U_{\theta} \equiv Q_F/A_F . \quad (1.2)$$

Another natural velocity scale would be one related to the overflow rate. Thus, with

$$U_z \equiv Q_o/A_o , \quad (1.3)$$

the following two dimensionless groups determine the behavior of the velocity field,

$$N_1 \equiv \frac{\nu}{U_\theta D} \quad (1.4)$$

and

$$N_2 \equiv \frac{U_z}{U_\theta} . \quad (1.5)$$

The characteristic length scale D is the diameter of the hydrocyclone and ν is the kinematic viscosity of the fluid. U_θ and U_z are simply the bulk average velocities in the feed and overflow lines, respectively. N_1 is a characteristic Ekman number for hydrocyclones and N_2 is a characteristic Rossby number (cf. Greenspan, p. 7). The relevant observation here is that the Ekman number (or, equivalently, the inverse Reynolds number) is extremely small in most cases of interest where the primary effects of rotation are important. In this study, $N_1 \text{Re}_F = D_F/D = 0.28$. So with $\text{Re}_F \approx 28,000$, $N_1 \approx 10^{-5}$. The Rossby number, however, varies from zero to unity depending on the split ratio Q_o/Q_u . The relationship between N_2 and Q_o/Q_u is

$$N_2 = \frac{A_F}{A_o} \frac{Q_o/Q_u}{1 + Q_o/Q_u} . \quad (1.6)$$

For the hydrocyclone used in this research, $A_F \approx A_o$.

The Ekman number multiplies the highest spatial derivatives in the dimensionless Navier-Stokes equation. Because N_1 is so small, boundary layers must exist somewhere within the flow domain. Thin

shear layers are certainly located along the conical surface of the hydrocyclone and these have been analyzed mathematically by G.I. Taylor [1950]; Binnie and Harris [1950]; Wilks [1968]; Bloor and Ingham [1976]; and, recently, by Som and Mukherjee [1980]. Viscous layers may also occur in the interior to offset the development of very steep velocity gradients in the core region. Thus, with the viscous action concentrated into narrow layers near the solid boundaries (and, perhaps, near the vortex core), the primary flow could easily be dominated by inviscid effects.

The major theoretical consequence of the foregoing observation follows by examining the θ -component of the Navier-Stokes equation (or, if turbulence is considered, the Reynolds equation). If viscous stresses and turbulent stresses are unimportant, then it is easy to show that (see Donaldson and Snedeker, 1962)

$$\frac{D}{Dt} (r\langle u_\theta \rangle) = 0 , \quad (1.7)$$

where $D/Dt \equiv \partial/\partial t + \langle \underline{u} \rangle \cdot \nabla$. This means that the axial component of the angular momentum is constant in a frame of reference which moves with the local mean velocity. A vortex flow which satisfies Eq. (1.7) is usually referred to as a "free" vortex. Obviously, this result would be rare for a confined vortex but the extent to which $\langle u_\theta \rangle$ deviates from this simple behavior provides some measure of the importance of turbulent mixing and viscous transport of momentum across the primary flow.

Heuristic thinking about swirling flows often centers around various mechanisms which attempt to explain how the flow tries to preserve angular momentum. The interactions between the secondary boundary layer structures and the primary flow are subtle and crucial. This is amply illustrated by Figure 1.3 which shows the results of a flow visualization study by Rosenzweig et al. [1962] in a jet-driven vortex tube. An insightful analysis of this flow by Rosenzweig et al. [1964] concluded that substantial turbulence levels must be assumed to explain these experimental results; boundary layer interactions alone were insufficient. However, mass ejection from the boundary layer is still an important process which supports the angular momentum distribution and retards the decaying process. For large Rossby numbers, Lewellen [1965] showed theoretically that axial decay of angular momentum retards the axial velocity on the axis and that the motion illustrated by Figure 1.3 is forced to be two-dimensional except in thin shear regions. Lewellen concluded that flow with a large swirl component offers a high resistance to radial flow. If axial variations in $\langle u_\theta \rangle$ occur, then this happens in a very thin shear layer (Ekman layer) which offers little resistance to radial flow. Thus, the physical picture of the flow pattern, which emerges from Lewellen's analysis and which is supported by experimental observation, is that the fluid seeks regions in the physical domain having a relatively low centrifugal force field. In this way, the circuitous secondary flows (see Figure 1.3) support the basic swirl pattern by transporting angular momentum from the

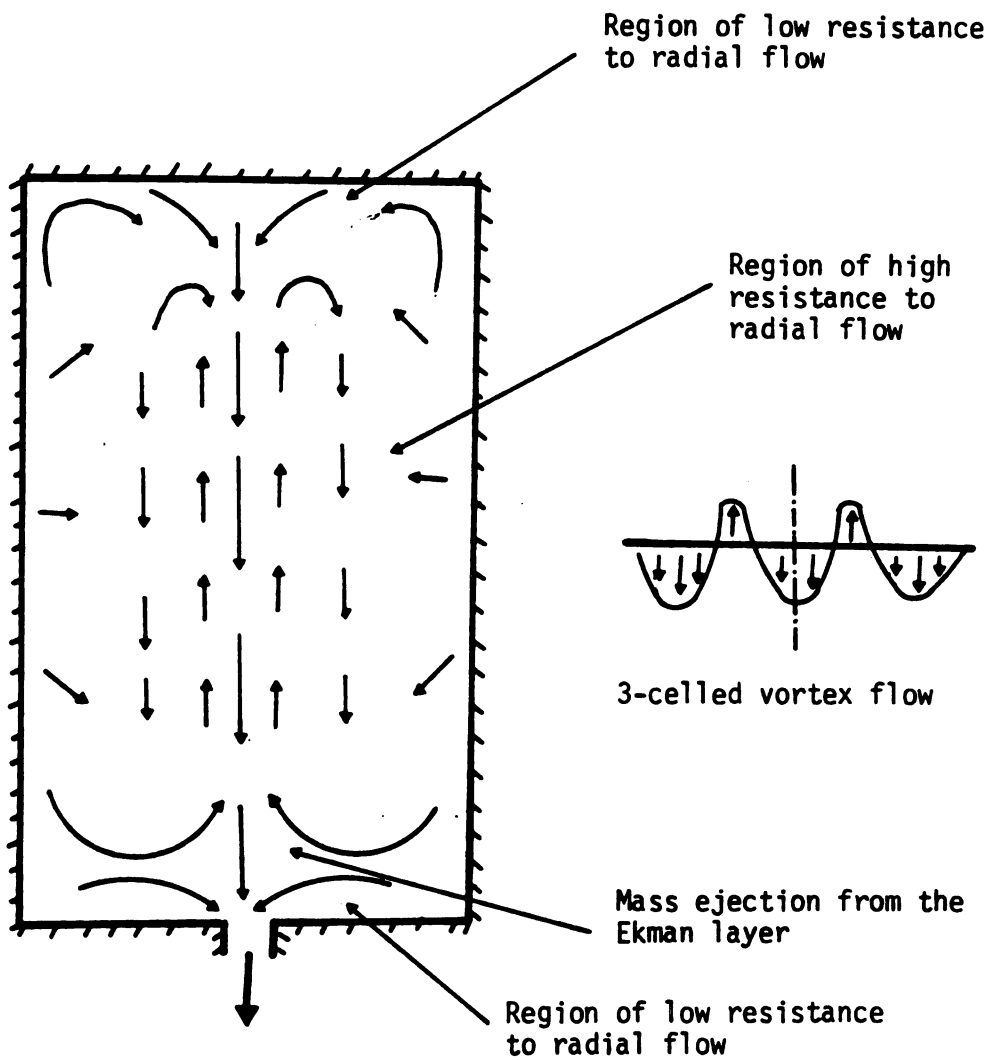


Figure 1.3. Secondary flows in the core region and on the boundaries in confined vortex flow (from Rosenzweig et al., 1962).

outer region to the inner core by radial convection. Apparently, the radial velocity distributes itself so the swirling motion is approximately two dimensional.

Within hydrocyclones, three regions of low centrifugal force exist: the conical boundary layer, the roof of the hydrocyclone, and the central core region. As suggested by Figure 1.1, fluid is injected tangentially at the outer wall and moves radially to the overflow and underflow through these three regions. Based on the analysis of Lewellen, it should not be surprising that the underflow fluid is carried to the apex region by the boundary layer. This is generally understood in the literature and is supported also by Taylor's earlier analysis of spray atomizers. However, what is not generally recognized is that a significant fraction of the overflow fluid arises from an ejection of mass from the conical boundary layer deep in the apex region (see, esp., Bhattacharyya, 1980a and b) rather than by a weak radial flux counter to the centrifugal force field across the primary swirling motion. The basic physical mechanism which causes this in an Ekman layer (see Figure 1.3) is also operative here. For solid-liquid separations, the ejection of fluid containing a high concentration of solids from the conical boundary layer into an upward directed flow toward the vortex finder could easily degrade the performance of a hydrocyclone. Indeed, this phenomenon may be more significant than the usual short-circuit effect on the roof of the hydrocyclone.

Bradley and Pulling [1959] studied the flow patterns inside a 3"-hydrocyclone using a flow visualization technique for different size vortex finders and cone angles. At a flow rate of $500 \text{ cm}^3/\text{sec}$ and a high split ratio, the flow patterns observed were similar to those reported earlier by Kelsall [1953], viz., an outer downward helical flow surrounding an inner upward helical flow. A stagnant zone surrounding the core indicated a region of negligible axial and radial velocities. Such a region, which has been observed by many researchers, is commonly referred to as the "mantle". Bradley [1959] observed that the "mantle" is basically unaffected by changes in the vortex finder dimensions, provided the overflow diameter is smaller than the "mantle" diameter. For large overflow diameters, the radial velocity is too large for a "mantle" to exist.

The "mantle" diameter increases as the cone angle increases (Bradley and Pulling, 1959) and, for large cone angles, double "mantles" can occur. Earlier, Fontein and Dijkstra [1953] suggested that such multiple recirculation zones exist below the roof of the hydrocyclone. These may result from an ejection of mass by the radially directed Ekman layer on the roof, or from a Taylor-like instability of the primary swirling motion. A specific mechanism for multiple circulation patterns in hydrocyclones has not been identified.

The swirling flow in the core region of a vortex tube (or hydrocyclone) can undergo sudden and dramatic changes involving flow reversals. This phenomenon, termed "vortex breakdown", is

often characterized by a region of closed circulation with a free stagnation point and surface of zero axial velocity perpendicular to the flow axis. The recirculation region appears as a hemispherical zone of almost stationary fluid relative to the surrounding flow field. As the swirl component of the velocity increases, the isolated fluid region stretches along the axis of the vortex tube. Three types of breakdown phenomena have been classified in the literature: double-helix, spiral form, and axisymmetric form (see, esp., Sarpkaya, 1971). The axisymmetric vortex breakdown may be a result of the first two types, or it may form directly by the swelling of the vortex core.

The vortex breakdown phenomenon involves very sensitive flow structures and should be studied by a nonintrusive technique such as laser doppler anemometry together with a passive flow visualization technique (see, e.g., Harvey, 1962; Cassidy, 1970; Sarpkaya, 1971; and Faler and Leibovich, 1978). Some summary conclusions regarding this phenomenon are as follows:

- (1) The primary parameter which determines vortex breakdown is the ratio of the swirl velocity to the axial velocity (i.e., an inverse Rossby number). Breakdown occurs at a critical Rossby number or, equivalently, swirl angle.
- (2) The location and occurrence of a vortex breakdown is closely associated with the degree of contraction of the vortex tube and the adverse pressure gradient along the axis.

- (3) The transition from non-reversal to reversal flow occurs smoothly rather than abruptly as in an instability (see, esp., Harvey, 1962).
- (4) The swirl angle and adverse pressure gradient are not the only parameters controlling vortex breakdown. The boundary layers along the divergent walls (see the paper by Sarpkaya, 1974) play an important and unpredictable role in the breakdown process.

Vortex breakdown due to an amplification of small disturbances (wave phenomenon) was first proposed by Squire [1960] and developed by Benjamin [1962] in a sequence of papers. Another approach, developed by Hall [1966], argues that small axial variations in the swirl velocity (due to decay or contraction) can produce significant changes in the axial velocity. Thus, for a given combination of swirl and axial velocity, a critical swirl angle exists which induces an infinitesimal expansion of the vortex core. This makes

$$\frac{\partial \langle u_z \rangle}{\partial z} < 0 \quad \text{and} \quad \frac{\partial \langle p \rangle}{\partial z} > 0 ,$$

which leads to stagnation on the axis and ultimate breakdown of the vortex flow.

1.2.2. Previous velocity measurements in hydrocyclones

With the exception of the entry region, the flow pattern in a hydrocyclone is axisymmetric. Therefore, it is natural to resolve

the mean velocity field into radial, tangential, and axial components:

$$\underline{u} = \langle u_r \rangle(r,z) \underline{e}_r + \langle u_\theta \rangle(r,z) \underline{e}_\theta + \langle u_z \rangle(r,z) \underline{e}_z . \quad (1.7)$$

Here \underline{e}_r , \underline{e}_θ , and \underline{e}_z are the unit base vectors for cylindrical geometry. Eq. (1.7) states explicitly that the mean velocity components do not depend on the θ -coordinate (axisymmetry) and time (statistically stationary flows). The instantaneous velocity field satisfies the full Navier-Stokes equation and the continuity equation for incompressible fluids (see p. 85 in Bird, Stewart, and Lightfoot, 1960). The mean velocity satisfies the so-called Reynolds equation for turbulent flows; for a specific application of Reynolds equation to gas cyclones see Boysan et al. [1982].

Based on the discussion in Section 1.2.1, we anticipate that experiments will verify some additional kinematic properties of \underline{u} . For instance, if the swirling flow tries to maintain a two dimensional behavior, then the magnitude of the radial component in the primary flow field should be much smaller than either the tangential or axial components. Furthermore, it is expected that

$$\frac{\partial}{\partial z} \langle u_\theta \rangle(r,z) \approx 0$$

in the primary flow field and that the radial distribution of $\langle p \rangle(r,z)$ is determined by Eq. (1.1). Understanding the interplay among all the velocity components where three dimensional behavior is expected is an important and challenging task for the design

engineer. Unfortunately, little attention has been given to this aspect of the problem. Standard reviews of the velocity field (see, for example, Chapter 3 in Rietema and Verver, 1961; Chapters 3 and 4 in Bradley, 1965; and Chapter 6 in Svarovsky, 1977) emphasize the behavior of $\langle u \rangle$ within the primary flow (see Figure 1.1) measured by Kelsall [1952] using an optical technique based on flow visualization.

Kelsall's study has had a major impact on the development of hydrocyclones over the past thirty years. His velocity data has been the major touchstone for theoretical studies on hydrocyclones (see, e.g., the analyses of Bloor and Ingham over the last ten years and the recent work of Bhattacharyya, 1980a and b). Two other quantitative velocity studies in hydrocyclones using a non-intrusive flow visualization technique have been reported (Ohasi and Maeda, 1958; and Knowles et al., 1973). These experimental studies also emphasized the primary flow domain and little insight regarding the boundary layer flows or the central core region can be developed from these data.

The 3"-hydrocyclone operating with an air core studied by Kelsall [1952] unfortunately had an unusually long vortex finder with a diameter much smaller than the "optimal" one recommended later by Rietema [1961]. The motion of small alumina particles (s.g. ≈ 2.7) was followed to determine $\langle u_\theta \rangle$ and $\langle u_z \rangle$. The radial component of the velocity was calculated by using the continuity equation.

Knowles et al. [1973] studied a 3"-hydrocyclone operating without an air core. Their design, unlike Kelsall's, satisfied the scaling rules of Rietema with one unfortunate exception in the vortex finder (see Figure 2.3 and Section 5.3 of this dissertation). The experimental methodology of visualizing the motion of a seed particle is similar to Kelsall's. Here high speed cine photography was used to follow anisole particles (s.g. ≈ 0.993 , particle size $\approx 50\text{--}300\ \mu$).

The basic results obtained earlier by Kelsall and, more recently, by Knowles are similar. The main flow feature observed consists of a strong downward velocity in the outer region close to the conical wall and an upward flow close to the core. A surface of zero axial velocity is located quantitatively in both studies. Along the rim of the vortex finder a strong downward flow was quantified. Presumably, this flow originated as an ejection from the short-circuit Ekman layer on the roof of the hydrocyclone. Below the vortex finder and close to the central axis, the tangential velocity profiles reported by Kelsall increase with the radial coordinate; Knowles' data are inconclusive. Thus, for a hydrocyclone operating with an air core, a region exists where the fluid rotates as a "forced" vortex. Quantification of this behavior for a hydrocyclone operating without an air core is one of the main objectives of this research.

At larger radial positions both Kelsall and Knowles observed a decrease in $\langle u_\theta \rangle$ with r . However, the "free" vortex behavior

which follows from Eq. (1.7) does not occur. Instead, $\langle u_\theta \rangle \propto r^{-n}$ where $n \approx 0.8$ with an air core and $n \approx 0.3$ without an air core. The difference here is significant and should be studied carefully. Based on this result, large differences in pressure losses under similar operating conditions could be anticipated between air core and no air core operations. Furthermore, and perhaps more to the point, if this difference in "n" holds upon further examination, then the ejection processes discussed in Section 1.2.1 would be quantitatively altered.

The magnitude of $\langle u_r \rangle$ in the primary flow domain determined by Kelsall and by Knowles turns out, as expected, to be small compared with the axial and tangential components. However, these two authors differ on the sign of $\langle u_r \rangle$, which suggests another significant difference between the two operations (air core vs. no air core). Kelsall's data seems to imply that $\langle u_r \rangle$ is negative and decreases monotonically with increasing r ; on the other hand, Knowles' data shows an outward radial flow in the inner region and an inwardly directed radial flow in the outer regions. This difference could be an important factor in solid-liquid separations.

The laser doppler anemometer is rapidly being employed to study swirling flows quantitatively. Orloff et al. [1973] studied some problems related to the vortex breakdown phenomenon (see Section 1.2.1) in a rotating tube and, more recently, Escudier et al. [1980] studied a confined vortex flow at high Reynolds numbers using LDA. The quantification of the core region using this technique is

exemplified in this study and led to the important conclusions regarding flow reversals previously mentioned in Section 1.2.1. Thew and his colleagues at the University of Southampton have been using LDA to study the mean velocity and turbulent intensities in a variety of swirling flows, including the hydrocyclone (see Bedi and Thew, 1973; Loader and Thew, 1975; and Thew et al., 1980). A recent report by Grabek et al. [1980] also illustrates the utility of using LDA for gas cyclones.

Loader and Thew [1975] measured instantaneous axial and tangential velocities in a vortex chamber using LDA. The exit tube had a mild contraction followed by a honeycomb flow straightener. The tangential velocity measured within the vortex chamber showed an unusual "kink" or shoulder in the outer "free" vortex region. The complementary axial velocity measurements indicated that this "kink" was caused by a complex multiple circulation zone induced by the exit design. The LDA measurements further showed that the axial and tangential turbulent intensities are about the same, even in regions where $\langle u_\theta \rangle$ was an order of magnitude larger than the mean axial velocity. For swirling flows, what mechanism keeps the turbulence isotropic? The question and answer go beyond the scope of this research.

1.2.3. Effect of polymer additives on secondary flows

Vortex formation for Newtonian fluids in draining tanks is a familiar phenomenon and can be inhibited by using mechanical devices (Hayduk and Neale, 1978) or by adding a high molecular weight polymer

(Balakrishnan and Gordon, 1971). Chiou and Gordon [1976] showed that only 3 wppm of Separan AP-273 reduces the maximum tangential velocity and the centerline axial velocity of a draining tank by a factor of 10. Chiou and Gordon attribute this phenomenon to the presumably large elongational viscosity of dilute polymer solutions. Coincidentally, inhibition of vortex stretching by polymers also plays a significant role in some explanations of drag reduction (see, e.g., Seyer and Metzner, 1969). Polymer additives, such as polyethylene oxide and guar gum, can also suppress flow induced cavitation (Ting, 1974). Both vortex inhibition and cavitation suppression by polymers could have important implications on hydrocyclone performance in which the secondary separation by the inner helical flow is significant.

The presence of a small amount of polymer can also have a dramatic effect on expanding and contracting motions. This phenomenon, exemplified in the work of Metzner et al. [1969] on converging flows of viscoelastic fluids (esp. Separan AP-30) at low Reynolds numbers, could also be important in hydrocyclones near the vortex finder or in the conical apex region. Even for fully developed turbulent flows in a square duct, Reischman and Tiederman [1975] have argued that the secondary motion in the corner of the duct for dilute polymer solutions is so strong that it can affect turbulent measurements in the buffer zone far from the corner. The separation efficiency and secondary flow structures within a hydrocyclone may similarly be altered by the presence of a high molecular weight polymer.

1.3. Objectives and Scope of This Research

Although a good qualitative understanding of the various mechanisms for solid-liquid separations in hydrocyclones is presently available, quantitative understanding is lacking. Several distinct flow structures such as helical flow, turbulent boundary layers, converging flows, and secondary circulation in the upper part of the hydrocyclone all have a direct influence on performance. The interactions among these (and other) flow structures are currently not understood--either experimentally or theoretically. One of the major objectives of this research is to provide an experimental basis from which important physical phenomena important for solid-liquid separations can be delineated. Toward this goal ten major tasks were completed during the course of this study. These are listed in Table 1.1 with references to specific sections of this dissertation where the results are presented.

Laser doppler anemometry (LDA) was the major experimental tool used. This non-intrusive technique permitted a quantitative study of the central core region of the hydrocyclone. These experiments are new and complement the earlier studies of Kelsall [1952] and Knowles et al. [1973]. One of the novel features of this work is the use of a high molecular weight polymer (Separan AP-30) to alter secondary flow structures. LDA is probably the only way this type of information could be developed accurately.

A systematic set of experiments was conducted to investigate the effect of feed pressure, split ratio, and vortex finder geometry

Table 1.1. Summary of problems studied for this research.

Task	Location of Results	Remarks
1. The Effect of Separan AP-30 on Solid-Liquid Separations in a 10-mm Hydrocyclone	See Dabir et al. [1980] and Section 1.1	The results found in this study provided ample motivation to develop the research reported in this dissertation.
2. Flow Visualization Study of the 3"-Hydrocyclone with a Contraction	Chapter 3	Numerous photographs and films were made of the mixing patterns to determine where detail velocity measurements should be made.
3. LDA Measurements in a 3"-Hydrocyclone with a Contraction	Chapter 4	One of the main objectives here was to quantify the flow reversals in the central vortex regions.
4. The Effect of Separan AP-30 on the Mean Velocity Profiles in a 3"-Hydrocyclone with a Contraction	Section 4.4	The objective here was to determine if vortex inhibition occurs in the core region.
5. LDA Measurement in a 3"-Hydrocyclone Satisfying "Optimal" Scaling Criteria	Section 5.1	Why should this design be "optimal" relative to others? An answer to this is given in Section 6.2.

Table 1.1 (cont'd.).

Task	Location of Results	Remarks
6. LDA Measurements for an Equal Area Discharge Hydrocyclone	Section 5.2	The results of this study provide some insights regarding the necessary conditions for flow reversals.
7. The Effect of Vortex Finder Design on the Mean Velocity Field and Flow Reversals	Section 5.3	Does the placement and the degree of a contraction in the vortex finder change the qualitative and quantitative flow patterns?
8. LDA Measurements of Axial Velocity for Fully-Developed Laminar Flow in a Circular Tube	Appendix A, Section A.5	This prototype problem provided an experiment to learn how to use the laser doppler anemometer.
9. Flow-Rate, Pressure-Drop Relationships for a 3"-Hydrocyclone	Appendix C	This data was useful (and necessary) to plan the LDA studies.
10. Viscosity and Drag Reduction Characteristics of Separan AP-30	Appendix B	The polymer solutions used for Task 4 needed some characterization. The % drag reduction in fully developed pipe flow was determined for these solutions.

on the mean axial and tangential components of the velocity at different levels in a 3"-hydrocyclone. Flow visualization studies were employed to identify specific regions within the flow domain where a quantitative set of velocity profiles would be useful.

Because flow reversals are quite common for swirling flows, the effects of the foregoing parameters on the morphology of the flow were examined. The transition from single-celled to multiple-celled vortex structures is quantified; some new and interesting results, which may eventually be translated into novel applications, emerged. Probably the most remarkable and surprising discovery, which helps to explain the scope of the research outlined here, is that a 2:1 contraction in the vortex finder induces an annular flow reversal back into the flow domain of the hydrocyclone: a sequence of experiments was designed to determine which physical parameters controlled this phenomenon.

Tables 1.2-1.5 define the conditions of each velocity profile measured. A total of 168 traverses were made and only a select number of these appear in this dissertation. An asterisk (*) is used to denote which profiles appear in graphical form. The others remain in our data files for subsequent analysis. Appendix D contains the actual data for a representative subset of the profiles defined in Table 1.4. These velocity profiles were developed in a 3"-hydrocyclone which satisfied the suggested scaling requirements of Rietema [1961a-d]. We feel that the actual data for these traverses would probably be most useful to another laboratory.

Table 1.2. Velocity profiles measured in the hydrocyclone with a 2:1 contraction in the vortex finder.

T = 20°C P _F ,psig	Geometry 2.5 c Z,cm	Split Ratio, Q _o /Q _u		
		0.25	4.0	∞
15	8	Z [*] ,θ	Z [*] ,θ [*]	Z,θ
	20	Z [*] ,θ	Z [*] ,θ [*]	Z,θ
	32	Z [*] ,θ [*]	Z [*] ,θ [*]	Z [*] ,θ [*]
10	4		Z, -	
	8		Z,θ	
	12		Z, -	
	16		Z, -	
	20		Z [*] ,θ	
	24		Z, -	
	28		Z, -	
	32		Z [*] ,θ	
5	8		Z,θ	
	20		Z [*] ,θ	
	32		Z [*] ,θ [*]	

Table 1.3. Velocity profiles measured in the hydrocyclone with a 2:1 contraction in the vortex finder for 100 wppm Separan AP-30.

T = 12°C 50% drag reduction P _F , psig	Geometry 2.5 c Z, cm	Split Ratio, Q _o /Q _u		
		0.25	4.0	∞
15	7	Z,-	Z,-	Z,-
	8	Z,θ	Z*,θ*	Z,θ
	19	Z,-	Z,-	Z,-
	20	Z,θ	Z*,θ*	Z,θ
	31	Z,-	Z,-	Z,-
	32	Z,θ	Z*,θ*	Z,θ

Table 1.4. Velocity profiles measured in the hydrocyclone which satisfy Rietema's optimal design criteria.

T = 12°C P _F , psig	Geometry 2.5 a Z, cm	Split Ratio, Q _o /Q _u				
		0	0.25	4.0	6.8	∞
18	20			-, θ*		
	1			Z*, -		
	2.2		Z*, -			
	2.5			Z, -		
	7		Z, -	Z, -		Z, -
	8	Z, θ	Z*, θ*	Z, θ		Z*, θ*
	15		Z, -	Z, -		Z, -
	19		Z, -	Z, -		Z, -
	20	Z*, θ*	Z*, θ*	Z*, θ*	Z*, -	Z*, θ*
	31		Z, -	Z, -		Z, -
15	32	Z, θ	Z*, θ*	Z, θ		Z*, θ*
	34.2			Z, -		Z*, -
	34.6					Z, -
10	20			Z*, θ*		-, θ
5	20	Z, -		Z*, θ*		Z, θ
2	20			Z*, -		

Table 1.5. Velocity profiles measured in the hydrocyclone with equal overflow and underflow areas.

T = 12°C P _F , psig	Geometry 2.5 d Z, cm	Split Ratio, Q _o /Q _u		
		0.25	4.0	∞
15	2		Z [*] , -	
	6	Z, -	Z, -	Z, -
	8	Z [*] , θ	Z [*] , θ	Z, θ
	18	Z, -	Z, -	Z, -
	20	Z [*] , θ	Z [*] , θ [*]	Z [*] , θ
	30	Z, -	Z, -	Z, -
	32	Z, θ	Z [*] , θ [*]	Z, θ
10	20	-, θ	-, θ [*]	-, θ
5	20	Z, -	Z [*] , θ [*]	Z, θ
2	20	-, θ	-, θ [*]	-, θ

Table 1.6. Velocity profiles measured in the hydrocyclone for other vortex finder geometries.

T = 12°C, P _F = 15 psig, Z = 32 cm		
Split Ratio Q _o /Q _u	Velocity Component Measured	Geometry see Figure 2.5
4	Z [*]	a, b, c, d, e
	θ [*]	a, c, d
	Z [*]	e, d

As mentioned in Section 1.2.1, two dimensionless groups (see Eqs. (1.4) and (1.5)) determine the behavior of the mean velocity field--the Ekman number and the Rossby number. In Tables 1.2-1.5 two independent parameters define each experiment: the feed pressure and the split ratio. Eq. (1.6) shows the relationship between Q_o/Q_u and the Rossby number. The relationship between P_F and the Ekman number, or equivalently the feed Reynolds number, is a little more complicated. This information is developed experimentally in Appendix C.

The following convention has been adopted to file the velocity traverses shown in Tables 1.2-1.5. For the mean axial profile,

$$\langle u_z \rangle(r, z) \rightarrow Z(z; P_F; Q_o/Q_u) . \quad (1.8)$$

For the mean tangential profiles,

$$\langle u_\theta \rangle(r, z) \rightarrow \Theta(z; P_F; Q_o/Q_u) . \quad (1.9)$$

For example, with $z = 8$ cm, $P_F = 15$ psig, and $Q_o/Q_u = 4$, the profiles for $\langle u_z \rangle$ and $\langle u_\theta \rangle$ from the axis to the outer wall are given by $Z(8;15;4)$ and $\Theta(8;15;4)$, respectively. If the reader would like to examine the actual data of one of the profiles listed in Tables 1.2-1.5, use of the above convention when making the request would be helpful.

CHAPTER 2

EXPERIMENTAL APPARATUS AND PROCEDURES

2.1. Flow Loop

A schematic of the flow loop used in this study is shown in Figure 2.1. The overflow and underflow streams from the hydrocyclone discharge freely into a large holding tank (200 liters) containing a cooling coil for temperature control. Some back pressure develops at the vortex and apex of the hydrocyclone because of the resistance to flow through the two copper pipes 170 cm in length. The inlet and outlet pressures around the hydrocyclone were measured manometrically. In all the studies reported herein, the hydrocyclone operated without an air core.

The flow loop was designed so that a portion of the flow could be recycled from the high pressure side of the centrifugal pump (Myer, QP 30-3) back into the holding tank. A surge tank (38 liters) in the feed line helped to reduce pressure fluctuations. The feed line (20 mm I.D., copper tubing) to the hydrocyclone contained a single gate valve, a manometer tap, and a pressure gauge. The nominal location of each is indicated in Figure 2.1. Flexible tygon tubing (19 mm I.D.) was used to connect the flow loop to the glass hydrocyclone. This permitted some movement in the test section which was useful for making velocity traverses.

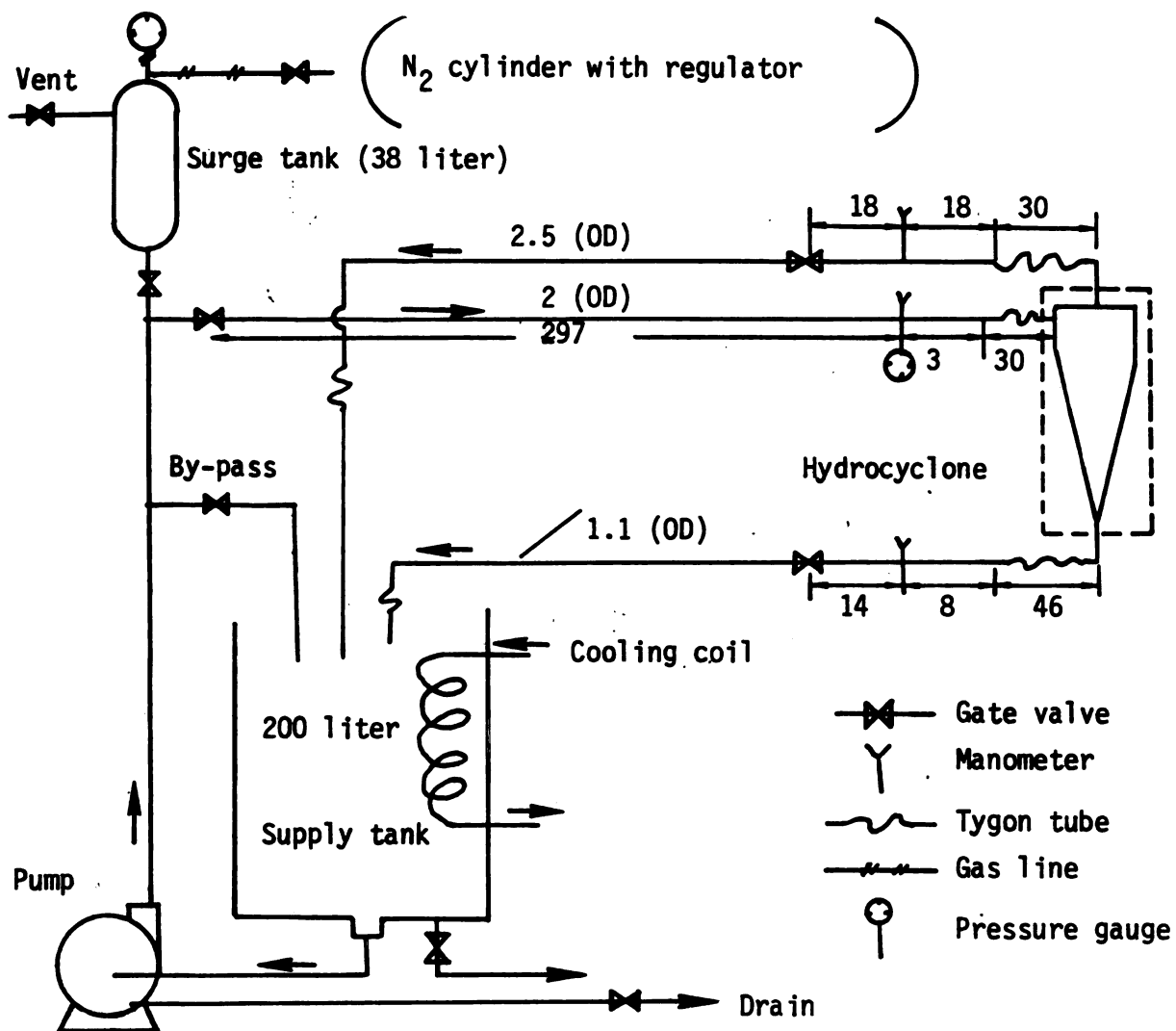


Figure 2.1. Flow loop (nominal lengths given in cm).

The 200 liter reservoir shown in Figure 2.1 was filled with tap water. The water quality was inspected for color and unusually large particles. Enough small scattering particles were present in the water so artificial seeding for the laser doppler measurements was unnecessary. The cooling water flow rate was adjusted to keep the water temperature in the supply tank constant at 20°C. The inlet and outlet valves were adjusted to fix the flow rate, split ratio, and pressure at the desired values. The flow rate was measured by recording the time needed to fill a precalibrated plastic container.

Some modifications in the flow loop were necessary so fresh polymer solutions could be injected into the feed line (Section 4.4). Figure 2.2 shows that an 87 liter tank (galvanized iron) was used to hold a concentrated polymer solution (2000 ppm) which was continuously injected into the suction of the centrifugal pump. The polymer reservoir was pressurized by connecting it to the same nitrogen cylinder as the surge tank. Pressure balance on the reservoir was maintained by a regulator. The concentrated polymer solution passed through 300 cm of 3.55 mm stainless steel tubing before being injected. A rotameter and small plastic valve were used to regulate the flow rate. This technique was followed to stretch the polymer before backmixing to the feed concentration (100 wppm). A plastic container was used to collect the overflow and underflow stream from the hydrocyclone so the extent of drag reduction (see Appendix B) of the spent liquid could be measured.

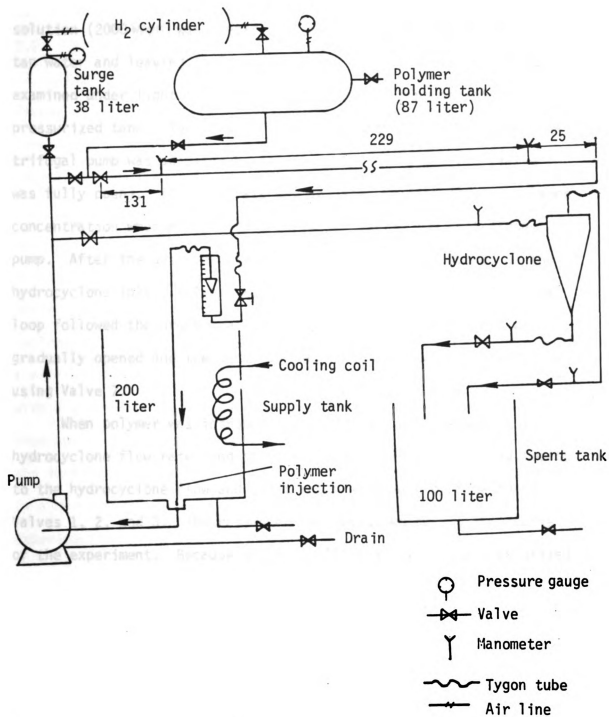


Figure 2.2. Flow loop for polymer studies.

To study the effect of a high molecular weight polymer on the flow structures inside the hydrocyclone, a concentrated polymer solution (2000 wppm) was prepared by dissolving Separan AP-30 in tap water and leaving it for twenty-four hours. The solution was examined under light for homogeneity before pouring it into the pressurized tank. The polymer flow rate to the suction of the centrifugal pump was adjusted by Valve 5 shown in Figure 2.2 (Valve 4 was fully open). The flow rate was adjusted to give 100 wppm polymer concentration when mixed with fresh water inside the centrifugal pump. After the desired polymer concentration was obtained at the hydrocyclone inlet, Valve 4 was closed. The operation of the flow loop followed the procedure as previously outlined. Valve 4 was gradually opened and the final polymer flow rate was adjusted by using Valve 7.

When polymer was introduced into the system, changes in the hydrocyclone flow rates and split ratio occurred. Final adjustments to the hydrocyclone flow and split ratio were made by fine tuning Valves 1, 2, and 3. The rotameter was monitored during the course of the experiment. Because of the small capacity of the pressurized tank used for polymer injection, these experiments were completed in about 40-50 minutes. After the velocity measurements were completed, the flow loop used for polymer injection was cleaned with fresh water and prepared for drag reduction measurements. The overflow and underflow streams from the hydrocyclone were mixed together

and the drag reduction characteristics of this composite solution were determined according to the procedure outlined in Appendix B.

2.2. The Hydrocyclone

The hydrocyclone* used in this study was made from pyrex (index of refraction ≈ 1.5) with dimensions as indicated in Figure 2.3. The optimal scale ratios recommended by Rietema are also listed in Figure 2.3 for comparison. To reduce optical distortion and minimize curvature effects, the hydrocyclone was surrounded with a plexiglass box (index of refraction ≈ 1.47) having flat surfaces. Glycerol (index of refraction ≈ 1.46) was placed in the space between the hydrocyclone and the plexiglass box. The hydrocyclone was attached to a flat plate (see Figure 2.4) mounted on a milling table which allowed horizontal movement in two directions with a precision of 0.0254 mm. Vertical adjustments were less precise and made with a hydraulic jack. For this study movement in the vertical was unnecessary. Once the test section was leveled in a horizontal plane, it remained fixed in this plane during the experiment.

Figure 2.5 shows the dimensions and designs of the various vortex finders studied in Chapter 5. A cylindrical aluminum rod was machined to slide inside the vortex finder. This allowed four additional configurations to be studied in addition to the one

*Professor Donald Woods of McMaster University kindly loaned us his 3"-hydrocyclone for this study. Velocity measurements for this equipment have been reported by Knowles et al. [1973] using a flow visualization technique.

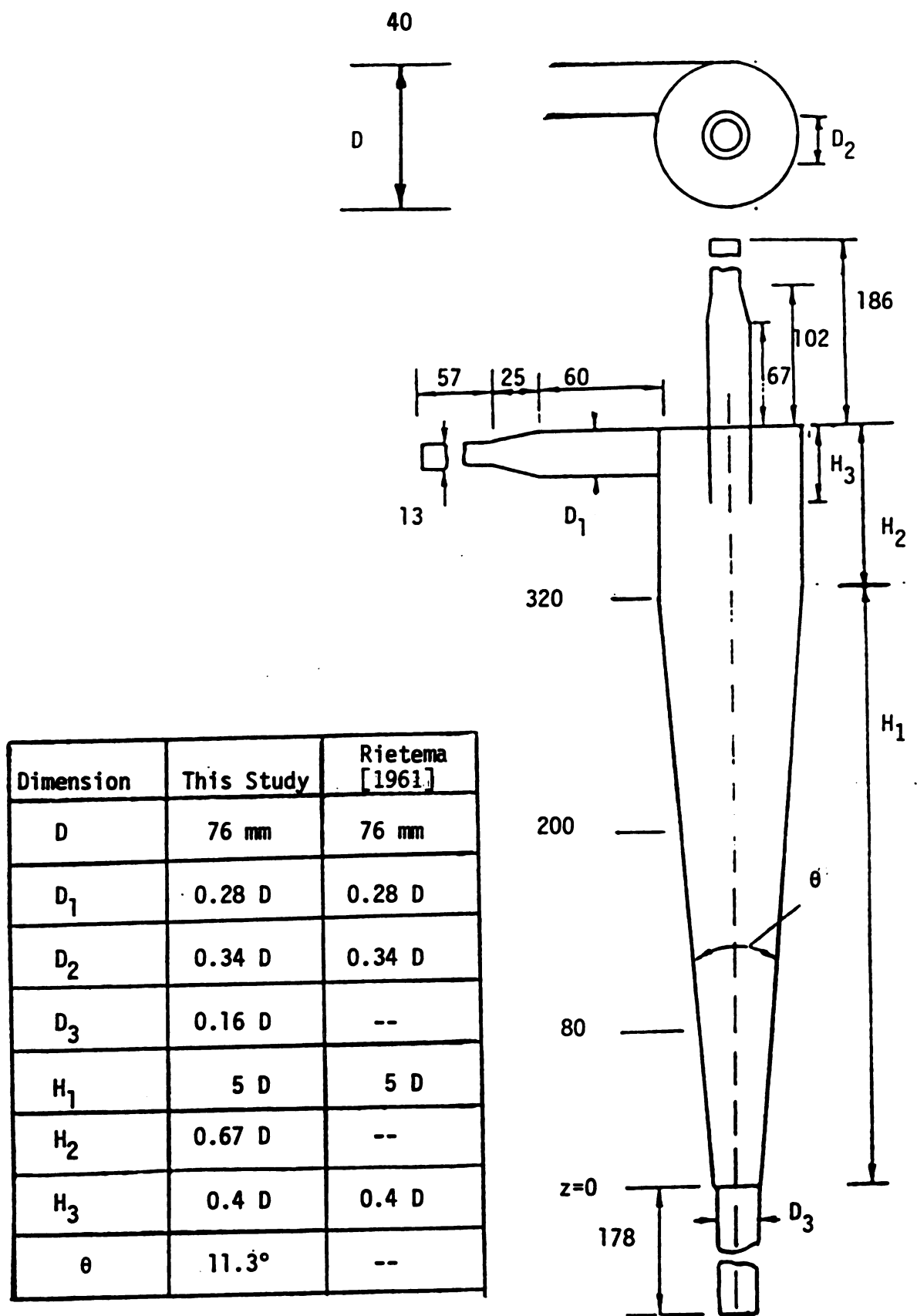


Figure 2.3. Dimensions of the Hydrocyclone used in this Study (nominal lengths given in mm).

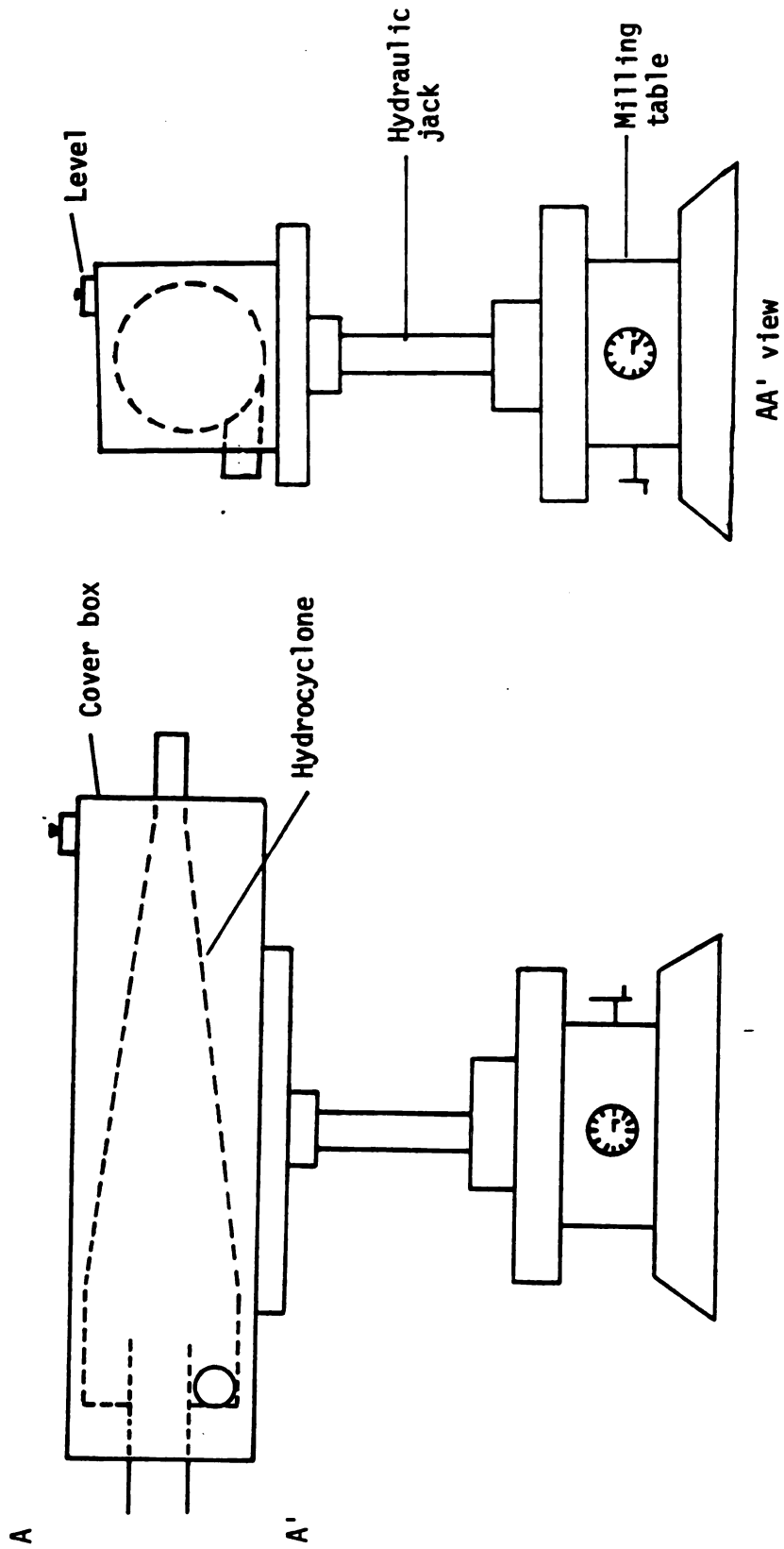


Figure 2.4. Side and front view of the test section.

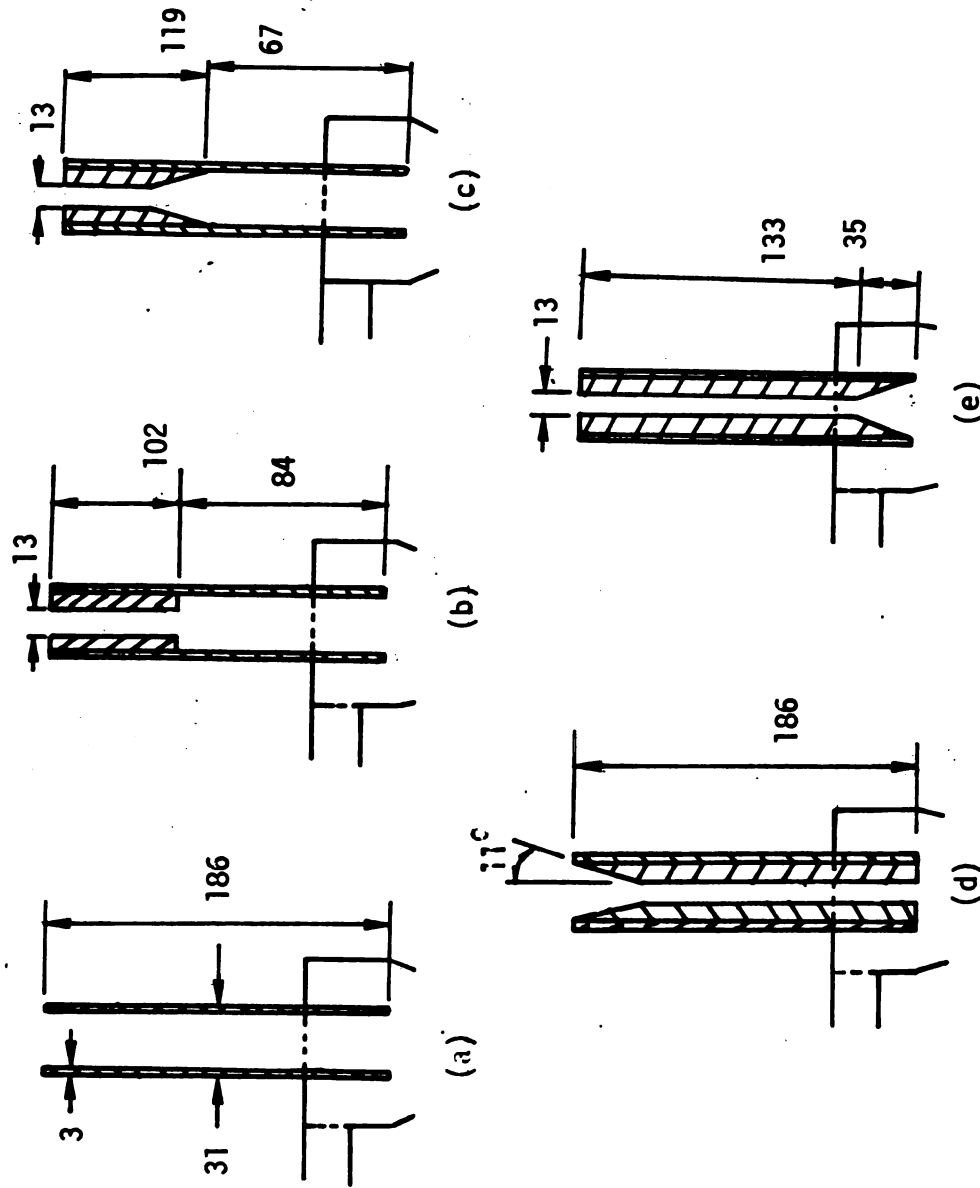


Figure 2.5. Vortex Finder Configurations Studied (all dimensions in mm).

defined by Figure 2.3. Cases (b) and (c) compare the effect of an abrupt and gentle contraction a significant distance from the entrance of the vortex finder, whereas Cases (d) and (e) place these contractions at the entrance. Case (c), which contains a 2:1 contraction, was originally studied by Knowles [1971]. Case (a) satisfies the original design criteria of Rietema. An interesting result of this research is the discovery that the core flows of Cases (a) and (c) are very different.

The results of a flow visualization study are given in Chapter 3. The specific connections between the hydrocyclone and the flow loop for these experiments and those discussed in Chapter 4 are slightly different. Figure 2.6 shows that a hypodermic needle (O.D. \approx 0.7 mm) with a flexible joint was fixed in the overflow and underflow exits. By inserting the long needle (\approx 30 cm) through the flexible joints, different places within the flow field could be marked with either Rodumine B dye (red) or green food coloring. The density of these dyes is approximately the same as water. The 3"-hydrocyclone obtained from Professor Woods originally contained a 2:1 contraction in the vortex finder so it could be interfaced with a standard fitting (see p. 20 in Knowles, 1971). Preliminary flow visualization studies (see Chapter 3) showed that the contraction in the vortex finder (see Figure 2.5c) causes a flow reversal which affects the flow patterns throughout the hydrocyclone. This surprising discovery prompted the study summarized by Chapter 4. Unfortunately, our experiments were not designed for simultaneous

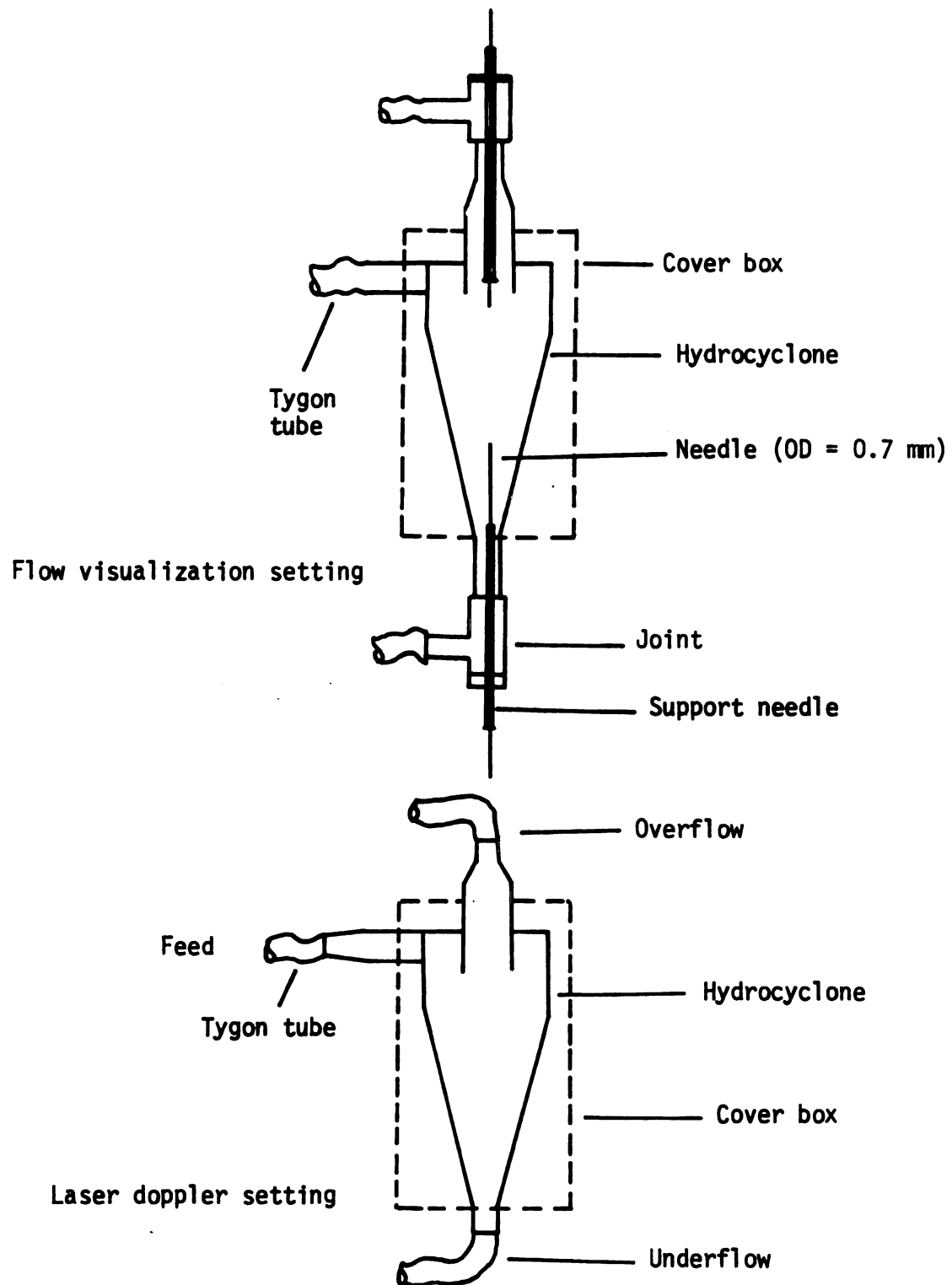


Figure 2.6. Schematic diagram of test section for laser doppler and flow visualization setting.

flow visualization and mean velocity measurements, so Chapter 3 only gives a visual map of the secondary flows for the original hydrocyclone on loan from McMaster University. Quantitative mean velocity data obtained using LDA are summarized in Chapters 4 and 5.

2.3. The Laser-Doppler System

Figure 2.7 shows the relative position of each part of the TSI laser-doppler anemometer used in this study. All experiments were performed in the dual-beam mode with forward scattering. A 35 mW He-Ne laser was used as a light source. Frequency shifting was necessary in this study to define the direction of flow and to reduce fringe bias. The system consists of an optics module and a down-mix circuit. The optics module contains an acousto-optic cell (Bragg cell) which shifts the frequency of one of the laser beams issuing from the beam splitter by 40 MHz. This is too high for the range of velocities encountered in this study, so a down-mix circuit was used to shift the frequency in twelve unequal increments from 2 KHz to 10 MHz.

The counter processor used in this study was specifically designed for processing signals from a photomultiplier of a laser-doppler anemometer. The data display gives an analog voltage as output which is directly proportional to either the mean velocity or the mean doppler frequency. During each experiment, the mean frequency of the doppler signal at each location in a traverse was read directly off the display panel and recorded. The mean velocity

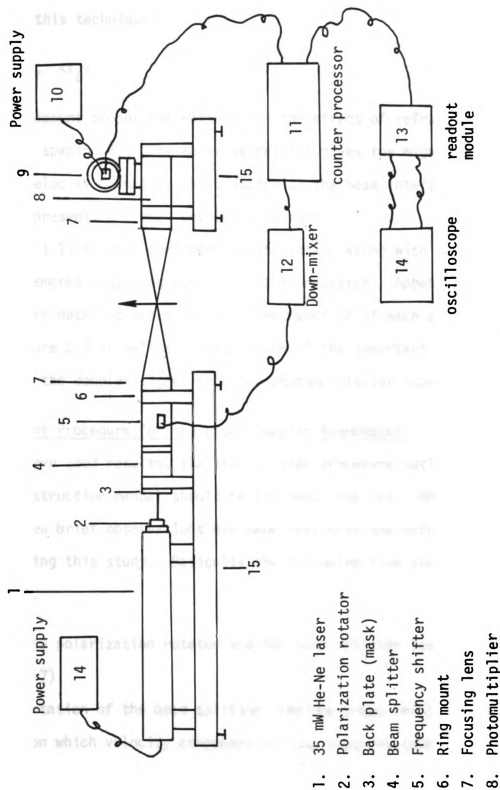


Figure 2.7. Schematic of laser doppler anemometer for forward scattering mode of operation.

was then calculated from the expression (see Appendix A for a brief tutorial of this technique)

$$\langle v \rangle = d_f \langle f_D \rangle \quad (2.1)$$

taking into account proper corrections for the effect of refraction on the fringe spacing d_f . The above expression gives the magnitude of the mean velocity normal to the bisector of the beam intersection; $\langle f_D \rangle$ represents the mean doppler frequency.

Table 2.1 lists each component in the set-up along with a few summary remarks regarding its use in this research. Appendix A contains a more detailed description of the function of each component in Figure 2.7 as well as a discussion of the important steps in processing the doppler signal from the photomultiplier tube.

2.4. Alignment Procedure for the Laser Doppler Anemometer

To achieve good results, the step-by-step procedure outlined in the TSI instruction manual should be followed (see TSI, 1982a). Here only a few brief observations are made regarding the methodology developed during this study. Basically the following five steps were followed.

- (1) Set up the polarization rotator and the beam splitter (see Figure 2.7).

The orientation of the beam splitter (and the Bragg cell) depends on which velocity component will be measured (see Appendix A). When the dual-beam mode is used, the beam intensity

Table 2.1. Components of the TSI laser doppler anemometer used in this study.

Item (see Figure 2.7)	TSI model number	Description	Remarks
1	9126-150A	He-Ne laser, 35 mW	---
2	9101-2	Polarization rotator	Only for He-Ne laser
3	---	Back plate	Mask
4	9115-2	Beam splitter	Splits the beam intensity 50-50% or 99.5-0.5%
5	9180-2A	Frequency shift assembly	2 KHz-40 MHz
6	9176	Ring mount	---
7	9118	Focusing lens (Achromat)	83 mm O.D., 250 mm F.L.
8	9140	Receiving optics assembly	---
9	9160A	Photomultiplier	200 MHz response
10	9165	Power supply	---
11	1990	Counter processor	100 MHz clock
12	9186	Down mixer	---
13	1992A	Readout module	Direct velocity display
14	465 M	Portable oscilloscope	100 MHz two channels

should be equally divided. The beam splitter is designed to do this provided the direction of polarization is perpendicular to the plane spanned by the two issuing beams. The polarization rotator, which is mounted on the front of the laser, is marked for the proper orientation but fine adjustments were made by simply turning the rotator until the two beams were visually of equal intensity.

(2) Set up the Bragg cell for frequency shifting.

The laser beam should be parallel to the mounting base for the Bragg cell to function properly, so care should be exercised in leveling the laser (see TSI manual, 1982b). Because the direction of the fringe movement (see Appendix A) depends on which beam enters the Bragg cell, this should be decided before mounting this optical component. For axial velocity measurements the Bragg cell was set up so the fringes moved in the opposite direction as the fluid in the outer region. Likewise, for tangential velocity measurements the cell was set up so the fringes moved in the opposite direction of the fluid. Frequency shifting causes the laser beam to split into several (sometimes four) closely spaced, parallel beams. The only one of interest, however, is the one which strikes the alignment mask at the 50 mm circle. Figure 2.8 shows a schematic of what is typically observed. The tilt in the Bragg cell is adjusted until the intensity of the beam on the 50 mm circle is about 75% of the original. The other minor beams

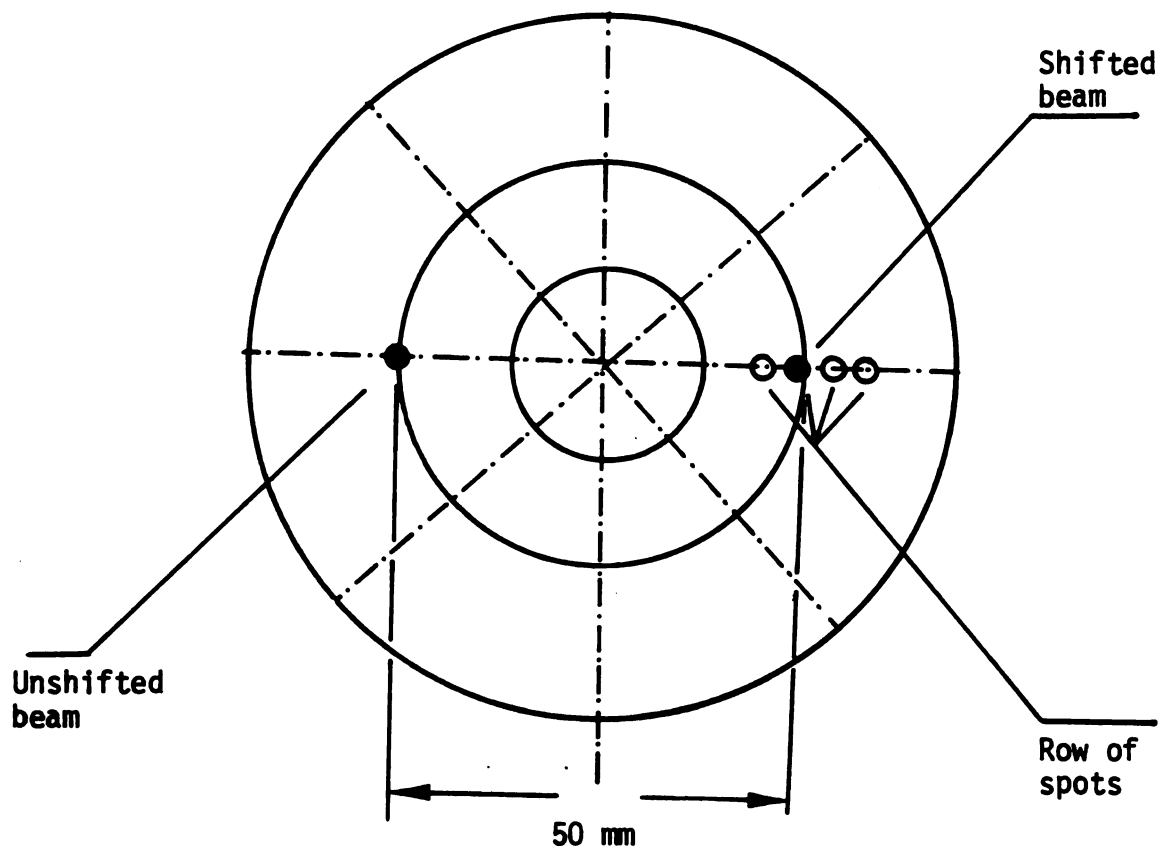
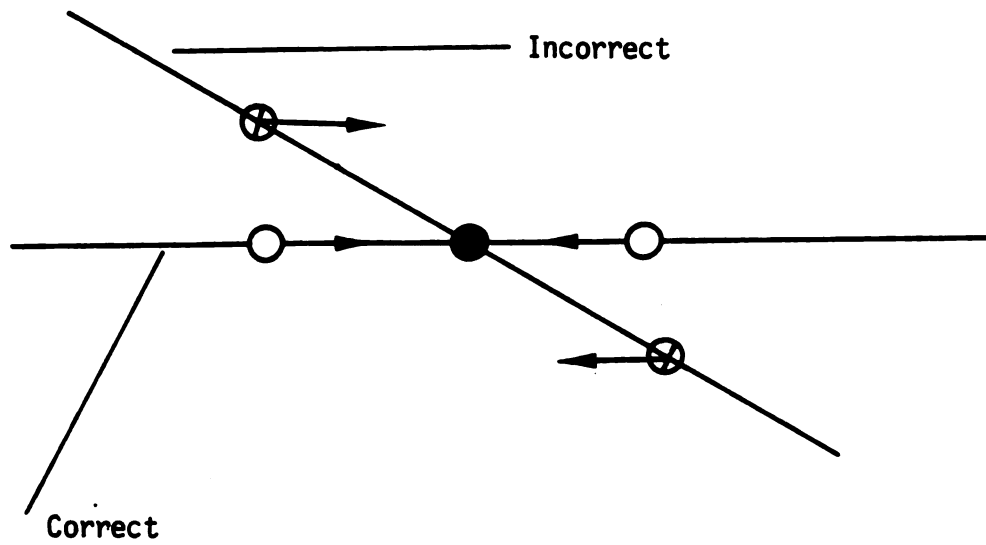


Figure 2.8. Shifted and unshifted beam location as seen on the alignment mask.

are blocked at the test section with a beam blocker. To avoid damage to the Bragg cell, the frequency shifter should not be turned on unless the Bragg cell has been connected to the A/O cell jack on the back of the frequency shifter module. This and other precautions listed in the instruction manual should be carefully observed.

- (3) Install the transmitting optics and adjust for polarity and beam crossing.

The transmitting optics assembly is positioned so that the optical axis is perpendicular to the test section. The axis of the test section, which is not in place during this adjustment, should be approximately 250 mm from the focusing lens (see Figure 2.7). The beam crossing in air is projected onto the wall by placing a microscope objective (eyepiece) near the focal point of the transmitting lens. By moving the eyepiece back and forth across the focal point, the horizontal or vertical alignment of the beam can be checked (see Figure 2.9). Fine adjustments can be made by turning the compensating wedge in the Bragg cell (see TSI instruction manual). It is important that this adjustment be made carefully since the refraction corrections (see Appendix A) assume that the beams enter the test section either in a horizontal plane (axial velocity measurements) or in a vertical plane (tangential velocity measurements).



● Beam crossing

○ Incident beam

⊗ Incident beam

Figure 2.9. Projection of beams to check the crossing of the beams.

(4) Align the test section.

A small diameter wire (O.D. ≈ 0.44 mm) is used to locate the center of the hydrocyclone. The wire is coated with an anti-reflective paint. Both ends of the wire are fixed in the center of two small fittings. These fittings are machined from aluminum and designed to fit the outlets of the hydrocyclone. By tightening two thumbscrews, the coated wire can be placed firmly in the center of the hydrocyclone. By slowly opening the inlet valve, the hydrocyclone is filled with water, and any trapped air in the hydrocyclone is removed. Both ends of the overflow and underflow are sealed by tightening the ends of the wire. The test section is raised until the laser beams strike the wire. By moving the test section horizontally, the beam crossing is centered on the wire. The minor laser beams induced by the Bragg cell are blocked by simply mounting on a magnet two small pieces of stainless steel plates which have been coated with an antireflective paint. The axial location of the beam crossing on the wire is located by moving the milling table forward and backward while viewing through the pinhole of a calibrated ruler positioned on the top surface of the hydrocyclone cover box. The axial reference point is the end of the apex region (see Figure 2.10). When the wire and the calibrated ruler are positioned correctly on the test section, the center wire can be viewed from all pinholes on the rule along the axis of the hydrocyclone. Once the beam crossing is located on the

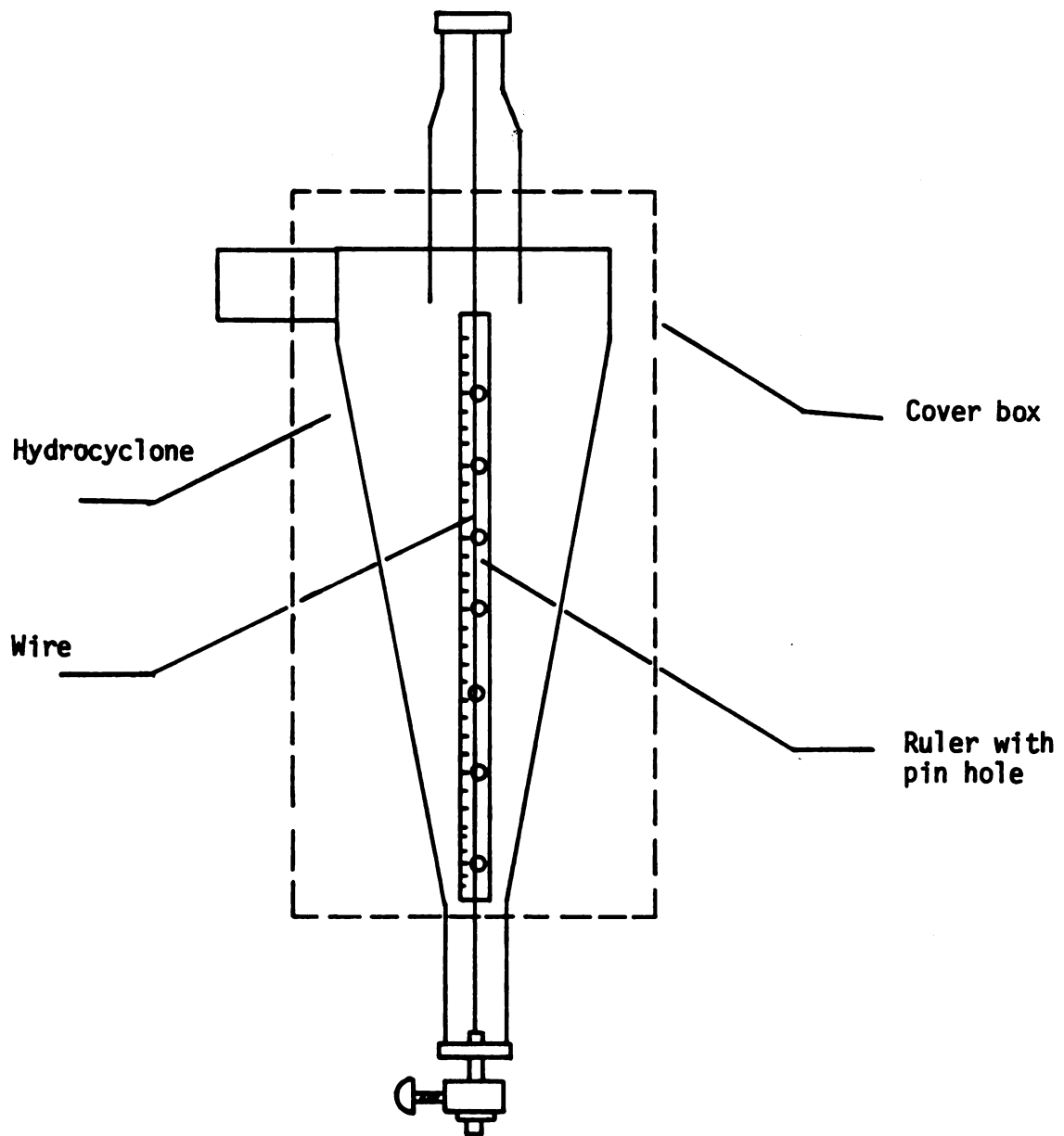


Figure 2.10. Test section set-up to locate center of the hydrocyclone.

center of the hydrocyclone at the desired axial location, the wire is removed from the test section and the hydrocyclone is gently connected to the flow loop without misaligning the test section. The cover box of the hydrocyclone should be perpendicular to the two laser beams. This is checked by using a mirror to reflect the laser light back onto a transparent sheet of paper. Final adjustments are made by either rotating the top of the milling table or by "jimmying" the test section with small pieces of paper.

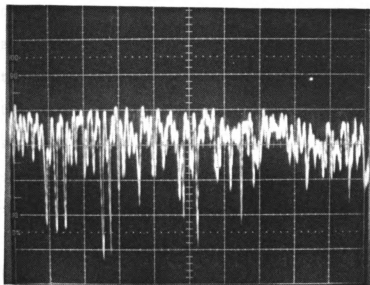
(5) Set up the receiving optics and photomultiplier tube.

The receiving optics assembly is positioned along the optical axis, allowing approximately 250 mm between the center of the hydrocyclone and the collecting lens. The best focus of the scattered light from the beam crossing is achieved by moving the receiving optic lens back and forth until the image viewed by an eyepiece is as small and clear as possible. The x-y adjustment thumbscrews on the photodetector mounting plate are used to move the image to the center of the eyepiece. The eyepiece is then removed from the mounting plate and the photodetector is attached.

2.5. Procedure for Obtaining Good Doppler Signals

The photomultiplier tube is connected to the oscilloscope. The x-y thumbscrews on the photomultiplier are adjusted until the output of the scope appears as shown in Figure 2.11a. Each peak

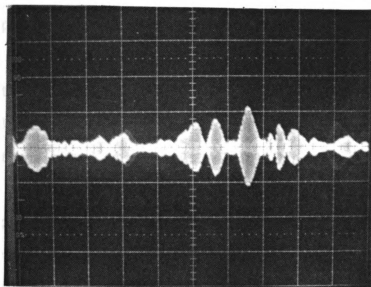
Volts
(50 mv/div)



Time (1 ms/div)

(a) Output of the photomultiplier

Volts
(10 mv/div)



Time (100 μ s/div)

(b) Output from the signal processor at
a low sweep speed

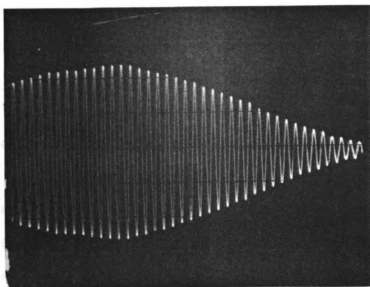
Figure 2.11a-b. Typical doppler signals obtained from the signal processor.

contains velocity information. At high sweep speeds these peaks can be expanded to show a doppler signal (see Appendix A for a discussion). After proper alignment, the photomultiplier output is connected to the signal processor. The filtered output from the signal processor is displayed on the oscilloscope. As oscilloscope sweep speed is increased, the pedestal component and the doppler frequency component of the signal appear. The high pass filter is positioned so the pedestal component and any signal asymmetry are removed without losing the doppler signal.

Figure 2.11b shows several doppler bursts at a low sweep speed. If the sweep speed is increased, the signal expands on the oscilloscope screen from which the doppler signal is easily obtained. Figure 2.11c is a complete doppler burst at a high sweep speed which has been properly filtered. The amplitude of the signal varies periodically from a minimum to a maximum. The maximum amplitude corresponds to scattered light coming from the central region of the probe volume with high light intensity. Figure 2.11d is a properly filtered signal which shows multiple bursts as a result of more than one particle passing simultaneously through the probe volume. To obtain these high quality signals several parameters related to the signal processor (see Figure 2.7) must be selected. A brief summary of these details is presented in Appendix A after the equipment shown in Figure 2.7 has been discussed.

When the internal wall of the hydrocyclone is struck by the beam crossing, the signal at a high sweep speed will appear as shown

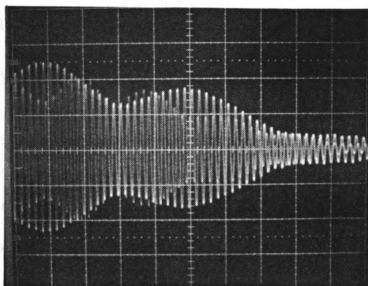
Volts
(10 mv/div)



Time (20 μ s/div)

(c) Properly filtered doppler signal

Volts
(10 mv/div)



Time (10 μ s/div)

(d) Multiple doppler signals due to several particles

Figure 2.11c-d. Typical doppler signals obtained from the signal processor.

in Figure 2.12. This position of the beam crossing on the wall can also be checked by visual inspection. The frequency of this signal should be the same as the shifted frequency of the beam. For a frequency shift of 1 MHz, this corresponds to a peak to peak distance of 1 $\mu\text{s}/\text{div.}$ on Figure 2.12.

The analog signals proportional to the instantaneous axial velocity are shown in Figure 2.13. Figure 2.13a is the analog output of the signal from the core region near the center of the hydrocyclone, and Figure 2.13b shows the signal from the outer region at the same axial location. The flow conditions and signal processor settings are similar for both measurements. This illustrates that axial velocity fluctuations in the core region are higher than those in the outer region. In this research, only the long time average (≈ 10 sec) of these signals are recorded and analyzed.

2.6. Data Analysis and Consistency Checks

In this study, the axial and tangential components of the mean velocity were measured using LDA. The radial component was estimated by using a material balance (see Section 4.1). Each axial velocity profile was checked for consistency by computing the underflow rate Q_u from $\langle u_z \rangle (r,z)$ and comparing the result with the measured rate. The difference was always less than 5%. Near the axis of the hydrocyclone, the axial velocity is very large for the conditions studied ($\approx 200\text{--}400$ cm/s) and, because of a reverse flow, drops off rapidly to zero over distances ≈ 5 mm. Although the velocity gradients were very steep ($\approx 10^3 \text{ s}^{-1}$), the mean velocity

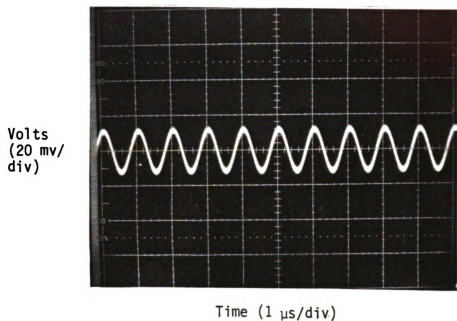
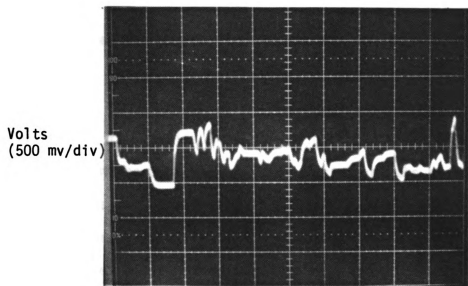
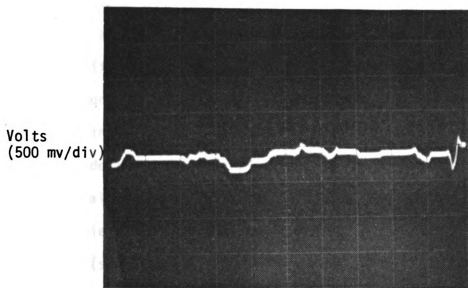


Figure 2.12. Output of the photomultiplier tube when the beam crossing intersects the hydrocyclone wall.



Time (500 μ s/div)

(a) Core region



Time (500 μ s/div)

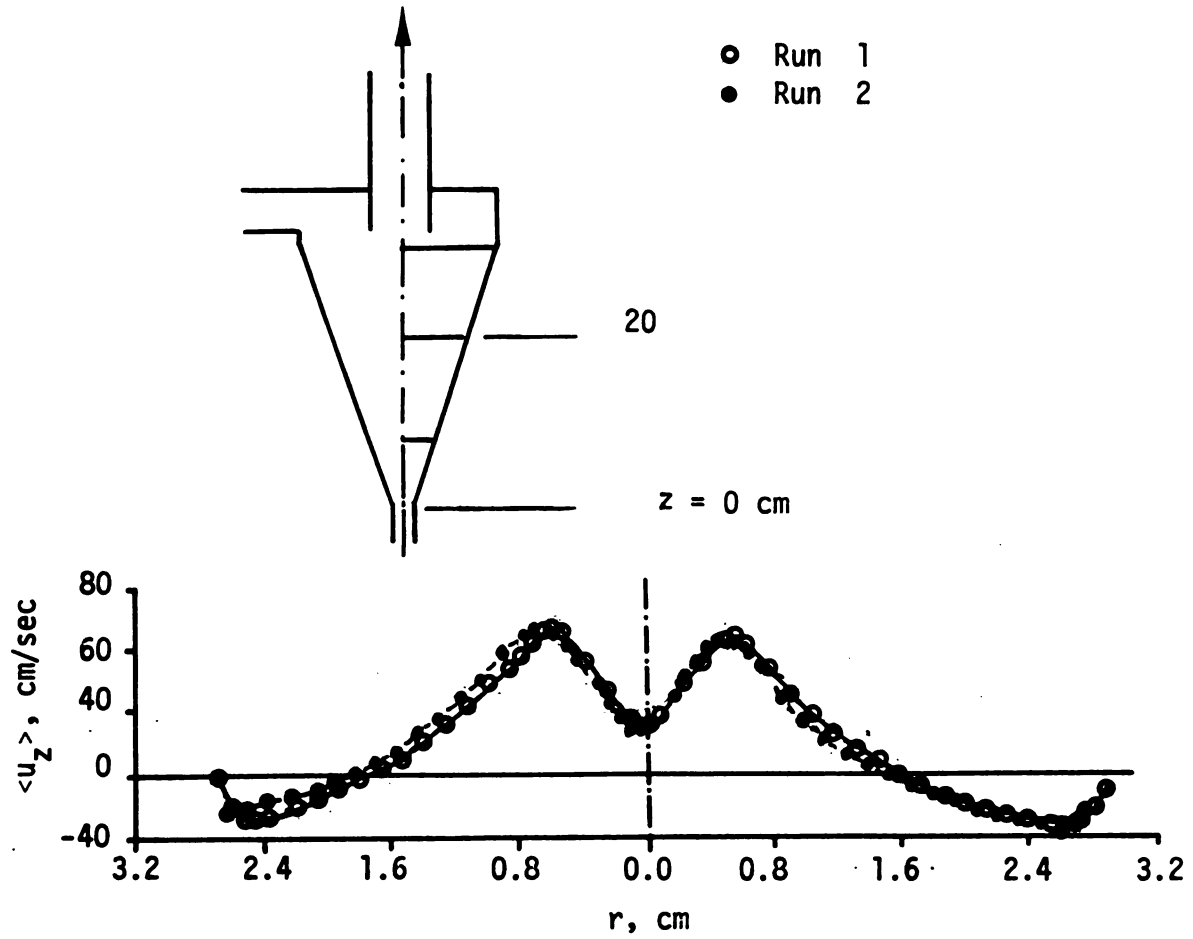
(b) Outer regions

Figure 2.13. Instantaneous axial velocity in the hydrocyclone (illustrative purposes only).

profiles measured in the core region were very stable and reproducible. Figure 2.14 shows typical traverses obtained on different days. The symmetry in the axial velocity should also be noted. Velocity data for many of the studies presented in Chapters 4 and 5 were taken only between the center of the core region and the hydrocyclone wall. It is noteworthy that the asymmetry in the velocity field, which is surely very strong in the upper portion of the hydrocyclone near the feed entry, has essentially disappeared in the conical section.

The velocity profiles were all corrected for index of refraction effects. The details of this procedure are delegated to Appendix A. Generally the most significant correction was in the radial position. Some experimentally determined points had to be adjusted by as much as 40% for the axial velocity and by 80% for the tangential velocity. Thus, the location of the axis of symmetry is crucial. In this study, we assumed that the flow was axisymmetric and thus made the final alignment between the test section and the light source by defining the center of the hydrocyclone as coinciding with a local extremum in the mean axial velocity. This procedure was convenient and agreed closely with using the wire previously discussed (see Figure 2.10).

When the center of the core was located, the position was marked as zero radius. The mean velocity distribution was obtained by moving the test section by small increments along the radius of the hydrocyclone. An increment advancement of the milling tables moves



Characteristics of Experiment	
vortex finder	Figure 2.5a
P_F	15.4 psig
P_0	13.6 psig
P_u	13.8 psig
Q_o/Q_u	∞

Figure 2.14. Symmetry and Reproducibility of Velocity Profiles.

the test section 0.024 mm. The traverse of the milling table and the mean velocity (or, frequency) were recorded on the data sheets (see Appendix D). To carry out a consistent policy in data recording, all information on the counter processor was recorded. During the course of the experiments, the flow conditions were monitored continuously. No significant changes occurred during any of the experiments.

CHAPTER 3

FLOW VISUALIZATION STUDIES

The qualitative flow patterns in a 3"-hydrocyclone were examined by dye injection for three different split ratios. Table 3.1 defines the parameters for each series of experiments and Figure 2.3 gives the dimensions of the hydrocyclone used. Rodamine B and a green food color were used to visualize the flow and the results were photographed. This information was valuable in planning the quantitative study of the velocity profiles using the laser doppler anemometer.

Figure 3.1a shows the result of injecting a green dye into the apex region of the hydrocyclone operating at a split ratio of 4.0. The hypodermic needle, which is slightly off-center and inserted some distance into the apex region, rotates freely with the flow. The stability and coherence of the central core region is remarkable. Little mixing with the outer swirling flow is evident, but this does not mean the absence of turbulent transport in the flow or radial directions. The existence of this flow structure presumably depends on an interaction between the downward moving boundary layer structure and the geometry of the apex region. For the flow conditions here (see Table 3.1) the reversal of the outer helical flow (see Figure 1.1) apparently occurs deep within the conical region, ≈ 4 cm from the bottom exit.

Table 3.1. Scope of flow visualization studies.

Series	Pressure psig P_F	Split Ratio Q_0/Q_u	Flow Rates cc/sec		Reynolds Number Re_F
			Q_0	Q_u	
I	5.2	4.0	400	100	24,850
II	5.2	0.24	96	400	24,651
III	5.2	∞	590	0	25,297



(a) Injection from apex only

$$Q_0/Q_u = 4.0$$



(b) Green dye injected from apex; red dye from vortex finder

Figure 3.1. Flow visualization of the core region for Series I.

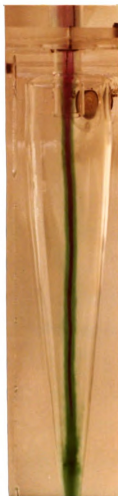
An interesting feature of Figure 3.1a is the appearance of a lightly colored sheath of upward moving fluid which surrounds a more darkly colored core of fluid moving at a much higher velocity. The green dye seems to persist around the core region after the dye supply has been interrupted. This nearly stationary layer, or "mantle", of fluid is due to a reverse flow which starts inside the vortex finder and surrounds the upward moving core of fluid.

Figure 3.1b shows an interesting discovery. A flow reversal within the vortex finder, which has a 2:1 contraction, causes an annular flow countercurrent to the upward flow on the axis. This secondary flow, which is surprisingly stable, is only 3 mm thick, yet extends over more than half of the length of the hydrocyclone. The diameter of the core fluid is also about 3 mm, so its length to diameter ratio is approximately 10^2 . The flow patterns shown in Figure 3.1 were unexpected and have raised many fundamental questions related to the performance of hydrocyclones. Clearly, the small secondary flows can have an important effect over the entire flow field. Figure 3.1b illustrates the possibility that two boundary layers separated by a significant distance (one deep in the apex region and another deep within the vortex finder) can still interact by ejecting two fluid streams which pass countercurrent to each other. This intriguing phenomenon could perhaps be exploited in the design of a novel classifier or separator.

Figure 3.2a illustrates the same flow structures as Figure 3.1, but now the red dye is introduced below the vortex finder with the



(a) Green dye injected from apex; red dye below the vortex finder



(b) Green dye from apex; red dye from vortex finder

Figure 3.2. Flow visualization of composite flows in the core region for $Q_0/Q_u = 4.0$ (Series I).

injection needle stabilized against the inner wall of the vortex finder. The swirling pattern of the flow is clearly evident. From this photograph a rough estimate of the pitch angle is 20° . For helical flow with zero radial velocity this implies that the ratio of axial to tangential velocity in this region is ≈ 0.36 , which should be viewed only as a crude guess.

The mixing outside the core region is very efficient as indicated by the rapid spread of the red dye in Figure 3.2a. Still, this is mainly confined to an upward swirling flow which runs counter-current to a downward outer helical flow (see Figure 1.1 again). Furthermore, the red dye is unable to penetrate the jet-like core flow (marked green) issuing from the apex region. Note also the faint trace of red dye surrounding the green core, which is the reverse flow illustrated in Figure 3.1b. The important conclusion from Figure 3.2a is that the annular reverse flow unambiguously comes from the outer flow inside the vortex finder tube rather than the axial core flow. Figure 3.2b shows the result of injecting green dye into the upward swirling flow which begins in the apex region and red dye into the reverse flow from the vortex finder. The dark green annular flow is part of the same upward flow marked initially by the red dye in Figure 3.2a. Note that the movement of the green fluid to larger radial positions is very restrictive. The central core in Figure 3.2b is entirely marked by red dye and extends deep into the apex region. The jet-like upward core flow, shown in the previous photographs, does not appear here, probably

because the dye needle has been extended into the apex region beyond the point where the jet forms. This disturbance has changed the typological structure of the flow.

The sequence of flow visualization photographs from Series I has shown the existence of four distinct, simultaneous, countercurrent flows in the conical section of a 3"-hydrocyclone. This four cell structure is very sensitive to end conditions in the vortex finder and in the apex. Earlier research (see, esp., Binnie, 1957) showed the possibility of three cells, but as far as we know this is the first report of four cells. Many additional photographs and films were taken and analyzed. Figure 3.3 portrays the composite results and conclusions of this analysis. The axial and tangential velocity profiles across the four cells discovered here were measured quantitatively using LDA; the results are reported in Chapter 4.

Reducing the split ratio eliminates the upward jet-like core flow shown in Figures 3.1a-c. For a split ratio of 0.25, a downward jet-like core flow issues from the vortex finder as shown by Figure 3.4a. No upward flow on the axis was ever observed for Series II, even when the needle shown in the apex was withdrawn as in Figure 3.1a. In a certain sense, Series II is just Series I turned upside down. The details of the vortex finder contraction and the convergence angle of the apex region are certainly important features in determining which jet flow will appear, but the split ratio may be the ultimate factor. It is tempting to speculate on the possibility that a jet flow could issue simultaneously from

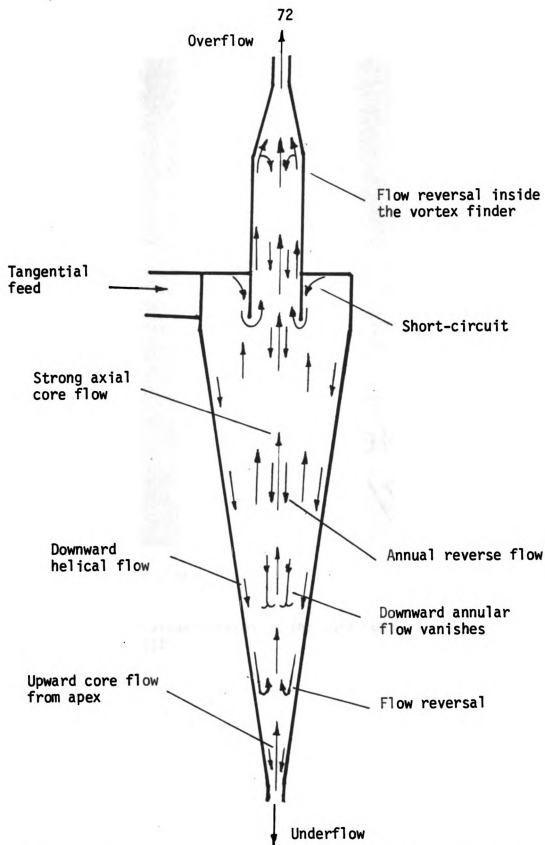


Figure 3.3. Flow patterns observed in the 3"-hydrocyclone using dye injection.



(a) $Q_0/Q_u = 0.25$



(b) $Q_0/Q_u = \infty$

Figure 3.4. Flow visualization of the core region for Series II and III.

both the vortex finder and the apex region with a stagnation plane separating them somewhere in the hydrocyclone body. In Chapter 5 data are presented which support this conjecture (see Figure 5.5).

Figure 3.4b implies that the outer helical flow (see Figure 1.1 once again) penetrates deep into the apex region even for an infinite split ratio. Even though the feed is introduced near the vortex finder at the top of the hydrocyclone, it does not simply short-circuit to the vortex finder. The swirling outer fluid still drives the boundary layer down into the conical region until the pressure builds up too much and causes the fluid to reverse direction.

Figure 3.5 shows a composite of the flow patterns observed in Series II and III. An interesting distinction between these results and the ones summarized by Figure 3.3 for Series I is the reduction in the number of cellular structures. For $Q_0/Q_u = 4.0$, four cells were observed. However, for $Q_0/Q_u = 0.25$ only three cells were detected, and for $Q_0/Q_u = \infty$, only two cells. Thus, the split ratio has an important influence on the secondary flow patterns in a hydrocyclone operating without an air core.

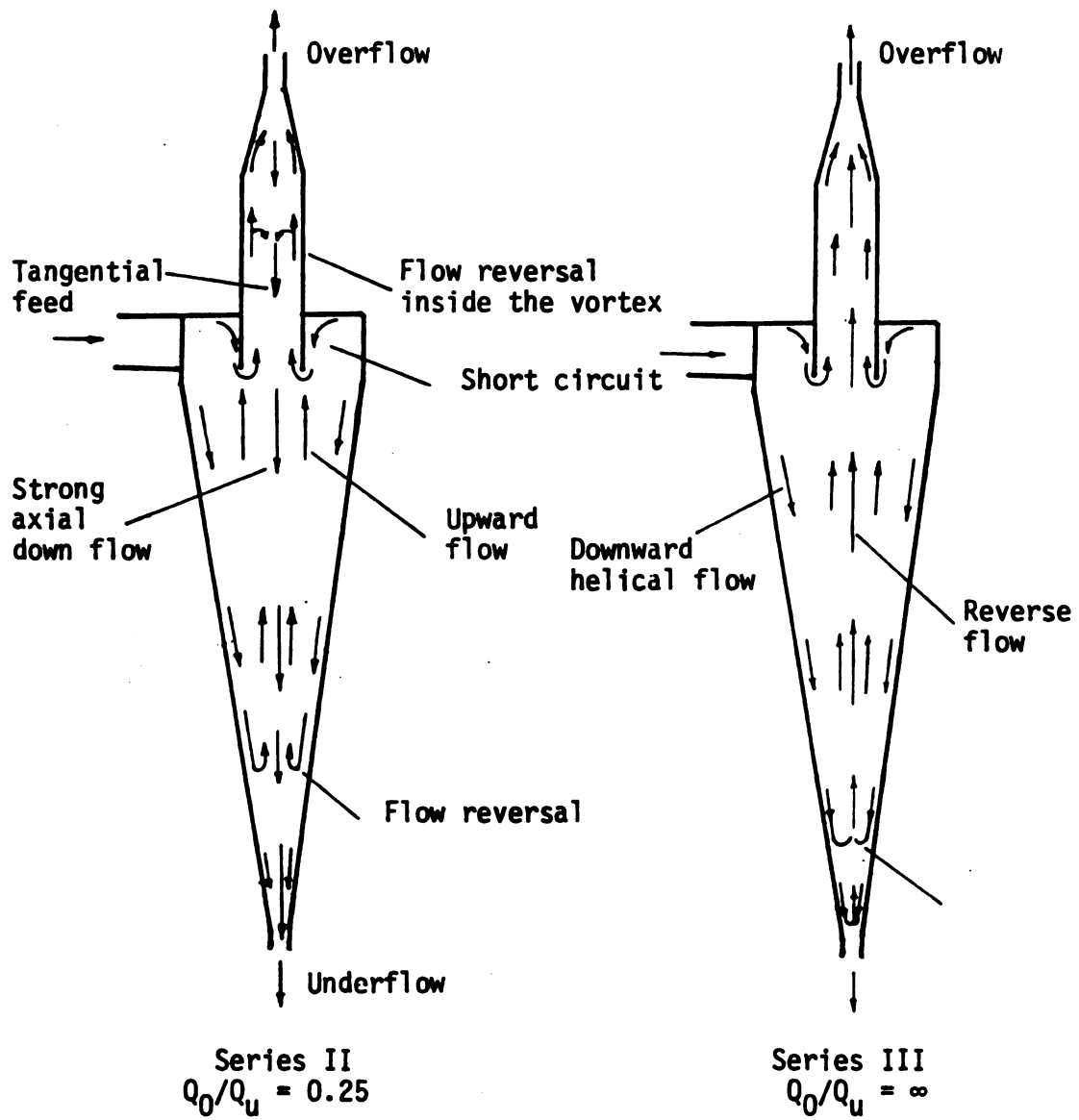


Figure 3.5. Composite results of flow visualization study for Series II and III.

CHAPTER 4

VELOCITY MEASUREMENTS IN A 3"-HYDROCYCLONE WITH A 2:1 CONTRACTION IN THE VORTEX FINDER

4.1. Axial and Tangential Profiles

Figure 4.1 shows how the axial component of the mean velocity varies with radial and axial position. These quantitative profiles are consistent with the flow visualization studies previously mentioned. The traverses at $z = 20$ and 32 cm definitely show a reverse flow over a very thin annular region surrounding an inner core. The volumetric flow of the central core is about 5% of the overflow rate and the flow rate of the reverse flow is much less than 5%. The reverse flow has disappeared at $z = 8$ cm but the velocity still goes through a minimum in this region. This type of behavior has also been reported by Nissan and Bresan [1961] for swirling flow in cylinders. Knowles et al. [1973] using the same hydrocyclone reported some undulations in the axial profile above $z = 32$ cm, but no reverse flows.

Further from the axis a strong upflow occurs with a slow transition to an outer downward flow. Because of no slip at the hydrocyclone wall, $\langle u_z \rangle$ decreases to zero across the boundary layer. The surface of zero axial velocity in the outer region conforms to the conical geometry of the hydrocyclone whereas the diameter of the central core region seems to be bounded above by the size

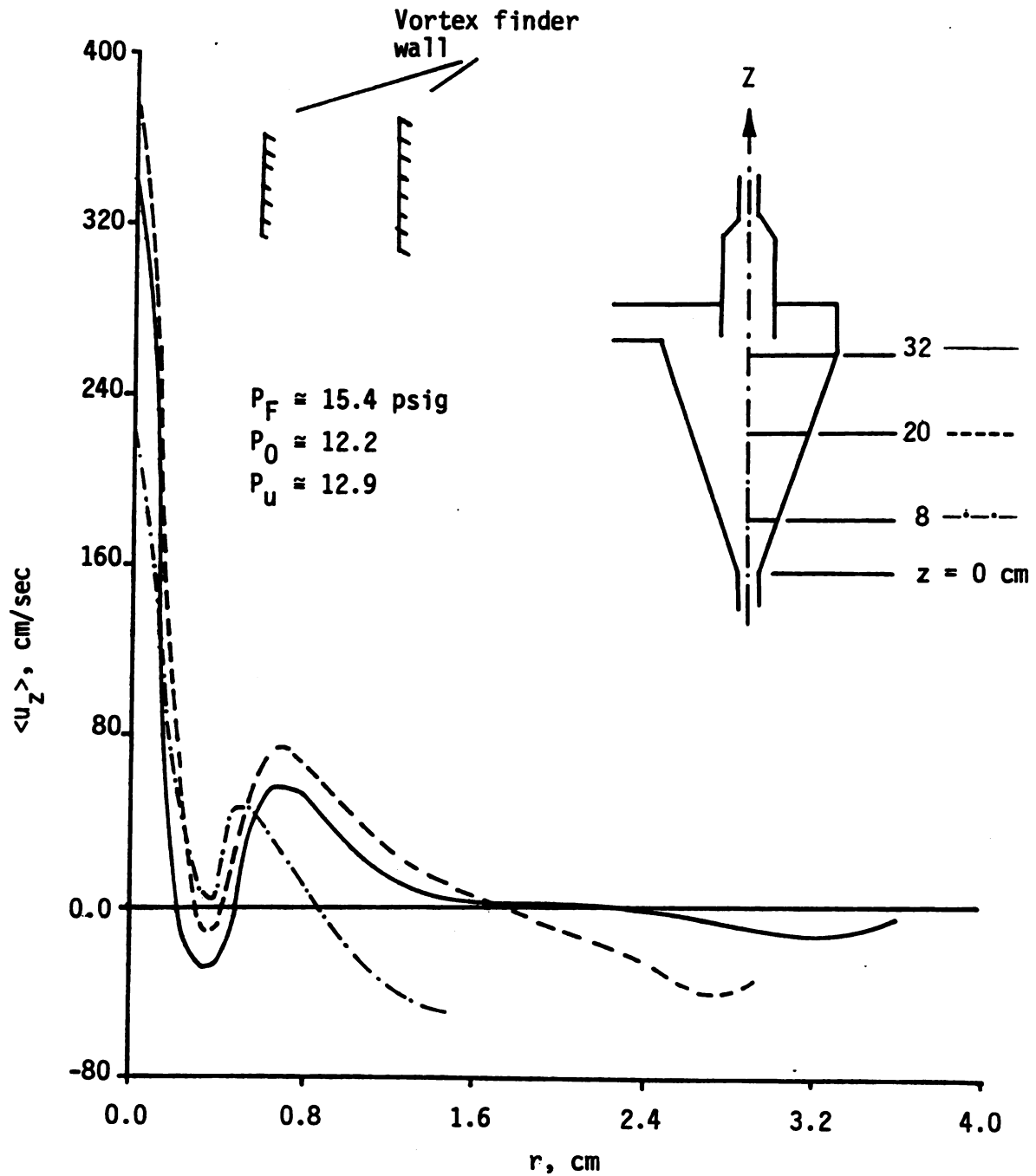


Figure 4.1. Mean axial velocity profiles for $Q_0/Q_u = 4$ and $Re_F \approx 30,000$.

of the contraction in the vortex finder. At $z = 32$ cm, the results show a fairly large annular region between the vortex finder and the hydrocyclone wall where $\langle u_z \rangle \approx 0$. This may correspond to a recirculation zone.

Figure 4.2 shows the mean tangential velocity at three different axial positions for the same flow conditions as before. $\langle u_\theta \rangle$ in the central core region is approximately proportional to r and independent of z . For non-turbulent flows, this feature would imply that the radial velocity is zero within the core region. It is noteworthy that the maximum angular velocity and the flow reversal, due to the contraction in the vortex finder, occur at the same radial position. Thus, with $\langle u_\theta \rangle \approx 400$ cm/s at $r = 0.5$ cm, the centrifugal force changes from zero on the axis to nearly four orders of magnitude larger than the force due to gravity. This happens uniformly over the core from $z = 8$ cm to $z = 32$ cm. This means that with negligible radial velocity in the central core region, an upward moving particle with a larger density than the fluid could easily migrate to the outer region given enough time. Apparently, the location of the maximum tangential velocity together with the length of the core region and its axial velocity account for some of the unique classifying characteristics of hydrocyclones.

In the outer region the tangential velocity decreases with radial position. A "free vortex" would be inversely proportional to r but Figure 4.3 shows a much weaker behavior. The smaller exponent observed experimentally can be attributed to the viscous

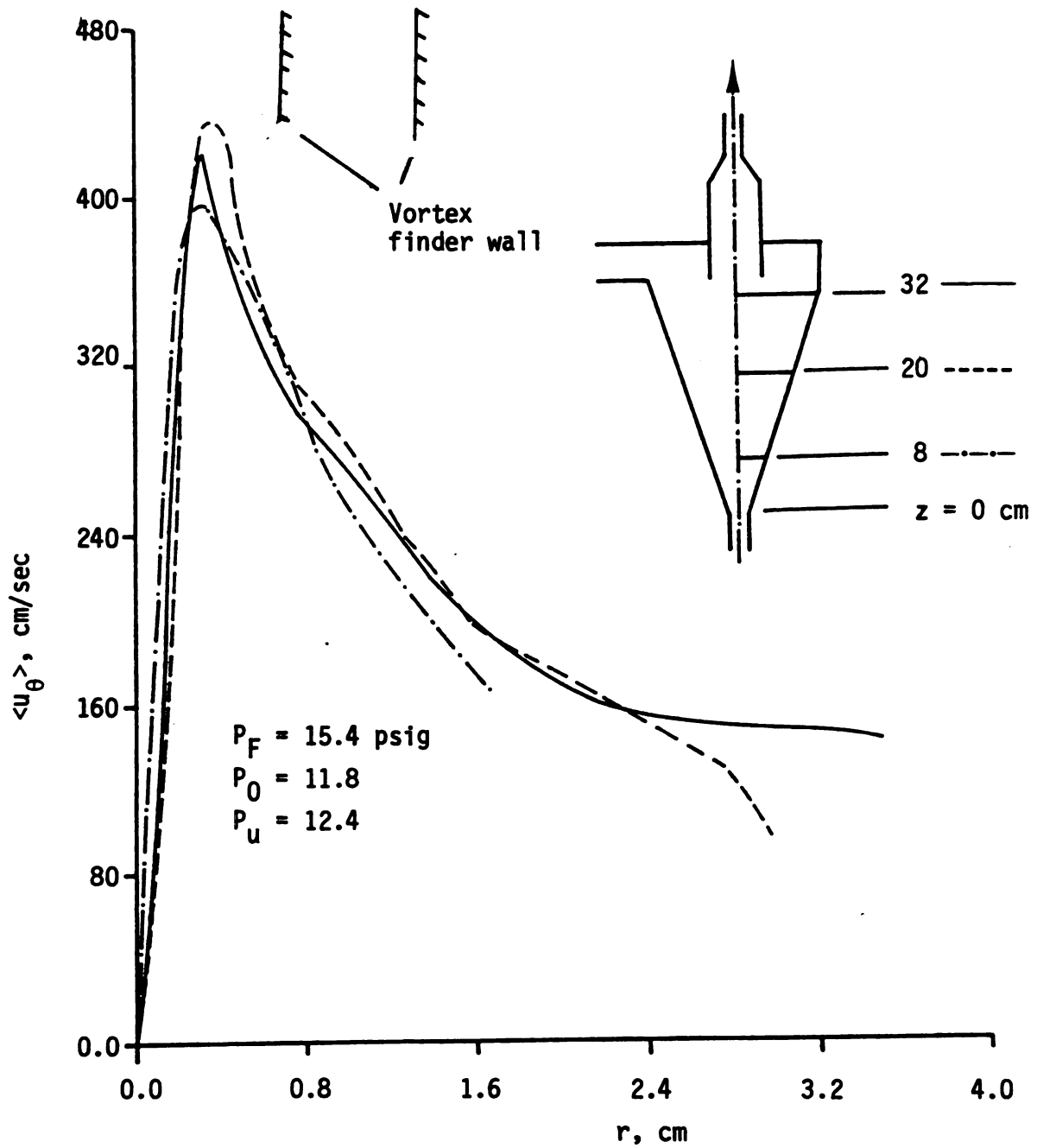
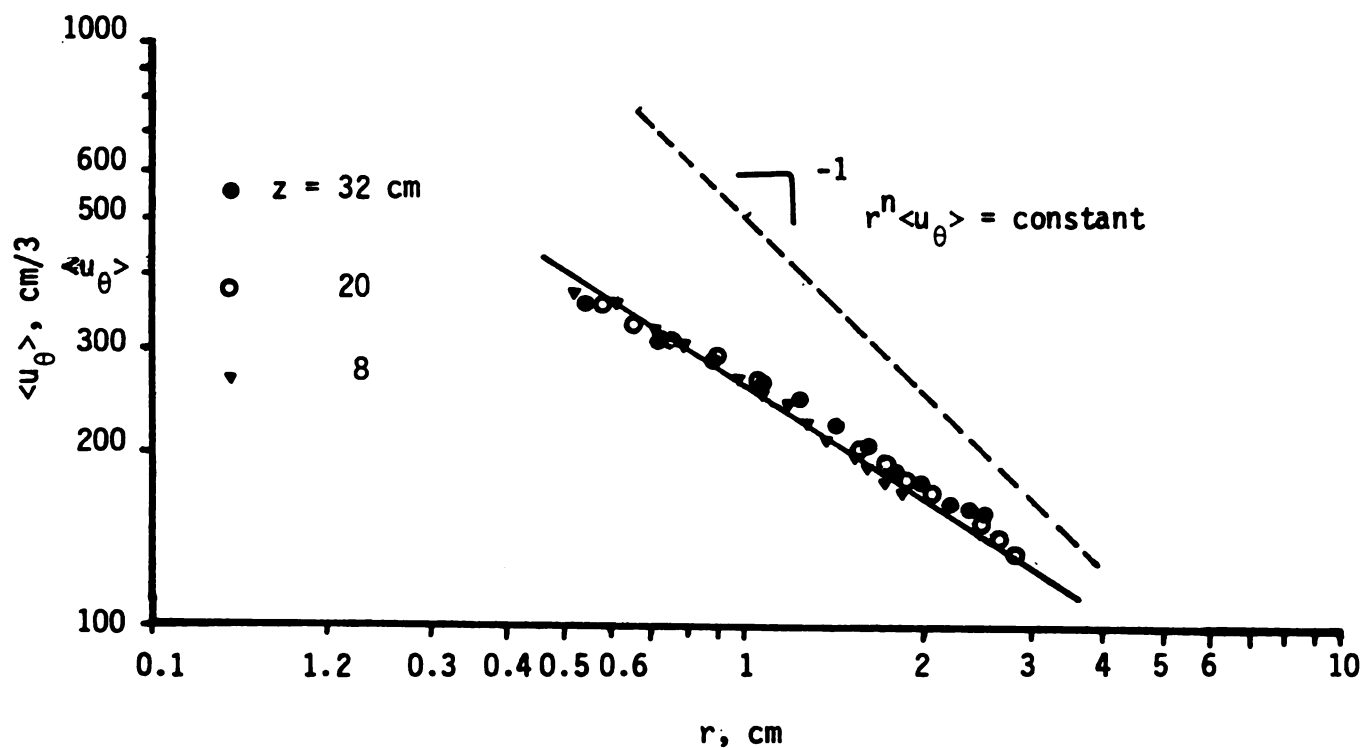


Figure 4.2. Mean tangential velocity profiles for $Q_0/Q_u = 4$ and $Re_F \approx 30,000$.



n	Type of flow
1	Free vortex
$\approx +0.8$	Air core (Kelsall, 1952)
0.62	No air core (this research)
≈ 0.3	No air core (Knowles, 1971)

Figure 4.3. Deviation from free vortex flow in the outer region for a split ratio of 4 and an inlet Reynolds number of 30,000.

or turbulent transport of momentum. Note that the dependence on r found here is comparable to the one reported by Kelsall [1952] for a 3"-hydrocyclone operating with an air core but significantly larger than the exponent found by Knowles et al. [1973]. The significant result illustrated by Figure 4.2 is that $\langle u_\theta \rangle$ does not change much with axial position even in the outer region. Of course, no slip at the hydrocyclone wall reduces $\langle u_\theta \rangle$ to zero across the boundary layer.

Figure 4.4 compares the axial and tangential velocities at $z = 32$ cm measured in this study with the ones reported by Knowles et al. [1973] using the same hydrocyclone. The flow rates, split ratio, and pressures are all approximately the same for the two studies. The mean axial data used for comparison are the locally averaged ones which close the internal mass balances (see p. 37 in Knowles, 1971). Axial velocities measured using laser doppler anemometry always yielded internal material balances which closed to within 5% (see Section 2.5). In the outer region, the results reported here for both $\langle u_z \rangle$ and $\langle u_\theta \rangle$ are in good agreement with the earlier experiments from McMaster; however, the reverse flows and the position of the maximum tangential velocity are both obscured by the measuring technique employed by Knowles.

The radial component of the velocity was not measured. However, from the three traverses of the mean axial velocity, an estimate of the mean radial velocity can be obtained. For instance, if the flow is axially symmetric (this was shown to be a good

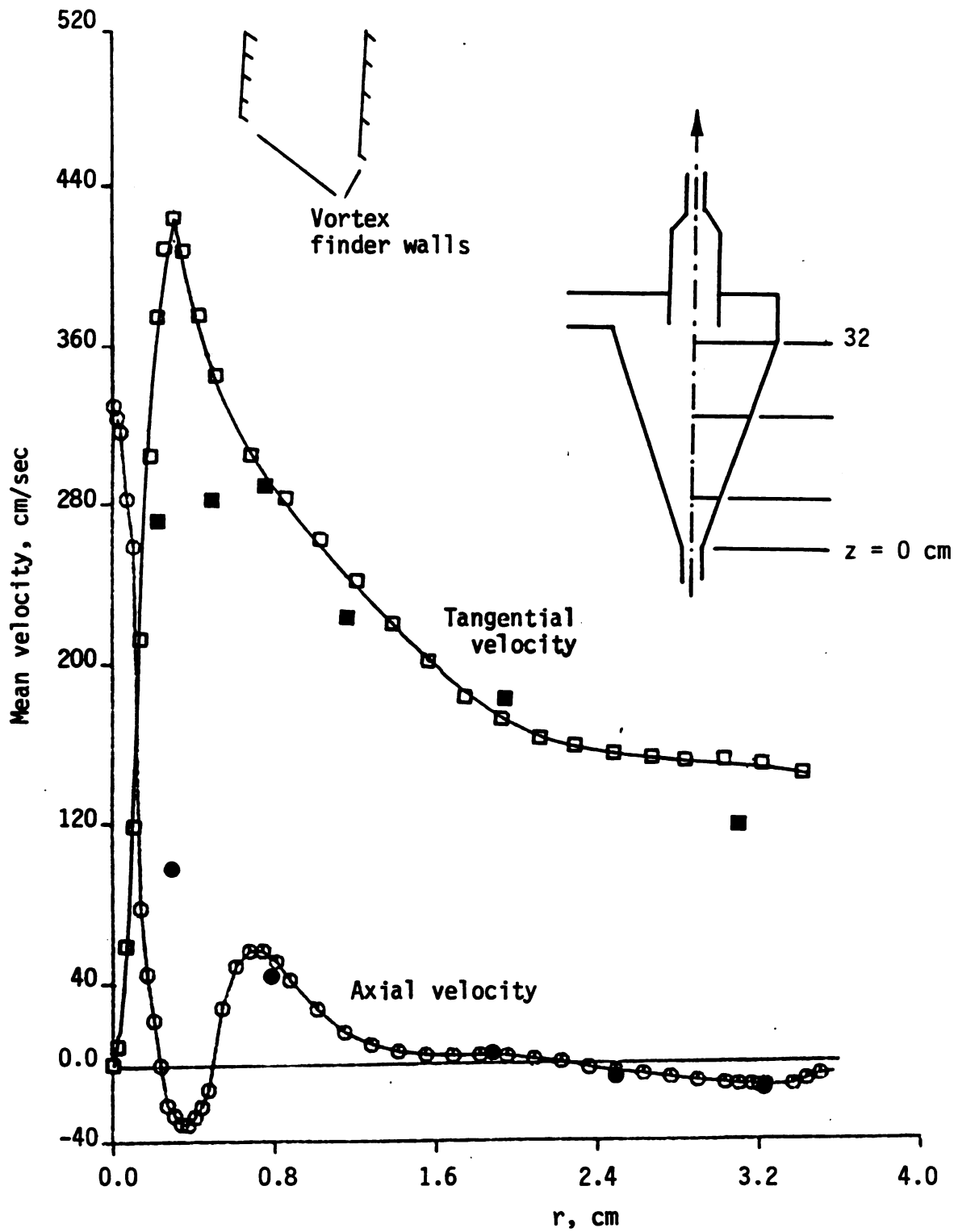


Figure 4.4. Mean axial and tangential velocity profiles at $z = 32$ cm for $Q_0/Q_u = 4$ and $Re_F \approx 30,000$ (o, \square present study; \bullet , \blacksquare Knowles, 1971).

approximation for this hydrocyclone), then a material balance between two level planes located at z_1 and z_2 implies that

$$r \int_{z_1}^{z_2} \langle u_r \rangle (r, z) dz = \int_0^r [\langle u_z \rangle (r, z_1) - \langle u_z \rangle (r, z_2)] r dr .$$

From this expression and the data from Figure 4.1, two characteristic radial profiles can be calculated. Figure 4.5 shows

$$\bar{u}(r) \equiv \frac{\int_{z_1}^{z_2} \langle u_r \rangle (r, z) dz}{(z_2 - z_1)}$$

for the lower and upper part of the hydrocyclone.

In the upper part, the radial flow is outward in the inner core region and inward for $r > 2$ cm. From Figure 4.1 the surface of zero axial velocity is located at radial positions greater than 2 cm for $z > 20$ cm. This is interesting because it suggests that an inwardly directed viscous force may counter the centrifugal force in this region and actually drag solid particles out of the downward moving boundary layer and into the upward swirling flow. This phenomenon would be even more pronounced at smaller axial positions. Finally, the outwardly directed radial flow in the upper part of the hydrocyclone would act in concert with the centrifugal force to clarify the core region of solid particles with densities larger than the continuous phase. Just the opposite would occur for lighter particles or oil droplets. Because $\bar{u}(r)$ changes sign in the lower

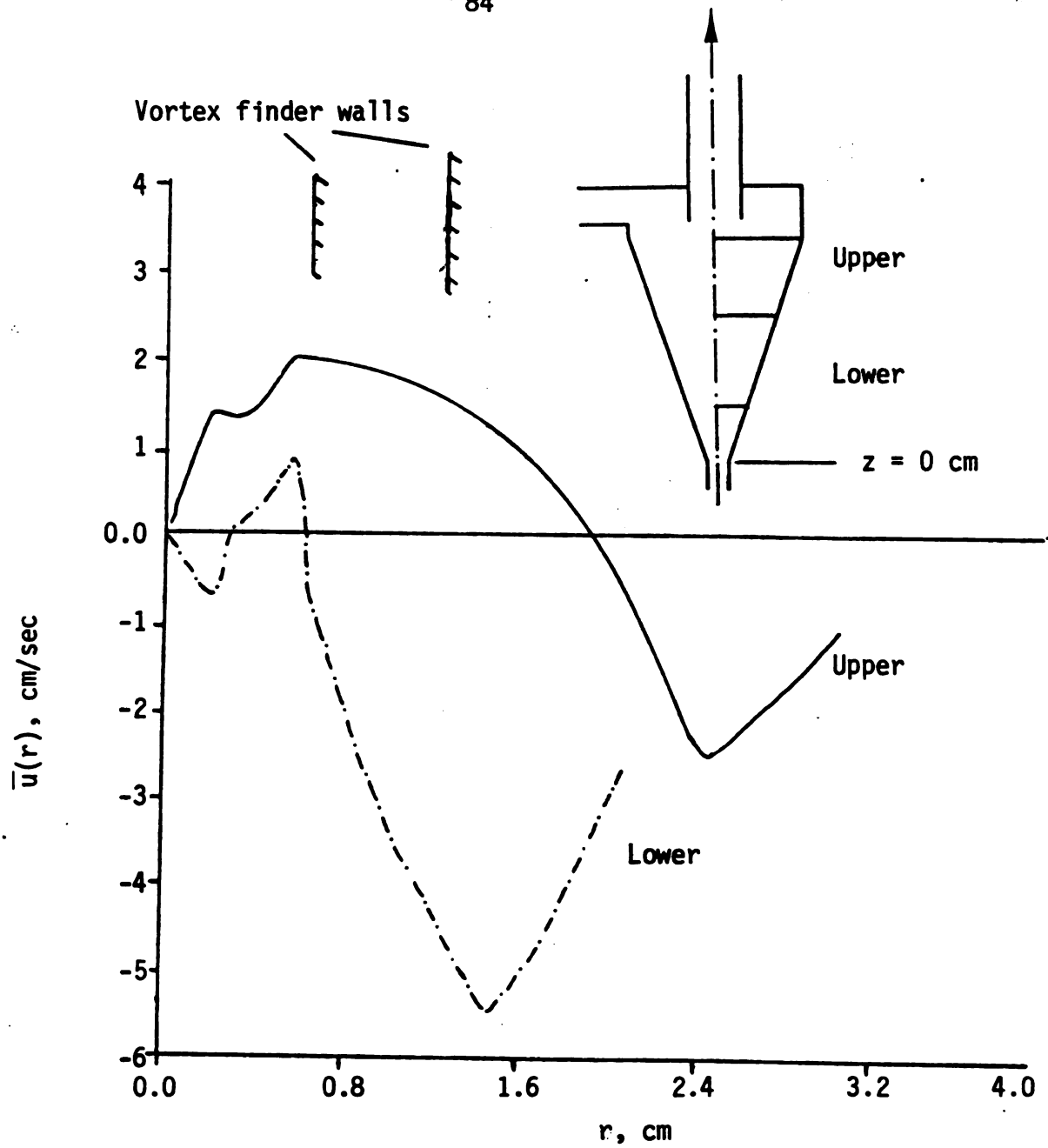


Figure 4.5. Average radial velocity profiles for $Q_0/Q_u = 4$ and $Re_F \approx 30,000$.

part of the hydrocyclone, this mechanism of classification may not be applicable for $z < 20$ cm.

4.2. The Effect of Split Ratio on the Velocity Profiles

Figures 4.6 and 4.7 respectively summarize the measurements of the axial and tangential velocities for three different split ratios at $z = 32$ cm. The striking conclusion from these data is that the split ratio has little noticeable effect on the outer flow. The position of the outer mantle (i.e., where $\langle u_z \rangle = 0$), for instance, seems oblivious to changes in Q_0/Q_u . This means that the split ratio would not be a good choice for a control variable for those applications, if any, where the outer structure determines the performance of a hydrocyclone. For some situations, however, the objective may be to alter the central core structure, and Figure 4.6 shows that this region changes dramatically with split ratio.

As illustrated by Figure 4.6, reverse flows are found as Q_0/Q_u decreases from ∞ . For $Q_0/Q_u = \infty$, the axial velocity has an interesting minimum value at the same radial position where the tangential profile is a maximum. Apparently, the transport of mean axial momentum into the velocity defect region makes a contribution to the kinetic energy of swirl rather than speeding up the axial component of velocity. Thus, the centrifugal force is balanced by other factors in addition to the radial pressure gradient. This undulatory type profile has also been observed by Knowles [1971] at a finite Q_0/Q_u in this hydrocyclone and by Thew et al. [1980] in a cylindrical hydrocyclone.

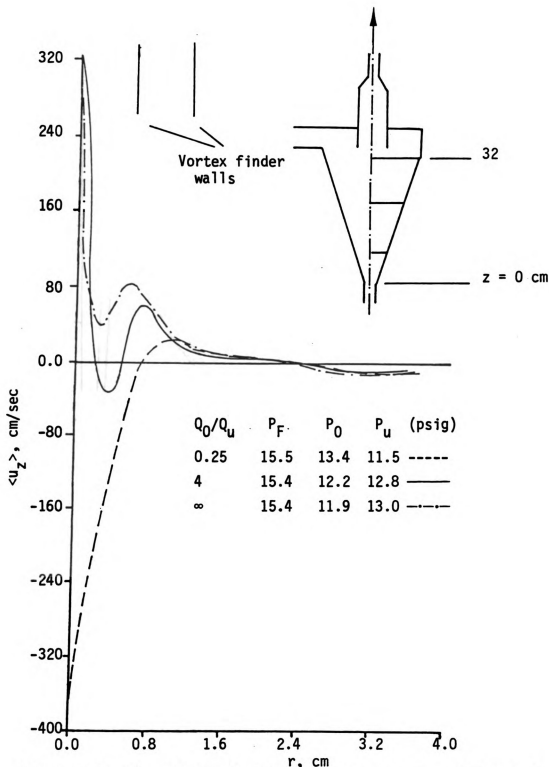


Figure 4.6. The effect of split ratio on $\langle u_z \rangle$ at $z = 32$ cm and $Re_F \approx 30,000$.

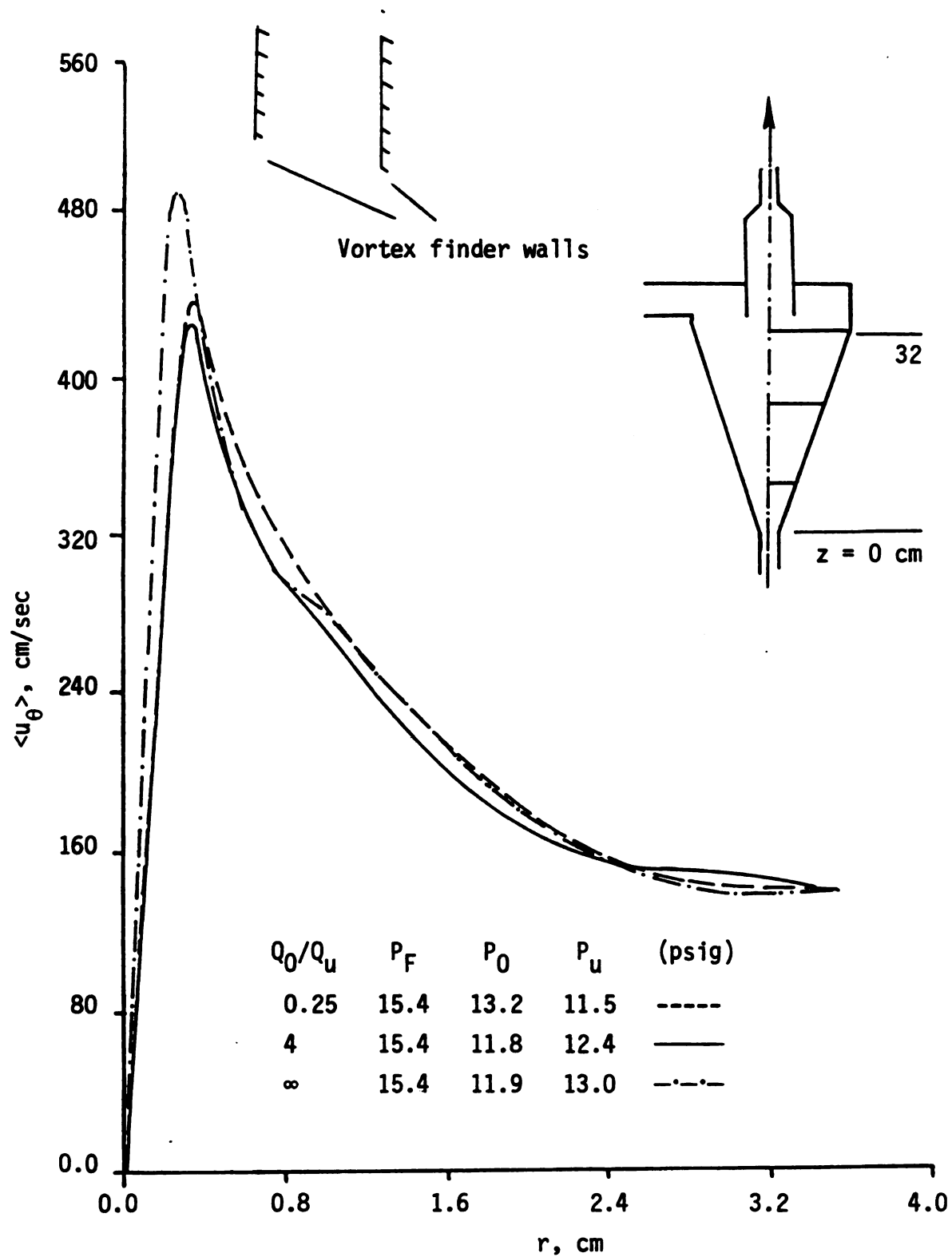


Figure 4.7. The effect of split ratio on $\langle u_\theta \rangle$ at $z = 32 \text{ cm}$ and $Re_F \approx 30,000$.

The axial profile for $Q_0/Q_u = .25$ is qualitatively similar to the three cell reversals reported earlier by Nuttal [1953] and by Binnie [1957] for confined vortex flows in cylinders. These earlier results were produced at a fixed flow rate by increasing the initial swirl of the feed (see Section 1.2). The new result here is that the split ratio also controls the morphology of the central core region. At a fixed flow rate, the transition from a two cell reversal to a three cell reversal has as an intermediate flow structure four cells. Data also show that this four cell reversal at $Q_0/Q_u = 4.0$ becomes a six cell structure by decreasing the backpressure. The additional countercurrent flow appears in the outer region where $\langle u_z \rangle = 0$.

The axial profile at $z = 8$ cm in Figure 4.8 shows that the three cell reversal at $z = 32$ cm becomes a two cell structure further down the conical section. This phenomenon is consistent with the study of Nissan and Bresan [1961], who showed that transition from three to two cells in a cylinder occurs simultaneously with a reduction in the swirl velocity. For this geometry, this is equivalent to either a reduction in the average angular momentum per unit volume in the cross section or to the circulation $\Gamma(z)$. With

$$\bar{\Gamma}(z) \equiv 2\pi \int_0^{R(z)} \langle u_\theta \rangle (r) r dr \quad (4.7a)$$

and with the data shown in Figures 4.2 and 4.3, it follows that

$$\bar{\Gamma}(z) \propto [R(z)]^2 \quad (4.7b)$$

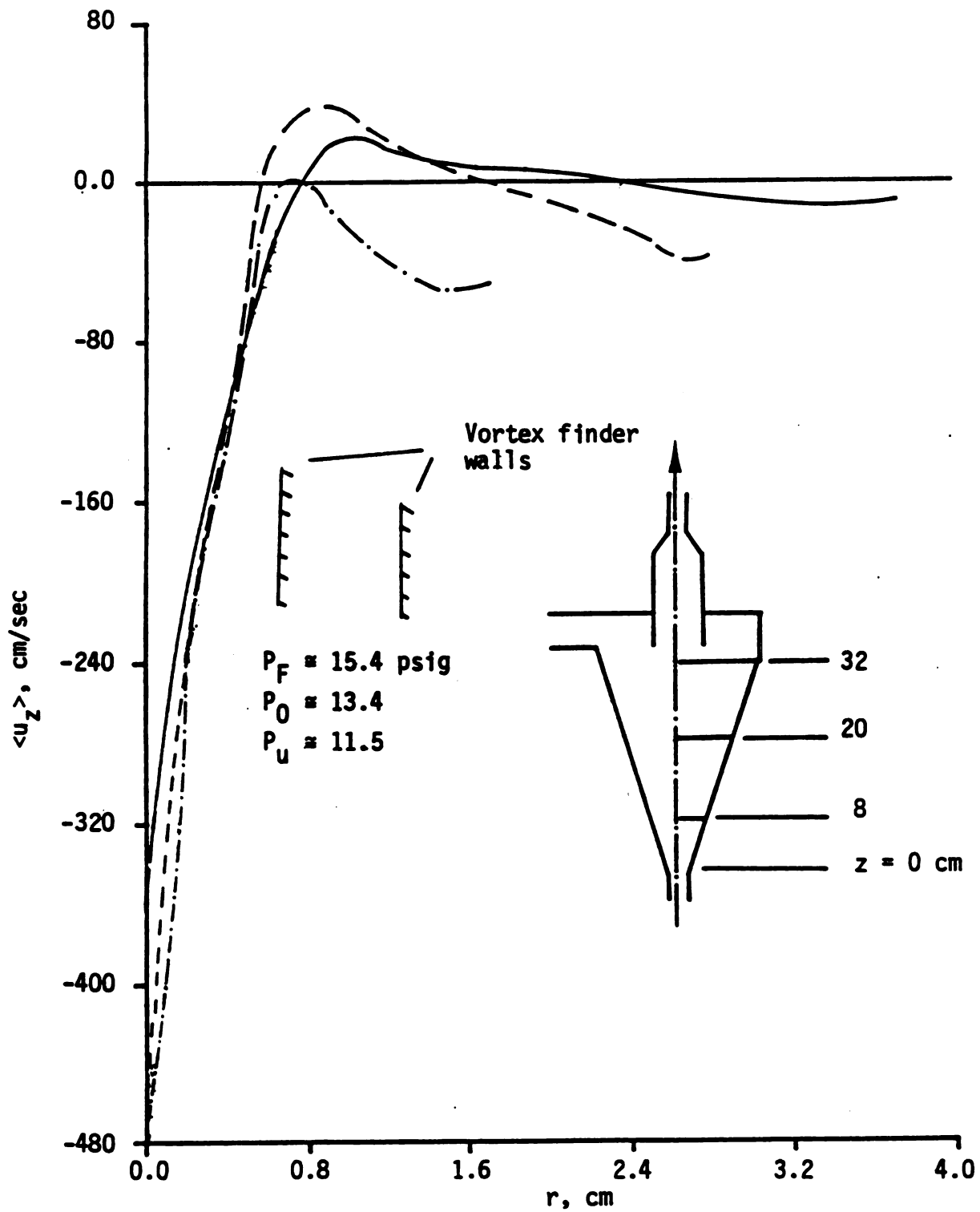


Figure 4.8. Mean axial velocity profiles for $Q_0/Q_u = 0.25$ and $Re_F \approx 30,000$.

for the hydrocyclone employed in this study. Actually, the tangential profiles for $Q_0/Q_u = 0.25$ were measured at different axial levels and the results, not reported here, are very similar to those displayed in Figure 4.2 for $Q_0/Q_u = 4.0$. Therefore, the proportionality expressed by (4.7b) is a good approximation for $8 < z < 32$ cm. The radius of the hydrocyclone decreases by about a half from $z = 32$ cm to $z = 8$ cm (see Figure 2.3). Therefore, the circulation is reduced by one-fourth so the results summarized by Figure 4.8 are qualitatively consistent with the previous findings of Nuttal [1953], Binnie [1957], and Nissan and Bresan [1961]. It is interesting that the design of this hydrocyclone maintains about the same centrifugal force distribution over a significant portion of the conical section. The reverse flows discussed so far apparently play a subtle, if not explicit, role in maintaining this feature.

Dye injection into the apex region for $Q_0/Q_u = 0.25$ picks up the reverse flow at $z \approx 8$ cm. Figure 4.8 shows that this annular upflow at $z = 20$ cm is approximately 1 cm thick and continues to grow with increasing z . The data also show that the maximum axial velocity in the outer downward flow increases as z decreases, which is probably due to a decrease in the cross sectional area. The profile at $z = 8$ cm has an undulating character like the one in Figure 4.6 for $Q_0/Q_u = \infty$. Similarly, the tangential velocity is a maximum in the region where $\partial \langle u_z \rangle / \partial r = 0$. Therefore, the steady state velocity defect which occurs at $z \approx 8$ cm implies once again that the mean axial momentum transported into this zone probably

makes an important contribution to the kinetic energy of the swirl velocity. It would be interesting to study, both theoretically and experimentally, the transition which occurs between $z = 8$ cm and $z = 20$ cm. Presumably, the wall boundary layer has grown sufficiently large at $z = 8$ cm that it begins to interact with the core vortex and ejects fluid upward (see discussion in Section 1.2). As illustrated by Figure 3.1, this phenomenon also caused a flow reversal in the vortex finder to form the core fluid in Figure 4.8.

4.3. The Effect of Reynolds Number and Backpressure on the Velocity Profiles

Increasing the Reynolds number (actually the flow rate) has a large quantitative effect on the axial and tangential profiles, but for the two comparisons made in Figures 4.9 and 4.10 the apparent qualitative behavior is unchanged. In the next chapter, results over a broader range of flow rates for this hydrocyclone without the 2:1 contraction in the vortex finder are presented. The results shown here clearly show that the magnitude of the reverse flow around the vortex core increases with Reynolds number. The average circulation at $z = 20$ cm for the second traverse in Figure 4.10 is obviously larger than $\bar{\Gamma}$ for traverse 1. Thus, the data presented for this case are consistent with the previous observations and with the criteria for reverse flows given by Binnie [1957]. Figure 4.9 suggests that transition from a two-cell to a four-cell vortex at $z = 20$ cm occurs for $\bar{\Gamma} \approx 6818$ if the split ratio is 4.0.

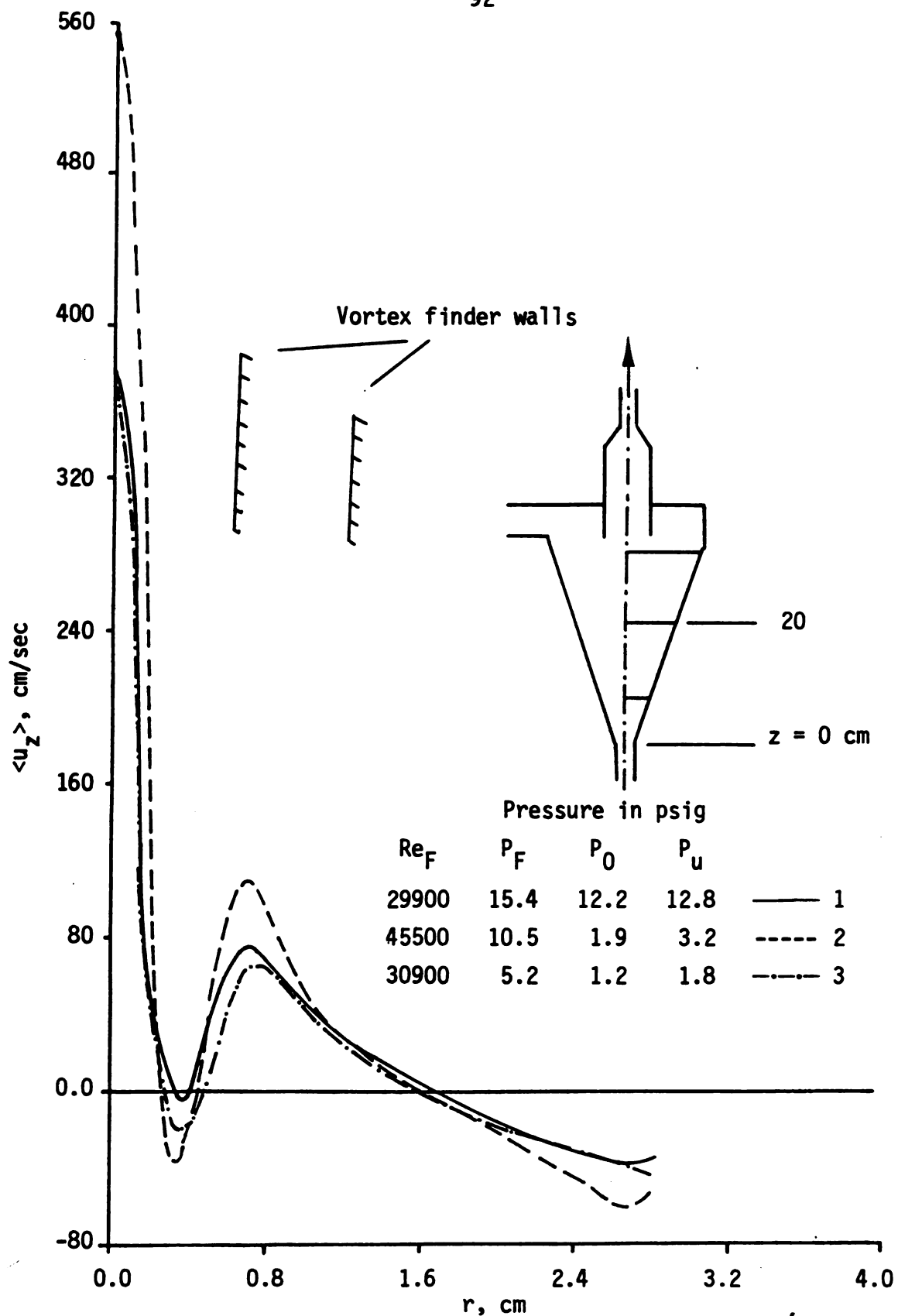


Figure 4.9. The effect of Reynolds number and back pressure on $\langle u_z \rangle$ for $Q_0/Q_u = 4$ at $z = 20$ cm.

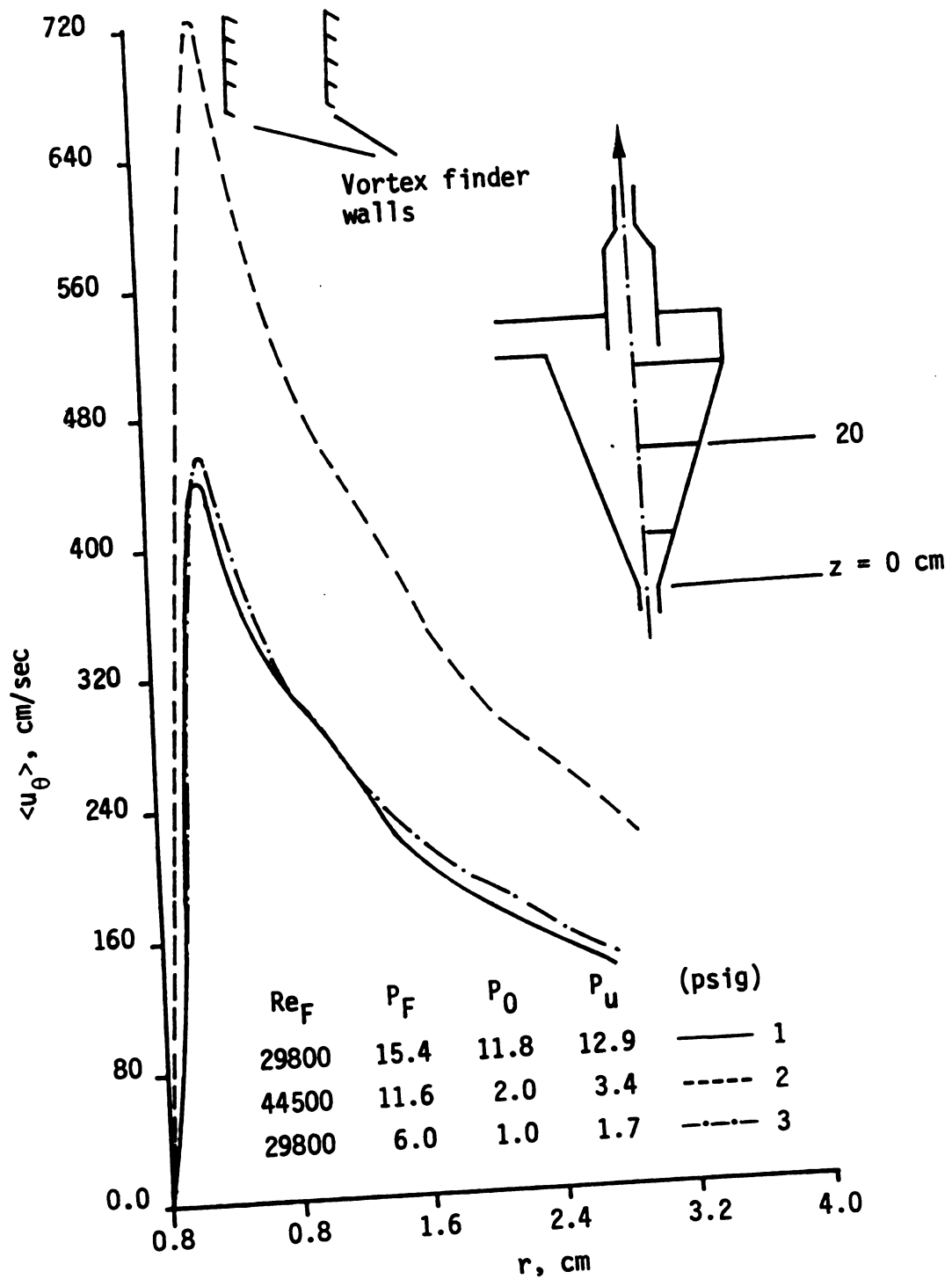


Figure 4.10. The effect of Reynolds number and back pressure on $\langle u_\theta \rangle$ for $Q_0/Q_u = 4$ at 20 cm.

Lowering the back pressure has little effect on the mean velocity profiles provided the pressure drop between the feed and the two exit streams remains balanced (see traverses 1 and 3 in Figures 4.9 and 4.10). The characteristic four cells are clearly present and the tangential velocity again peaks in the region of flow reversal around the inner core. The small differences in the outer and the reserve flow regions may be due to slight differences in the flow rates and unevenness in the actual pressure drops (see data listed in Figure 4.9). It seems noteworthy, however, that lowering the backpressure on the vortex finder did not remove the reverse flow at the 2:1 contraction. Figure 4.9 does suggest that increasing the backpressure, rather than decreasing it, may remove the flow reversal induced by the 2:1 contraction. This experiment could not be run because of the pressure limitations on the glass hydrocyclone.

Figure 4.11 shows the axial profile close to the vortex finder for approximately the same conditions as traverse 3 in Figure 4.9. Another set of flow reversals in addition to the four already shown in Figure 4.1 seems to have been triggered by reducing the backpressure. This broad region of small axial velocities suggests that a recirculation zone occurs in the outer part of the hydrocyclone. Fontein [1961] has previously discussed the existence of multiple eddies and their significance in separation performance.

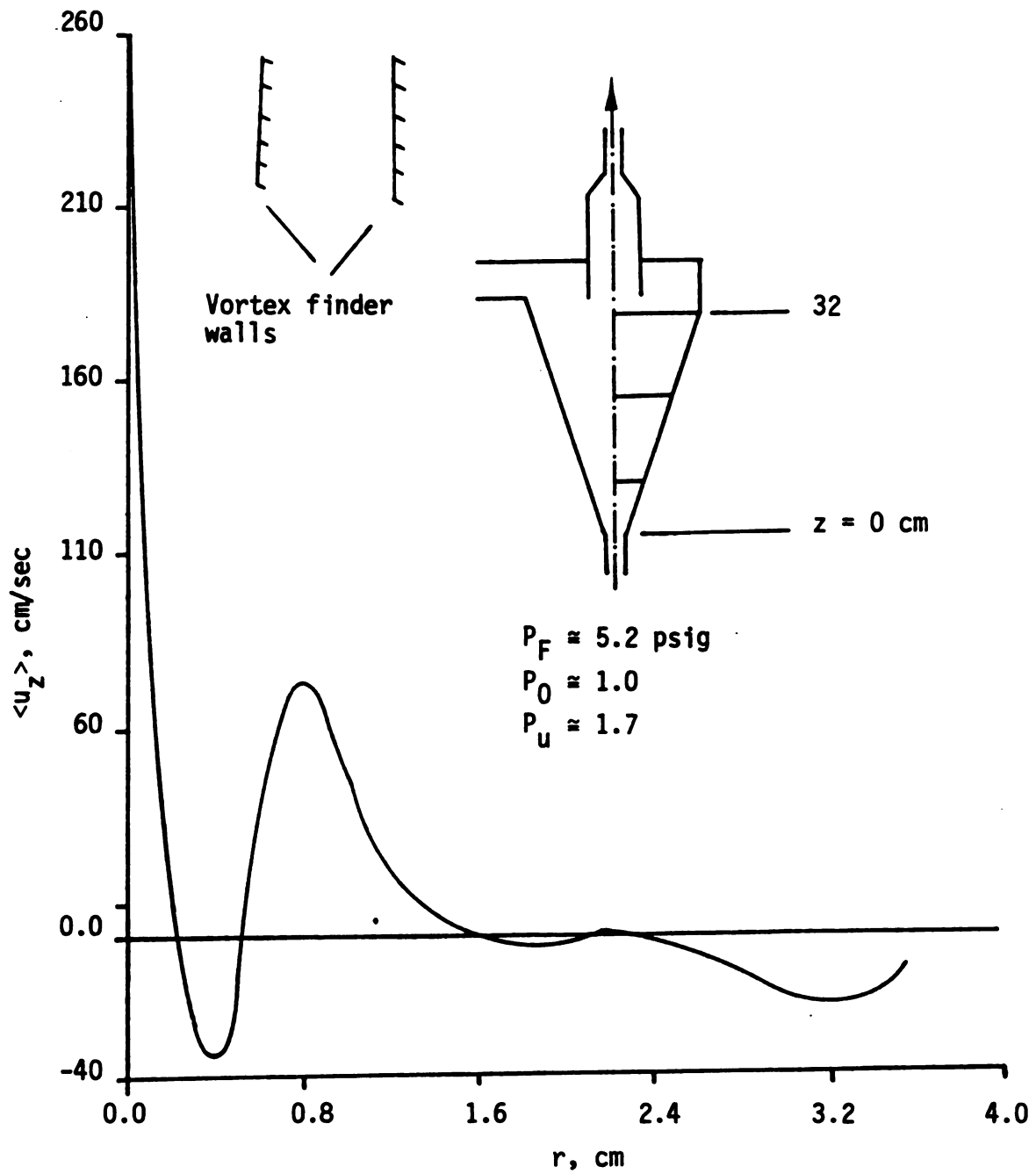


Figure 4.11. The effect of low back pressure on flow reversals for $Q_0/Q_u = 4$ and $Re_F \approx 30,000$ at $z = 32$ cm.

4.4. The Effect of Separan AP-30 on the Velocity Profiles

Some preliminary measurements of the velocity profiles with 100 wppm Separan AP-30 in water show little, if any, differences with the results already reported. Experiments for $Q_0/Q_u = \infty, 4.0$, and 0.25 are qualitatively the same with only some minor quantitative differences. Because the polymer was prepared and used immediately, its temperature was only 12°C compared with 20°C for the water studies. This difference has a significant effect on the viscosity of the solvent, not to mention the polymer-water mixture. Therefore, any quantitative comparisons with the results in Sections 4.1 and 4.2 should be cautious.

Figures 4.12 and 4.13 summarize the results obtained with polymer additive. The experiments with water alone are shown for comparison and, although the temperatures are different between these two studies, it is nevertheless useful to speculate a little on some of the potentially significant differences. Note that the addition of polymer seems to have eliminated the flow reversal surrounding the central core vortex. At the same flow rate, only two cells were observed, but the undulating axial profile remains. A decrease in viscosity would perhaps give a similar result but this conclusion requires additional experiments.

Figure 4.13 shows that the polymer may (excluding viscosity effects) decrease the tangential velocity with the largest effect occurring in the axial velocity defect region. The central core still has a tangential velocity proportional to "r" and a center-line

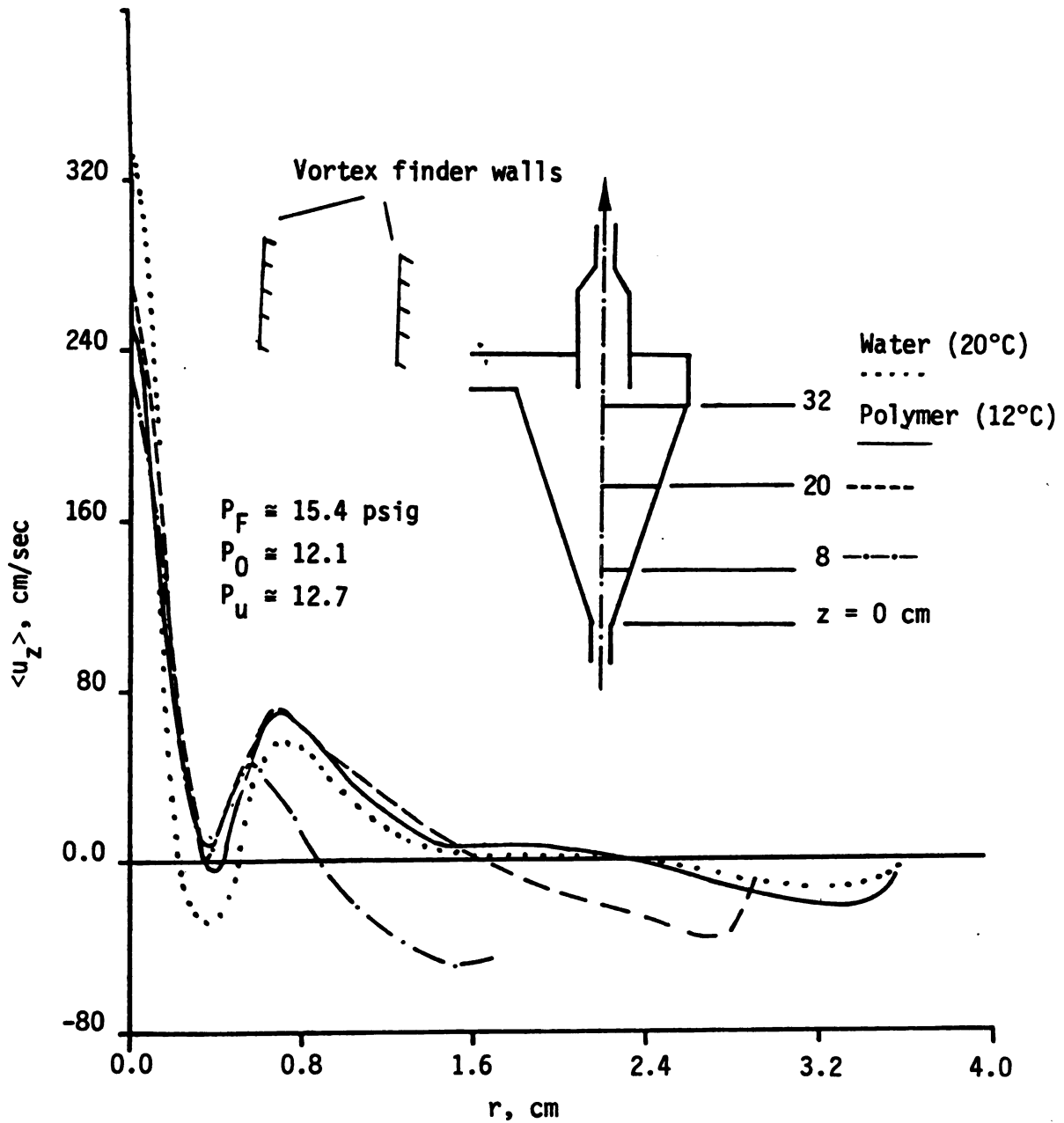


Figure 4.12. Mean axial velocity profiles for 100 wppm Separan AP-30 with $Q_0/Q_u = 4$ and $Re_F \approx 24,300$ ($Q_F = 500 \text{ cm}^2/\text{sec}$, $T = 12^\circ\text{C}$).

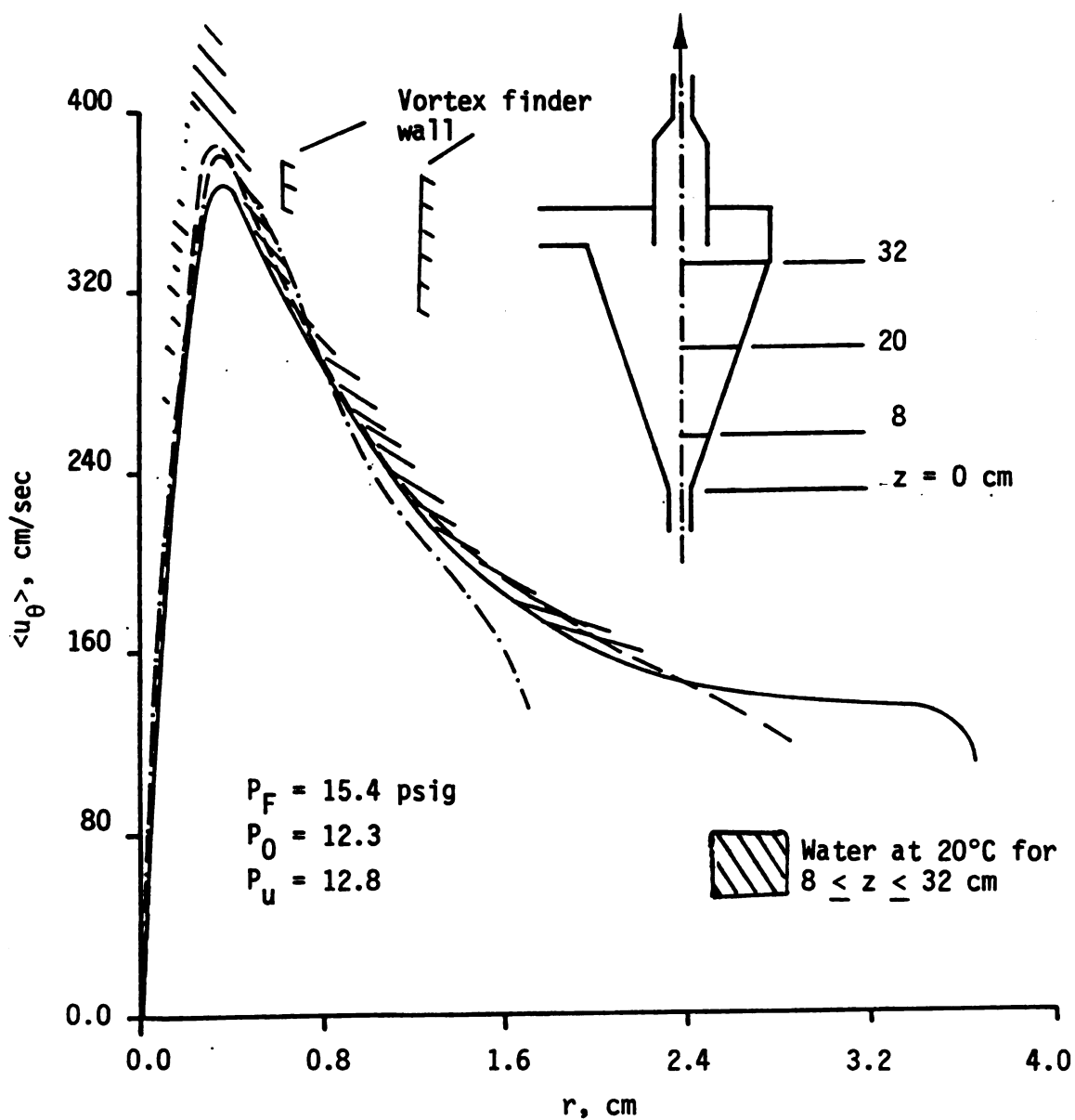


Figure 4.13. Mean tangential velocity profiles for 100 wppm Separan AP-30 with $Q_0/Q_u = 4$ and $Re_F \approx 24,300$ ($Q_F \approx 500$ cm³/sec, $T = 12^\circ\text{C}$).

axial velocity which changes with "z", but not nearly as much as before. The axial velocity at $r = 0$ also shows a maximum in the range $8 \leq z \leq 32$ cm. The deceleration on the axis may indicate that a fluid particle sees an adverse pressure gradient as it approaches the vortex finder. Once again, a combination of $\langle u_\theta \rangle \propto r$ and $\partial \langle u_z \rangle / \partial z \neq 0$ within the central core implies that turbulent transport of momentum may play a key role in balancing the convective radial transport into this region. Because the axial velocity in Figure 4.12 does not change as much as the water case shown in Figure 4.1, a tentative indirect conclusion is that the addition of Separan AP-30 has reduced turbulent transport within the core region (see Section 6.3).

CHAPTER 5

VELOCITY MEASUREMENTS FOR DIFFERENT VORTEX FINDER CONFIGURATIONS

5.1. Rietema's "Optimal" Design

In the 3"-hydrocyclone without the contraction in the vortex finder, a three cellular structure was observed at $z = 20$ cm for split ratios between 0 and ∞ . The inlet Reynolds number was $\approx 24,200$ (feed rate of $500 \text{ cm}^3/\text{sec}$ and $T = 12^\circ\text{C}$) for all runs. For $Q_0/Q_u = \infty$, only a two-cell structure was observed at $z = 20$ cm, but the axial profile has a velocity defect around the axis. This was also observed at $z = 8$ and 32 cm for $Q_0/Q_u = \infty$. The results for both the axial and tangential components of the mean velocity are summarized in Figures 5.1 and 5.2.

The most remarkable, and obviously apparent, difference in the results reported here without the contraction in the vortex finder and the results of Chapter 4 is the absence of a jet-like core on the axis running from the apex and out the vortex finder (also see Figure 3.2). Figure 4.12, which is at the same Reynolds number as the study summarized by Figure 5.1, suggests that the 2:1 contraction is responsible for the jet-like vortex on the center line.

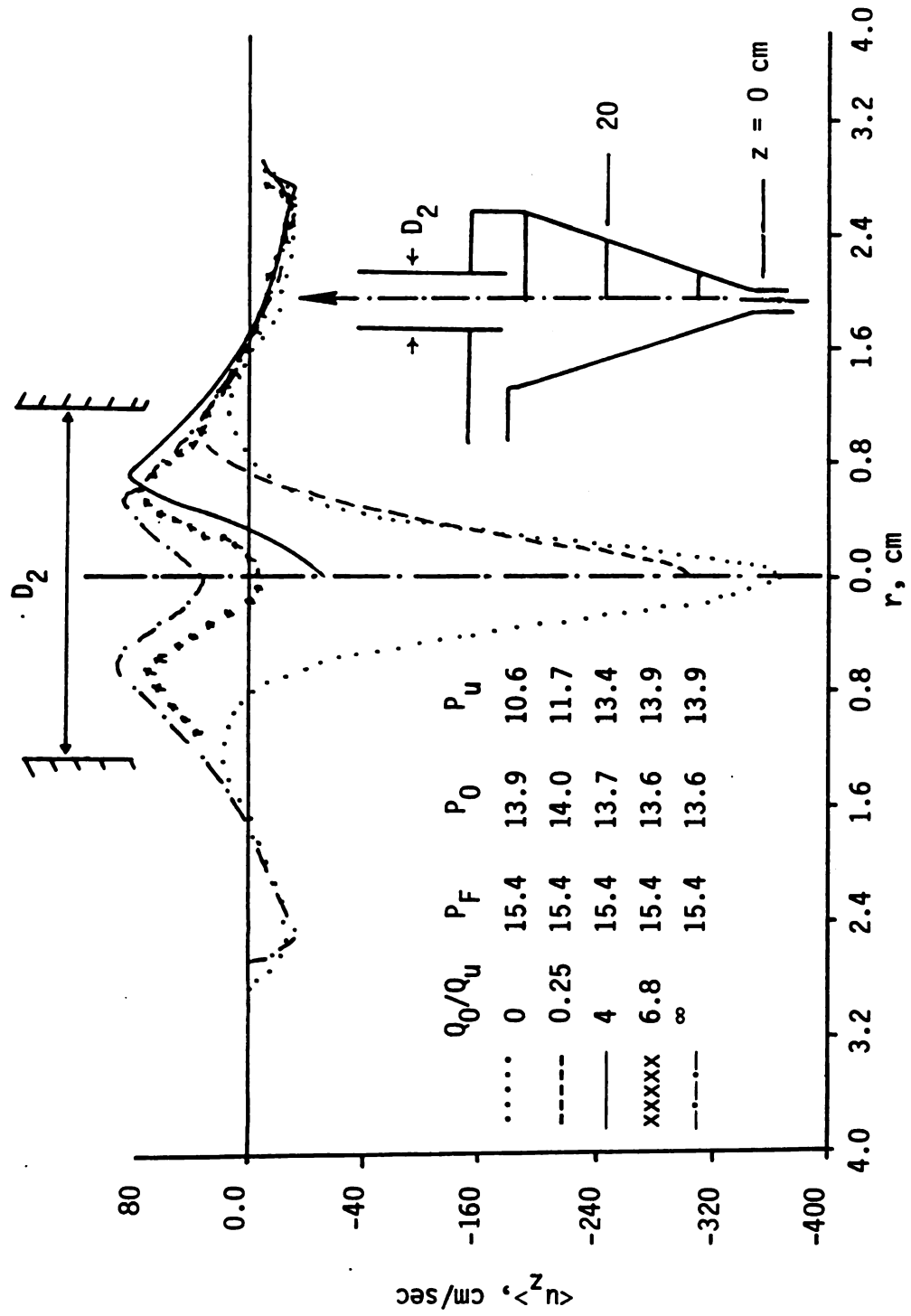


Figure 5.1. The effect of split ratio on $\langle u_z \rangle$ for $Re_F \approx 24,200$ at $z = 20$ cm.

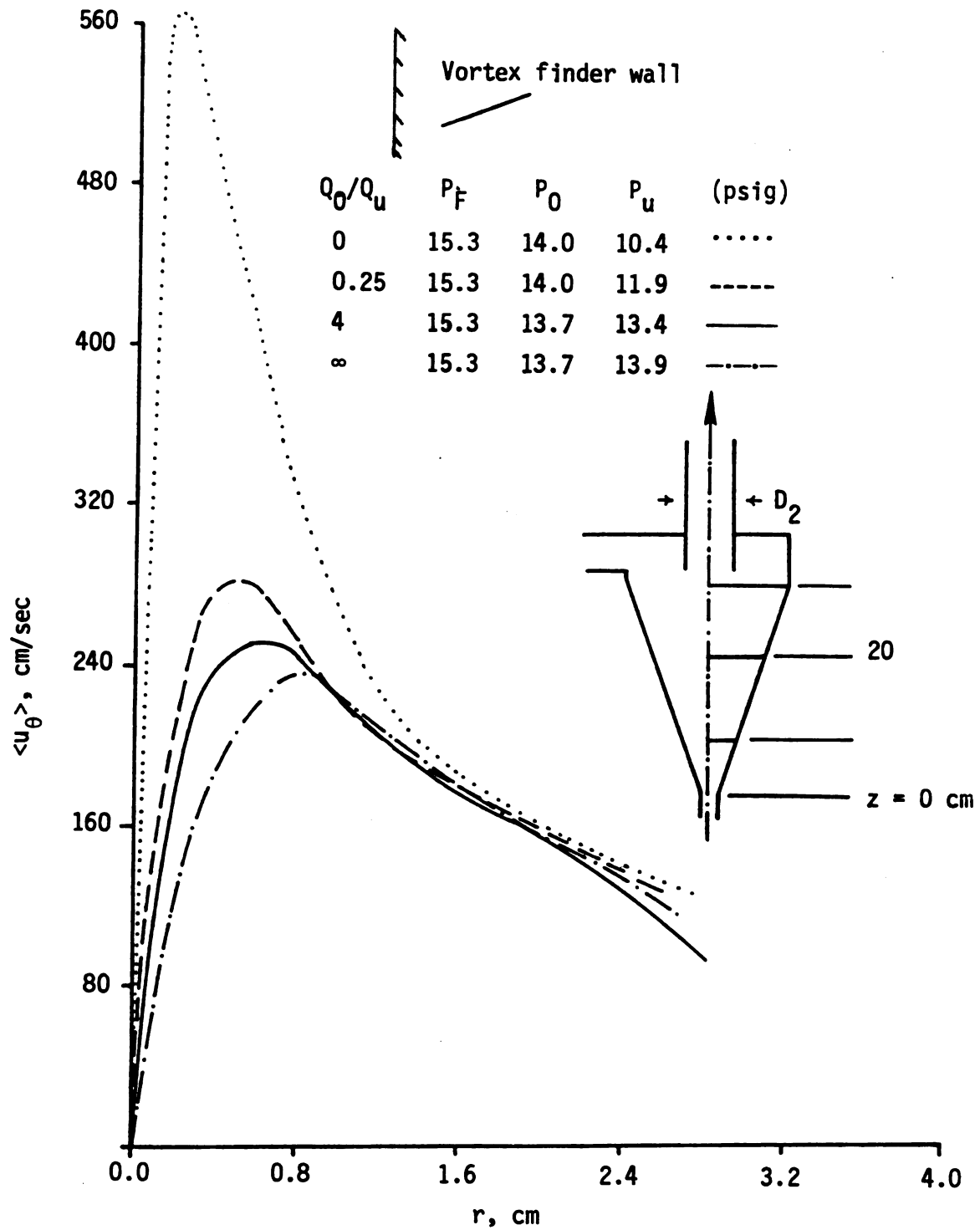


Figure 5.2. The effect of split ratio on $\langle u_\theta \rangle$ for $Re_F \approx 24,200$ at $z = 20$ cm.

The size of the core region, as measured by the location of the maximum tangential velocity, is a more sensitive function of split ratio at this lower Reynolds number (c.f. Figure 4.7). As seen from Figure 5.1, the strength of the downward flow in the core is increased when the split ratio is decreased. Obviously, this causes the core diameter to increase. The mass flux of the upward flow is less for $Q_0/Q_u = 0$ compared with other split ratios. Thus, for low split ratios, a high inward radial flow is expected in the core region. However, a significant fraction of the inward flux of momentum is transferred to the tangential component inasmuch as the maximum value of $\langle u_\theta \rangle$ changes by more than a factor of 2 when Q_0/Q_u decreases from 0.25 to 0 (see Figure 5.2). Note that the increase in $\langle u_z \rangle$ at $r = 0$ is less than 20% for the same change in split ratio (see Figure 5.1). In the outer region, the mean radial velocity is inward and independent of the split ratio, so it is expected that the swirl velocity closer to the axis should increase with a decrease in split ratio to conserve angular momentum.

Because the axial velocity in the outer region is independent of split ratio for $z = 20$ cm (see Figure 5.1) and for $z = 32$ cm as well as $z = 8$ cm (not reported here), it follows that $\langle u_r \rangle$ is also independent of Q_0/Q_u in the outer region, provided the flow is axisymmetric. This implies that $\langle u_\theta \rangle$ should have a similar behavior, which is confirmed by the data shown in Figure 5.2 in the outer region.

It is noteworthy that a reverse annular flow still occurs for $Q_0/Q_u = 0$ at $z = 20$ cm. For $Q_0/Q_u = \infty$, a reverse flow on the core probably happens within the vortex finder. Evidence for this is given later.

Figures 5.3 and 5.4 show the effect of feed rate (i.e., Reynolds number) on the tangential and axial profile at $z = 20$ cm and a split ratio of 4.0. All of the experiments were conducted at $T = 12^\circ\text{C}$. Changes in Q_F have a pronounced effect, as expected, on the tangential profile. These results underscore one of the characteristic difficulties in operating a hydrocyclone compared to a centrifuge. A small reduction in Q_F will decrease the centrifugal force field in the inner and outer region. Figure 5.1. shows that a reduction in split ratio, which will dilute the underflow suspension, may partly compensate for this in the inner region where the secondary separation of solids and liquid occurs.

As Q_F increases, $\langle u_z \rangle$ in the core region tends to increase with a slight increase in the diameter of the downward core flow. At the same time, the upward flow around the core and the downward flow near the wall also increase. This suggests that a large internal recirculation flow occurs for large Q_F (also see the velocity profiles in Figure 5.7 at $z = 8$ cm). Thus two factors seem important as the Reynolds number increases: (1) the centrifugal force field obviously increases (see Figure 5.4); and (2) the increase

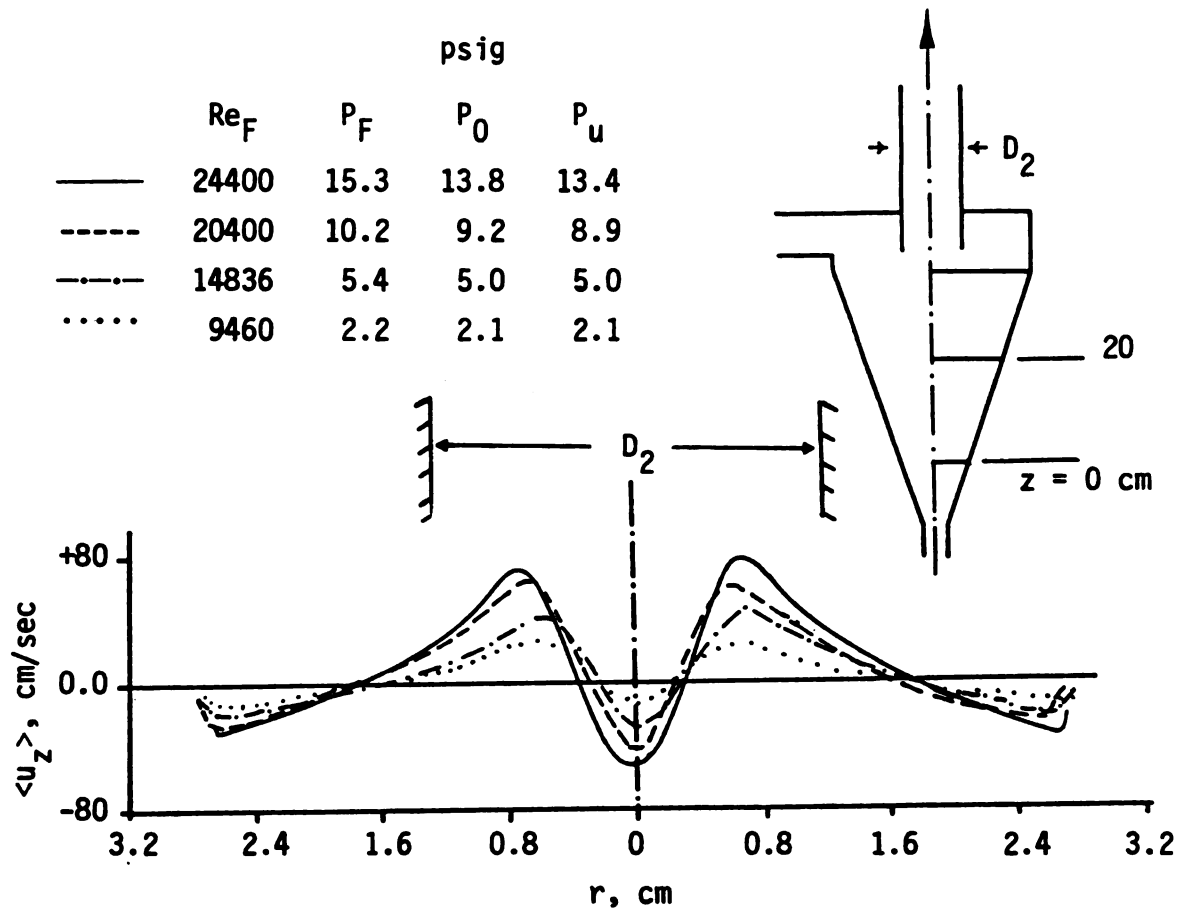


Figure 5.3. The effect of Reynolds number on $\langle u_z \rangle$ for $Q_0/Q_u = 4$ at $z = 20$ cm.

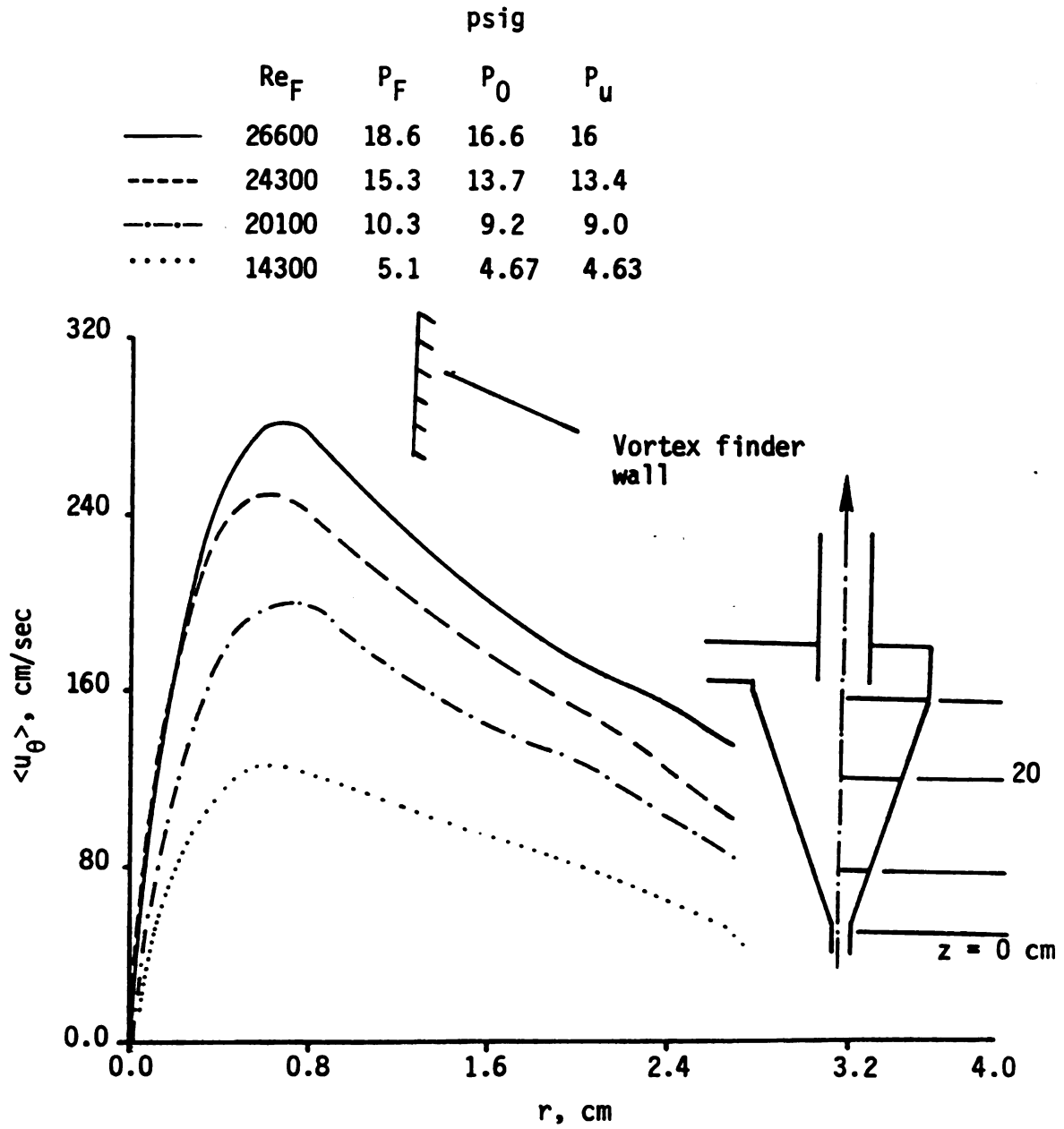


Figure 5.4. The effect of Reynolds number on $\langle u_\theta \rangle$ for $Q_0/Q_u = 4$ at $z = 20$ cm.

recirculation of the fluid from the vortex finder increases the importance of secondary separation by the inner swirling flow.

As seen from Figures 5.1 and 5.3, the locus of zero axial velocity in the outer region is insensitive to operating condition. These results support the previous speculation by many researchers that this parameter is determined mainly by the geometry (see p. 15 in Bradley, 1965). Note also that the size of the core region for fixed split ratio is also insensitive to the flow rate (see Figure 5.4). Apparently, the diameter of the vortex finder determines the size of the core region, which is a new result with this research.

The data in Figures 5.2 and 5.4 show that $\langle u_\theta \rangle$ decreases with r in the outer core. The index n , defined in Figure 4.3, for this set of data is approximately 0.5 at $z = 20$ cm for all operating conditions. This result is smaller than the one observed with a hydrocyclone having a 2:1 contraction in its vortex finder (see Figure 4.3) and with a 3"-hydrocyclone operating with an air core (see Kelsall, 1953), yet larger than the one reported by Knowles et al. [1973] for this hydrocyclone. The value $n \approx 0.5$ is universally reported for the operation of a gas cyclone (see, e.g., Ter Linden, 1949). Here n varies slightly from $z = 32$ cm to $z = 8$ cm, which shows some retardation of swirl due to viscous effects.

Figures 5.2 and 5.4 show another important feature of this hydrocyclone. From other data, Bradley [p. 39, 1965] has shown that the reduction in the swirl velocity at the inlet is given by

$$\alpha = 3.7 D_1/D \quad (5.1)$$

where α is simply the ratio of the peripheral tangential velocity to the inlet average velocity, Q_F/A_F . From Figure 2.3, $D_1/D \approx .28$ for this hydrocyclone, so according to Eq. (5.1) $\alpha \approx 1.04$. This is very consistent with the data reported in Figures 5.2 and 5.4 and elsewhere in this dissertation.

Figures 5.5-5.10 show the axial and tangential profiles measured at different axial levels in the hydrocyclone for $Q_0/Q_u = 0.25$, 4.0, and ∞ , respectively. The results are qualitatively similar to what has been discussed before, but a few features are worth noting.

Figure 5.5 shows that the three cell structure at $z = 32$ and 20 cm has disappeared at $z = 8$ and 2 cm. Table 5.1 shows that this correlates with a reduction in the circulation (i.e., loss of angular momentum) as suggested by the previous work of Nuttal [1953], Binnie [1956], and Nissan and Bresan [1961]. Note that a small velocity defect at $r \approx 0.8$ remains at $z = 2$ cm.

Figure 5.9 shows a stagnation point on the axis just below the entrance to the vortex finder for $Q_0/Q_u = \infty$. Apparently, a flow reversal occurs in the vortex finder even for this extreme case. This observation yields the interesting, and most remarkable, conclusion that two stable vortex flows aligned with the axis of symmetry can exist with a surface of zero axial velocity between them! This phenomenon has been reported before for confined swirling flows (see Chanaud, 1965), and is one of the consequences of an instability known as "vortex breakdown" (see, esp., Lewellen, 1971).

Table 5.1. Change in flow topology with average circulation.

Position z, cm	Circulation $\bar{\Gamma}$, cm ³ /sec	Volumetric flow rate, cm ³ /sec	Type of flow
0	--	400	--
8	1683	401	1-cell with velocity defect
20	3673	383	3 cells
32	6878	325	3 cells

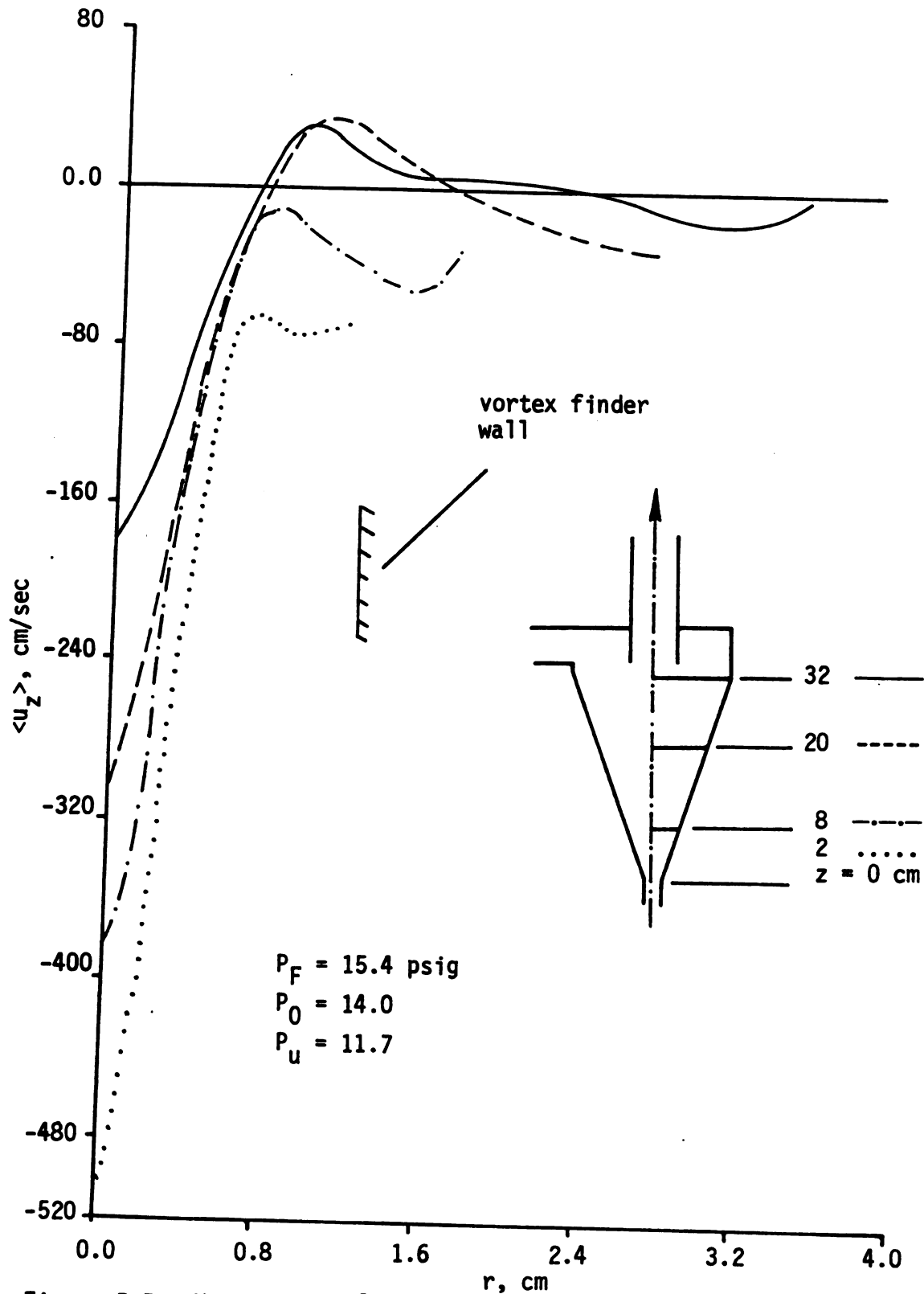


Figure 5.5. Mean axial velocity profiles for $Q_0/Q_u = 0.25$ and $Re_F \approx 24,200$.

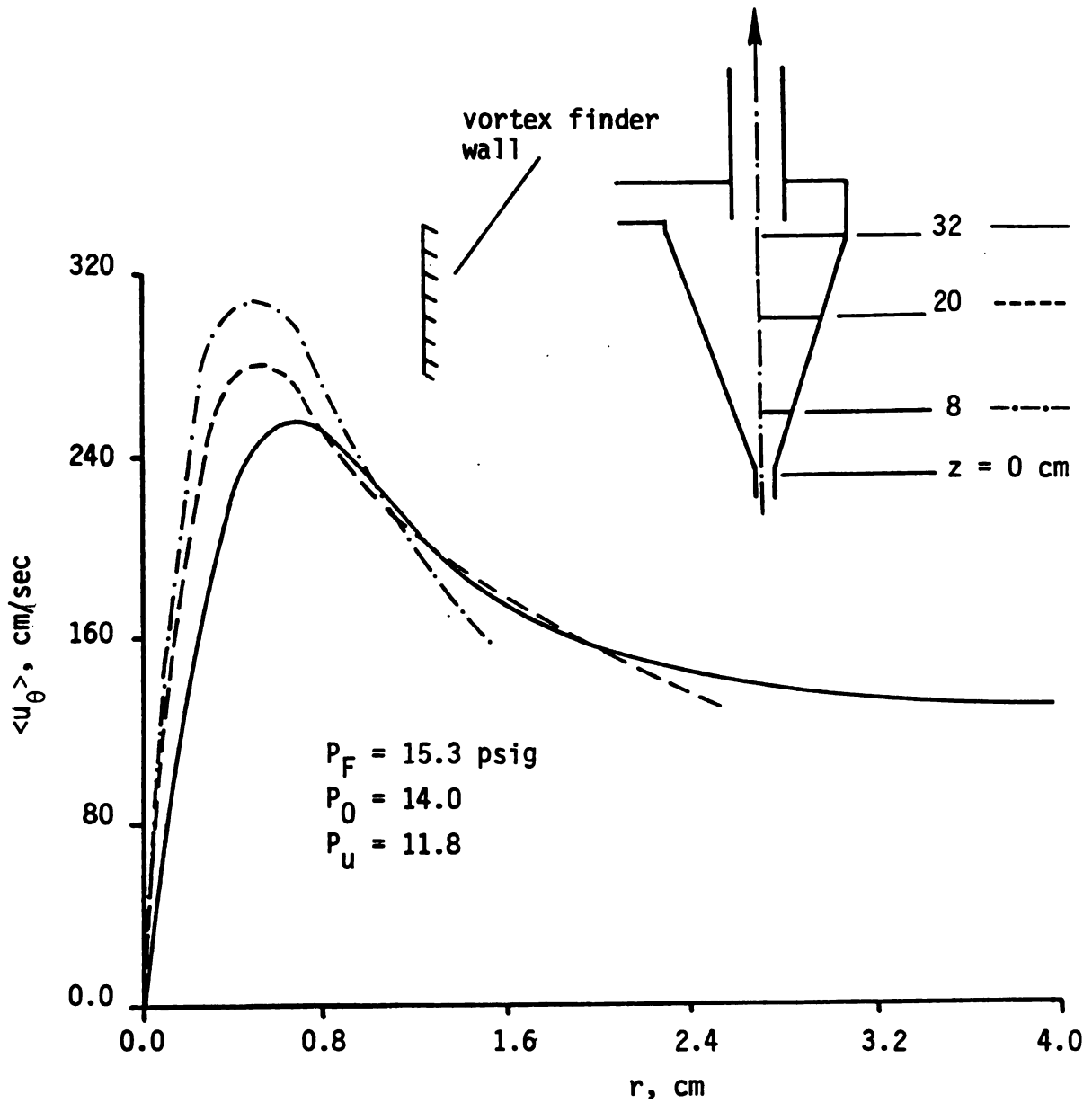


Figure 5.6. Mean tangential velocity profiles for $Q_0/Q_u = 0.25$ and $Re_F \approx 24,200$.

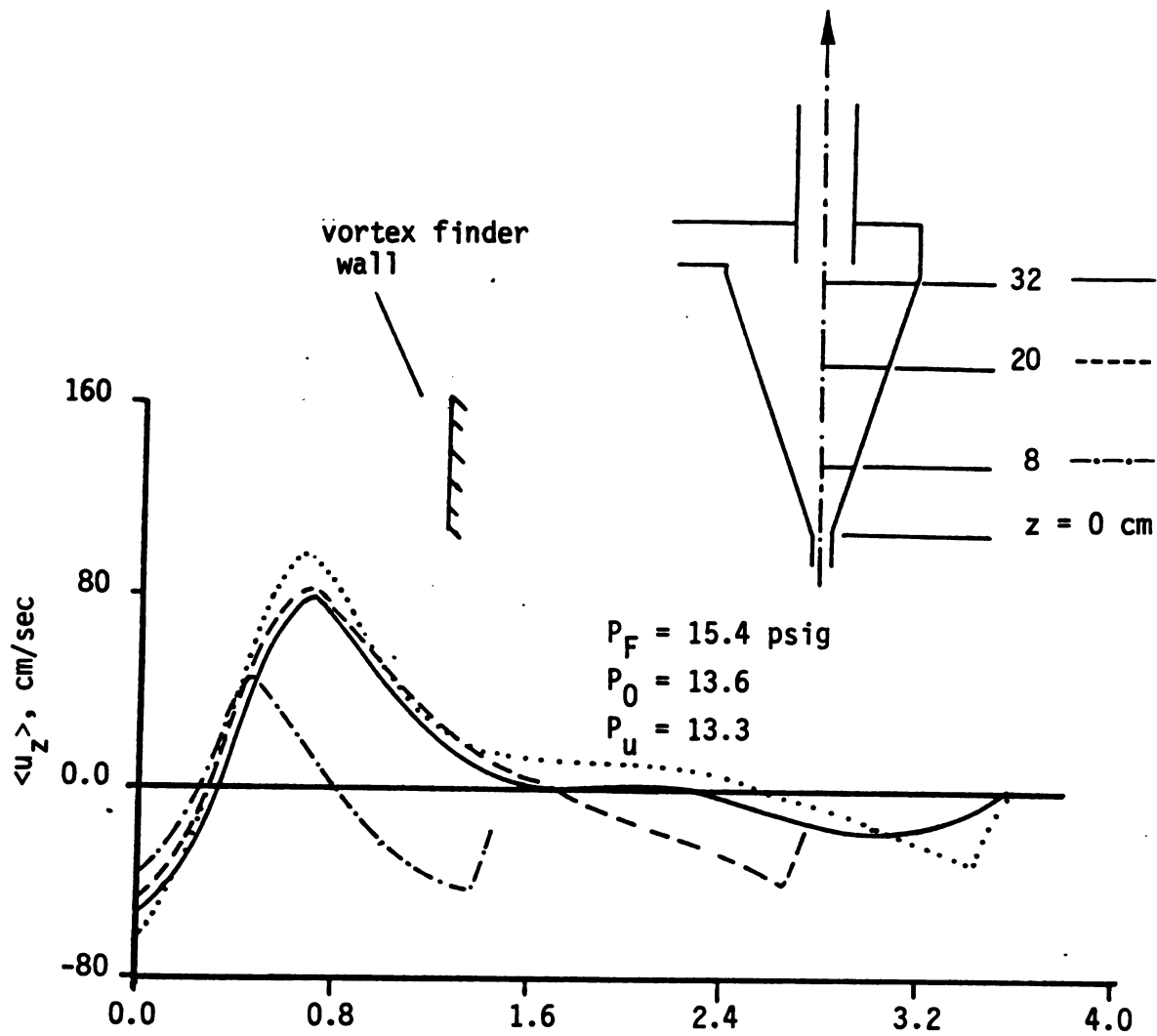


Figure 5.7. Mean axial velocity profiles for $Q_0/Q_u = 4$ and $Re_F \approx 24,300$.

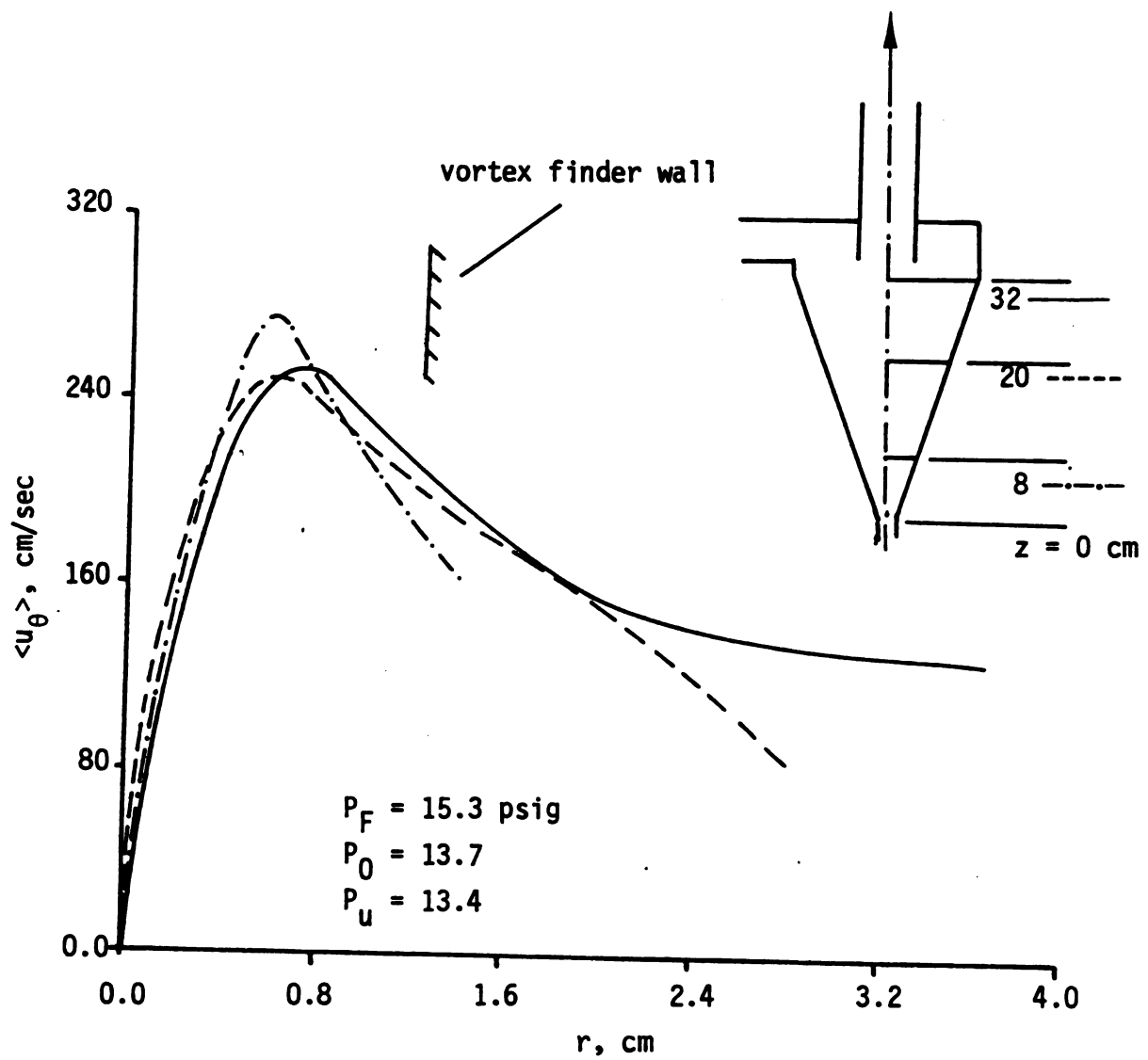


Figure 5.8. Mean tangential velocity profiles for $Q_0/Q_u = 4$ and $Re_F \approx 24,300$.

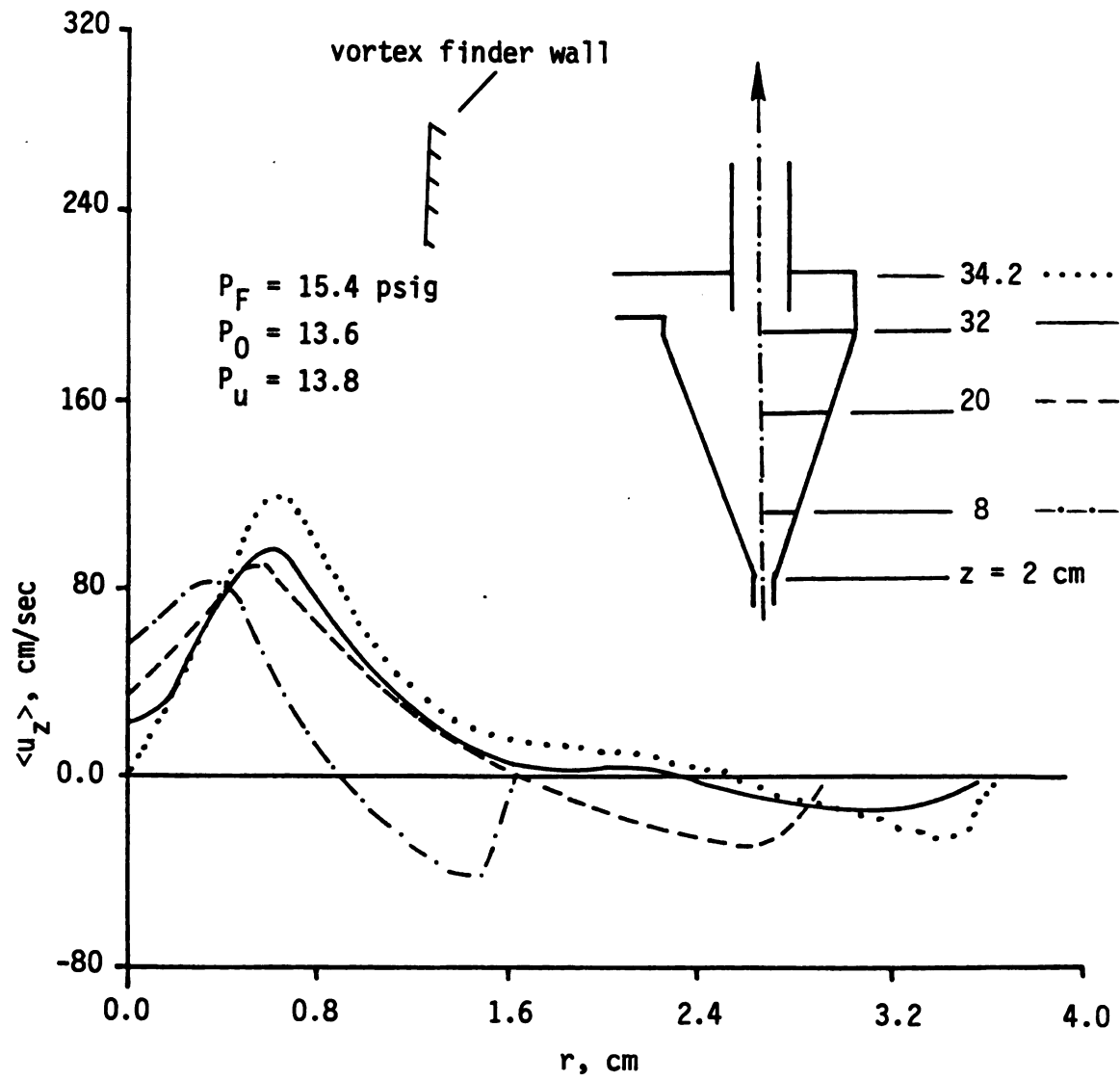


Figure 5.9. Mean axial velocity profiles for $Q_0/Q_u = \infty$ and $Re_F \approx 24,100$.

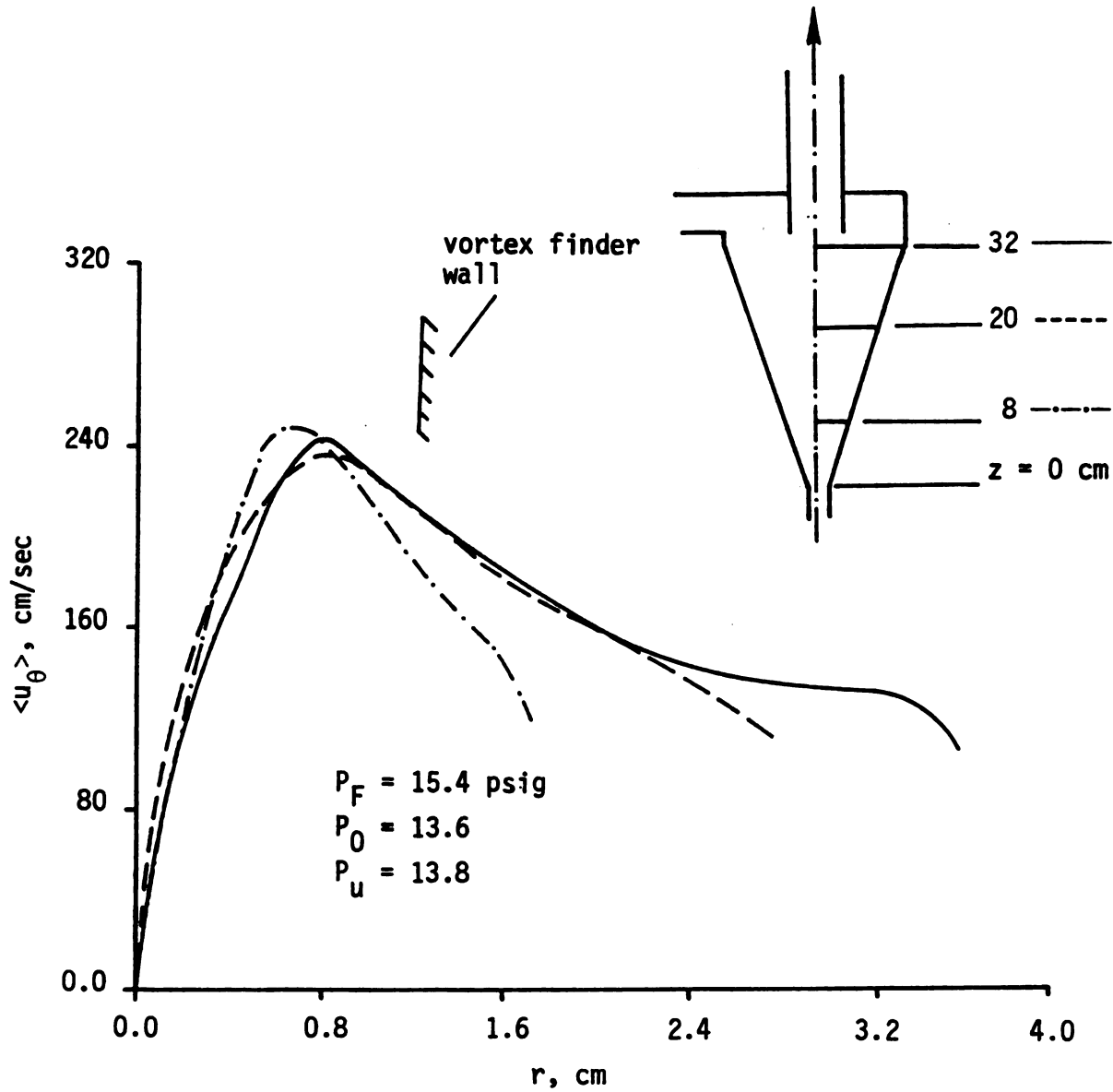


Figure 5.10. Mean tangential velocity profiles for $Q_0/Q_u = \infty$ and $Re_F \approx 24,100$.

As far as we know this is the first time that such a structure has been observed in hydrocyclone flows.

The average radial velocity was determined by applying Eq. (4.1) to the data shown in Figure 5.7. Figure 5.11 shows the average radial velocity profiles which are similar in the outer region to the results shown in Figure 4.5. In the upper part of the hydrocyclone, $\bar{u}(r)$ is still slightly positive and, thereby, would work in concert with the centrifugal force to remove solids from the central core region by convection and viscous drag. $\bar{u}(r)$ in the lower portion also looks like the results found earlier with the exception of the core flow. This was expected since the jet-like core with its characteristic negative radial velocity (see Figures 4.1 and 4.5) is absent in these experiments.

5.2. Equal Overflow and Underflow Areas

The predominant three cell reversal structures characteristic of the large vortex finder with and without a contraction are essentially equal overflow and underflow areas; the exception occurs for a split ratio of 0.25 as illustrated by Figures 5.12-5.14. These qualitative findings were also observed by Escudier et al. [1980] for converging, swirling flows with only a single exit. They reported transition from a three-cell to a two-cell structure for a 2:1 contraction. These results provide some understanding of why the design criteria of Rietema (see Figure 2.3) are optimal. With a three-cell structure like the one shown in Figure 5.7, entrainment of solids from the apex region should be less than what

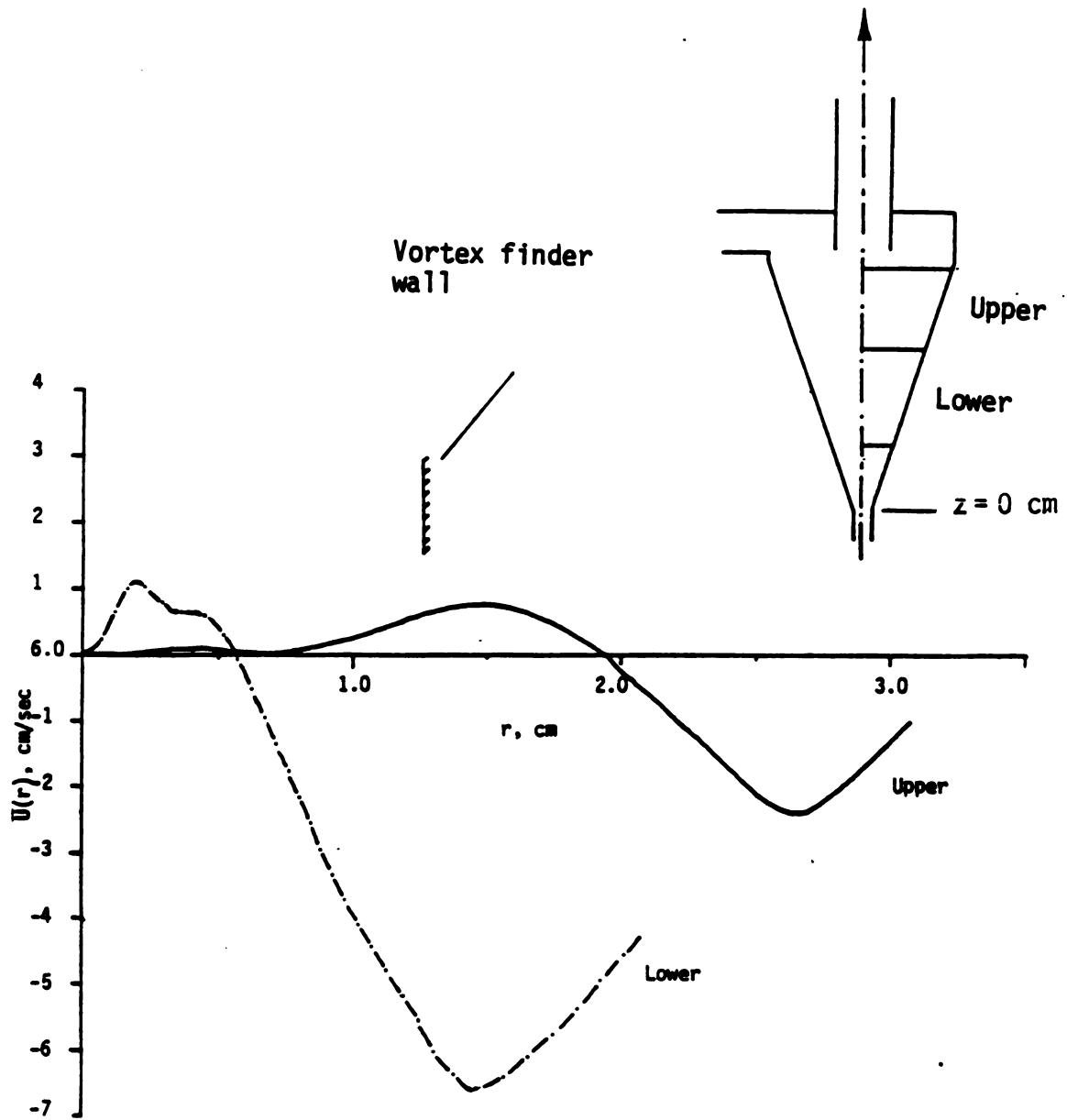


Figure 5.11. Average radial velocity profiles for $Q_0/Q_u = 4$ and $Re_F \approx 24,300$.

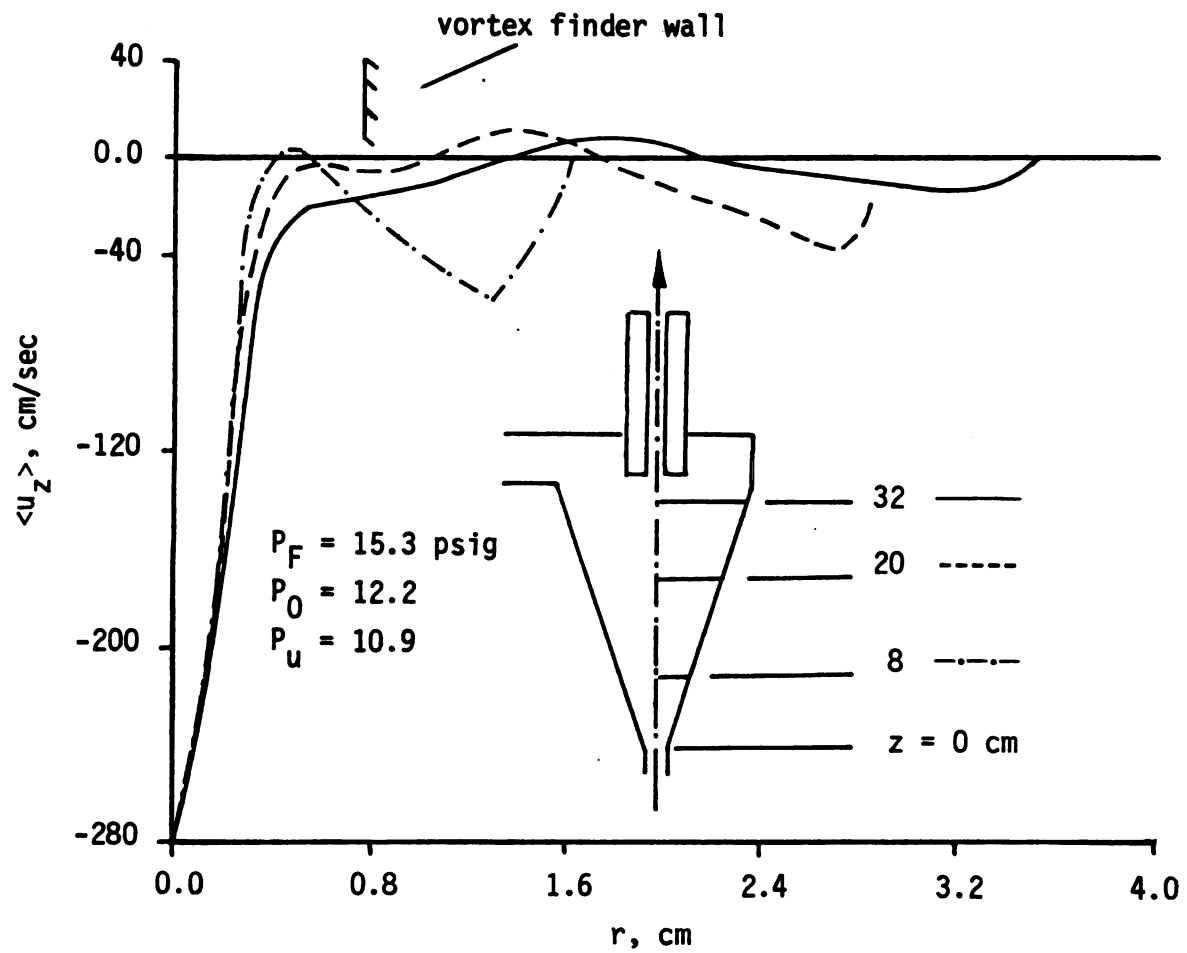


Figure 5.12. Mean axial velocity profiles for $Q_0/Q_u = 0.25$ and $Re_F \approx 24,300$.

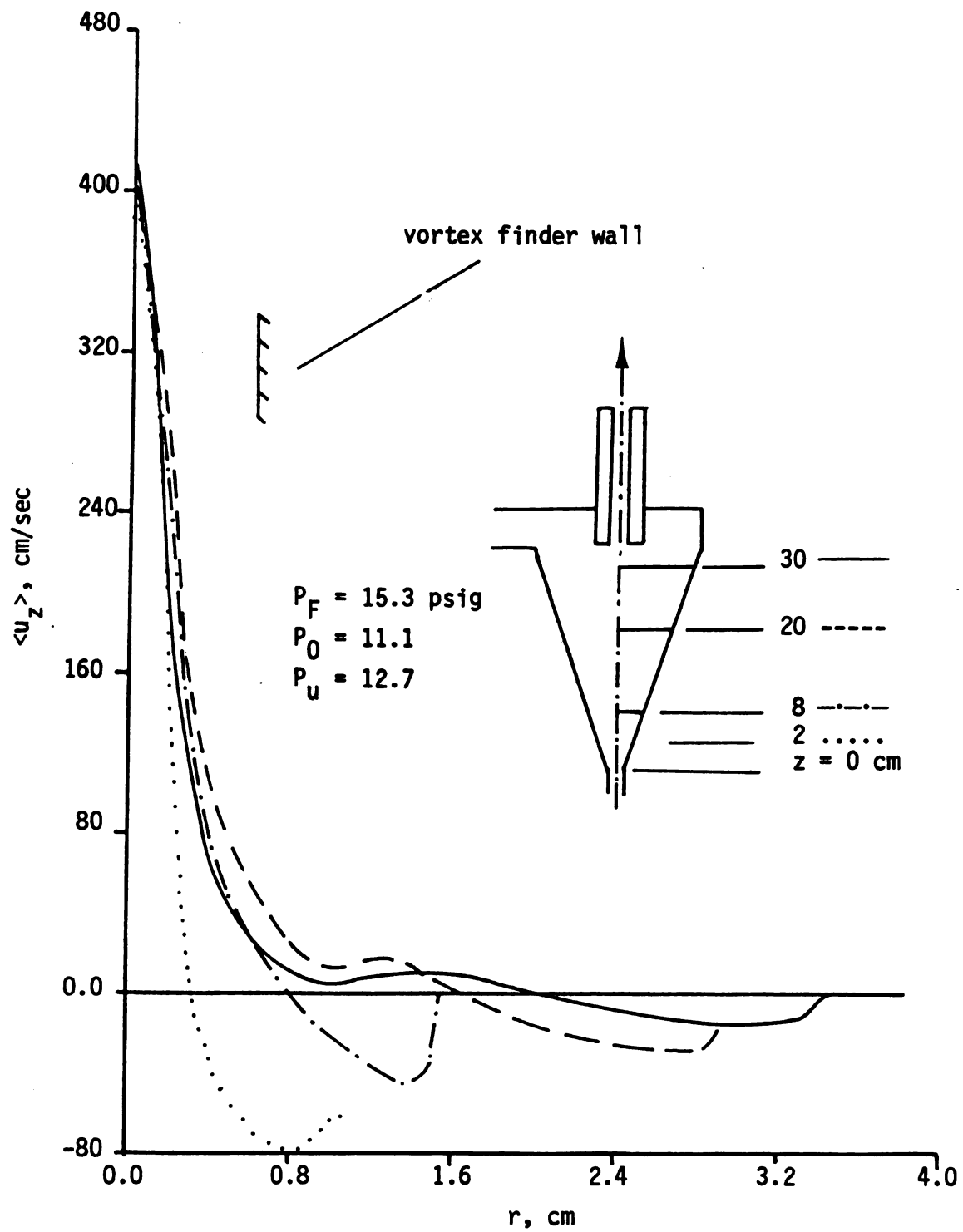


Figure 5.13. Mean axial velocity profiles for $Q_0/Q_u = 4$ and $Re_F \approx 24,300$.

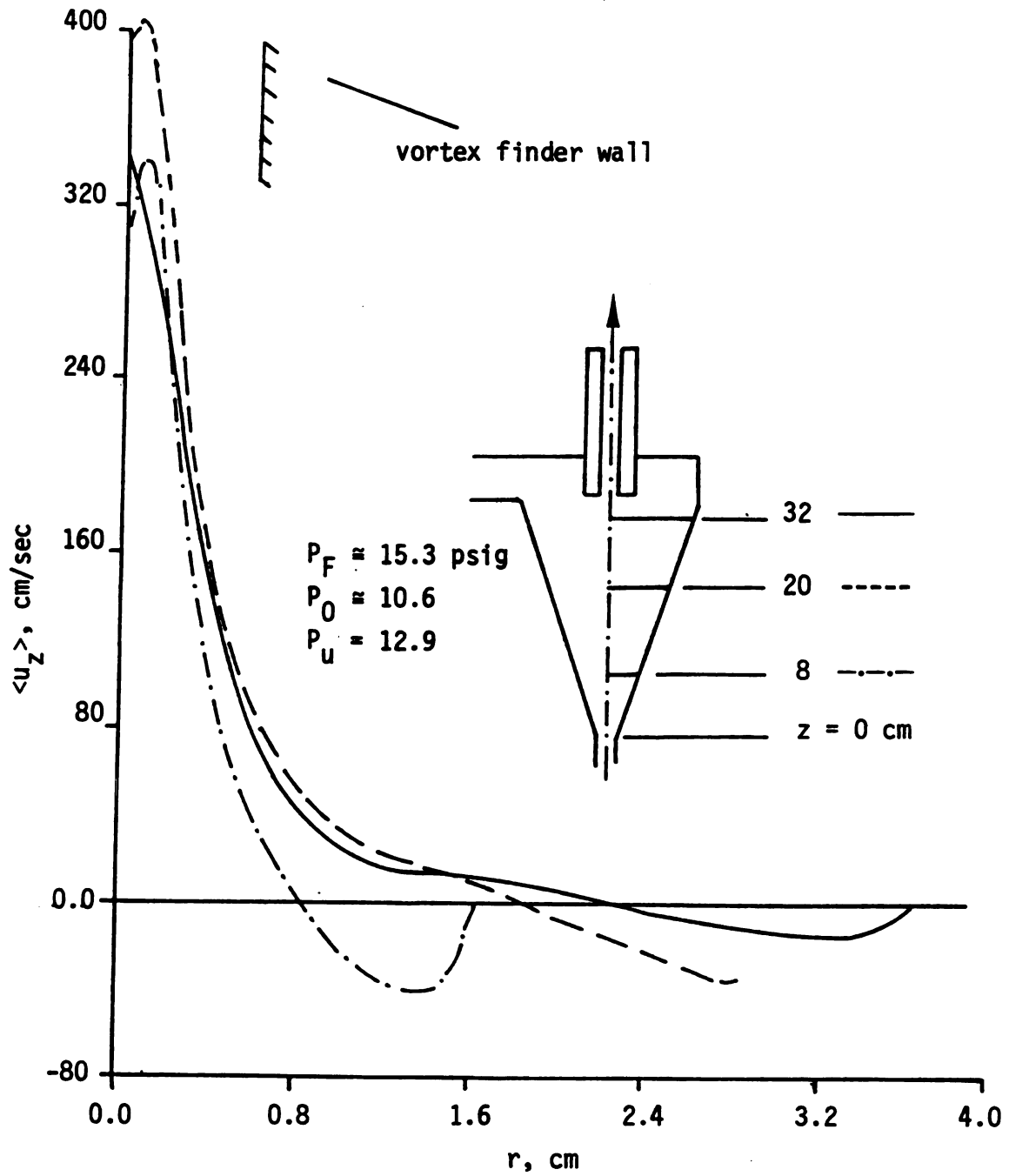


Figure 5.14. Mean axial velocity profiles for $Q_0/Q_u = \infty$ and $Re_F \approx 24,300$.

would occur with the two-cell structure shown in Figure 5.13. This important conclusion is discussed further in Chapter 6.

The velocity defect at $r = 0$ and $z = 8$ and 20 cm in Figure 5.4 may be the result of some small gas bubbles in the core region when these experiments were conducted; therefore, the physical significance of these profiles for $r < 3$ mm may be questionable.

The tangential profiles at $z = 32$ for the three split ratios studied are shown in Figure 5.15. Once again the outer core does not change much with Q_0/Q_u but the tangential velocity in the forced vortex region changes significantly. The results of Figure 5.13, which shows that the mean axial velocity for $r = 0$ is essentially constant for $2 \text{ cm} \leq z \leq 32 \text{ cm}$, and Figure 5.15, which shows that $\langle u_\theta \rangle \propto r$ for $r \leq 4$ mm, imply that the mean radial flow in the forced vortex region is negligible (c.f. Section 4.1). A corollary to this conclusion is that the turbulent transport of momentum in the vortex core is also negligible. This could be an important feature for the equal area discharge design but the evidence for this (and the reason) is minimal.

Figures 5.16 and 5.17 show, respectively, the effect of capacity (i.e., Reynolds number) on the axial and tangential velocities. It is interesting that the location of the zero axial velocity is insensitive to the Reynolds number and that it occurs at about the same radial location as the outer "mantle" in the Rietema design (see Figure 5.2). The tangential profiles shown in Figure 5.12 have a much broader shoulder and a sharper maximum than those in Figure 5.2.

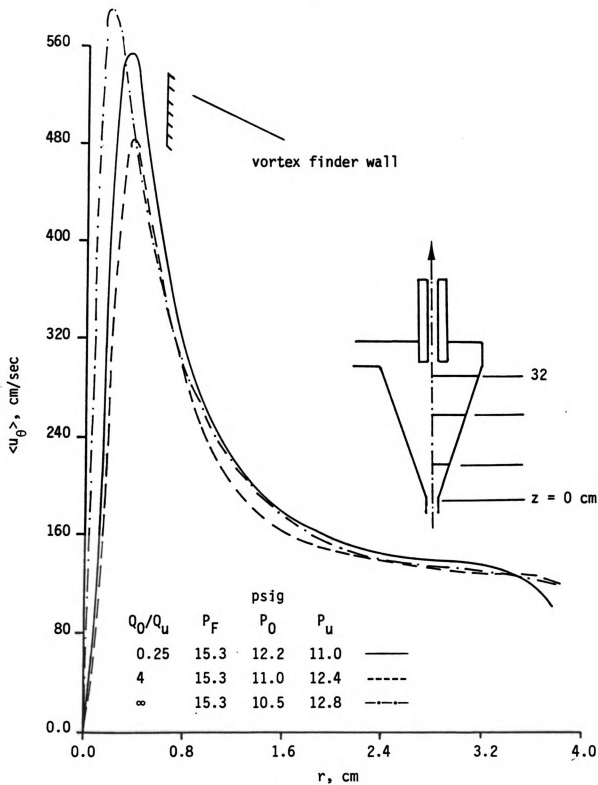


Figure 5.15. The effect of split ratio on $\langle u_\theta \rangle$ for $Re_F \approx 24,300$ at $z = 32$ cm.

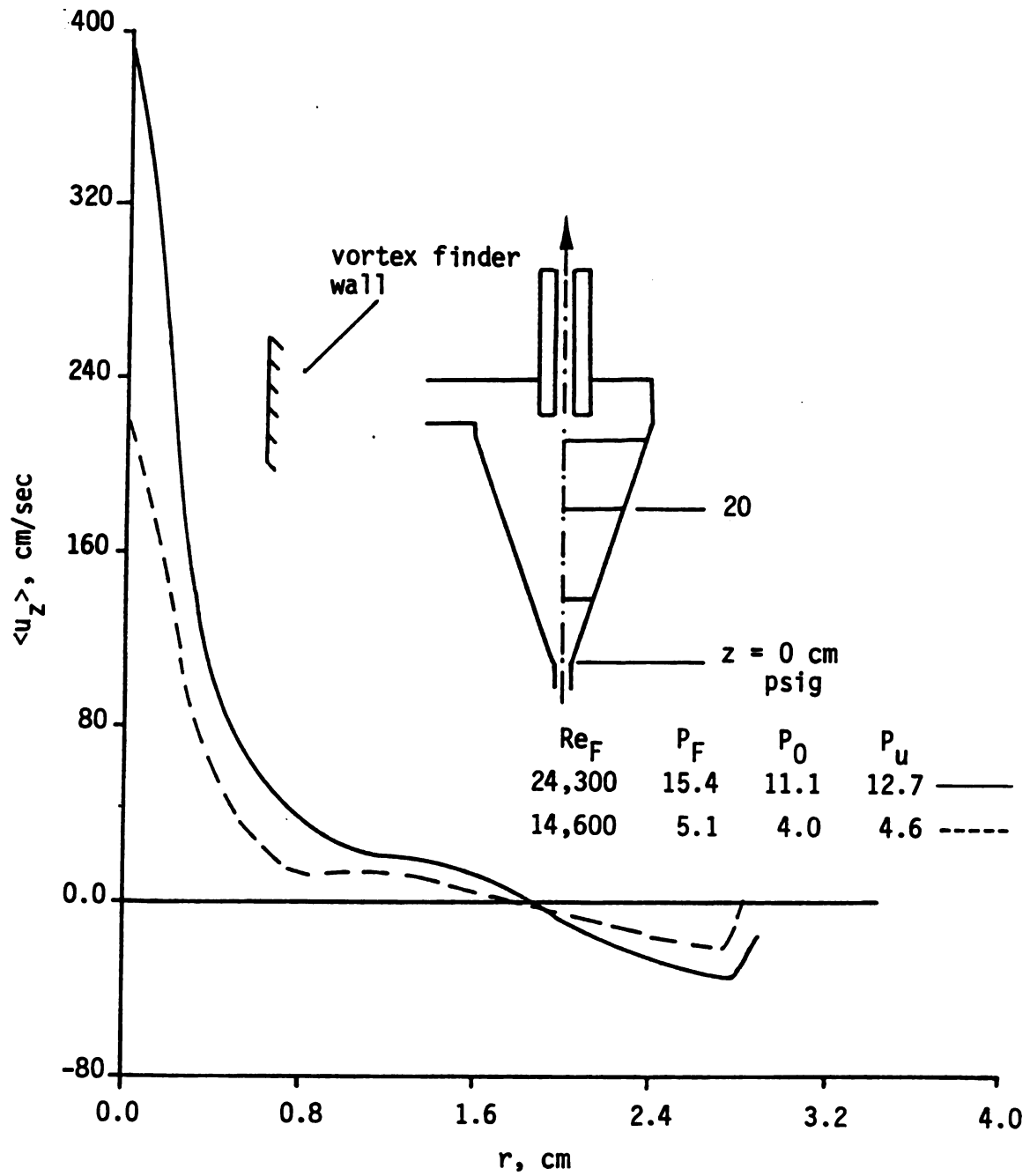


Figure 5.16. The effect of Reynolds number on $\langle u_z \rangle$ for $Q_0/Q_u = 4$ at $z = 20$ cm.

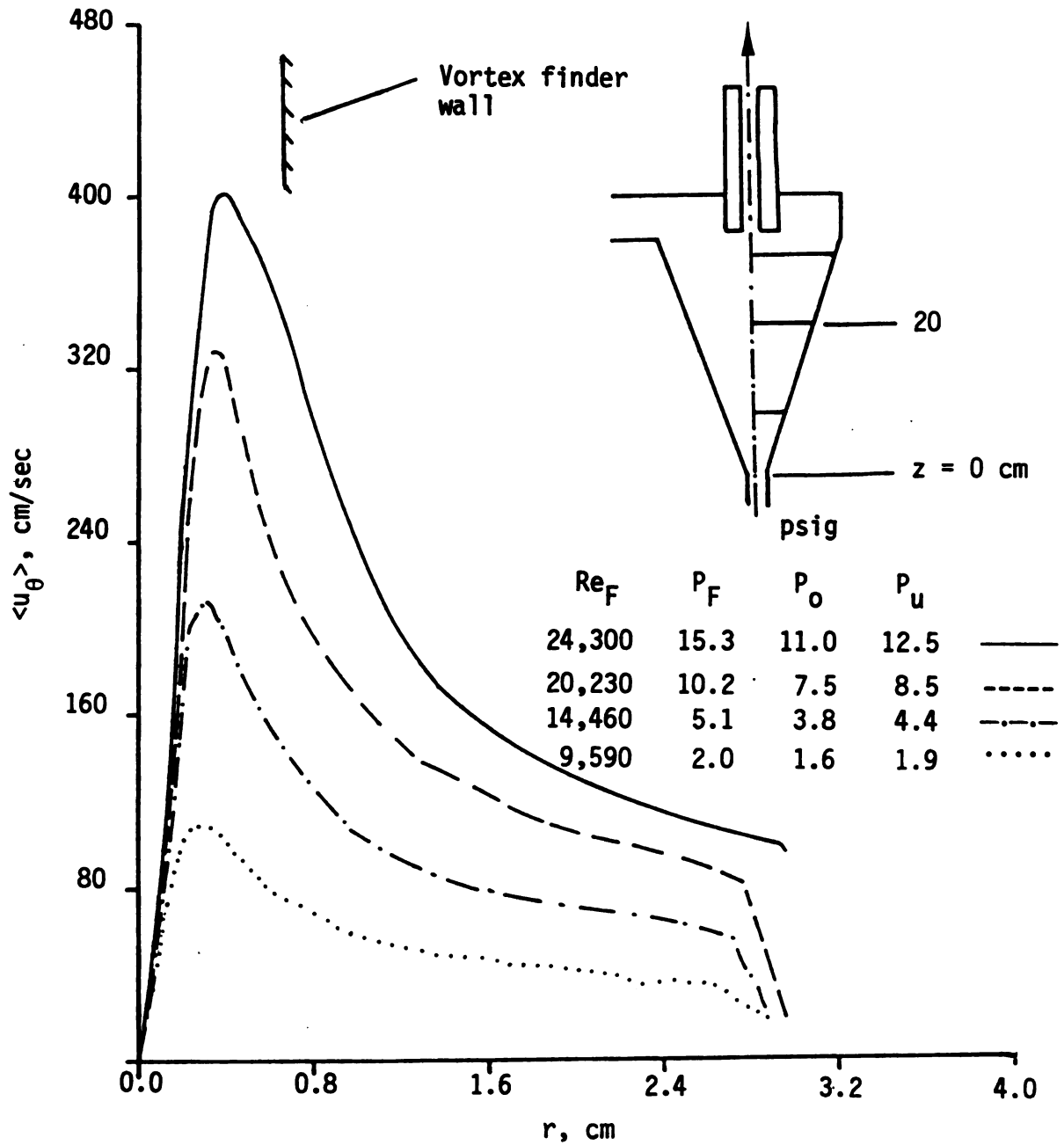


Figure 5.17. The effect of Reynolds number on $\langle u_\theta \rangle$ for $Q_0/Q_u = 4$ at $z = 20$ cm.

For $P_F = 15.3$ psig, the maximum tangential velocity observed for the hydrocyclone fitted with the smaller vortex finder is about 33% larger than the results for the optimal design. The values of $\langle u_\theta \rangle$ in the outer region for these two cases are nearly equal. The reason for this difference is probably due to the reverse flow phenomenon not seen in the equal area discharge case.

5.3. The Effect of Vortex Finder Design on Flow Reversals

During the course of this research, it was discovered that the geometry of the vortex finder plays an important role in determining the flow patterns in the core region. A series of experiments was conducted under similar operating conditions to catalogue some of the possibilities. Figure 2.5 shows the various vortex finders studied.

The axial velocity is unaffected by the shape of a contraction within the vortex finder (see Figure 5.18). However, Figure 5.19 shows that for a finite split ratio (here $Q_0/Q_u = 4$) the axial velocity profile obtained with a smooth contraction at the inlet has a "defect" of $r \approx 3$ mm. If the split ratio is increased to ∞ , then the qualitative behavior for the two entries is the same, as shown in Figure 5.20.

Figure 5.21 shows that the detail design of a vortex finder does not influence the outer swirl velocity, but has a significant effect, as expected, on the inner region. For the same split ratio and capacity, the tangential velocity for the small diameter vortex finder is higher and the core diameter is smaller. This occurs

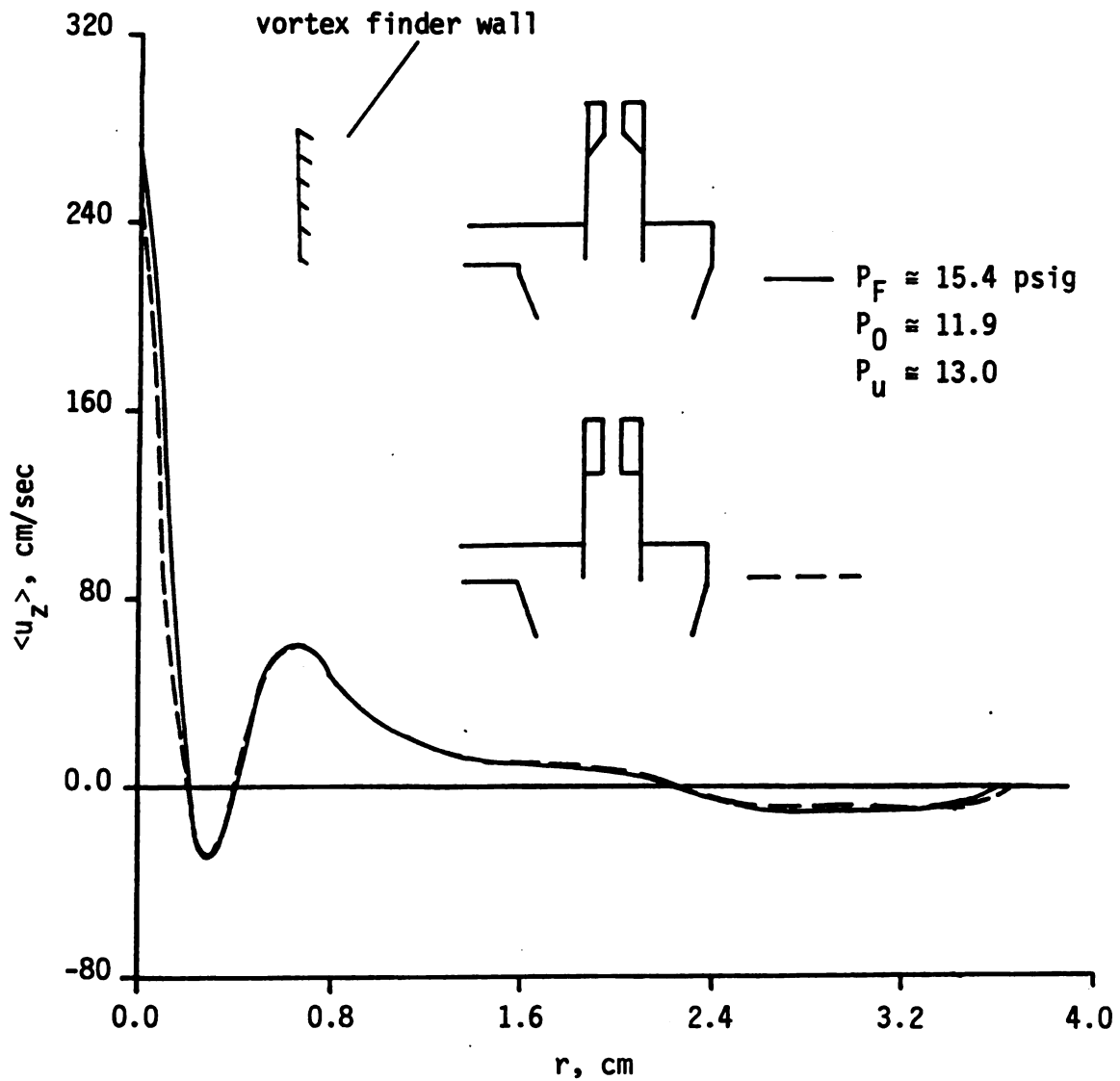


Figure 5.18. The effect of the degree of contraction in the vortex finder on $\langle u_z \rangle$ for $Q_0/Q_u = 4$ and $Re_F \approx 24,300$ at $z = 32$ cm.

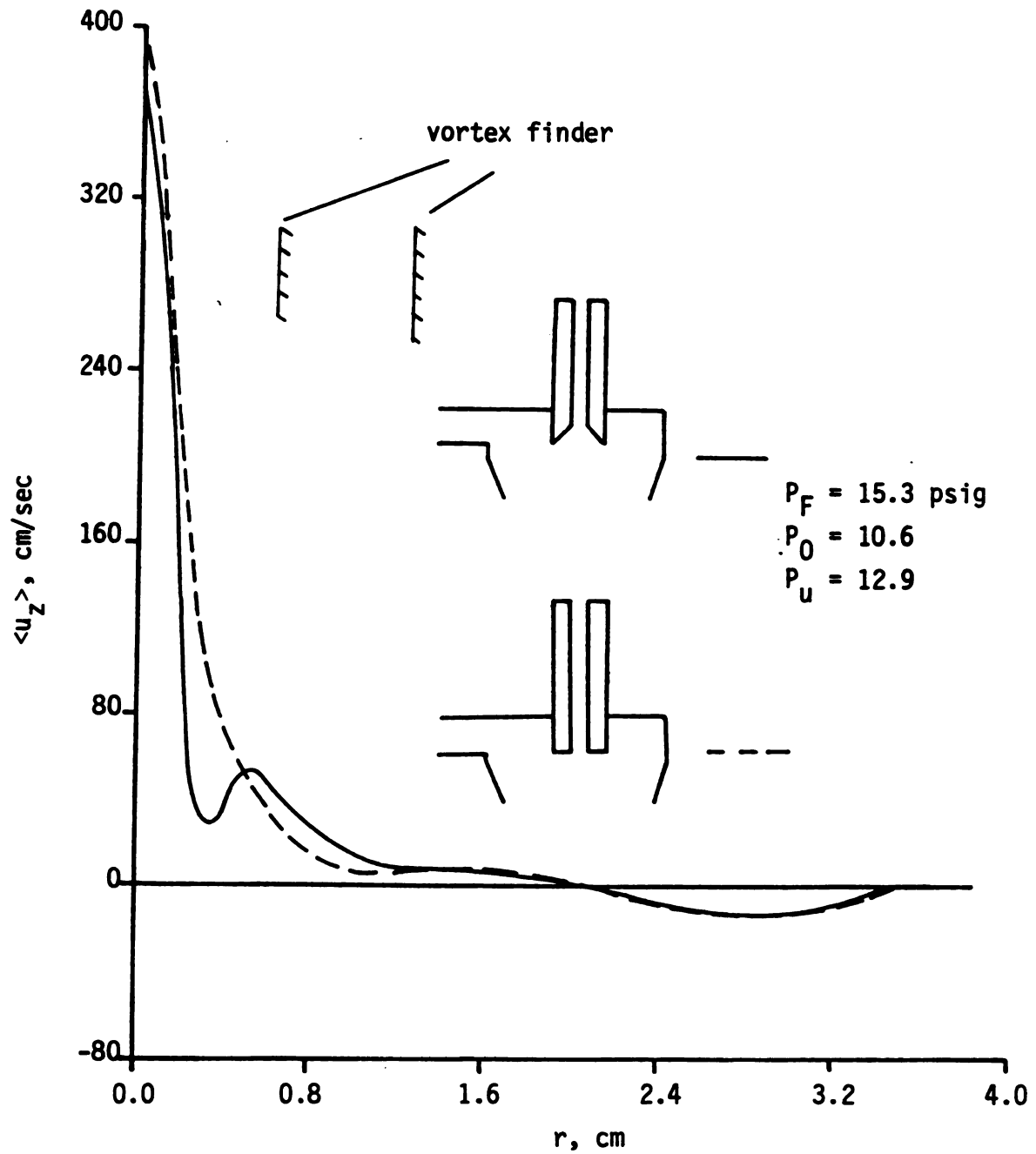


Figure 5.19. The effect of the degree of contraction on $\langle u_z \rangle$ for $Q_0/Q_u = 4$ and $Re_F \approx 24,300$ at $z = 32$ cm.

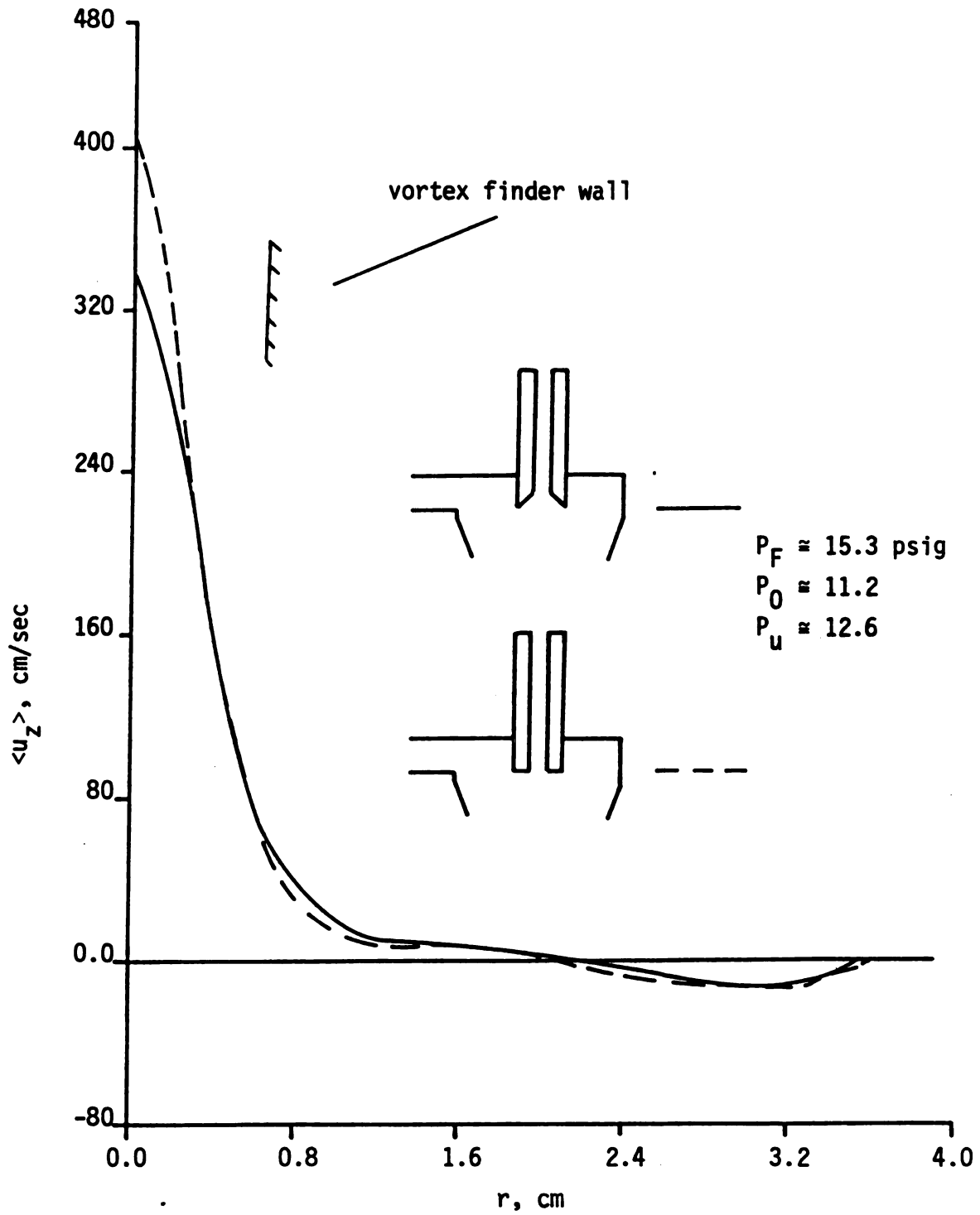


Figure 5.20. The effect of the degree of contraction on $\langle u_z \rangle$ for $Q_O/Q_U = \infty$ and $Re_F \approx 24,300$ at $z = 32$ cm.

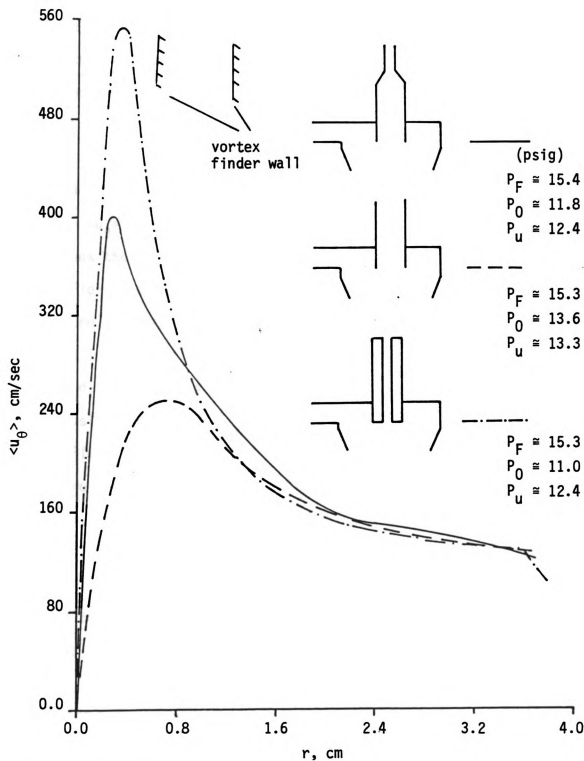


Figure 5.21. The effect of vortex finder configuration on $\langle u_\theta \rangle$ for $Q_O/Q_U = 4$ at $z = 32$ cm.

because the acceleration of the fluid, caused by the contraction, tends to preserve angular momentum by increasing the swirl to compensate for the reduction in the cross sectional area.

Figure 5.21 also illustrates that the "size" of the core region scales with the smallest diameter in the contraction. Bradley [p.115, 1965] mentions that the vortex finder radius is usually specified to make $\langle u_\theta \rangle$ a maximum at a radial position within the vortex finder. He argues that this would give a very high and desirable centrifugal force field near the mouth of the vortex finder. However, the results of Figure 5.21 imply that this occurs for any vortex finder diameter, so this is really a tenuous design criterion. Perhaps the vortex finder diameter should be related to the flow reversal phenomenon previously discussed.

Figure 5.22 summarizes how the number of flow reversals in the core region changes with design. For the design specified by Rietema, three cells occur with a core flow toward the apex. By decreasing the diameter, the morphology of the flow changes from a three to a two cell structure with a core flow toward the vortex finder tube. Finally, with a 2:1 contraction in the vortex finder tube, a four cell flow pattern occurs with a jet-like core flow toward the vortex finder. These results are currently not applied to design hydrocyclones, but a better understanding of their quantitative importance may lead to significant improvements in some applications.

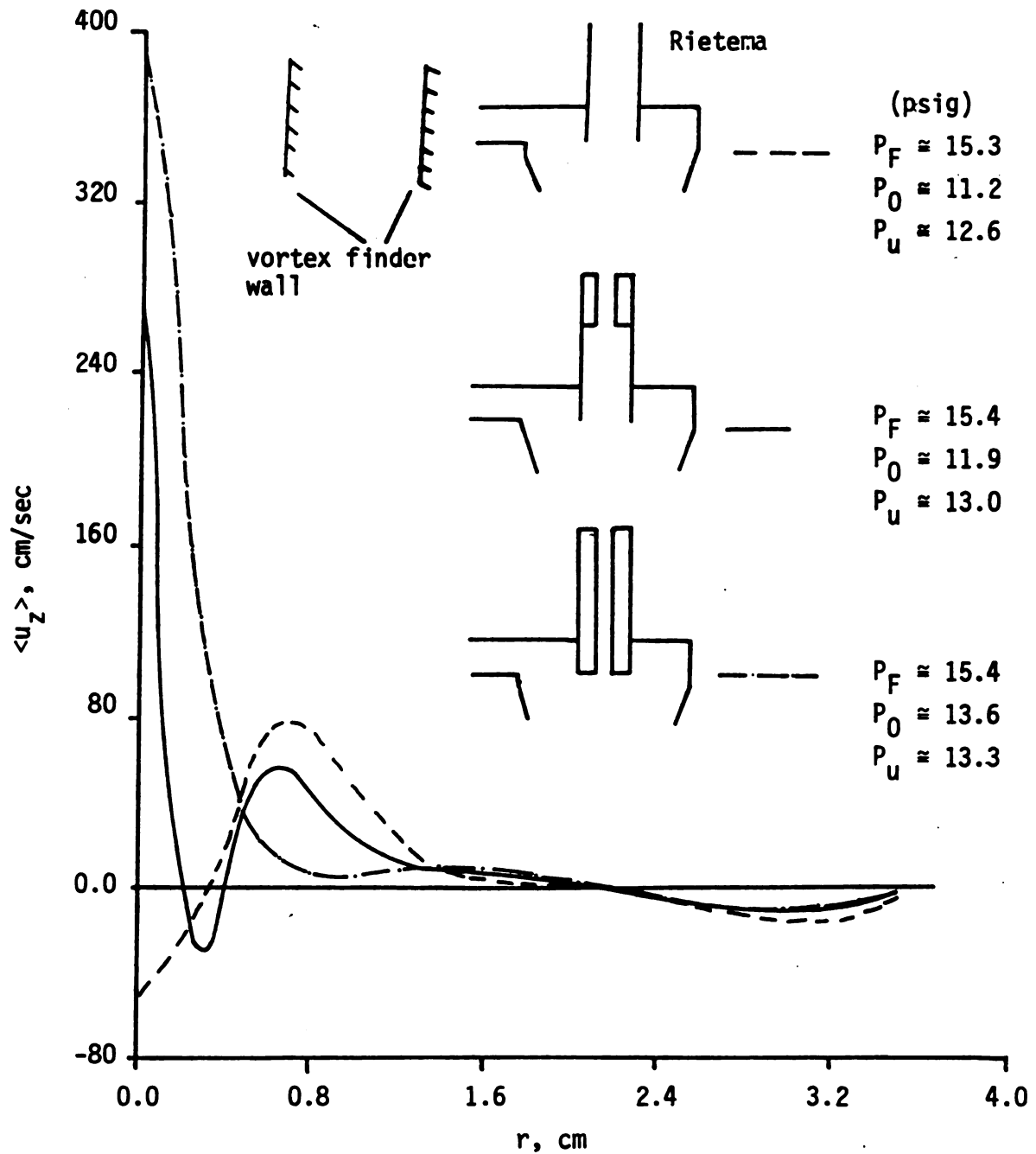


Figure 5.22. The effect of vortex finder configuration on $\langle u_z \rangle$ for $Q_0/Q_u = 4$ at $z = 32$ cm.

CHAPTER 6

DISCUSSION AND CONCLUSIONS

6.1. Summary Discussion of Results

A systematic set of experiments were conducted in order to investigate the effect of operating conditions and design variables of a 3"-hydrocyclone on the mean velocity field. The conclusions developed from these experiments resulted in new findings as well as confirmation of some previous results obtained by other researchers.

Mean velocity measurements for the hydrocyclone with a 2:1 contraction resulted in very complex and interesting flow patterns inside the core region. For a split ratio of 4, four helical reverse flows were measured quantitatively and confirmed by flow visualization (see Figure 4.1). The central core region for this configuration is a stable and coherent high velocity region, which extends over the entire length of the hydrocyclone. A reverse flow is initiated from the contraction zone within the vortex finder and tends to fade close to the apex region (see Figures 3.1 and 3.2). For this flow condition, the locus of zero axial velocity is located on a conical surface in the outer region and on a cylindrical surface in the inner region. This shows that the surfaces of zero axial velocity are determined by the geometry rather than the operating conditions.

The axial location of the contraction inside the vortex finder was found to be an important factor in creating multiple helical flows. However, the degree of contraction has little effect (see Section 5.3). The morphology of the flow field is also affected by the split ratio. As the split ratio changes from ∞ to 4, the flow pattern increases from a two-celled to a four-celled vortex flow. With a further decrease in the split ratio, the number of cells drops from four to three.

The velocity field in a hydrocyclone based on Rietema's "optimal" design criteria was studied quantitatively using LDA. The results of this study illustrate the effect of the split ratio and the inlet flow rate on the tangential and axial velocities. The split ratio completely altered the flow field qualitatively whereas the inlet pressure affected the flow quantitatively. A region of reverse flow was studied for a split ratio of 4. This reverse flow started inside the vortex finder and its magnitude decreased as it moved toward the apex region. For a split ratio of 0.25, the high velocity core region tends to increase as it moves downward (see Figures 5.5, 5.7, and 5.9). The flow in the outer region was unaffected by variations in the split ratio.

The complete flow pattern for a hydrocyclone with equal overflow and underflow areas revealed only two regions of flow: an upward helical flow in the core region and a downward helical flow surrounding the core flow (see Figure 5.13).

A comparison study of the axial velocity for different vortex finder configurations showed that the vortex finder design influences the core region but not the outer region. The velocity profiles measured for all vortex finder configurations discussed in this study revealed no significant change in outer region as a result of change in the split ratio; however, the effect of the vortex finder on the core flow is important. Depending on the specific design, a three-celled, a two-celled, or a one-celled vortex flow is obtained (see Figure 5.22).

Mean tangential velocity measurements showed two regions of flow: force and free vortex. In the force vortex region, the tangential velocity changes linearly with radius and, in the 'free' vortex region, the relationship is described by

$$\langle u_{\theta} \rangle \cdot r^n = \text{constant}$$

where the index n ranges from 0.5 - 0.7 for the majority of experiments. For the hydrocyclone investigated, the tangential velocity profiles are approximately independent of axial location. The split ratio affects the maximum tangential velocity and the core diameter only slightly; however, for smaller vortex finder diameters, the maximum tangential velocity and the core diameter are affected significantly (see Figure 5.21).

The inlet flow rate affects the flow pattern inside the hydrocyclone quantitatively, not qualitatively. The locus of zero axial

velocity and the core diameter are unaffected by changes in the inlet flow rate.

Over the operating range of the hydrocyclone with a contraction, the addition of 100 wppm Separan AP-30, which showed 50% drag reduction in fully developed pipe flow, eliminated the flow reversal and suppressed the tangential velocity. Figures 4.12 and 4.13 illustrate this quantitative effect.* The effect of polymer on specific flow structures in the hydrocyclone at higher Reynolds numbers remains unclear.

The effective viscosity of fresh Separan AP-30 is a function of chemical composition of the solvent (pH and salt content). Results obtained for drag reduction in a capillary tube for fresh polymer solution with pH \approx 10.5 exceeded Virk's maximum drag reduction asymptote (see Figure B.4). This is a new discovery which merits additional attention.

The flow-rate, pressure drop relationship for the 3"-hydrocyclone used in this research was found to be in good agreement with other investigators (see Table B.1). The theoretical result,

$$Q_F \propto (P_F - P_0)^{\frac{1}{2}},$$

*The mean axial velocity profiles measured at 12° and 20° showed only minor differences in the viscous core region. Therefore, the above effect is probably due to the viscoelastic nature of the fluid rather than to the 24% difference in the viscosity. This should, however, be studied further.

is consistent with the experimental findings of this study. The small difference between the experimentally determined exponent of 0.42 on ΔP and the theoretical result is due to entrance effects.

6.2 Conclusions Based on this Research

Flow Reversals

A 2:1 contraction in the vortex finder plays an important role in the formation of four distinct, simultaneous, countercurrent axial flows in the conical section of the hydrocyclone. The contraction causes an annular flow reversal. Without the contraction a flow reversal is still possible, but it contains the axis.

The Effect of Split Ratio

The morphology of the flow field is affected by the split ratio. With a 2:1 contraction in the vortex finder, as the split ratio decreases from ∞ to 4, transition from a two-celled structure to a four-celled structure implies that a critical Rossby number exists between 1 and 0.8 (see Eq. (1.7)). With further decreases in split ratio from 4 to 0.25, transition from a four-celled structure to a three-celled structure occurs (critical Rossby number between 0.8 and 0.2). In the upper part of the hydrocyclone a six-celled vortex flow was detected by reducing the backpressure. This could result in a multiple recirculation zone.

For Rietema's 'optimal' design as the split ratio is changed from ∞ to 0, transition from a two-celled to three-celled vortex flow occurs at $Q_0/Q_u = 6.8$. Four cells were not encountered for this

hydrocyclone configuration. For this hydrocyclone design, a stagnation point on the axis just below the entrance to the vortex finder for $Q_0/Q_u = \infty$ was observed. Apparently, two stable vortex flows aligned with the axis of symmetry can exist with a surface of zero axial velocity between them. The outer region of the hydrocyclone is unaffected by the split ratio.

The Effect of Vortex Finder and its Contraction

Change in the design of the vortex finder only affected the core region. The locus of zero axial velocity remained unchanged. Results of this research show that the location of the maximum tangential velocity is unaffected by the size of the vortex finder. This conclusion is in sharp contrast to the current understanding of vortex finder design discussed by Bradley [p. 115, 1961]. The flow field is unaffected by the degree of contraction in the vortex finder, but its morphology is strongly dependent on the location of the contraction.

The Effect of Polymer on the Flow Field

A dilute polymer solution (100 wppm Separan AP-30) eliminated the flow reversal and suppressed the tangential velocity in a 3"-hydrocyclone with a 2:1 contraction. Figure 6.1 shows the axial profiles obtained with and without polymer additive at the same Reynolds number (different temperature including viscosity effect). Note that the addition of polymer seems to have eliminated the flow reversal surrounding the central core vortex due to viscoelastic

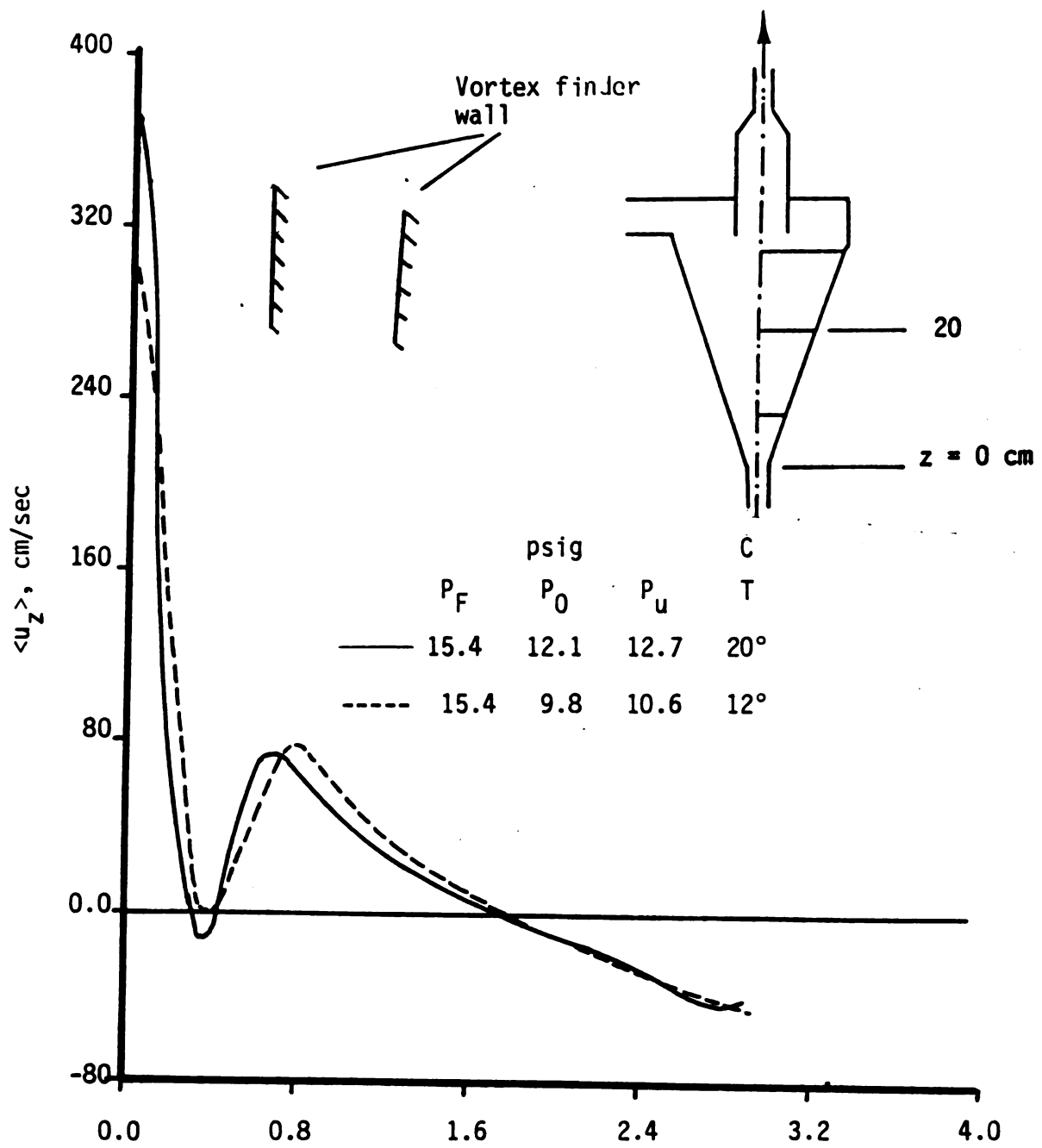


Figure 6.1. The effect of polymer (100 wppm Separan AP-30) on $\langle u_z \rangle$ for $Q_0/Q_u = 4$ and $Re_F \approx 30,000$.

property of the dilute polymer solution. Drag reduction experiments in a capillary tube for this polymer at $\text{pH} \approx 10.5$ exceeded Virk's maximum drag reduction asymptote. This enhancement in drag reduction can be interpreted as a result of molecular expansion due to electrostatic repulsion between like charges in the polymer chain.

The Effect of Inlet Flow Ratio

The morphology and the locus of zero axial velocity are unaffected by the inlet flow rate; however, the magnitude of the velocity profiles is changed to compensate for flow displacement inside the hydrocyclone.

Comparison of Rietema's 'Optimal' Design with other Hydrocyclone Designs

Comparison of Rietema's optimal design with other hydrocyclone configurations revealed low swirl and a smaller outward radial velocity for the optimal design. A lower centrifugal field and a low outward radial flux create an unfavorable condition for separation. Although a high centrifugal field is desirable, the entrainment of solid particles from the conical boundary-layer into an upward flow deep in the apex makes other hydrocyclone designs inferior to Rietema's optimal design. This conclusion stems from Figure 6.2 which shows a comparison between the axial velocities in the two different hydrocyclones in the apex region. Note the absence of upward jet-like flow in the Rietema design.

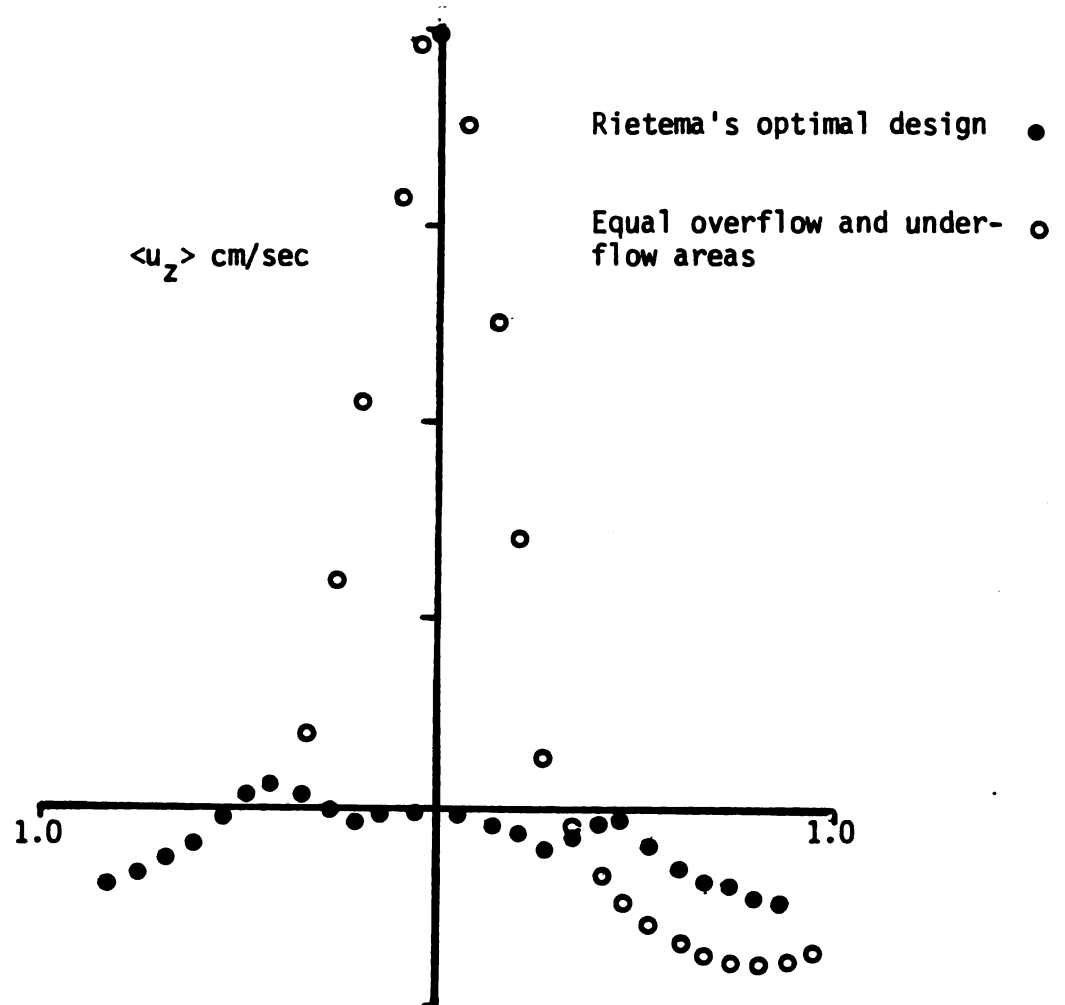


Figure 6.2. Mean axial velocity profiles for $Q_0/Q_u = 4$, $Re_F \approx 24,300$, and at $z = 2$ cm.

6.3. Indirect Conclusions Suggested by the Results of this Research

Mechanism for the Formation of Multiple Axial Cells

Figures 4.6, 5.1, and 5.22 show that the mass flux through the conical boundary layer is independent of the split ratio. At a very high split ratio (or Rossby number) the vortex flow in the underflow chokes because of the relatively large back pressure compared with the fluid pressure in the apex zone. The result of this is an ejection of mass from the viscous boundary with a strong jet-like flow appearing at high split ratios (see Figure 3.4b and the central core region of Figure 4.1). On the other hand, as the split ratio decreases more of the boundary layer fluid can discharge through the underflow. If an upward flow on the axis occurs for $Q_0/Q_u = 0.25$, it is not strong enough to be detected. What is observed is an axisymmetric downward core flow, which forms in the vortex finder and covers the entire length of the hydrocyclone. As the split ratio increases, an upward jet-like flow forms on the axis in the apex as previously mentioned (see Figure 3.2). The annular reverse flow caused by the contraction in the vortex finder at $Q_0/Q_u = 4.0$ is unable to penetrate the axial jet and the net result is a four-celled vortex structure.

What is the physical origin of the jet-like behavior? Based on the experiments developed in this research, it is conjectured that the axial upward jet flow results when the viscous boundary layer begins to interact with the core flow. This happens deep within the apex region. Above this region and in the primary flow,

the θ -component of the Reynolds equation is balanced by the inertial terms. The coriolis force of the mean field and the radial convection of θ -momentum balance the axial and radial transport of fluctuating θ -momentum. The Reynolds equation in cylindrical coordinates is given by Boysan et al. [1982]. The above physical situation implies the following simplification:

$$\langle u_r \rangle \frac{\partial \langle u_\theta \rangle}{\partial r} + \frac{\langle u_r \rangle \langle u_\theta \rangle}{r} \approx \frac{\partial}{\partial z} \langle u'_z u'_\theta \rangle - \frac{\partial}{\partial r} r \langle u'_r u'_\theta \rangle - \frac{\langle u'_r u'_\theta \rangle}{r} \quad (6.1)$$

In this equation, the viscous transport terms have been neglected as well as

$$\langle u_z \rangle \frac{\partial \langle u_\theta \rangle}{\partial z} \approx 0 . \quad (6.2)$$

Equation (6.2) follows from the experimental data obtained in this research.

Equation (6.1) cannot hold deep in the apex where the viscous boundary layer begins to interact with the core flow. Furthermore, our previous analysis of $\langle u_r \rangle$ suggests that $\langle u_r \rangle = 0$ at some $r > 0$ and we conjecture that this will also occur for $z < 8$ cm. Now, if $\langle u_\theta \rangle$ begins to decay slightly in the apex, then Eq. (6.2) is no longer true. Indeed, for $z \rightarrow 0$, we anticipate that

$$\frac{\partial \langle u_\theta \rangle}{\partial z} > 0$$

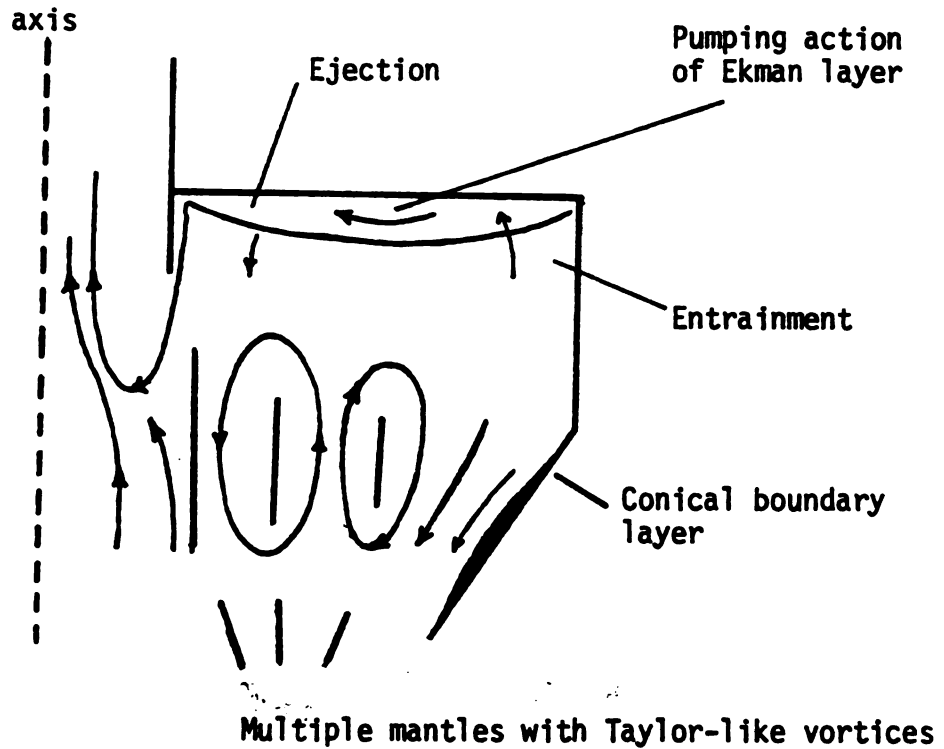
and that the viscous transport of momentum dominates the turbulent transport. Whence, the θ -component of the Reynolds equation reduces to a balance between the axial convection of the average θ -momentum and its viscous transport, i.e.,

$$\langle u_z \rangle \frac{\partial \langle u_\theta \rangle}{\partial z} \approx \nu \frac{\partial}{\partial r} \left[\frac{1}{r} \frac{\partial}{\partial r} (r \langle u_\theta \rangle) \right]. \quad (6.3)$$

As already noted, Eq. (6.3) is conjectured to hold in the region where the viscous boundary layer interacts with the vortex core. The right-hand-side represents the viscous transport of angular momentum from the boundary layer to the core, so it is positive. Now, if $\langle u_\theta \rangle$ decays slightly, then (6.3) is balanced by a positive value of $\langle u_z \rangle$. Thus, an upward jet-like (if the right-hand-side is large and $\frac{\partial \langle u_\theta \rangle}{\partial z}$ is small) flow is expected.

Mechanism for the Formation of Multiple Mantles

Figure 4.11 shows that for low back pressures several reverse flows may occur in the upper portion of the primary flow domain. The possibility of multiple mantles has been discussed before (see Bradley and Pulling, 1959). The idea is illustrated by the following simple schematic.



If the angular momentum $r\langle u_\theta \rangle$ decreases with increasing r in the outer region of the primary flow, Rayleigh's criterion for centrifugal instability is satisfied (see p. 272 in Greenspan, 1968). In physical terms, if a fluid particle at r with tangential velocity $\langle u_\theta \rangle(r)$ moves to $r + \Delta r$, then it attains a swirling velocity equal to

$$\left(\frac{r}{r + \Delta r}\right) \langle u_\theta \rangle(r) ,$$

provided angular momentum is conserved. For this situation, the centrifugal force which acts on the particle at $r + \Delta r$ is

$$\frac{r^2}{(r + \Delta r)^3} \langle u_\theta \rangle^2(r) .$$

This force opposes the inwardly directed pressure force with magnitude

$$\frac{\langle u_{\theta} \rangle^2 (r + \Delta r)}{(r + \Delta r)} \cdot$$

Obviously, this force cannot balance the outward centrifugal force if the angular momentum decreases with r . Thus, based on an inviscid analysis, the outer primary flow is unstable and Taylor-like roll cells would occur. However, viscosity tends to stabilize the flow and obviously plays an important implicit role in maintaining the two-dimensional character of the outer primary flow.

In the upper portion of the hydrocyclone additional effects must be considered. Here the angular momentum distribution is more complicated because of the vortex finder and the presence of an Ekman layer, which can eject mass in the vicinity of the maximum swirl velocity (see Section 1.2.1). Loss of mass from the boundary layer is compensated by entrainment of fluid from the primary flow so a pumping action on the roof occurs. In this way, a local region of circulation develops which supports the basic Rayleigh instability mechanism. The net result is the appearance of multiple mantles.

Suppression of Turbulent Transport in
the Core Region by Polymer Additives

In the vortex core, the mean tangential velocity is approximately independent of z and linear in r , i.e.,

$$\langle u_{\theta} \rangle = Kr \tag{6.4}$$

where K is a constant. Donaldson and Snedeker [1962] have shown that for the special case when the tangential velocity depends only on r , the r, θ -component of the total stress (viscous and turbulent) can be determined from a measurement of the mean velocity profiles $\langle u_r \rangle$ and $\langle u_\theta \rangle$. The r, θ -component of the viscous stress is zero for $\langle u_\theta \rangle$ given by (6.4). The result, which also assumes that $u'_z u'_\theta$ is independent of z , is

$$\langle u'_r u'_\theta \rangle = - \frac{1}{r^2} \int_0^r r \langle u_r \rangle \frac{\partial}{\partial r} (r \langle u_\theta \rangle) dr . \quad (6.5)$$

With $\langle u_\theta \rangle$ given by Eq. (6.4) and using the continuity equation, the above result implies that

$$\langle u'_r u'_\theta \rangle = \frac{\partial \langle u_z \rangle}{\partial z} \Big|_{r=0} \frac{K}{4} r^2$$

(6.6)

near the axis of the forced vortex. This equation can be used to determine the effect of a polymer additive on the turbulent flux.

Figure 4.13 shows that the addition of Separan AP-30 (100 wppm) does not affect the parameter K . However, an analysis of $\partial \langle u_z \rangle / \partial z$ between $z = 8$ cm and 20 cm shows a significant effect. From Figure 4.1, it follows that with no polymer additive

$$\frac{\partial \langle u_z \rangle}{\partial z} \Big|_{r=0} \cong \frac{150}{12} .$$

With the addition of polymer, the experiments shown in Figure 4.12 yield the following estimate

$$\left. \frac{\partial \langle u_z \rangle}{\partial z} \right|_{r=0} \approx \frac{40}{12} .$$

Thus, according to Eq. (6.6), the Reynolds stress near the core axis is reduced by about a factor of 3 when polymer is added. Unfortunately, these two experiments were run at different temperatures and the viscosity of the solvent (water) at 12°C is about 24% higher than the viscosity at 20°C. Our tentative conclusion, however, is that this reduction in the Reynolds' stress is due to the viscoelastic nature of the polymer solution rather than to differences in viscosity (see the discussion in Section 1.2.4 on the effect of Separan AP-273 in vortex flows). This interesting result obviously deserves further study.

CHAPTER 7

RECOMMENDATION FOR FURTHER RESEARCH

Experimental findings of this research have raised many new questions regarding the mechanism of solid-liquid separations within hydrocyclones. Additional experiments outlined in Section 7.1 are required to answer completely some of the questions in this study. In Section 7.2, new experiments are suggested which could provide additional fundamental understanding of the flow phenomena within hydrocyclones. Hopefully, the extension of this research will eventually lead to some new applications as outlined in Section 7.3.

7.1. Experiments Needed to Complete This Study

Three important problems remain for further study. These include the following.

Radial Velocity

In this investigation, it was necessary to make theoretical corrections for the refraction of the laser beam (see Section A.3). Because of the lens effect, direct measurements of the radial component of the velocity were difficult and, unfortunately, were not made. It is strongly recommended that the experimental test section be designed to eliminate the refraction phenomenon. This can easily be done by matching the refractive index of the test fluid and the glass walls of the hydrocyclone. For this situation, a direct

measurement of the radial velocity is possible without any difficulties. The radial velocity component plays an important role in the performance of hydrocyclones.

Turbulent Intensities

Unfortunately, because of difficulties in obtaining proper computer facilities, turbulent measurements were not made. Use of a computer to record velocity fluctuations can provide additional information related to the velocity field inside the hydrocyclone. Any theoretical modeling of the flow field within the hydrocyclone would require this information.

Feed Pressure

All of the experiments in this research were conducted for relatively low inlet flow rates and pressures. It is desirable to insure that the basic results obtained from this study are also applicable at other operating conditions, especially for the experiments with polymer. The effect of 100 wppm Separan AP-30 may have very important consequences in the core region (e.g., on flow reversal). The effect of polymer concentration (for optimum condition of polymer solution (see Appendix B) for relatively high inlet flow rates) will provide some fundamental information related to the effect of polymer in the core region. Results of polymer experiments compared with the Newtonian solution with high viscosity will illustrate the viscoelastic property of the polymer.

7.2. Problems Which Would Provide New Fundamental Understanding

Among the numerous problems which could provide significant new information only the following are mentioned.

The Effect of Particle Loading

Fine glass beads with the same index of refraction of water can be used to study the effect of solids loading on the velocity field. Simultaneous velocity and grade efficiency measurements should provide valuable information related to the performance of the hydrocyclone under different operating conditions. This information should provide the means to improve either specific applications or design.

Flow Visualization

Flow visualization for these studies was conducted under circumstances where the hypodermic needle was inside the hydrocyclone. In order to trace the dye path precisely, it is recommended to conduct a full set of experiments where an organic dye is excited by a high energy laser beam. A high speed camera is necessary to record the stream of dye for further analysis.

Short Circuit Phenomena

Interesting flow features above the vortex finder are expected due to short circuit and multiple mantles. Information related to the interaction between the boundary layer on the top roof of the

hydrocyclone and the main fluid body of the hydrocyclone should provide some understanding of the short circuit phenomenon. These short circuits and multiple mantles are related to residence time and primary separation of particles, which influence separation efficiency.

The Effect of Air Core

LDA measurements of the velocity field using the back scattering mode in a hydrocyclone operating with an air core are recommended. Comparison of velocity profiles obtained with and without an air core may provide some additional understanding of flow reversals as well as the ejection phenomenon in the apex and the vortex finder.

Interaction of Vortex Finder and the Hydrocyclone

During the course of these experiments it was noticed that flow reversals begin inside the vortex finder. It is highly recommended that the flow characteristics of this part of the hydrocyclone be probed quantitatively using LDA. The flow fields inside the vortex finder are apparently coupled and, in order to clarify this phenomenon, it is suggested that a series of experiments for a hydrocyclone without a vortex finder be conducted and the flow field compared with those measured with the vortex finder.

7.3. Problems Which Could Lead to New Applications

Two novel applications of hydrocyclones which exploit the underlying secondary flows are suggested.

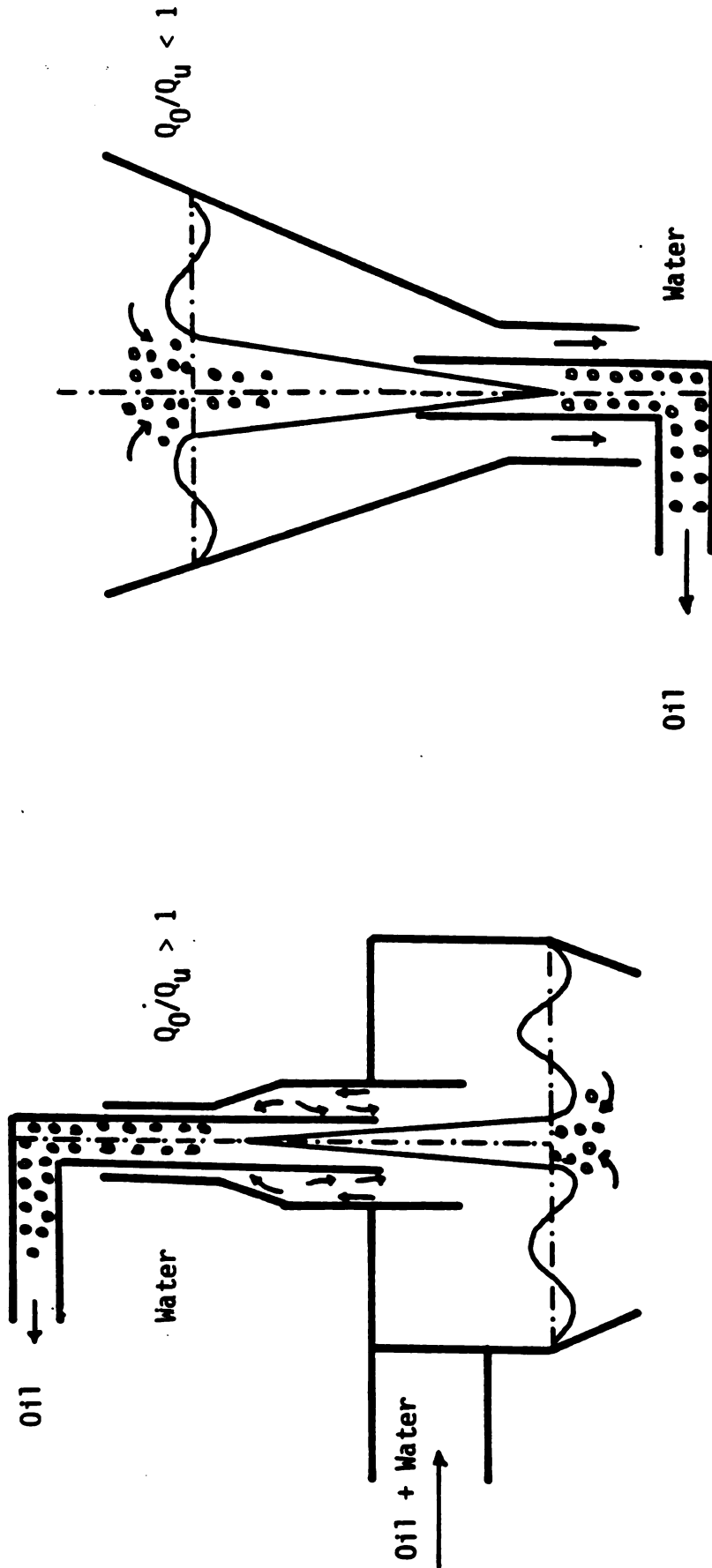
Oil Water Separation

The stable and coherent structure of the core region, obtained for a hydrocyclone with a 2:1 contraction and confirmed by flow visualization, might be used as a means to separate oil contaminate from water (e.g. crude oil). Figure 7.1 illustrates the possibility, which should be compared with the strategy being pursued by Thew and his colleagues at Southampton (see, esp. Colman and Thew [1980]). The application of hydrocyclones to this separation problem may be possible provided the following conditions are met:

- (i) Stable and coherent flow structure is formed in the core region for split ratios of 0.0 and 4.
- (ii) The flow pattern in the core region is not affected adversely by the presence of a suction tube inside the hydrocyclone.

The Hydrocyclone as a Chemical Reactor

Trajectory calculations can be used to estimate the residence time of particles inside a hydrocyclone. A hydrocyclone may be uniquely suited for suspension or for crystallization processes. In reactions where residence time may be crucial to product quality or selectivity, hydrocyclones may be used to perform separation and reaction simultaneously (see, esp. Beenackers [1978]).



Lighter oil migrates and coalesces in a jet-like flow; high molecular weight polymer minimizes turbulent fluctuations in the core.

Flow reversal due to vortex finder contraction helps core stability.

Figure 7.1. Formation of oil core in a hydrocyclone with a contraction.

APPENDIX A

APPLICATION OF LASER DOPPLER ANEMOMETRY TO VELOCITY MEASUREMENTS IN A HYDROCYCLONE

APPENDIX A

APPLICATION OF LASER DOPPLER ANEMOMETRY TO VELOCITY MEASUREMENTS IN A HYDROCYCLONE

A.1. Basic Principles

A laser anemometer uses a laser beam to measure the doppler frequency of light scattered by small seed particles moving with the local fluid velocity. The particle diameter may be as small as the wavelength of the laser light so the particles have approximately the same local velocity as the flow medium, even in turbulent streams. The velocity component measured is the one normal to the bisector of two beams with an intersection angle θ_I and parallel to the beam plane. The magnitude of the velocity is determined by the following expression (see Durst et al., 1976; and Durani, 1977)

$$u = \lambda f_D / 2 \sin \theta_I . \quad (A.1)$$

Here λ is the wavelength of light in the test medium and f_D is the doppler frequency. Yeh and Cummins [1964] were the first researchers to use LDA. They developed the basic theory for a reference beam laser doppler velocimeter and obtained excellent data for laminar flow in a circular tube.

George and Berman [1973] showed that unsteady measurements of fluid velocities with LDA are difficult because of doppler

ambiguity and broadening. Doppler ambiguity arises from the random arrival and departure of the scattering particles in the sampling volume. Turbulence, velocity gradients, refractive index fluctuations, and noise all contribute to broadening. George and Lumley [1973] have discussed the effect of this phenomenon on the doppler signal and have presented an analysis of its effect on the beat frequency and signal demodulation. They illustrated how two-point velocity correlations could be made using two independent anemometers to eliminate ambiguity.

The components of the laser anemometers may be arranged in three different modes of operation (see Durst et al., 1976): the dual beam mode, the reference beam mode, and the dual scatter modes. The selection of a suitable mode depends on the specific application and the signal-to-noise ratio at the photodetector (see Figure 2.11). Some of the variables which affect the selection include (1) the number of the velocity components measured; (2) the phase (liquid or gas) of the test fluid; (3) the type of seeding; (4) the accessibility of the measuring point; and (5) the type of data required.

The dual-beam mode, applied in this research, uses two incident beams of equal intensity. This configuration is often referred to as a "fringe" mode because interference fringes are formed when the two beams intersect. In this case, the scattered light can be picked up over a wide angle, since the differential doppler frequency is independent of direction of detection.

There are two types of operation in dual-beam mode: one uses forward scattering (see Figure A.1) and the other uses backward scattering. In the backward scattering mode, the flow is viewed from only one side. Since the dual beam mode is independent of the direction of the scattered light, all derivations are valid for both forward and backward scattering.

To obtain a better intuitive understanding of the LDA technique, a brief derivation of Eq. (A.1) using the real fringe concept will be given. The distribution of scattered light on the photo-detector surface is used to discuss the fringe spacing, probe volume, and the relationship between the velocity and the doppler frequency.

The doppler shift was named after Christian Doppler in 1842. Basically, an observer moving away from a fixed source of light sees the light at a lower frequency than a stationary observer. Thus, light scattered from a moving particle appears to have a lower or higher frequency, depending on its relative motion. The frequency relationship between a scattered light wave and a stationary light source can be deduced from the vector diagram shown in Figure A.2.

The frequency of the stationary light source shown in Figure A.2 is

$$f_{i1} = \frac{c}{\lambda} \quad (A.2)$$

where c is the speed of light and λ its wavelength. The frequency seen by a moving observer (i.e., seed particle) is simply

$$f_p = \frac{1}{\lambda} [c - \underline{u} \cdot \underline{e}_{i1}] ,$$

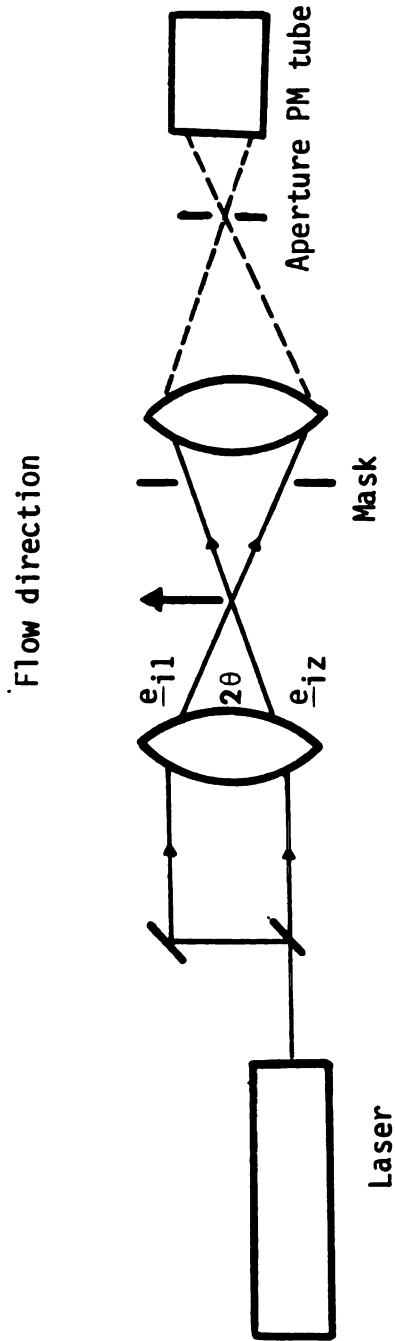


Figure A.1. Dual beam mode.

c , speed of light

\underline{e}_{i1} incident unit vector

\underline{e}_{s1} scatter unit vector

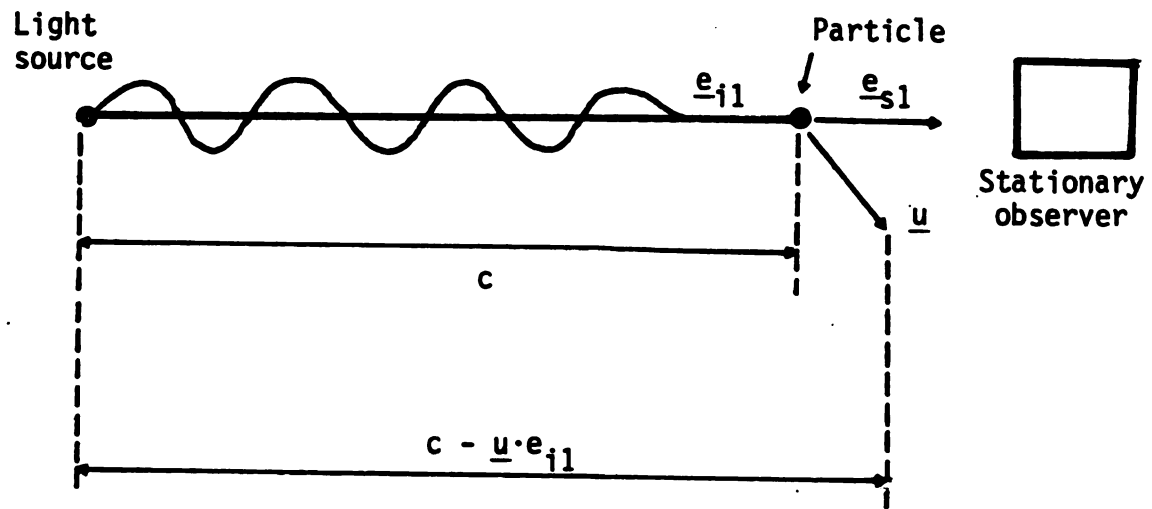


Figure A.2. Vector diagram of light propagation.

which can also be written as

$$f_p = f_{i1} \left[1 - \frac{\underline{u} \cdot \underline{e}_{i1}}{c} \right] . \quad (\text{A.3})$$

Now the frequency of the light scattered by the moving particle is

$$f_p = f_{s1} \left[1 - \frac{\underline{u} \cdot \underline{e}_{s1}}{c} \right] \quad (\text{A.4})$$

where f_{s1} is the frequency detected by a stationary observer.

Equating Eqs. (A.3) and (A.4) shows that f_{s1} and f_{i1} are related by

$$f_{s1} = f_{i1} \frac{[c - \underline{u} \cdot \underline{e}_{i1}]}{[c - \underline{u} \cdot \underline{e}_{s1}]} \quad (\text{A.5})$$

A similar expression can be written for the second beam:

$$f_{s2} = f_{i2} \frac{[c - \underline{u} \cdot \underline{e}_{i2}]}{[c - \underline{u} \cdot \underline{e}_{s2}]} . \quad (\text{A.6})$$

The two scattered light waves will interfere with each other and yield a beat signal which has a frequency given by

$$f_D = f_{s1} - f_{s2} . \quad (\text{A.7})$$

Because both beams are from the same light source $f_{i1} = f_{i2}$. Moreover, because the light is collected in the same direction for both beams, the unit vectors \underline{e}_{s1} and \underline{e}_{s2} are equal. Therefore, the beat frequency f_D is given by

$$f_D = f_{i1} \frac{\underline{u} \cdot (\underline{e}_{i2} - \underline{e}_{i1})}{c - \underline{u} \cdot \underline{e}_{s2}} . \quad (\text{A.8})$$

Because $\underline{u} \cdot \underline{e}_{s2} \ll c$, the speed of light, Eq. (A.8) can be approximated by

$$f_D = \frac{1}{\lambda} \underline{u} \cdot (\underline{e}_{i2} - \underline{e}_{i1}) . \quad (\text{A.9})$$

Thus, the component of \underline{u} which is measured by recording the beat (or doppler) signal is the one parallel to $\underline{e}_{i2} - \underline{e}_{i1}$ (see Figure A.1), and thus normal to the bisector of the beam intersection.

If θ_I represents the half-angle of the beam intersection, then

$$\underline{u} \cdot \underline{e}_{i2} = |\underline{u}| \cos \left(\frac{\pi}{2} - \theta_I \right)$$

$$\underline{u} \cdot \underline{e}_{i1} = -|\underline{u}| \cos \left(\frac{\pi}{2} - \theta_I \right).$$

Therefore, with $\cos \left(\frac{\pi}{2} - \theta_I \right) = \sin \theta_I$, Eq. (A.9) becomes

$$\boxed{f_D = \frac{2|\underline{u}| \sin \theta_I}{\lambda}} ,$$

which is Eq. (A.1). Thus, $|\underline{u}| = d_f \cdot f_D$ where the "fringe" spacing is given by $\lambda/(2 \sin \theta_I)$.

Optical interference between two light beams and the formation of a fringe pattern is fundamental in LDA. To illustrate the fringe pattern and intensity distribution in the probe volume, it is helpful to derive the interference formula for two coherent laser beams having the same intensity and polarization direction.

Consider the crossing of two light beams from the same source as illustrated by Figure A.3. The complex electric field vectors for the incident beams can be expressed as (see p. 28 in Durst et al., 1976)

$$\underline{E}_1 = \sqrt{I_0} \underline{P}_1 \exp[i(\omega_0 t - \frac{2}{\lambda}(x \cos \theta + z \sin \theta))] \quad (A.10)$$

$$\underline{E}_2 = \sqrt{I_0} \underline{P}_2 \exp[i(\omega_0 t - \frac{2\pi}{\lambda}(-x \cos \theta + z \sin \theta))] . \quad (A.11)$$

Here I_0 is the intensity of the incident beams, θ is the half-angle of the intersection, λ is the wavelength of light, and ω_0 is the frequency (i.e., c/λ). \underline{P}_1 and \underline{P}_2 indicate the direction of polarization of the beams. The electric vector within the probe volume is just the superposition of \underline{E}_1 and \underline{E}_2 , viz.,

$$\underline{E} = \underline{E}_1 + \underline{E}_2 . \quad (A.12)$$

The intensity of light in the probe volume is given by

$$I = \underline{E} \cdot \underline{E}^* \quad (A.13)$$

where \underline{E}^* is the complex conjugate of \underline{E} . From Eqs. (A.10) and (A.11), it follows that (see p. 33 in Durst et al. [1976] for details)

$$I = 2I_0 [1 + \underline{P}_1 \cdot \underline{P}_2 \cos (\frac{4\pi x \sin \theta}{\lambda})] . \quad (A.14)$$

This equation can be used to estimate the fringe spacing by recognizing that I is a maximum at the zeros of $\cos (2\pi m)$. Thus, for

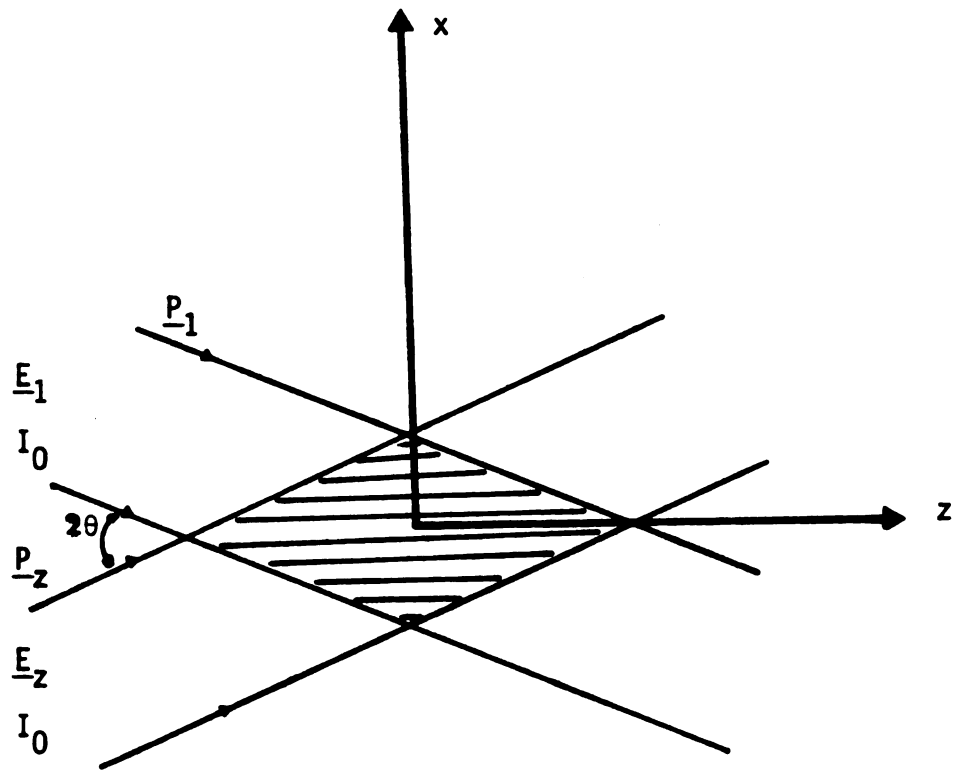


Figure A.3. Cross section of two beams from the same source.

$$x_n = \frac{n\lambda}{2 \sin \theta}, \quad n = 0, 1, 2, \dots \quad (\text{A.15})$$

the intensity I is a maximum. The difference between these uniformly spaced zeros gives the fringe spacing, i.e.,

$$d_f = \frac{\lambda}{2 \sin \theta}. \quad (\text{A.16})$$

The maximum fringe visibility is obtained when $\underline{P}_1 \cdot \underline{P}_2 = 1$. This condition is satisfied when the polarization direction of both incident beams are normal to the plane containing the beams. In the other extreme, $\underline{P}_1 \cdot \underline{P}_2 = 0$, and the interference pattern vanishes (cross polarized light waves).

To analyze the probe volume and its dimensions, let us examine the light waves in three dimensions. The flow is along the x axis, with the y axis normal to the plane of x and z ; (x_1, y_1, z_1) and (x_2, y_2, z_2) are coordinates referring to the direction of the illuminating beams. The coordinate system is shown in Figure A.4. Assume that the photocurrent is generated only by light scattered from a particle in the probe volume and moving with a uniform flow velocity in the x direction. At any time, the location of the particle in the coordinate system is

$$x_p = u t + x_{p0}$$

where x_{p0} is the location of the particle when it entered the probe volume.

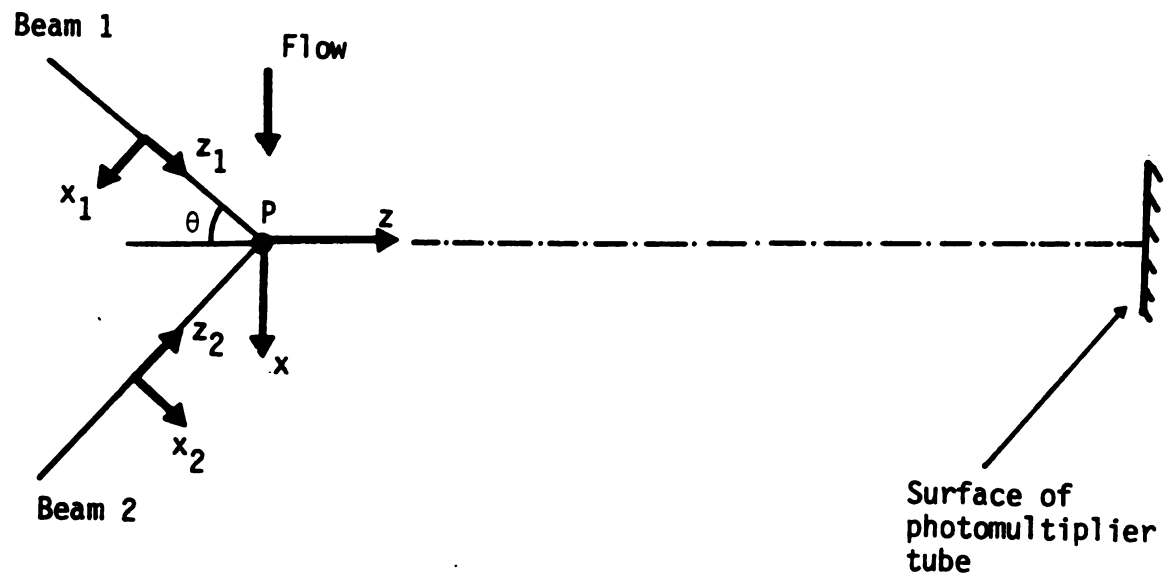


Figure A.4. The coordinate system used for a fringe system.

The photocurrent on the surface of the detector is given by
(see p. 129 in Durrani, 1976)

$$i_F(t) \propto 2\eta \left(\frac{1}{2} M C_{sc}\right)^2 \epsilon_0^2 \exp\left(-\frac{x^2 \cos^2 \theta + y^2 + z^2 \sin^2 \theta}{r_0^2}\right) \times$$

$$\left[1 + \cos\left(\frac{4\pi}{\lambda}(ut + x_{p0})\sin \theta\right)\right]$$

(A.17)

where M is the magnification factor of the receiving optics, C_{sc} is called the scattering cross section of the particle, η is the sensitivity of the photodetector (i.e., the ratio of the photocurrent to the incident power of the radiation), and ϵ_0^2 is the intensity of the beams at the point $P(0, 0, 0)$. Inspection of this result shows that the maximum current occurs when the particle passes the center of the coordinate system. The photocurrent drops by a factor e^{-1} when the particle moves to the edge of the probe volume defined by

$$x^2 \cos^2 \theta + y^2 + z^2 \sin^2 \theta = r_0^2.$$

Thus, the shape of the probe volume is an ellipsoid with dimensions

$$\Delta x = \frac{2r_0}{\cos(\theta)}$$

$$\Delta y = 2r_0$$

$$\Delta z = \frac{2r_0}{\sin(\theta)}.$$

Here $2r_0$ is the diffraction-limited beam diameter. Some researchers

define the probe volume as the region over which the photocurrent decays by e^{-2} , rather than e^{-1} . The probe volume and fringe pattern are shown in Figure A.5. Δx is the diameter of the cross section of the ellipsoid where the particles pass, and d_f is the fringe spacing. The ratio of Δx and d_f is defined as the total number of fringes within the probe volume:

$$N_f = \frac{\Delta x}{d_f} = \frac{4r_o \tan \theta}{\lambda} \quad (\text{A.18})$$

Once a scattering particle enters the probe volume ($t = 0$), the maximum amplitude does not occur until the particle crosses the center. This occurs at

$$t_{\max} \equiv |-x_o/u| .$$

Now the output of the photodetector includes a mean component (low frequency) and a periodic component (doppler frequency). The mean value of the signal has a Gaussian distribution in time and is often referred to as the pedestal or dc-component. Figure A.6 shows a typical signal (also see Figure 2.11).

An interpretation of Figure A.6 follows from Eq. (A.17). The intensity fluctuates because a particle of velocity u (see the cosine term in Eq. A.17)) moves across the fringe pattern and scatters light. The frequency of this scattered light has been shifted slightly from the incident light. The distance between the maximum peaks in Figure A.6 is just the time required for the particle to

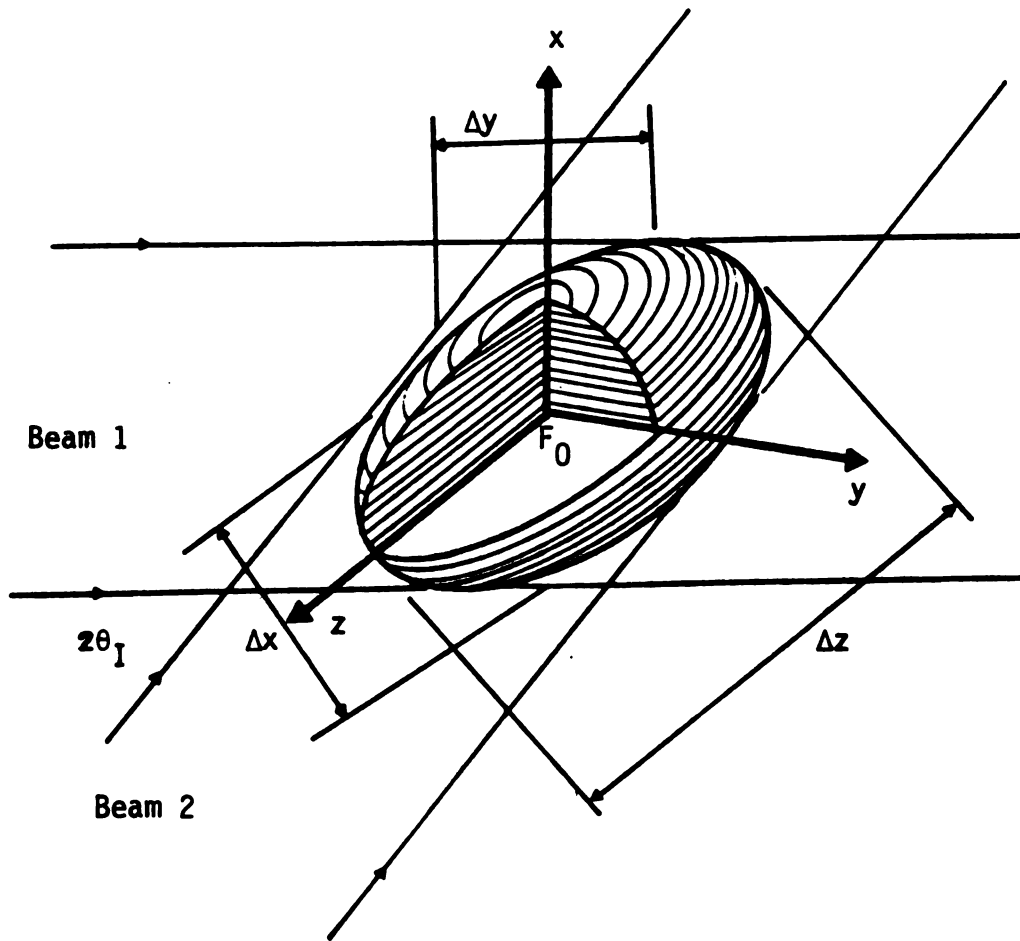


Figure A.5. Beam intersection region in the real fringe system. The inner ellipse represents Eq. (A.17) and the outer ellipse is the locus of points at which the signal falls to e^{-2} of its maximum.

Signal processor checks for
consistant reading

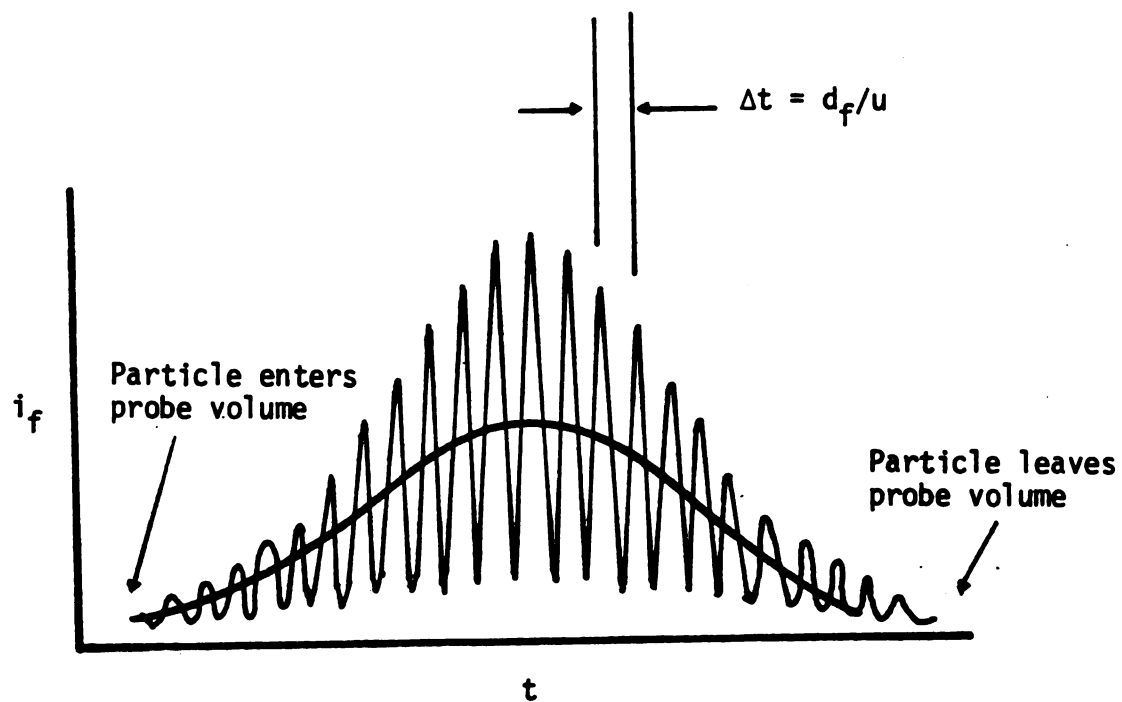


Figure A.6. Typical signal from the photodetector.

move between fringes, i.e., $t = d_f/u$. Basically, the LDA technique measures the time between peaks and, if a consistent set of Δt 's can be detected in one doppler burst, then u can be calculated as described.

A.2. Frequency Shifting

In measuring the velocity by LDA a difficulty often encountered is the inability to determine the direction of flow. Eq. (A.1) only gives the magnitude. The most convenient way of overcoming this ambiguity is to frequency shift one of the beams. This also shifts the observed doppler frequency, so the direction of movement can be determined by an increase or decrease in the doppler frequency. In the dual beam mode, shifting the frequency of one of the beams can be thought of as moving the fringe system (see Figure A.3). If the velocity is in the direction of the fringe movement then the frequency will decrease, otherwise there will be an increase in the frequency of the doppler signal. For a stationary particle in the probe volume the output signal is the same as the frequency shift. This can be used to detect the presence of the hydrocyclone wall (see Figure 2.13).

Frequency shifting permits measurements in reverse flows, in secondary circulations, and in periodic flows. The frequency shifting is also a useful tool to bring the doppler frequency into a range which will be easy to process (i.e., the doppler signal can be increased relative to the pedestal signal). For low velocity convective flows and for measuring turbulent components perpendicular

to the flow, frequency shifting has been a useful tool. Measuring flow reversals is probably the most common application of frequency shifting. To measure negative flows, the direction of frequency shifting should be against the mean flow. To measure flow reversals successfully requires careful consideration of the number of fringes that the particle passes when it traverses the probe volume.

Adrian and Fingerson [1981] have developed an expression for the number of effective fringes in the probe volume when frequency shifting is employed. The final result is

$$N_S = N_F \left| 1 \pm \frac{f_S}{f_D} \right|$$

where N_S and N_F represent, respectively, the number of doppler cycles generated by a particle with and without frequency shifting. f_S is the amount of frequency shifting induced and f_D is the doppler frequency without shifting. The "+" sign is used if frequency shifting is counter to the flow, whereas the "-" sign is for shifting in the direction of flow.

A.3. Corrections Due to Refraction Phenomena

If the optical bisector of two intersecting laser beams is perpendicular to the z-coordinate direction, then the magnitude of $\langle u_z \rangle$ at the point of intersection is given by

$$|\langle u_z \rangle| = d_f(\underline{x}) \langle f_D \rangle(\underline{x}) . \quad (A.18)$$

Frequency shifting unambiguously determines the sign of the velocity.

A similar expression holds for $\langle u_\theta \rangle$.

Eq. (A.18), although simple in appearance, may be difficult to apply if the laser beams pass through several different optical media with curved surfaces. The actual measuring point \underline{x} and the fringe spacing d_f may both be affected. d_f depends on the half-angle of the refracted beams and the wavelength of the laser light in the test medium. The relationship is

$$d_f(\underline{x}) = \frac{\lambda_3}{2 \sin \theta_I(\underline{x})} \quad . \quad (A.19)$$

If β_1 and β_3 represent, respectively, the index of refraction in air and in the test fluid (water), then (see p. 843 in Sears and Zemansky, 1964)

$$\lambda_3 = \beta_1 \lambda_1 / \beta_3 \quad (A.20)$$

where λ_1 is the wavelength of the laser light in air (≈ 632.8 nm for the 35 mW He-Ne laser used in this research). The half-angle $\theta_I(\underline{x})$ must be determined theoretically by using principles of geometric optics (Snell's law) and trigonometry. Expressions for the actual measuring point \underline{x} and $\theta_I(\underline{x})$ are developed in what follows by assuming that the half-angle of the two incident laser beams is small enough to justify replacing $\sin \theta$ with θ . This is an excellent approximation in practice. Bicen [1982] and Durst et al. [1976] have also developed equations for these corrections in

cylindrical geometries but the development for the conical portion of the hydrocyclone appears new with this study.

A.3.1. The cylindrical section

Axial Velocity

Figure A.7 illustrates the path of the two laser beams through the hydrocyclone when the axial velocity is measured in the cylindrical section. The angles in the figure have all been greatly exaggerated for clarity. The axis of symmetry lies in the optical plane and is perpendicular to the optical bisector. Because the outward pointing normal vectors at the two interfaces (points "A" and "B") are also in the incident optical plane, the refracted beams remain in the plane containing the optical bisector and the axis of symmetry of the test rig. However, differences in the index of refraction between the phases cause the two refracted beams to intersect at point "I" rather than the focal point "F".

The region between R_1 and R_2 contains glycerin, the glass wall of the hydrocyclone, and the wall of a pyrex box (see Figure 2.4). This is considered as one homogeneous optical medium with an index of refraction β_2 . β_1 and β_2 represent, respectively, the indices of refraction for air and the test fluid (water). For this situation, the refraction phenomenon is symmetric about the optical axis; however, this will not occur for the conical section.

From Figure A.7 it follows that

$$\underline{x}_I = \underline{x}_A + \overline{AI} \underline{e}_3 \quad (A.21)$$



where

$$\underline{x}_A = -R_2 \underline{e}_x + R_2 \tan \theta_A \underline{e}_z \quad (\text{A.22})$$

and

$$\underline{l}_3 = \cos \theta_I \underline{e}_x - \sin \theta_I \underline{e}_z . \quad (\text{A.23})$$

Symmetry about the x-axis implies that $\underline{x}_I \cdot \underline{e}_z = 0$, so

$$\underline{x}_I = \underline{x}_A - \left(\frac{\underline{x}_A \cdot \underline{e}_z}{\underline{l}_3 \cdot \underline{e}_z} \right) \underline{l}_3 . \quad (\text{A.24})$$

For the small angle approximation, Eq. (A.24) gives the x-component of the beam intersection point in terms of R_2 , θ_I , and θ_A :

$$x_{Ix} = R_2 \left(\frac{\theta_A}{\theta_I} - 1 \right) . \quad (\text{A.25})$$

Repeated application of Snell's law for small angles gives
(see Figure A.7)

$$\theta_I \approx \frac{\beta_2}{\beta_3} \theta_{2A} \approx \frac{\beta_2}{\beta_3} \frac{\beta_1}{\beta_2} \kappa . \quad (\text{A.26})$$

This is an important result because it shows that the fringe spacing formed for axial velocity measurements does not change with position. Thus, Eqs. (A.19), (A.20), and (A.26) give

$$\boxed{d_f = \lambda_1 / (2\kappa)} . \quad (\text{A.27})$$

For $\lambda_1 = 632.8 \text{ nm}$, and $\kappa = 5.71^\circ$, Eq. (A.27) shows that $d_f = 3177 \text{ nm}$.

An equation for θ_A follows easily from the relationships (see Figure A.7).

$$\underline{x}_A = -R_1 \underline{e}_x + \overline{CB} \underline{e}_z + \overline{BA} \underline{e}_2 \quad (\text{A.28})$$

$$\underline{x}_A = -R_2 \underline{e}_x + \overline{DA} \underline{e}_z \quad (\text{A.29})$$

$$\underline{e}_2 = \cos \theta_{2B} \underline{e}_x - \sin \theta_{2B} \underline{e}_z \quad (\text{A.30})$$

$$\tan \kappa \approx \kappa = \overline{CB} / (R_1 + \underline{x}_F \cdot \underline{e}_x) . \quad (\text{A.31})$$

The vector \underline{x}_F locates the focal point "F" relative to the coordinate system at "O". Equating the x- and z-components of Eqs. (A.28) and (A.29) gives two equations for \overline{BA} and \overline{DA} . Applying the small angle approximation to these equations yields

$$\overline{BA} \approx R_1 - R_2 \quad (\text{A.32})$$

and

$$\overline{DA} \approx \kappa [R_1 + x_{Fx} - \frac{\beta_1}{\beta_2} (R_1 - R_2)] \quad (\text{A.33})$$

where Snell's law has been used to replace θ_{2B} with $\beta_1 \kappa / \beta_2$. Now, because $\tan \theta_A \approx \theta_A = \overline{DA} / R_2$, Eq. (A.25) can be rewritten as

$$x_{Ix} = \frac{\beta_3}{\beta_1} [R_1 + x_{Fx} - \frac{\beta_1}{\beta_2} (R_1 - R_2)] - R_2 . \quad (\text{A.34})$$

Note that $x_{Ix} = x_{Fx}$ for $\beta_1 = \beta_2 = \beta_3$.

In making a traverse across the hydrocyclone, the test rig moves toward the laser source by a known increment ϵ (> 0). If $\underline{\overset{\circ}{x}}_I$ and $\underline{\overset{\circ}{x}}_F$ denote the initial positions of the real probe volume and the focal point of the unrefracted laser beams, then

$$\underline{x}_F = \underline{\overset{\circ}{x}}_F + \epsilon \underline{e}_x \quad (\text{A.35})$$

and

$$\boxed{x_{Ix} - \overset{\circ}{x}_{Ix} \equiv \Delta x_{Ix} = \beta_3 \epsilon / \beta_1} \quad (\text{A.36})$$

This expression applies for traverses in the cylindrical section when the optical plane passes through the axis of symmetry and when the bisector angle κ is small.

Tangential Velocity

Asymptotic expressions for the fringe spacing and the coordinates of the probe volume are developed here using a similar strategy as before. Figure A.8 shows the path of the two laser beams through the cylindrical section of the hydrocyclone when the tangential component of the velocity is being measured. Once again the angles have been exaggerated for clarity. "I" represents the point of intersection of the refracted beams, and "F" is the focal point of the unrefracted beams. Here the optical plane containing the two incident laser beams is perpendicular to the axis of symmetry and its optical bisector intersects the axis of symmetry. Unlike the orientation for measuring $\langle u_z \rangle$, the outward pointing normal



Figure A.8. Refraction of laser beams during tangential velocity measurements in the cylindrical section.

vectors at "A" and "B" are not oriented in the same direction. However, they are in the same plane.

From Figure A.8 it follows that

$$\underline{x}_I = \underline{x}_A + \overline{AI} \underline{l}_3 . \quad (\text{A.37})$$

Because of symmetry about the y-axis, $\underline{x}_I \cdot \underline{e}_y = 0$ and $\overline{AI} = -\underline{x}_A \cdot \underline{e}_y / \underline{l}_3 \cdot \underline{e}_y$.

The vectors \underline{x}_A and \underline{l}_3 can be written as

$$\underline{x}_A = -R_2 \cos \theta_A \underline{e}_x + R_2 \sin \theta_A \underline{e}_y \quad (\text{A.38})$$

$$\underline{l}_3 = \cos \theta_I \underline{e}_x - \sin \theta_I \underline{e}_y . \quad (\text{A.39})$$

Combining Eqs. (A.38) and (A.39) and assuming that θ_A and θ_I are small angles, we obtain

$$x_{Ix} = R_2 \left(\frac{\theta_A}{\theta_I} - 1 \right) \quad (\text{A.40})$$

which is similar to Eq. (A.25). Here θ_A and θ_I will have a different dependence on κ and the indices of refraction.

It follows from Figure A.8 that $\theta_I = \theta_A - \theta_{3A}$. Application of Snell's law at "A" gives for small angles

$$\theta_{3A} = \frac{\beta_2}{\beta_3} \theta_{2A} . \quad (\text{A.41})$$

Once again, an analysis of Figure A.8 shows that

$$\theta_{2A} = \pi - \theta_{2B} - (\pi - \theta_A) = \theta_A - \theta_{2B} ,$$

so with another application of Snell's law at point "B", which gives $\theta_{2B} \approx \beta_1 \kappa / \beta_2$, an expression for θ_I in terms of θ_A follows, viz.,

$$\theta_I = (1 - \frac{\beta_2}{\beta_3})\theta_A + \frac{\beta_1}{\beta_3} \kappa . \quad (\text{A.42})$$

With $\beta_2 = \beta_3$, this gives the same result as Eq. (A.26).

The angle θ_A can be determined from the observation that \underline{x}_A can also be written as (cf. Eq. (A.29)),

$$\underline{x}_A = -R_1 \underline{e}_x + \overline{CB} \underline{e}_y + \overline{BA} \underline{l}_2 \quad (\text{A.43})$$

where

$$\underline{l}_2 = \cos \theta_{2B} \underline{e}_x - \sin \theta_{2B} \underline{e}_y . \quad (\text{A.44})$$

Equating the x- and y-components of Eqs. (A.38) and (A.43) yields for the small angle approximation

$$\overline{BA} = R_1 - R_2 \quad (\text{A.45})$$

and

$$\overline{CB} = R_2 \theta_A + (R_1 - R_2) \theta_{2B} , \quad (\text{A.46})$$

where $\theta_{2B} = \beta_1 \kappa / \beta_2$ and $\tan \kappa \approx \kappa = \overline{CB} / (R_1 + \underline{x}_F \cdot \underline{e}_x)$. Collecting these results shows that

$$\theta_A = \kappa \frac{R_1}{R_2} - \frac{\beta_1}{\beta_2} \left(\frac{R_1}{R_2} - 1 \right) + \frac{x_{Fx}}{R_2} \quad (\text{A.47})$$

and, from Eqs. (A.42) and (A.40),

$$x_{Ix} = \frac{\beta_2^2}{\beta_1 \beta_3} \frac{(1 - \frac{\beta_1}{\beta_2}) R_1 + x_{Fx}}{1 + (\frac{\beta_3 - \beta_2}{\beta_1}) [\frac{R_1}{R_2} - \frac{\beta_1}{\beta_2} (\frac{R_1}{R_2} - 1) + \frac{x_{Fx}}{R_2}]} \quad (A.48)$$

Note that for $\beta_1 = \beta_2 = \beta_3$, x_{Ix} reduces to x_{Fx} . Also, with $\dot{x}_{Ix} = 0$ for $\epsilon = 0$, it follows from Eq. (A.48) that

$$\dot{x}_{Fx} = - (1 - \frac{\beta_1}{\beta_2}) R_1 \quad (A.49)$$

and (cf. Eq. (A.37))

$$\Delta x_{Ix} = \frac{\frac{\beta_2^2}{\beta_1 \beta_3} \epsilon}{1 + \frac{\beta_3 - \beta_2}{\beta_2} (1 + \frac{\beta_2}{\beta_1} \frac{\epsilon}{R_2})} \quad (A.50)$$

Eq. (A.50) reduces to Eq. (A.36) when $\beta_3 = \beta_2$ and, when all the phases are optically equivalent, $\Delta x_{Ix} = \epsilon$.

Because θ_I changes with position for tangential velocity measurements, the fringe spacing varies with ϵ . Combining the definition (A.19) with Eqs. (A.20) (A.42), (A.47), and (A.49) shows that for the small angle approximation

$$d_f = \frac{d_f^0}{1 + \frac{\beta_2}{\beta_1} (1 - \frac{\beta_2}{\beta_3}) \frac{\epsilon}{R_2}} \quad (A.51)$$

where

$$d_f^0 = \beta_2 \lambda_1 / 2 \beta_3 \kappa \quad (A.52)$$

For $\epsilon = 0$ and $\beta_1 = \beta_2$, Eq. (A.51) gives the same result as Eq. (A.27). However, for $\epsilon > 0$ and $\beta_2 < \beta_3$, the fringe spacing for the tangential velocity measurements is less than d_f for the axial velocity measurements. On the other hand, Eq. (A.51) also shows that for $\beta_2 > \beta_3$ the opposite occurs. Thus, the curvature of the cylindrical section together with the differences in the indices of refraction gives a significant lens effect which can be corrected by applying the foregoing results. Figure A.9 summarizes the main conclusions of this section for the specific experimental system studied.

A.3.2. The conical section

Axial Velocity

Figure A.10 shows the path of the laser light through the conical section of the hydrocyclone when the axial velocity is being measured. As before, the optical plane defined by the two incident beams passes through the axis of symmetry; however, the problem here is not symmetric about the optical bisector. The intersection point "I" does not necessarily fall on the x-axis as defined in Figure A.10, so in the analysis which follows both beams must be considered separately. The notation used here employs a tilde (\sim) to denote geometric parameters related to the lower beam--for instance, compare the physical meaning of A and \tilde{A} . The three optical phases have the same physical meaning as before; the basic difference here is that the outward pointing unit normal vectors at "A" and " \tilde{A} " are rotated by an amount θ_H relative to their counterparts at

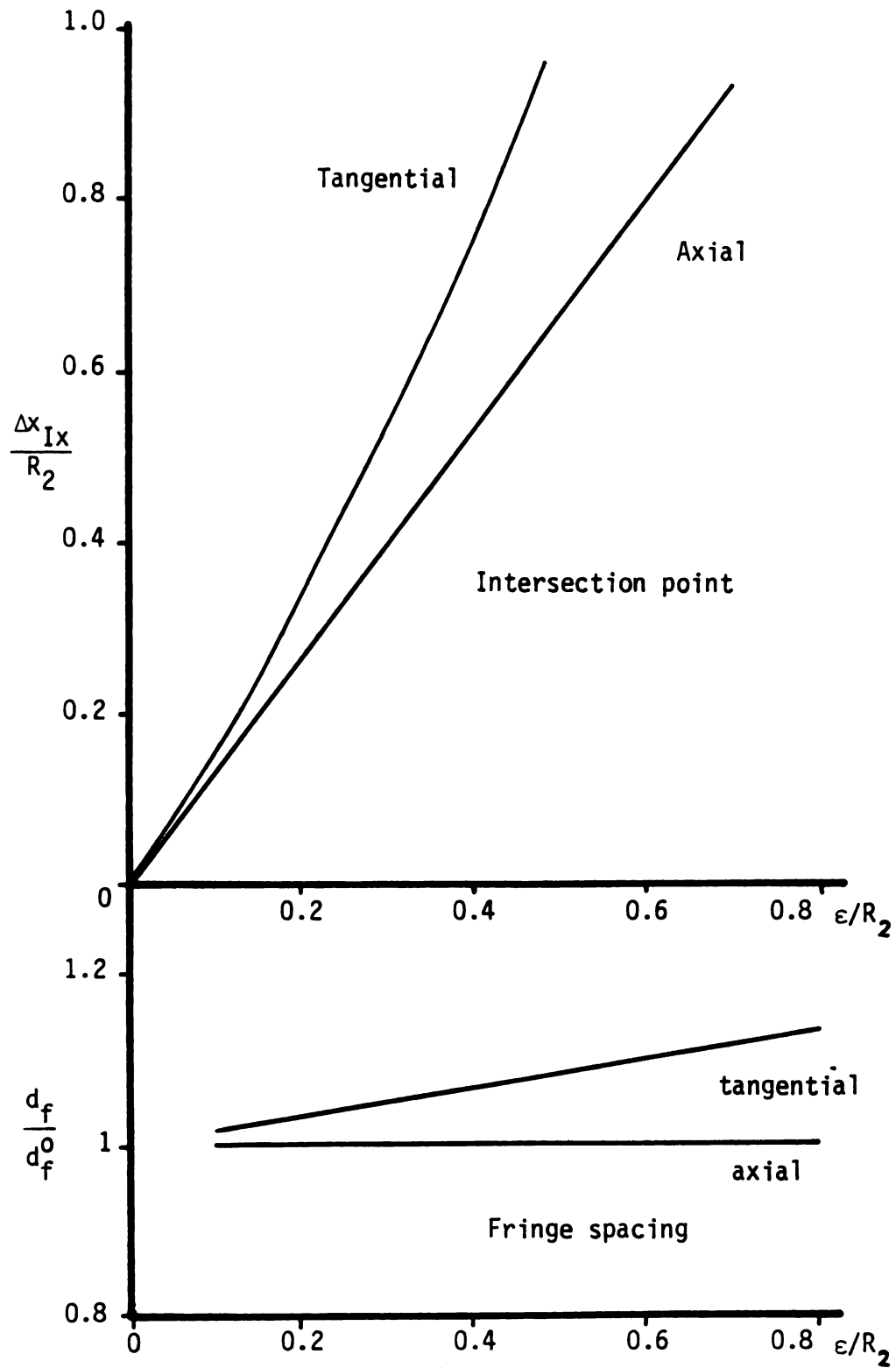


Figure A.9. Refraction corrections for the cylindrical section.

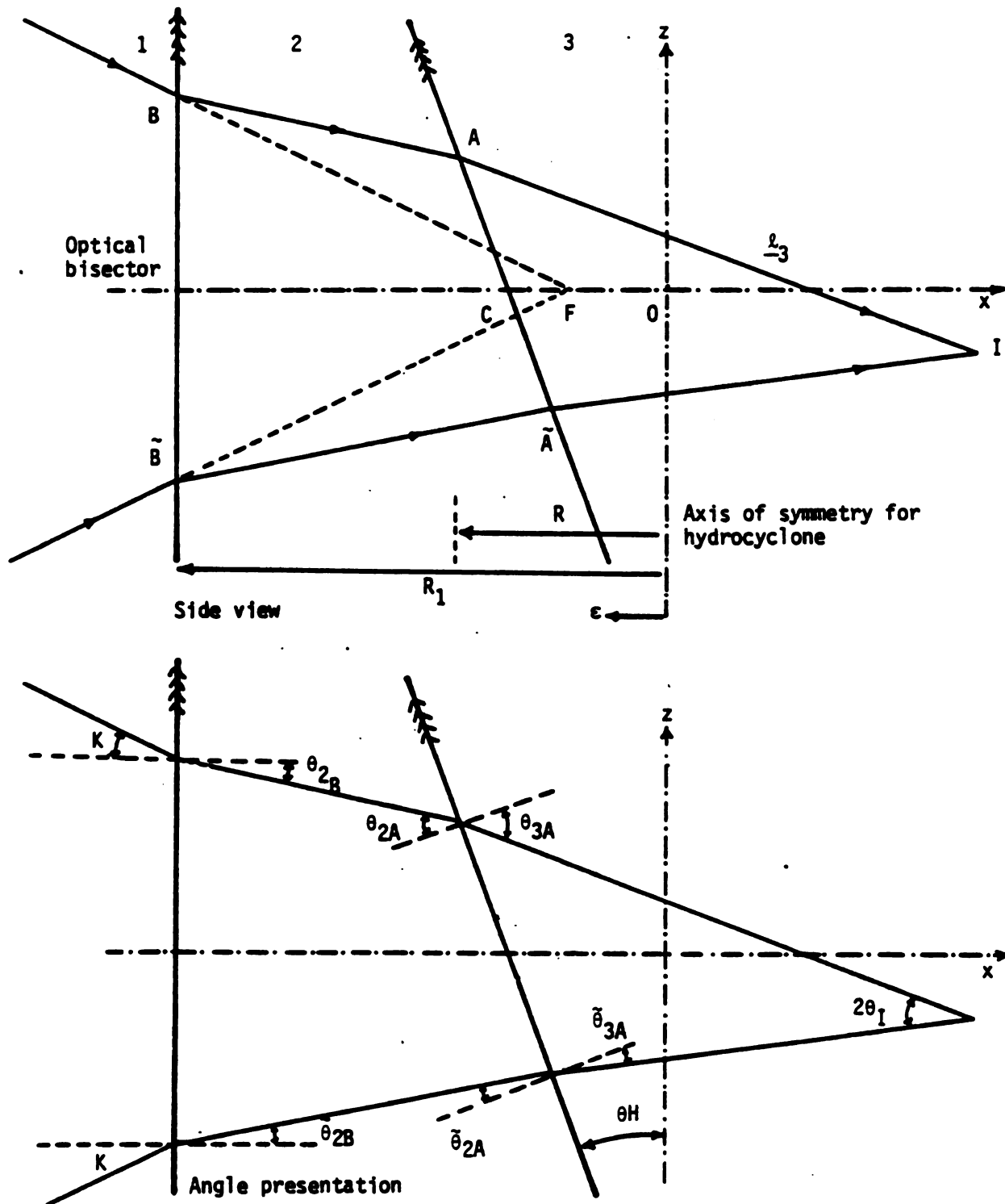


Figure A.10. Refraction of laser beams during axial velocity measurements in the conical section.

"B" and "B̃". θ_H is the half-angle of the cone, which is about 11.3° for the apparatus used in this research.

If \underline{l}_3 and $\tilde{\underline{l}}_3$ represent unit vectors in the direction of the upper and lower refracted beams in phase 3 (see Figure A.10), then the angle of intersection θ_I can be determined by

$$\underline{l}_3 \cdot \tilde{\underline{l}}_3 = \cos (2\theta_I) . \quad (\text{A.53})$$

This requires, however, a representation of \underline{l}_3 and $\tilde{\underline{l}}_3$. Consider \underline{l}_3 first. Figure A.10 shows that $\underline{l}_3 \cdot \underline{e}_x = \cos (\theta_H - \theta_{3A})$ and that $\underline{l}_3 \cdot \underline{e}_z = \sin (\theta_H - \theta_{3A})$. Here θ_{3A} is defined as the angle between $-\underline{n}_A$ and \underline{l}_3 (i.e., $-\underline{l}_3 \cdot \underline{n}_A = \cos \theta_{3A}$). These considerations imply that

$$\underline{l}_3 = \cos (\theta_H - \theta_{3A}) \underline{e}_x + \sin (\theta_H - \theta_{3A}) \underline{e}_z . \quad (\text{A.54})$$

A similar analysis for the lower beam leads to

$$\tilde{\underline{l}}_3 = \cos (\theta_H - \tilde{\theta}_{3A}) \underline{e}_x + \sin (\theta_H - \tilde{\theta}_{3A}) \underline{e}_z \quad (\text{A.55})$$

where $\cos \tilde{\theta}_{3A} = -\tilde{\underline{l}}_3 \cdot \tilde{\underline{n}}_A$. The negative sign appears because $\tilde{\underline{n}}_A$ is the outward pointing normal vector at \tilde{A} .

Eq. (A.53) relates θ_I to θ_H , θ_{3A} , and $\tilde{\theta}_{3A}$. For small angles, the trigonometric functions expanded through second order give

$$\begin{aligned} \cos (2\theta_I) &\approx 1 - \frac{(2\theta_I)^2}{2} \\ \underline{l}_3 \cdot \tilde{\underline{l}}_3 &= \cos (\theta_H - \theta_{3A}) \cos (\theta_H - \tilde{\theta}_{3A}) \\ &+ \sin (\theta_H - \theta_{3A}) \sin (\theta_H - \tilde{\theta}_{3A}) \approx \left(1 - \frac{a^2}{2}\right) \left(1 - \frac{b^2}{2}\right) + ab \end{aligned}$$

where $a \equiv \theta_H - \theta_{3A}$ and $b \equiv \theta_H - \tilde{\theta}_{3A}$. Equating these two expressions and simplifying the algebra yields

$$(2\theta_I)^2 = (\theta_{3A} - \tilde{\theta}_{3A})^2, \quad (\text{A.56})$$

which does not depend on the relative magnitudes of θ_{3A} and $\tilde{\theta}_{3A}$.

Equation (A.56) is important because the angles can be related to κ by several applications of Snell's law as follows (see Figure A.10). For the upper beam,

$$\beta_3 \sin \theta_{3A} = \beta_2 \sin \theta_{2A}$$

$$\theta_{2A} = \theta_H + \theta_{2B}$$

$$\beta_2 \sin \theta_{2B} = \beta_1 \sin \kappa.$$

For the lower beam,

$$\beta_3 \sin \tilde{\theta}_{3A} = \beta_2 \sin \tilde{\theta}_{2A}$$

$$\tilde{\theta}_{2A} = \theta_H - \tilde{\theta}_{2B}$$

$$\beta_2 \sin \tilde{\theta}_{2B} = \beta_1 \sin \kappa.$$

For the small angle approximation, the above set of equations implies that

$$\theta_{3A} = \frac{\beta_2}{\beta_3} \left(\theta_H + \frac{\beta_1}{\beta_2} \kappa \right)$$

and

$$\tilde{\theta}_{3A} = \frac{\beta_2}{\beta_3} \left(\theta_H - \frac{\beta_1}{\beta_2} \kappa \right).$$

Therefore, Eq. (A.56) becomes

$$\boxed{\theta_I = \frac{\beta_1}{\beta_3} \kappa} , \quad (A.57)$$

which is the same result derived for θ_I in the cylindrical section (see Eq. (A.26)). Obviously, Eq. (A.27) gives the fringe spacing and shows that this does not vary across the traverse (i.e., $-R(z) \leq x \leq +R(z)$).

Determining the coordinates of "I" is a little more difficult. From Figure A.10 it follows that

$$\underline{x}_I = \underline{x}_A + \overline{AI} \underline{\ell}_3 \quad (A.58)$$

and

$$\underline{x}_I = \tilde{\underline{x}}_A + \tilde{\overline{AI}} \tilde{\underline{\ell}}_3 . \quad (A.59)$$

Equating (A.58) and (A.59) gives two equations for \overline{AI} and $\tilde{\overline{AI}}$, viz.,

$$\tilde{\overline{AI}} \tilde{\underline{\ell}}_3 - \overline{AI} \underline{\ell}_3 = \underline{x}_A - \tilde{\underline{x}}_A . \quad (A.60)$$

Rather than relating \underline{x}_A (and $\tilde{\underline{x}}_A$) to an angle as before, it is more convenient here to recognize that

$$\underline{x}_A = -R \underline{e}_x + \overline{CA} \underline{\ell}_H \quad (A.61)$$

and

$$\tilde{\underline{x}}_A = -R \underline{e}_x - \tilde{\overline{CA}} \tilde{\underline{\ell}}_H \quad (A.62)$$

where

$$\underline{l}_H \equiv -\sin \theta_H \underline{e}_x + \cos \theta_H \underline{e}_z . \quad (\text{A.63})$$

Equations for \overline{CA} and $\overline{C\tilde{A}}$ follow by realizing that \underline{x}_A and $\underline{\tilde{x}}_A$ are also equivalent to (see Figure A.10)

$$\underline{x}_A = \underline{x}_B + \overline{BA} \underline{l}_2 \quad (\text{A.64})$$

$$\underline{\tilde{x}}_A = \underline{\tilde{x}}_B + \overline{\tilde{B}\tilde{A}} \underline{\tilde{l}}_2 . \quad (\text{A.65})$$

The foregoing set of equations can now be organized to give

$$\overline{CA} \underline{l}_H - \overline{BA} \underline{l}_2 = R \underline{e}_x + \underline{x}_B \quad (\text{A.66})$$

$$- \overline{C\tilde{A}} \underline{l}_H - \overline{\tilde{B}\tilde{A}} \underline{\tilde{l}}_2 = R \underline{e}_x + \underline{\tilde{x}}_B . \quad (\text{A.67})$$

Here R is the radius of the hydrocyclone at the axial position z ;

\underline{l}_H is defined by Eq. (A.63); and, according to Figure A.10,

$$\underline{l}_2 = \cos \theta_{2B} \underline{e}_x - \sin \theta_{2B} \underline{e}_z \quad (\text{A.68})$$

and

$$\underline{\tilde{l}}_2 = \cos \tilde{\theta}_{2B} \underline{e}_x + \sin \tilde{\theta}_{2B} \underline{e}_z . \quad (\text{A.69})$$

We have previously shown how θ_{2B} and $\tilde{\theta}_{2B}$ are related to κ by applying Snell's law at B and \tilde{B} . Thus, once we find \overline{CA} and $\overline{C\tilde{A}}$ from Eqs. (A.66) and (A.67), respectively, (Eq. 60) can be solved for \overline{AI} and $\overline{A\tilde{I}}$. The vectors \underline{x}_B and $\underline{\tilde{x}}_B$ are given by (see Figure A.10)

$$\underline{x}_B = -R_1 \underline{e}_x + (R_1 + \underline{x}_F \cdot \underline{e}_x) \tan \kappa \underline{e}_z \quad (\text{A.70})$$

$$\tilde{\underline{x}}_B = -R_1 \underline{e}_x - (R_1 + \underline{x}_F \cdot \underline{e}_x) \tan \kappa \underline{e}_z \quad (\text{A.71})$$

For the small angle approximation, the x- and z-components of Eq. (A.66), together with the other definitions mentioned, yield

$$\begin{pmatrix} \theta_H & 1 \\ 1 & \theta_{2B} \end{pmatrix} \begin{pmatrix} \overline{CA} \\ \overline{BA} \end{pmatrix} = \begin{pmatrix} R_1 - R \\ \kappa(R_1 + x_{Fx}) \end{pmatrix} .$$

Thus,

$$\overline{CA} = \frac{\kappa(R_1 + x_{Fx}) - \theta_{2B}(R_1 - R)}{(1 - \theta_H \theta_{2B})} . \quad (\text{A.72})$$

Likewise, the x- and z-components of Eq. (A.67) can be written as

$$\begin{pmatrix} -\theta_H & 1 \\ 1 & \theta_{2B} \end{pmatrix} \begin{pmatrix} \tilde{\overline{CA}} \\ \tilde{\overline{BA}} \end{pmatrix} = \begin{pmatrix} R_1 - R \\ \kappa(R_1 + x_{Fx}) \end{pmatrix} ,$$

which gives

$$\tilde{\overline{CA}} = \frac{\kappa(R_1 + x_{Fx}) - \theta_{2B}(R_1 - R)}{(1 + \theta_H \theta_{2B})} . \quad (\text{A.73})$$

Finally, we return to Eq. (A.60), which is equivalent to

$$\begin{pmatrix} -1 & 1 \\ \theta_{3A} - \theta_H & \theta_H - \tilde{\theta}_{3A} \end{pmatrix} \begin{pmatrix} \overline{AI} \\ \tilde{\overline{AI}} \end{pmatrix} = \begin{pmatrix} -\theta_H & -\theta_H \\ 1 & 1 \end{pmatrix} \begin{pmatrix} \overline{CA} \\ \tilde{\overline{CA}} \end{pmatrix}$$

Inserting Eqs. (A.72) and (A.73) into this result and solving for \overline{AI} yields

$$\overline{AI} = \frac{2[\kappa(R_1 + x_{Fx}) - \theta_{2B}(R_1 - R)][1 + \theta_H(\theta_H - \tilde{\theta}_{3A})]}{(\theta_{3A} - \tilde{\theta}_{3A})(1 - \theta_H^2 \theta_{2B}^2)} . \quad (A.74)$$

The components of the beam intersection can now be determined by combining Eqs. (A.58), (A.61), (A.72), and (A.74). The result for the small angle approximation is

$$\begin{aligned} x_{Ix} = & -R - \kappa \theta_H \frac{[R_1 + y_{Fx} - \frac{\beta_1}{\beta_2}(R_1 - R)]}{[1 - \frac{\beta_1}{\beta_2} \kappa \theta_H]} \\ & + \frac{\beta_3}{\beta_1} \frac{[R_1 + y_{Fx} - \frac{\beta_1}{\beta_2}(R_1 - R)][1 + \theta_H(\theta_H - \frac{\beta_2}{\beta_3}(\theta_H - \frac{\beta_1}{\beta_2} \kappa))]}{[1 - (\frac{\beta_1}{\beta_2})^2 \kappa^2 \theta_H^2]} \end{aligned} \quad (A.75)$$

$$\begin{aligned} x_{Iz} = & \kappa \frac{[R_1 + x_{Fx} - \frac{\beta_1}{\beta_2}(R_1 - R)]}{[1 - \frac{\beta_1}{\beta_2} \kappa \theta_H]} \\ & - \frac{[\kappa - (\frac{\beta_3}{\beta_1} - \frac{\beta_2}{\beta_1})\theta_H][R_1 + x_{Fx} - \frac{\beta_1}{\beta_2}(R_1 - R)][1 + \theta_H(\theta_H - \frac{\beta_2}{\beta_3}(\theta_H - \frac{\beta_1}{\beta_2} \kappa))]}{[1 - (\frac{\beta_1}{\beta_2})^2 \kappa^2 \theta_H^2]} \end{aligned} \quad (A.76)$$

Eqs. (A.75) and (A.76) are the main results of this section. It is easy to show that for $\theta_H = 0$, Eq. (A.75) reduces to Eq. (A.69)

and that $x_{Iz} = 0$. Furthermore, if $\beta_1 = \beta_2 = \beta_3$, Eqs. (A.75) and (A.76) give $x_{Ix} = x_{Fx}$ and $x_{Iz} = 0$, respectively.

It is convenient to express the above results relative to some specific intersection point " \hat{I} ". With $x_{Fx} = \hat{x}_{Fx} + \epsilon$ and $\underline{x}_I = \underline{x}_I - \hat{\underline{x}}_I$, we finally have

$$\Delta x_{Ix} = \frac{\beta_3}{\beta_1} \epsilon \frac{1 + \theta_H^2 \left[1 - \frac{\beta_2}{\beta_3} \left(1 + \left(\frac{\beta_1 \kappa}{\beta_2} \right)^2 \right) \right]}{1 - \theta_H^2 \left(\frac{\beta_1 \kappa}{\beta_2} \right)^2} \quad (A.77)$$

which is (A.71) for $\theta_H = 0$. Also,

$$\Delta x_{Iz} = \frac{\beta_3}{\beta_1} \left(1 - \frac{\beta_2}{\beta_3} \right) \epsilon \theta_H \frac{1 + \theta_H^2 + \frac{\beta_1^2}{\beta_2 \beta_3} \kappa^2}{1 - \theta_H^2 \left(\frac{\beta_1 \kappa}{\beta_2} \right)^2} \quad (A.78)$$

It is noteworthy that the first order effect of curvature on $\underline{x}_I \cdot \underline{e}_x$ is negligible (i.e., $\Delta x_{Ix} \approx \beta_3 \epsilon / \beta_1$) yet

$$\Delta x_{Iz} \approx \frac{\beta_3}{\beta_1} \left(1 - \frac{\beta_2}{\beta_3} \right) \epsilon \theta_H. \quad (A.79)$$

Eq. (A.79) again shows why phases 2 and 3 should be optically equivalent. Unfortunately, this is not a characteristic of the set-up studied in this research; but, for the parameters which do define our experiments, the variation in Δx_{Iz} across the traverse is insignificant. None of the axial velocities reported in this dissertation were corrected for axial refraction--therefore, some

of our quantitative remarks regarding flow reversals may be only preliminary. For $\beta_1 = 1$, $\beta_2 = 1.47$, $\beta_3 = 1.33348$ (water at 14°C), $\theta_H = 5.65^\circ$, and $\kappa = 5.71^\circ$, Eq. (A.78) becomes

$$\Delta x_{Iz} = -0.0136 \epsilon . \quad (\text{A.79})$$

In the experiments, $\epsilon = 0$ on the axis of the hydrocyclone and $\epsilon \approx 28.7$ mm at the wall (i.e., $\Delta x_{Ix} = R = 38.1$ mm according to Eq. (A.77). Therefore, Eq. (A.79) shows that $|\Delta x_{Iz}| \leq 0.4$ mm, which should not modify any of the qualitative (or quantitative) conclusions regarding the mean axial velocity.

Tangential Velocity

The top view of the laser path illustrated in Figure A.8 for measuring the tangential velocity in the cylindrical section applies here with one fundamental difference not shown in this projection. The outward pointing normal vectors at "A" and "B" are still rotated relative to each other but now they are no longer in the plane defined by \underline{l}_2 and \underline{n}_B . Thus, although the refracted beams retain their symmetry about the x-axis so the y-coordinate of the intersection point is still $y = 0$, the probe volume does not remain in a plane of constant z .

For the cylindrical geometry,

$$(\underline{n}_A)_{\text{cylinder}} = -\cos \theta_A \underline{e}_x + \sin \theta_A \underline{e}_y$$

but for the conical geometry,

$$(\underline{n}_A) = (\underline{n}_A)_{\text{cylinder}} \cos \theta_H \underline{e}_y - \sin \theta_H \underline{e}_z ,$$

which reduces to \underline{n}_A for the cylinder when $\theta_H = 0$. This difference in geometry expresses itself whenever Snell's law is applied across the conical boundary. For example, suppose the direction of some incident light beam has been specified relative to a coordinate system. That is, we know \underline{l}_2 . Furthermore, if \underline{n}_A has been specified as well as the indices of refraction β_2 and β_3 of the two phases in contact, then Snell's law includes the following five mathematical statements:

- 1) $\beta_2 \sin \theta_{2A} = \beta_3 \sin \theta_{3A}$
- 2) $(\underline{l}_2 \wedge \underline{l}_3) \cdot \underline{n}_A = 0$
- 3) $-\underline{l}_2 \cdot \underline{n}_A = \cos \theta_{2A}$
- 4) $-\underline{l}_3 \cdot \underline{n}_A = \cos \theta_{3A}$
- 5) $\underline{l}_3 \cdot \underline{l}_3 = 1$.

In our previous examples, some of the above requirements were used implicitly (especially "2") because of the simplicity of the beam unit vector (i.e., \underline{l}_3) and the two angles θ_{2A} and θ_{3A} must be determined by (i.e., \underline{l}_3) and the two angles θ_{2A} and θ_{3A} must be determined by using the foregoing explicit statement of Snell's law.

For the small angle approximation, the intersection point is not expected to change much in the z direction but the effect of $\theta_H > 0$ on θ_I and x_{IX} could be important. The main contribution, however, will still be the local curvature of the cone (i.e., $1/R_2 \rightarrow \infty$ as $z \rightarrow 0$). Therefore, with

$$R_2 = z \tan \theta_H \approx z \theta_H, \quad (A.80)$$

the tangential data were corrected by applying (A.50) and (A.51) using (A.80). We emphasize that additional corrections should be investigated carefully by following the theory outlined here.

A.4. Additional Remarks on Experimental Apparatus and Techniques

A.4.1. Light source

The 35 mW He-Ne laser used in this study consists of a plasma tube, two reflectors mounted at an angle (adjustable), a support structure, and a magnet system designed to enhance the laser operation. The plasma tube is mounted using four clamps inside a heat shield structure. The laser is mounted to a black-anodized aluminum base with adjustable feet.

The He-Ne gas laser operates with a simple DC glow discharge in a plasma tube containing 90% helium and 10% neon. The total pressure is 2-3 torr (mm Hg). To achieve continuous wave laser oscillation, a mirror is placed at each end of the plasma tube to form a cavity resonator. This stores most of the optical radiation by reflection back and forth along the axis of the tube. Only a small transmission is permitted through one of the reflectors giving a spatially coherent and monochromatic output beam. The coherent length of the He-Ne laser, which has a wavelength of 632.8 nm, may exceed many kilometers. The laser light is linearly polarized by placing Brewster angle windows ($\phi = 35^\circ$, 31") at the ends of the plasma tube so that only one component of polarization is transmitted

with negligible loss. The other component suffers a loss greater than the amplification per pass.

A.4.2. Optical components

A polarization rotator (see Figure 2.7; component 2) is a half wave retarder that changes the direction of polarization of an outgoing light beam. This is a necessary function because the beam splitter divides the incident laser beam into two equal intensity beams, provided the polarization of the original beam is perpendicular to the plane of the two exiting beams. Thus, the polarization rotator takes the light from the laser, which is linearly polarized in the vertical direction, and rotates it a desired amount so that the polarization of the two resulting beams leaving the beam splitter is consistent with the measuring plane in the test section. The polarization rotator is mounted to a threaded plate and can be attached either directly to the laser or to the back of the first optics module. The beam splitter (component 4, Figure 2.7) is used to split the laser beam into two parallel beams of equal intensity 50 mm apart from each other. A back-plate, with a small hole in the center, is used to help prevent extraneous light from entering the beam splitter. The beam splitter can be rotated at 45° intervals in order to measure other components of the velocity, but special care should also be taken to rotate the polarization of the beam for optimum signals.

Frequency shifting was employed in this study to define the direction of flow and to reduce fringe bias. The system consists

of an optics module (component 5, Figure 2.7) and a down-mix circuit. The optics module contains an acousto-optic cell (Bragg cell) which shifts the frequency of one of the laser beams from the beam splitter by 40 MHz. The cell is installed in a cylindrical housing that aligns it with the other modules. A compensating wedge is used to correct shifted beam deflection. A tilt adjustment allows shifting of the light intensity to the deflected beam. The brightness of the shifted light beam is controlled by adjusting the voltage of an RF potentiometer.

A frequency shift of 40 MHz is too high for the range of velocities encountered in this study. A down-mix circuit permits shifting the frequency in twelve unequal increments from 2 KHz to 10 MHz. If other down-mixing frequencies are desired, an external oscillator can easily be interfaced with the system. However, maximum frequency from the down-mix circuit to the signal processor is only 25 MHz.

The optical lenses (component 7, Figure 2.7) have been designed to minimize spherical and chromatic aberrations. They are cemented doublet achromats and have dielectric, multi-layer, anti-reflective coatings. These lenses have a focal distance of 250 mm. The transmitting lens, with standard 50 mm beam spacing, results in a measuring volume that has 64 fringes and is typically 1.9 mm long and 0.18 mm in diameter. The half angle for the transmitting lens is 5° , $43''$ for the forward scatter mode of operation (see Figure A.1).

The receiving assembly (component 8) focuses the scattered light collected by the receiving lens onto the pinhole of the photomultiplier. The photodetector mount has positive X-Y adjustments for the photomultiplier aperture. The front lens of the module is adjustable by two thumb screws for optimum focus. This adjustable lens has anti-reflective coating, with 90% reflectance at a 45° incident angle for the He-Ne laser beam.

The photomultiplier system consists of the photomultiplier tube with a removable aperture, integral preamplifier, and photomultiplier power supply. The photomultiplier tube is made of a cathode with a quantum efficiency of 13% for a He-Ne laser beam ($\lambda = 632.8 \text{ nm}$). The removable aperture has a diameter of 0.2 mm. The photomultiplier high quantum efficiency and low noise preamplifier generates good signal amplitude for low light levels. For high levels of light, the built-in automatic control circuit decreases cathode voltage (fail safe system). The photomultiplier is capable of handling frequencies of 200 MHz. The high power supply operates with an input voltage of either 115 or 230 volts ($\pm 10\%$ volts) and has an adjustable maximum cathode potential level knob. Maximum anode current is indicated by a red light on the front panel. This light should be off during the course of the experiment. The termination box connects the photomultiplier output into a capacitor-coupled 50 ohm load, which reduces the signal amplitude ten fold. This is useful when viewing the signal on an oscilloscope directly from the photomultiplier and signal processor.

A.4.3. Data processing

The counter processor is designed specifically for processing signals from the photomultiplier of a laser doppler anemometer. The counter processor consists of three major components: (a) an input conditioner; (b) a timer; and (c) a data display module.

The input conditioner converts the doppler signal from the photomultiplier to an envelope to be timed. This envelope represents either the time for N cycles or the time for the total burst mode. Input and output jacks, installed on the front panel, receive signals from the photomultiplier and transmit signals to the oscilloscope for monitoring. To remove low and high frequency noise and to make the doppler signal symmetric, two filter banks using low and high pass filters are employed. The ranges of the low and high pass filters are from 10 KHz to 100 MHz and from 1 KHz to 10 MHz, respectively. The amplitude limit sets the maximum input signal allowable to help eliminate large particles from the measurement. The gain knob adjusts the gain of the input signal, and a light above it indicates the condition of the signal. A green light indicates proper signal amplitude, red indicates high amplitude, and off is low amplitude. The minimum cycles/burst sets the number of cycles to be timed.

It is important to remove the pedestal and asymmetry component of the signal. As mentioned above, this is accomplished by using a high pass filter. When frequency shifting is employed, the setting of this filter is not crucial. To reduce high frequency noise, the

range of a low pass filter is decreased to the threshold of the maximum expected doppler signal.

The gain controls the amplitude of the signal from the photo-multiplier tube to the counter processor. The increase in gain results in a higher data rate but, unfortunately, this could cause the noise to exceed a threshold level of 5 mV, which would make the Schmitt-trigger inoperable. This introduces "false" data to the counter processor. For best operation the amplitude of the doppler burst should exceed a threshold level of 5 mV while the "noise" is kept below ± 2 mV around the zero. Therefore, the gain level is adjusted on the input conditioner to a reasonable sample rate to eliminate "false" data. If "false" data are present in the signal, they can be detected by viewing the analog output from the signal processor on an oscilloscope screen. False data would create spots on Figure 2.13.

The purpose of the amplitude limit is to minimize the number of doppler signals from unusually large particles which may not be following the flow. There is no clear criterion to set the amplitude limit. However, during the course of this study, the location of the amplitude limit did not seem to affect the results, so it was kept at 90%.

The function of the timer is to measure the length of the envelope provided by the input conditioner. The timer is a high speed clock which can measure 10^8 cycles per second with an accuracy of $\pm \frac{1}{2}$ Hz. An analog voltage proportional to the time of the envelope from the input conditioner is available through a jack. Another

function of the timer is to compare the envelope time between N cycles and $\frac{N}{2}$ cycles in order to reject false data.

The number of fringes per burst is designated as "N". These fringes are timed by the counter processor. The selection of the number of fringes mainly depends on optics and flow condition, and should not exceed more than half of the total number of fringes which exist in the probe volume.

A parameter "n" defines the maximum time envelope to be accepted by the counter processor. The time envelope larger than the selected exponent "n" will be rejected by a reset pulse. The value of the exponent time not only depends on the flow condition, but also the total number of fringes "N". In the auto-position for a given "N", the upper and lower limit of the exponent time "n" will be selected.

The transfer function is the ratio between input frequency and output voltage, where "X" is the transfer function for a given combination of "N" cycles and exponent number "n" (see Table II-3 on page 24a in TSI [1982b]). The maximum frequency is equal to the transfer function for a 10:1 range. For this range setting, the minimum frequency should not be lower than $X/10$; otherwise, the results are less accurate. Attempts are made to read all data on the middle range of the transfer function for better accuracy. When the data reaches the limit of the transfer function, a new exponent value is selected and the calibration procedure repeated. The time constant and data rate resolution on the readout module

are set on the desired values. The manual/auto button is pushed into the manual position, and the exponent buttons are set corresponding to the selected transfer function. Manual option is most appropriate when analog output is used. The location of the low pass filters is rechecked by the readout module or oscilloscope information for noise clean signals.

A convenient feature of the readout module is the flexibility to display either frequency (i.e., f_d) or velocity directly by setting a calibration factor. For an optic orientation, the fringe spacing remains constant as the hydrocyclone is moved relative to the laser source. Thus, for axial velocity measurements (see Section A.3) the readout module is calibrated to read directly in velocity units (see p. 54 in TSI, 1982b). However, for tangential velocity measurements the half angle of the refracted beams changes with position and this results in a variable fringe spacing. For this case the readout module is calibrated to display frequency rather than velocity.

The data display module gives a direct readout of the analog voltage on a digital voltmeter with a selectable time constant of 0.1, 1, and 10 seconds. The data rate readout is a frequency counter that counts the data ready pulses from the timer. The resolution of the data rate can be selected as 10, 1, and 0.1 seconds. The digital data lines are all brought into the 37 pin plug-in connector on the front panel and can provide time, exponent, cycles, and other information to a computer for further processing. Unfortunately,

this capability was unavailable during this study. Instead, during each experiment the mean frequency of the doppler signal at each location in a traverse was read directly off the display panel and recorded. The mean velocities were calculated using Eq. (A.19) at a later time taking into account proper corrections for the effect of refraction on the fringe spacing.

A.5. Example Problem: Laminar Flow in a Circular Tube

LDA measurements for fully developed laminar flow in a circular tube were made for two different flow rates. The test section was located about 34 diameters from the tube entrance as indicated in Figure A.11. The circular tube was connected to the flow loop shown in Figure 2.1. A plexiglass box was built around the test section and filled with glycerin to minimize curvature effects.

A dual-beam, forward-scattering mode (see Section A.1) was used to measure the axial velocity. The test section was mounted on a milling table which permitted up to 5 cm movement in the horizontal plane. The volumetric flow rate was measured very accurately by weighing a known amount of fluid collected during a specified increment of time. The results are shown in Figure A.12 and agree nicely with the expected parabolic behavior. The parameters for the counter processor were chosen from an estimate of the maximum velocity using the theoretical parabolic profile.

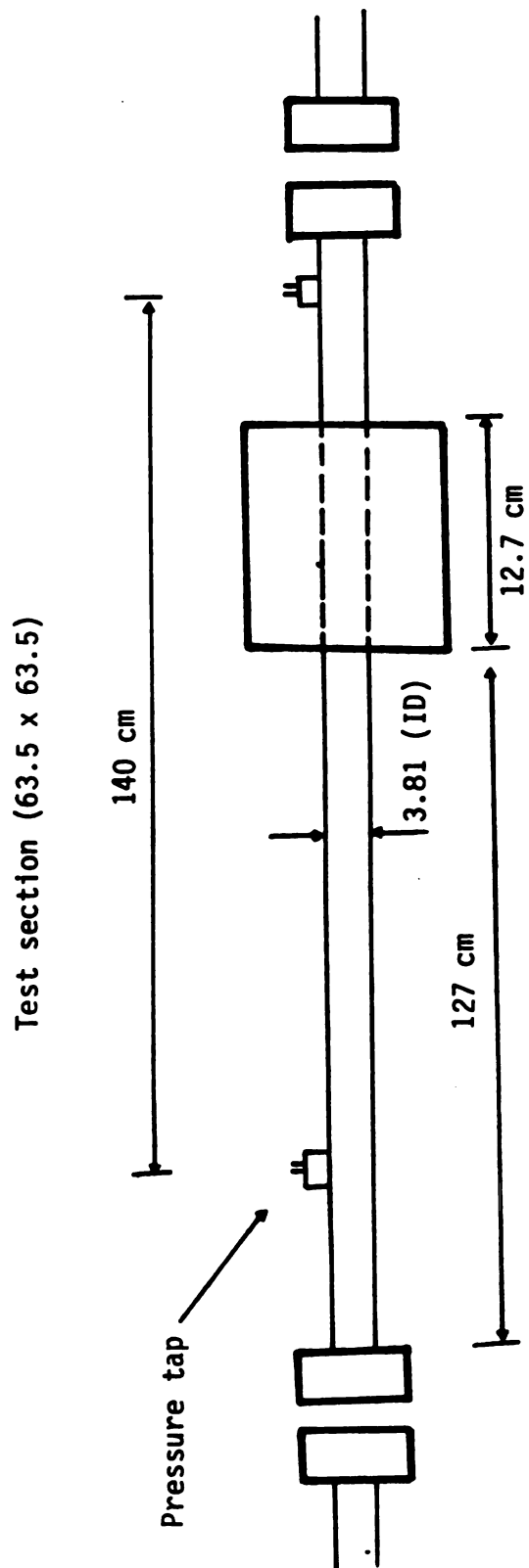
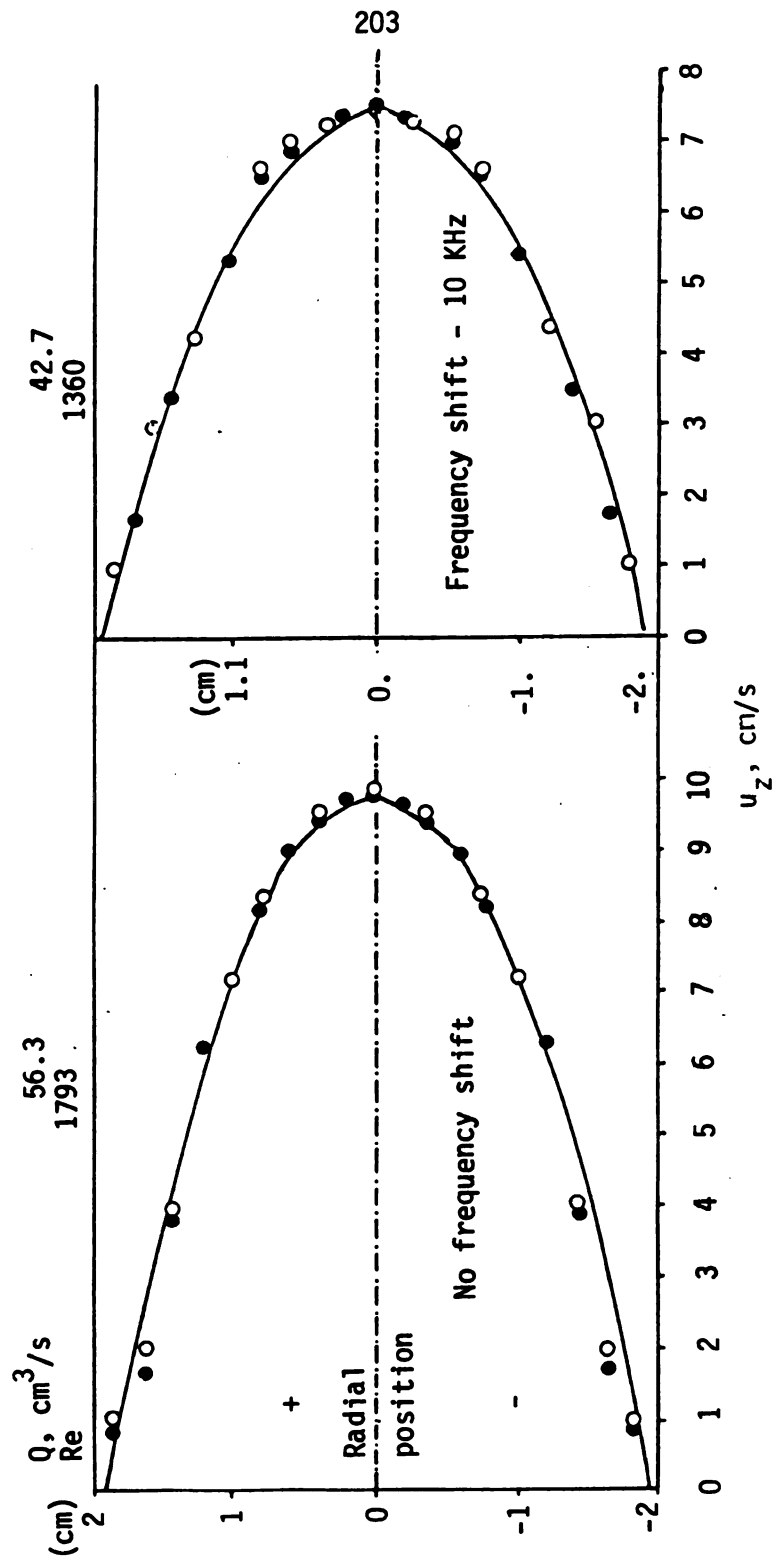


Figure A.11. Geometry of test ring for LDA measurements of parabolic profiles.

Flow parameters



Counter Parameter

N	8
n	14
Date	> 400
% of comparison	3

Figure A.12. Mean velocity profile for fully developed laminar flow in a circular tube.

A.6. Example Problem: Axial and Tangential Velocity Profiles in a Hydrocyclone

In this study, the axial and tangential components of the mean velocity were measured by recording traverse of the milling table and the mean velocity (or, frequency) on the data sheets. During the course of experiments, the flow conditions were recorded (flow rates and pressures) to define the experiment. The velocity profiles were all corrected for index of refraction effects (see Section A.3). Samples of the raw data for axial and tangential velocity profiles are presented in Tables A.1 and A.2 to illustrate the procedure for obtaining the corrected velocity profiles. The data presented in this section are all taken in a hydrocyclone with a configuration shown in Figure 2.5a.

Table A.1 presents the mean axial velocity for the axial location of $z = 20$ cm and $Q_0/Q_u = 4$. Column 1 of the table gives the increment advancement of the milling table. Column 2 shows the velocity data directly obtained from counter processor, which includes frequency shift. Column 3 is obtained from column 1, taking into consideration that increment advancement of the milling tables moves the test section 0.024 mm; therefore, this column represents the traverse of milling table (or test section). Real probe volume distance from axis of the hydrocyclone is presented by X_I . Similar expressions as those of (A.77) have been used to correct for radial position due to refractive index problem (see Appendix A.3). Because the fringe spacing does not change with position for axial velocity no correction is required for axial velocity. For the experiment

Table A.1. Mean axial velocity data measured in the hydrocyclone which satisfies Rietema's optimal design criteria.

z (20; 5.3; 4), $Re_F \approx 24,300$

Increment advancement of the milling table	Velocity (include shift) m/sec	ϵ mm	x_I mm	Velocity m/sec
0	3.680	0.00	0.00	-0.503
40	3.534	1.02	1.36	-0.357
40	3.278	2.03	2.7	-0.101
40	2.894	3.05	4.05	0.283
80	2.376	5.08	6.75	0.801
80	2.613	7.11	9.45	0.564
60	2.8	8.64	11.48	0.377
80	3.011	10.67	14.18	0.166
80	3.15	12.70	16.88	0.027
80	3.281	14.74	19.59	-0.104
80	3.365	16.77	22.27	-0.188
80	3.473	18.8	24.97	-0.296
100	3.287	21.34	28.34	-0.11

reported in Table A.1 frequency shift of 1 MHz is applied to define the flow reversals. Using Eq. (A.18) and fringe spacing of 3177 nm the velocity corresponding to this frequency shift is 3.177 m/sec. This velocity is subtracted from the velocity recorded in column 2 to obtain the velocity of the fluid (column 5).

Table A.2 presents the mean tangential velocity for the same flow condition of axial velocity. One MHz frequency shift is applied to define the flow direction. The first column of Table A.2 is similar to those described in Table A.1. Because fringe spacing varies with position for tangential velocity measurements, the frequency is recorded instead of velocity directly from the counter processor. Column 2 presents this frequency including frequency shift. The third column obtained from column 1 is the same as those described for axial velocity. The amount of frequency shift (1 MHz) is subtracted from the frequency obtained from the counter (column 2) to obtain the frequency of fluid particles (column 4). A similar expression to that of Eq. (A.50) is used to obtain the real position of the probe volume (column 5). In order to obtain tangential velocity of fluid, the fringe spacing is calculated at each radial position (see Section A.3). Then Eq. (A.18) is applied to calculate the tangential velocity. The result of this calculation is presented in column 6. Mean axial and tangential velocity shown in Tables A.1 and A.2 are graphically presented in Figures 5.7 and 5.8, respectively.

Table A.2. Mean tangential velocity data measured in the hydro-cyclone which satisfies Rietema's optimal design criteria.

$$\theta(20; 15.3; 4), Re_F \approx 24,300$$

Increment advancement of the milling table	Frequency (include shift) MHz	ϵ mm	Frequency MHz	x_I mm	Velocity m/sec
0	1.022	0	0.022	0	0.077
5	1.11	0.13	0.11	0.21	0.386
40	1.427	0.89	0.427	1.45	1.504
40	1.61	1.90	0.61	3.13	2.161
40	1.688	2.92	0.688	4.83	2.452
20	1.695	3.43	0.695	5.68	2.485
20	1.688	3.94	0.688	6.54	2.466
80	1.697	5.97	0.697	10.04	2.202
80	1.515	8.00	0.515	13.62	1.891
80	1.45	10.03	0.45	17.29	1.673
40	1.388	12.06	0.388	21.05	1.46
80	1.273	14.10	0.273	24.90	1.04
80	1.211	16.13	0.211	28.78	0.809

APPENDIX B

DRAG REDUCTION CHARACTERISTICS OF SEPARAN AP-30

APPENDIX B

DRAG REDUCTION CHARACTERISTICS OF SEPARAN AP-30

A series of experiments were conducted to study some of the parameters which influence the ability of Separan AP-30 to reduce the drag in fully developed pipe flow. The information developed here helps to define the system studied in Section 4.4. Basically, we examine the effect of temperature and pH on the friction factor and apparent viscosity for a range of dilute polymer-water mixtures.

B.1. Viscosity Measurements

Viscosity measurements were made at various temperatures using a Cannon-Fenske pipette type viscometer. Polymer solutions were made from a stock solution of 2000 wppm. The polymer used in the experiments was Separan AP-30, which has a molecular weight of about 10^6 ; the chemical structure of the repeat unit is shown in Figure B.1. The concentrated polymer solution was prepared in a 200 liter plastic container filled with distilled water. The polymer was sprinkled on the surface and gently stirred with a plastic rod. This stock solution was made prior to the experiment and was later diluted to a desired concentration in a 100-liter plastic container. The stock solution was made at least one day prior to any experiment and checked under the light for homogeneity. The pH of the distilled water was adjusted by adding NaOH or HCL; salt was used to prepare a 0.5 M NaCl

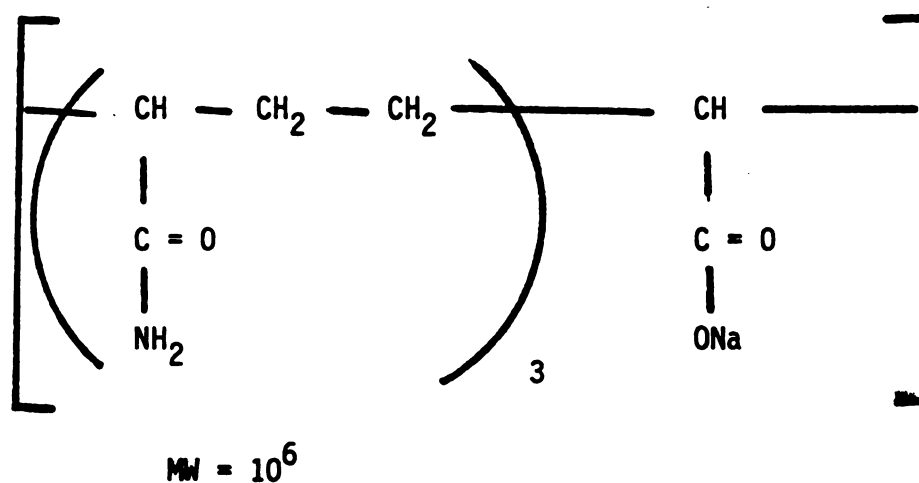


Figure B.1. Chemical structure of Separan AP-30, a co-polymer of polyacrylamide and polyacrylic acid.

polymer solution. An automatic temperature control tank was used to maintain the viscometer at a constant temperature.

Figure B.2 shows the apparent viscosity of polyacrylamide solutions at a low shear rate for the temperature ranging from 10°C to 40°C. The solvent is distilled water with pH = 6. Figure B.3 illustrates the effect of water composition on the viscosity. It is noteworthy that the viscosity of the polymer increases significantly with pH, up to a certain point. Thereafter, the viscosity declines. The lowest viscosities observed were those at low pH and salt composition.

Polyacrylamide is an anionic polyelectrolyte which easily uncoils in solution because of the electrostatic repulsion of chain ionic groups. The decrease in viscosity at high pH levels may result from a shielding effect caused by a large number of counter-ions in the domain of the polymer molecules. This phenomenon seems to suggest molecular expansion diminishes at higher pH levels after the maximum value is attained. After comparing the polymer-distilled water results with the polymer-salt water results, it is apparent that the added electrolyte has essentially neutralized the electrostatic repulsions between the chains. This type of behavior is well known for polyelectrolytes. The expansion of the poly-ions eventually reaches an upper limit and the decrease in the apparent viscosity upon further dilution merely reflects the decreasing interference between the expanded chains.

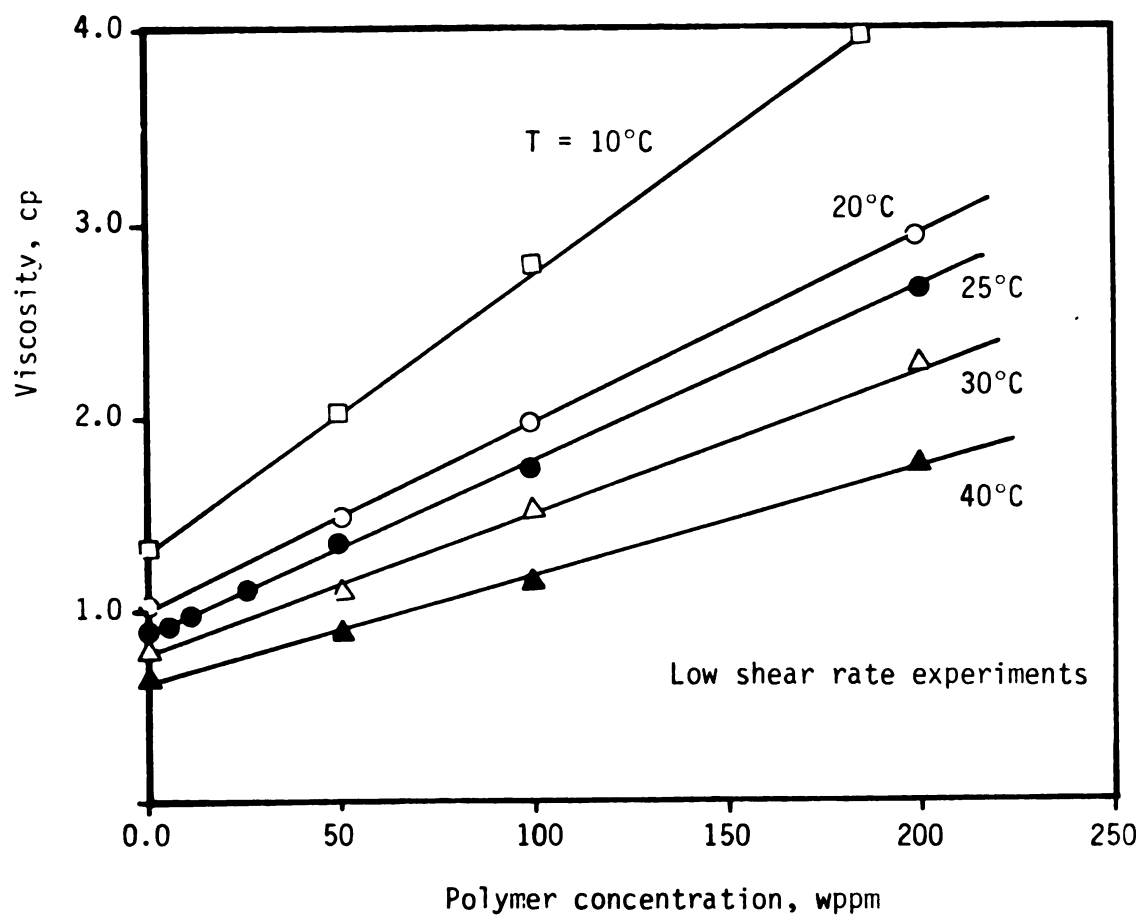


Figure B.2. The effect of polymer concentration on the apparent viscosity of aqueous AP-30 mixtures at different temperatures.

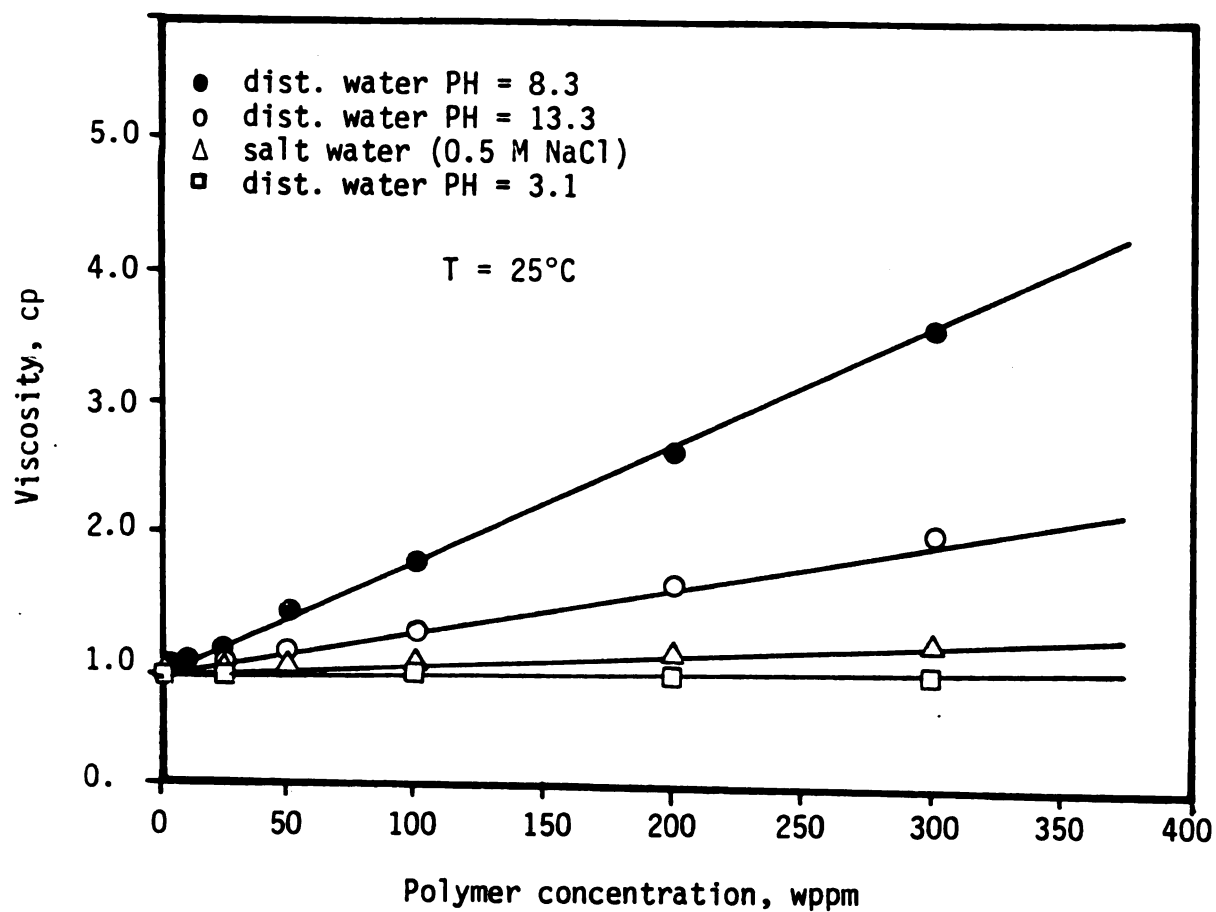


Figure B.3. The effect of polymer concentration and PH on the apparent viscosity of aqueous AP-30 mixture.

The viscosity behavior of dilute solutions of partially hydrolyzed polyacrylamide has also been investigated by Sylvester and Tyler [1970]. Three different solvents were used: distilled water, salt water (0.55 M NaCl), and simulated sea water. The intrinsic viscosity found for salt water and distilled water are comparable with the findings reported here.

Figure B.3 also shows the effect of low pH on the apparent viscosity. Apparently, the molecules possess a compact, impermeable structure in the acidic range. This phenomenon has also been observed by Katchalsky and Eisenberg [1951] for other high molecular weight polyelectrolytes (polymethacrylic acid) and by Kim et al. [1973] for polyacrylamide.

B.2. Drag Reduction Results

Drag reduction experiments were conducted to characterize the polymer used in the hydrocyclone experiments reported in Section 4.4. The data are plotted using Von Karman coordinates

$$f \equiv \frac{g_c (-\Delta p) D}{2U_b^2 \rho L}$$

$$R_e = \frac{DU_b \rho}{\mu} .$$

Δp is the observed pressure drop; U_b , the bulk average velocity; D , the inside capillary diameter; and L is the length over which Δp is measured. The density and viscosity of the fluid are ρ and μ , respectively.

To minimize the mechanical degradation of the polymer, a once-through flow system was designed. The system is basically the one shown in Figure 2.2. A small tube (I.D. = 3.55 mm) made from stainless steel was connected to the flow loop. Pressure taps were located 229 mm apart with the location of the first tap more than 250 diameters from the entrance. The pressure taps were connected to a mercury manometer, and the flow rate was measured by recording the time necessary to fill a precalibrated plastic container.

The homogeneous polymer solution was poured into the pressurized tank and sealed for leaks. Pressure was applied to the supply tank through a regulator, and the polymer flow rate was adjusted by a valve. After the pressure stabilized and the flow rate became steady, the flow rate, pressure drop, and temperature were recorded. The pH of the solution was also measured. Special care was taken to maintain stable flow rate and pressure drops. Viscosities were determined by requiring

$$f = 16/Re$$

for the low Reynolds number data.

Figure B.4 shows the effect of pH on the friction factor for a 100 wppm polymer solution. The % drag reduction increases sharply with increasing ionization. This enhancement can be interpreted as a result of molecular expansion due to electrostatic repulsion between like charges in the polymer chain. No significant effects due to polymer concentration were noticed from 50-300 wppm.

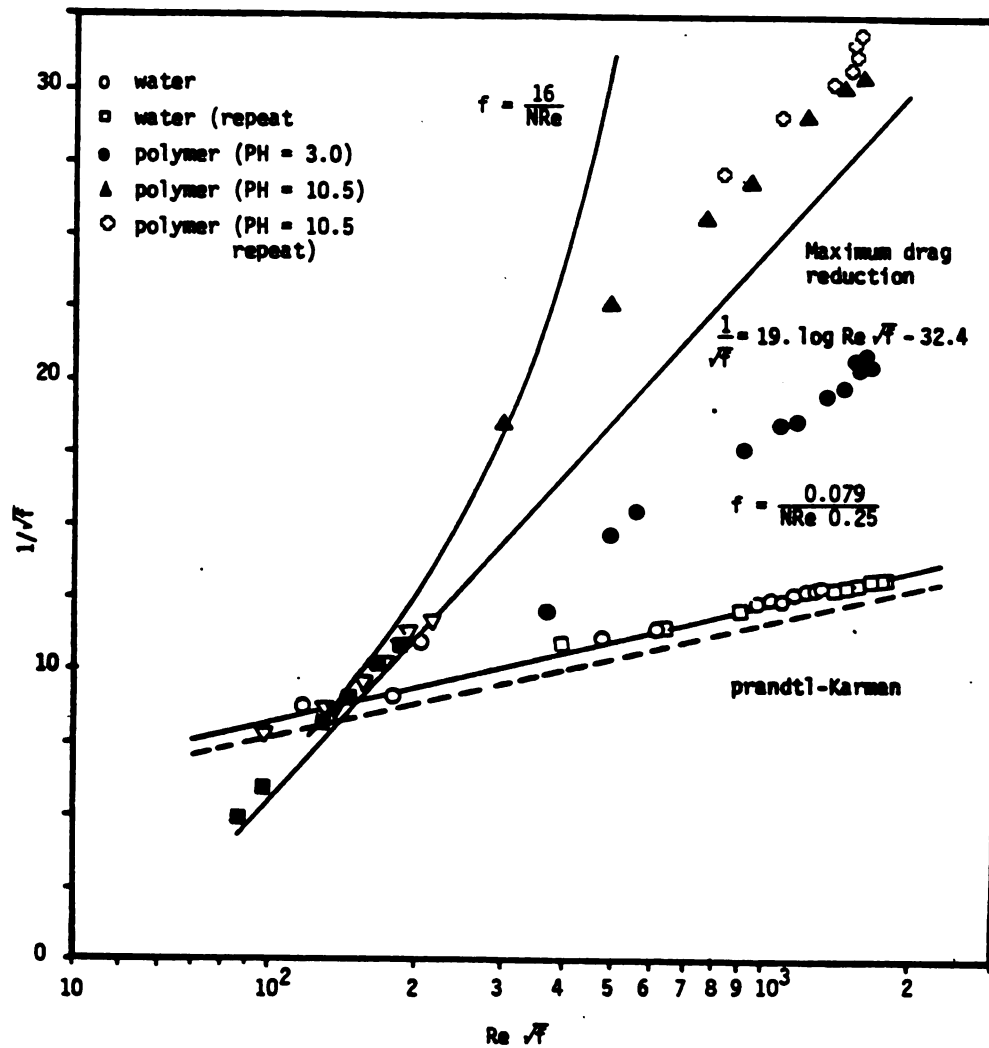


Figure B.4. The effect of PH on drag reduction characteristic of Separan AP-30 (100 wppm).

If the polymer solution is continuously sheared in a turbulent flow, the drag reduction effect is lost. This phenomenon is demonstrated very vividly in Figure B.4 which shows the % drag reduction versus time. The decreasing nature of this graph is an indication of polymer degradation. Two pH levels are examined. Both solutions reach the same asymptote after two hours of shearing through the flow loop; the last two points on the graph represent the same polymer solution after sitting eighteen hours. Note that the % drag reduction continues to decay slightly without shear. Thomas [1982] has recently shown that if 100 wppm Separan AP-30 solution sits for eighteen hours without shearing, then the % drag reduction is comparable to the sheared results shown in Figure B.4. This suggests that the effect of shear is to disentangle the polymer rather than degrading them by breaking molecular bonds. If this occurs then degradation should be reversible.

All the solutions used in the hydrocyclone experiments recorded in Section 4.4 showed significant drag reduction properties after the velocity traverses were recorded. The % drag reduction was $\approx 50\%$ at $Re = 10^4$ for all the solutions. The important conclusion here is that these solutions, which passed through the flow loop only once, were viscoelastic and any significant differences between the results with and without polymer could very well be attributed to the elastic properties of Separan AP-30. Unfortunately, very few data are available for direct comparisons since the temperature of the experiments recorded in Section 4.4 are almost 8° below the ones in Section 4.1; however, for a comparison see Figure 5.18.

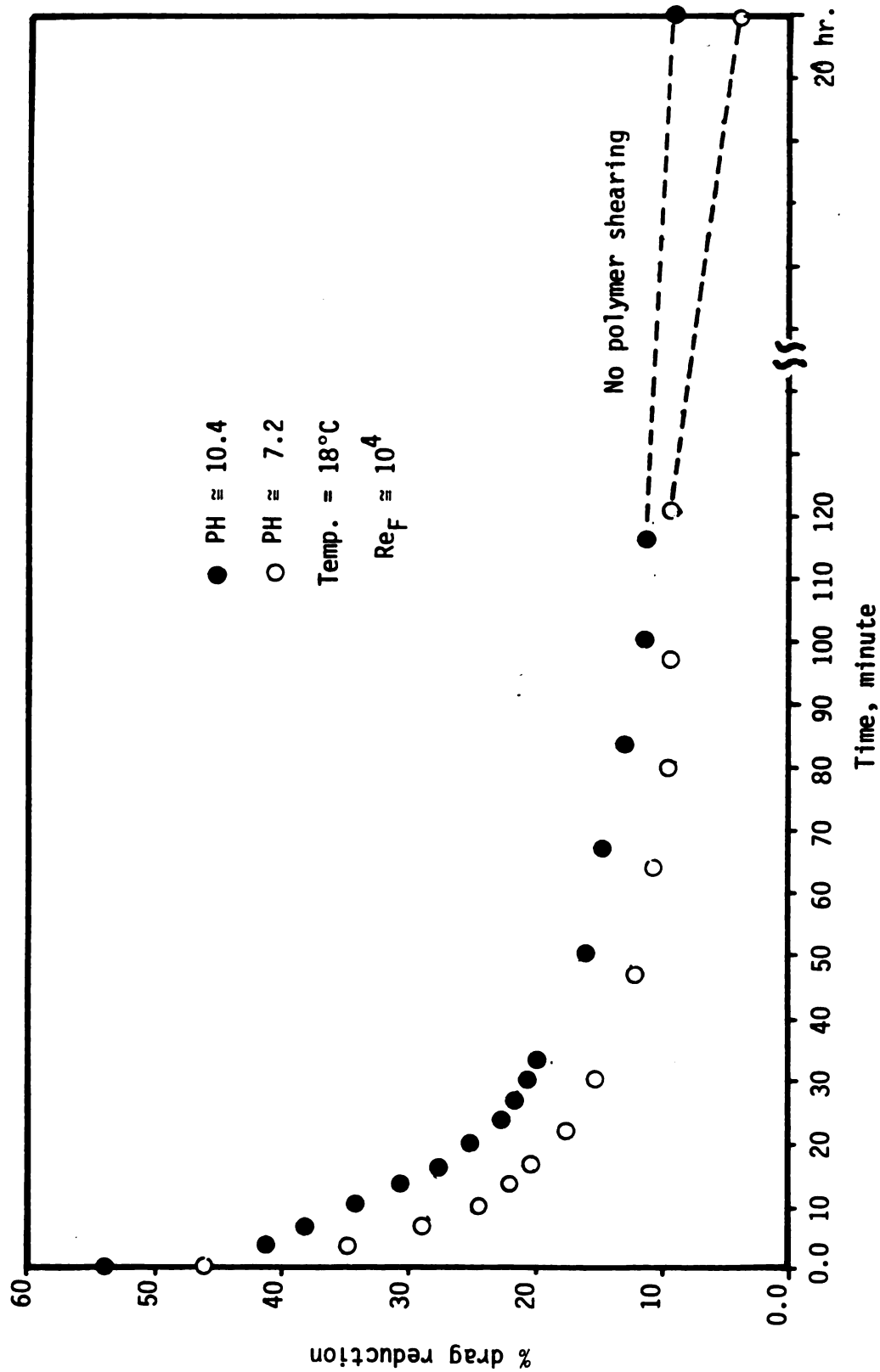


Figure B.5. The effect of shear on the % drag reduction for 100 wppm Separan AP-30.

APPENDIX C

FLOW CHARACTERISTICS FOR THE 3"-HYDROCYCLONE

APPENDIX C

FLOW CHARACTERISTICS FOR THE 3"-HYDROCYCLONE

Pressures and flow rates for different split ratios and vortex finder configurations were measured to characterize the hydrocyclone. A schematic of the flow loop used to carry out the experiments is shown in Figure 2.1. The hydrocyclone overflow and underflow were not connected to the atmosphere. The valves labeled 1, 2, and 3 in Figure 2.1 were used to control the flow through the loop and provide the desired flow rates and split ratios. The pressures at the inlet and outlets were measured by a mercury manometer and checked by a standard pressure gauge. The underflow and overflow rates were measured by a precalibrated plastic container over a period of time.

A series of experiments were conducted to characterize the 3"-hydrocyclone with a 2:1 contraction above the vortex finder (see Figure 2.3). Inlet and outlet flow rates at different inlet pressures were measured for $Q_o/Q_u = 0.25, 4, \text{ and } \infty$. The results are summarized in Figures C.1-C.2. The effect of feed pressure on the overflow and underflow rates are also indicated. Table C.1 compares the exponent on Δp in the empirical correlation

$$Q_F = K(\Delta p)^m$$

found in this study and with other results in the literature.

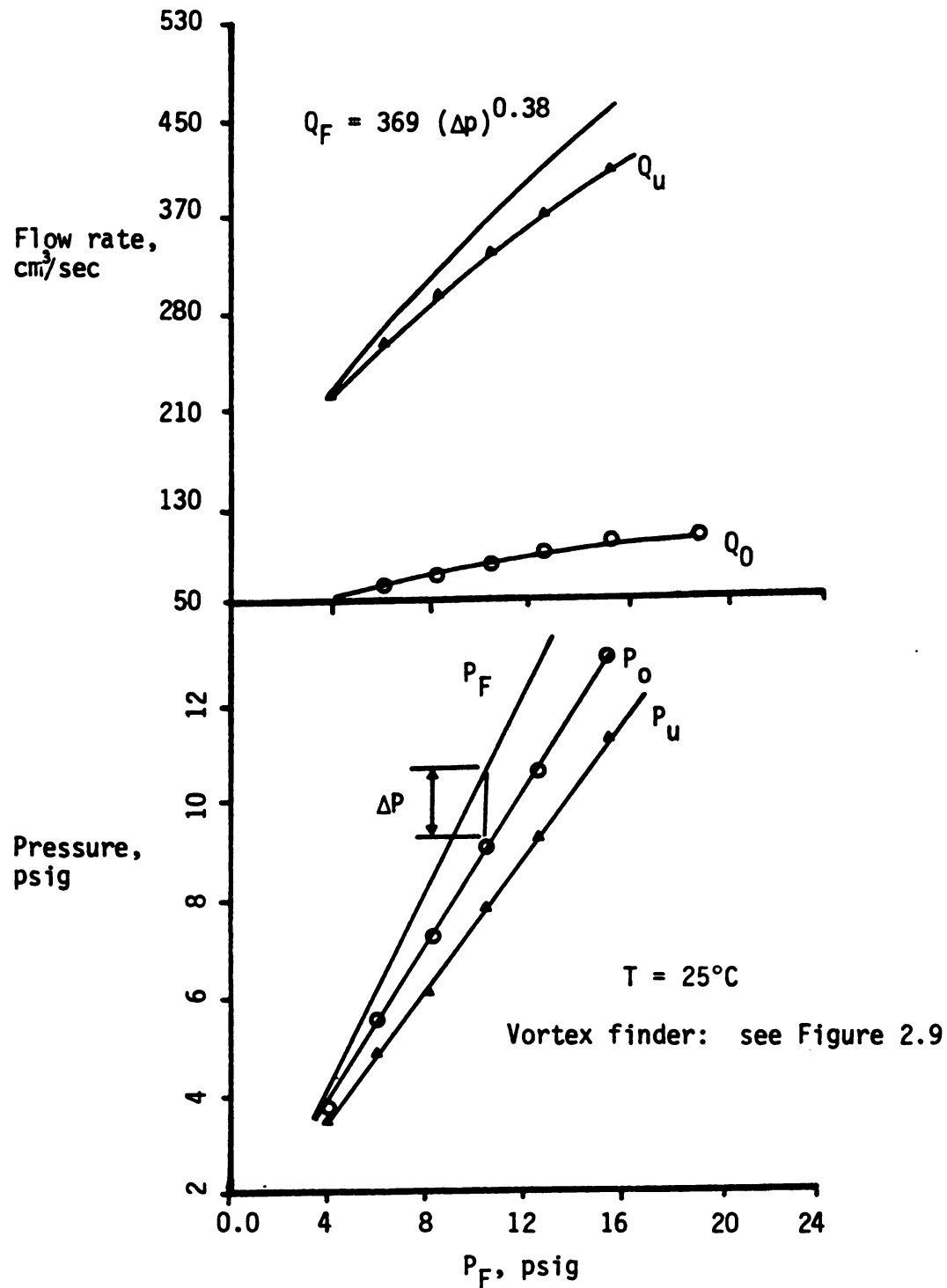


Figure C.1. Operating characteristics of a 3"-hydrocyclone for $Q_O/Q_U = 0.25$.

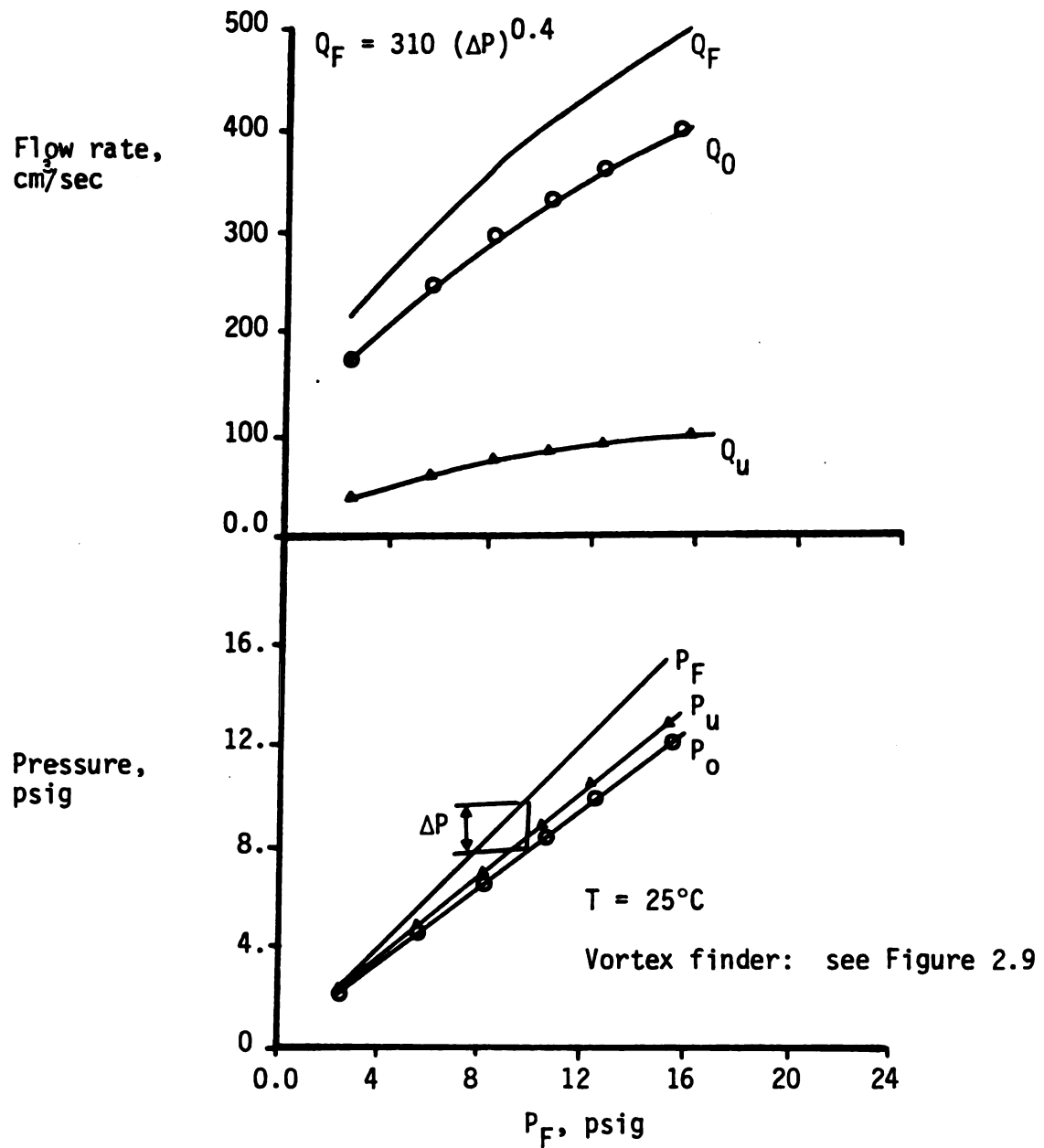


Figure C.2. Operating characteristics of a 3"-hydrocyclone for $Q_O/Q_U = 4$.

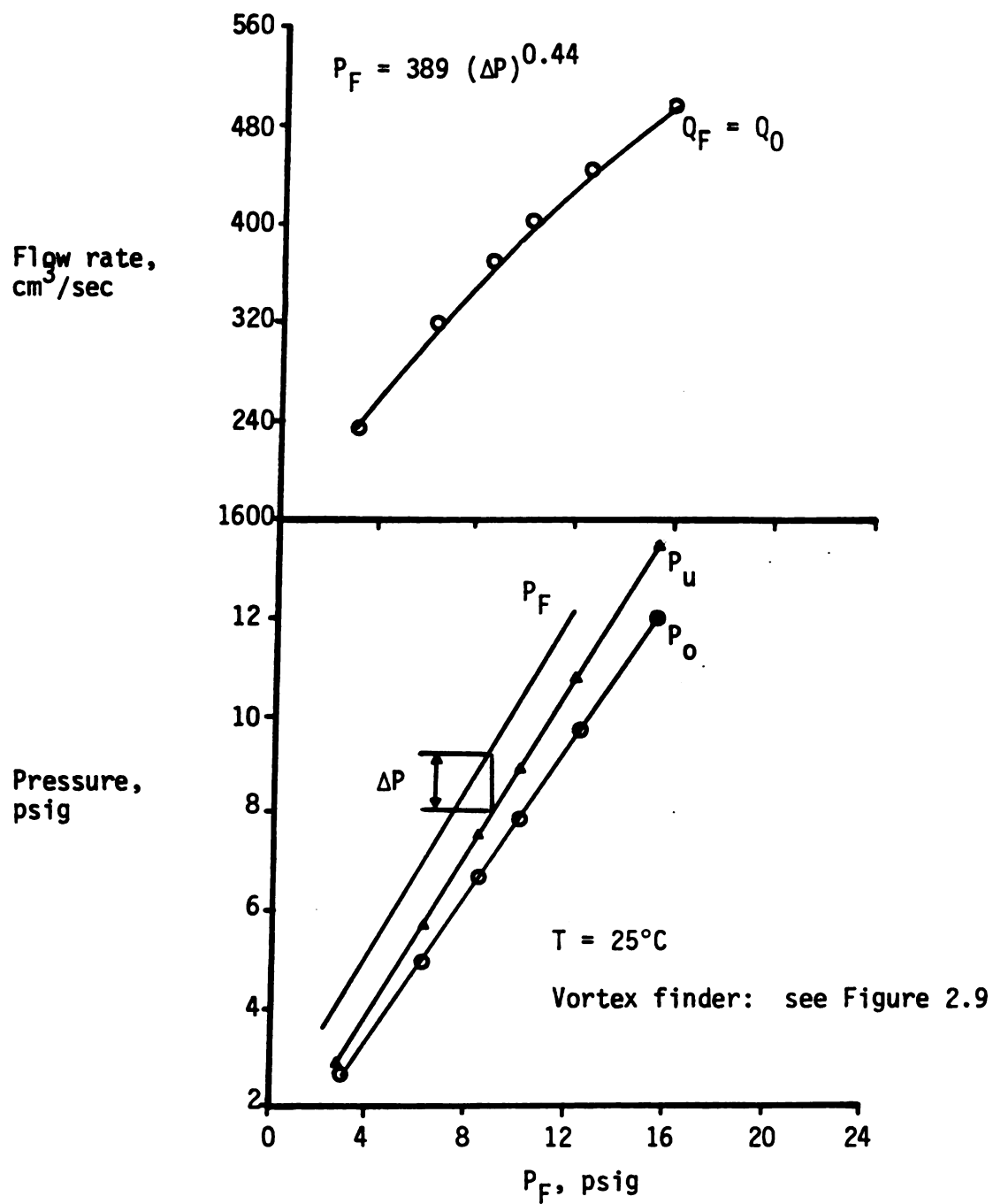


Figure C.3. Operating characteristic of a 3"-hydrocyclone for $Q_0/Q_u = \infty$.

Table C.1. Values of exponent 'm' for various size hydrocyclones.

Source	D, mm	'm'	Remarks
Kelsall [1953]	76	0.416	air core
Bradley and Pulling [1959]	76	0.425	air core
Present study	76	0.42	no air core

The variation in the split ratio with changes in inlet pressure is given in Figure C.4. Several researchers have shown that the split ratio is a weak function of the inlet flow rate (equivalent to P_F), geometry, and viscosity. For a 13 mm hydrocyclone, Haas et al. [1957] have observed a weak dependence of split ratio on the flow rate. The important effect of viscosity on the split ratio is summarized by Bradley [1965, see p. 143]. Usually, an increase in viscosity causes the split ratio to decrease. This decrease is related to the suppression of the swirl velocity, which reduces the upward reverse flow.

Changes in the inlet flow rate have no significant effect on Q_o/Q_u over the range investigated. However, at low flow rates with a high split ratio setting, Q_o/Q_u increases with decreasing inlet pressure; the opposite behavior was observed for low split ratio settings.

The flow characteristics of the other vortex finder configurations shown in Figure 2.5 were also measured and analyzed, but are not reported here.

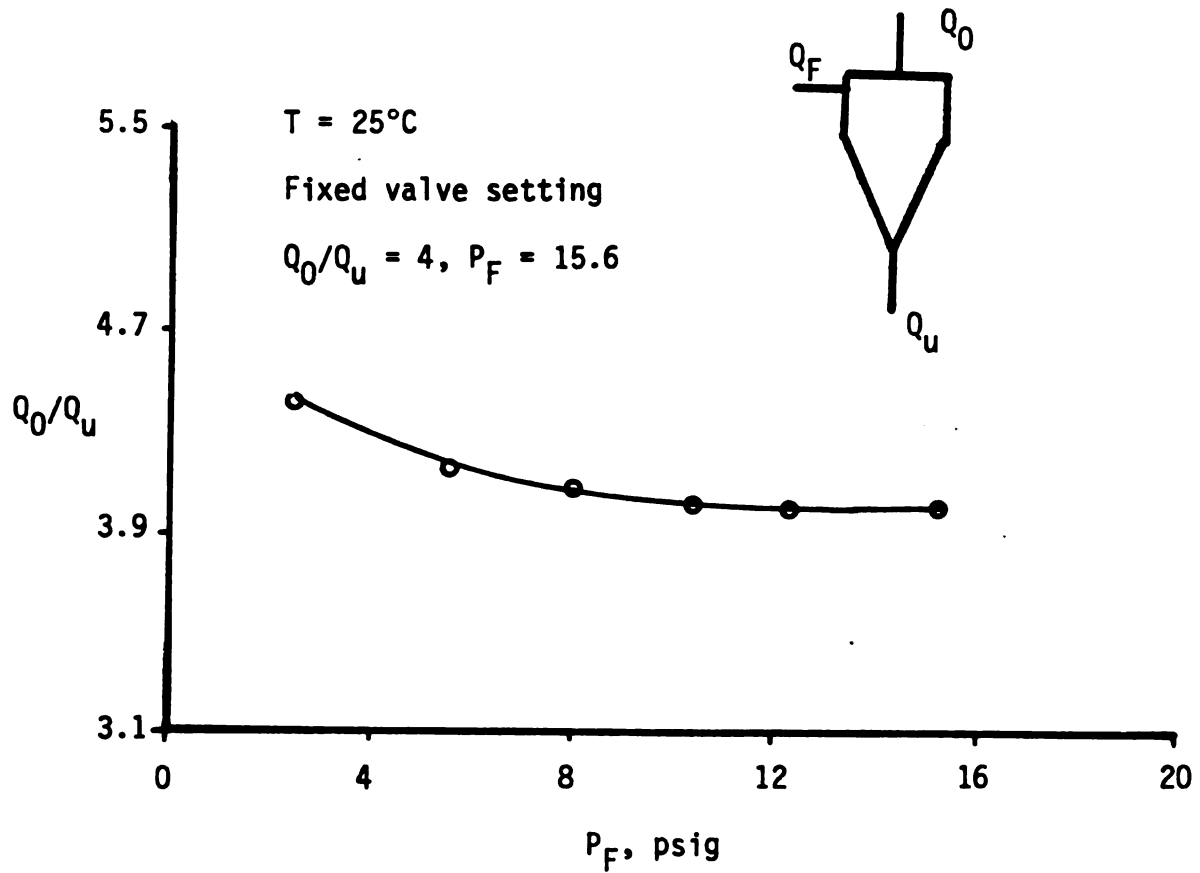


Figure C.4. Effect of inlet pressure on the Q_0/Q_u of a 3"-hydrocyclone with a 2:1 contraction above the vortex finder.

APPENDIX D

**DATA FOR THE 3"-HYDROCYCLONE WHICH SATISFIES
RIETEMA'S DESIGN CRITERIA**

APPENDIX D

DATA FOR THE 3"-HYDROCYCLONE WHICH SATISFIES RIETEMA'S DESIGN CRITERIA

Data for Rietema's optimum hydrocyclone design are presented in Table D.1. All velocity traverses are obtained at a temperature of 12°C. The following convention has been adopted to present the mean axial and tangential velocity. For the mean axial profile,

$$\langle u_z \rangle (r,z) = z(z; P_F; Q_0/Q_u) .$$

For the mean tangential profiles,

$$\langle u_\theta \rangle (r,z) = \theta(z; P_F; Q_0/Q_u) .$$

The characters $z(\text{cm})$, $P_F(\text{psig})$, and Q_0/Q_u represent the axial location, inlet feed pressure, and split ratio, respectively. For each velocity traverse in Table D.1, the actual displacements of the test section (ϵ, mm) and either mean velocity or mean frequency are presented. For tangential velocity measurements, the fringe spacing varies with ϵ (see Eq. (A.51)). Data for tangential velocity profiles are shown in the term of mean frequency rather than mean velocity. An asterisk ^{*} is used to denote which profiles appear in graphical form, which are presented in Chapters 4, 5, and 6.

Table D.1. Mean velocity data measured in the hydrocyclone which satisfy Rietema's optimal design criteria.

$Z(8; 15.3; 0)$, $Re_F = 24,200$

ϵ, mm	$\langle u_z \rangle \text{ m/sec}$	ϵ, mm	$\langle u_z \rangle \text{ m/sec}$	ϵ, mm	$\langle u_z \rangle \text{ m/sec}$
0.00	- 4.296	4.58	-0.387	11.2	-0.537
0.51	- 4.180	5.08	-0.227	11.70	-0.079
1.02	- 3.83	5.60	-0.17	12.21	-0.02
1.53	- 3.209	6.10	-0.186		
2.03	- 2.468	6.62	-0.221		
2.54	- 1.774	7.12	-0.266		
3.05	- 1.281	8.14	-0.391		
3.56	- 0.825	9.16	-0.485		
4.07	- 0.546	10.17	-0.556		

$\theta(8; 15.5; 0)$, $Re_F = 24,300$

ϵ, mm	$\langle f_\theta \rangle \text{ MHz}$	ϵ, mm	$\langle f_\theta \rangle \text{ MHz}$	ϵ, mm	$\langle f_\theta \rangle \text{ MHz}$
0.00	0.049	2.67	1.28	8.76	0.454
0.13	0.226	3.17	1.16	9.27	0.429
0.38	0.944	3.68	1.061		
0.63	1.42	4.19	0.951		
0.89	1.534	4.70	0.853		
1.14	1.593	5.20	0.71		
1.39	1.588	6.22	0.646		
1.65	1.535	7.24	0.563		
2.10	1.428	8.25	0.485		

$Z^*(20; 15.3; 0)$, $Re_F = 24,100$

ϵ, mm	$\langle u_z \rangle \text{ m/sec}$	ϵ, mm	$\langle u_z \rangle \text{ m/sec}$	ϵ, mm	$\langle u_z \rangle \text{ m/sec}$
-21.36	- 0.042	- 3.05	-1.409	12.72	-0.066
-19.33	- 0.282	- 1.53	-3.047	14.75	-0.181
-17.29	- 0.252	- 0.51	-3.538	16.78	-0.255
-15.26	- 0.163	0.51	-3.615	18.82	-0.315
-13.22	- 0.053	2.54	-1.635	19.84	-0.324
-11.19	0.063	4.58	-0.376	20.85	-0.273
- 9.15	0.187	6.61	-0.024	21.36	-0.179
- 7.12	0.115	8.65	0.135		
- 5.09	- 0.183	10.68	0.083		

Table D.1 (cont'd.).

$\theta^*(20; 15.3; 0), Re_F = 24,100$					
ϵ, mm	$\langle f_\theta \rangle$ MHz	ϵ, mm	$\langle f_\theta \rangle$ MHz	ϵ, mm	$\langle f_\theta \rangle$ MHz
0.0	0.0	2.79	1.24	11.43	0.435
0.25	0.561	3.30	1.17	12.44	0.403
0.59	0.912	4.32	0.928	13.46	0.374
0.76	1.512	5.33	0.768	14.48	0.35
1.02	1.58	6.35	0.645	15.49	0.322
1.27	1.59	7.36	0.587		
1.52	1.584	8.38	0.54		
1.78	1.523	9.40	0.498		
2.28	1.392	10.41	0.468		
$Z(32; 15.3; 0), Re_F = 24,200$					
ϵ, mm	$\langle u_z \rangle$ m/sec	ϵ, mm	$\langle u_z \rangle$ m/sec	ϵ, mm	$\langle u_z \rangle$ m/sec
0.00	-3.243	8.14	0.018	20.34	-0.071
0.51	-2.933	9.16	0.066	22.38	-0.113
1.53	-2.003	10.17	0.087	24.42	-0.069
2.54	-1.258	11.19	0.104	26.45	-0.019
3.56	-0.773	12.218	0.121		
4.58	-0.423	13.22	0.11		
5.59	-0.245	15.26	0.054		
6.61	-0.124	16.28	0.025		
7.63	-0.012	18.31	-0.024		
$\theta(32; 15.4; 0), Re_F = 24,100$					
ϵ, mm	$\langle f_\theta \rangle$ MHz	ϵ, mm	$\langle f_\theta \rangle$ MHz	ϵ, mm	$\langle f_\theta \rangle$ MHz
0.00	0.006	2.16	1.239	9.78	0.468
0.13	0.18	2.67	1.132	10.79	0.444
0.38	0.526	3.17	1.064	11.81	0.424
0.63	0.782	3.68	0.961	12.83	0.409
0.89	0.999	4.70	0.828	13.84	0.393
1.14	1.119	5.71	0.699	14.86	0.383
1.40	1.23	6.73	0.615	15.87	0.374
1.65	1.292	7.75	0.55	16.89	0.367
1.90	1.286	8.76	0.50	17.91	0.363
				18.92	0.361
				19.94	0.348
				20.95	0.33

Table D.1 (cont'd.).

Z(20; 5.1; 0), $Re_F = 14.100$					
ϵ, mm	$\langle u_z \rangle \text{ m/sec}$	ϵ, mm	$\langle u_z \rangle \text{ m/sec}$	ϵ, mm	$\langle u_z \rangle \text{ m/sec}$
0.00	-1.97	6.10	-0.13	15.26	-0.081
1.02	-1.83	7.12	-0.032	16.27	-0.113
2.03	-1.36	8.14	0.053	17.29	-0.133
3.05	-0.91	9.16	0.098	18.31	-0.153
4.07	-0.51	10.17	0.089	19.33	-0.164
5.09	-0.28	11.19	0.054	20.35	-0.167
		12.21	0.016	21.36	-0.05
		13.22	-0.02		
		14.24	-0.047		
Z*(2.2; 15.3; 0.25), $Re_F = 24,200$					
ϵ, mm	$\langle u_z \rangle \text{ m/sec}$	ϵ, mm	$\langle u_z \rangle \text{ m/sec}$	ϵ, mm	$\langle u_z \rangle \text{ m/sec}$
-8.14	-0.623	0.00	-5.081		
-7.63	-0.844	1.02	-4.037		
-7.12	-1.046	2.03	-2.361		
-6.10	-0.991	3.05	-1.281		
-5.09	-0.932	4.07	-0.721		
-4.07	-0.967	5.09	-0.733		
-3.05	-1.639	6.10	-0.801		
-2.03	-2.93	7.12	-0.733		
-1.02	-4.161	7.63	-0.713		
Z(7; 15.3; 0.25), $Re_F = 24,200$					
ϵ, mm	$\langle u_z \rangle \text{ m/sec}$	ϵ, mm	$\langle u_z \rangle \text{ m/sec}$	ϵ, mm	$\langle u_z \rangle \text{ m/sec}$
0.00	-4.109	4.57	-0.291	9.14	-0.516
0.51	-3.723	5.08	-0.193	9.65	-0.553
1.2	-3.133	5.59	-0.179	10.16	-0.574
1.52	-2.635	6.10	-0.202	10.67	-0.526
2.03	-2.157	6.60	-0.256	11.17	-0.024
2.54	-1.666	7.11	-0.322		
3.05	-1.204	7.62	-0.383		
3.56	-0.835	8.13	-0.435		
4.06	-0.493	8.64	-0.465		

Table D.1 (cont'd).

$Z^*(8; 15.3; 0.25), Re_F = 24,200$					
ϵ, mm	$\langle u_z \rangle \text{ m/sec}$	ϵ, mm	$\langle u_z \rangle \text{ m/sec}$	ϵ, mm	$\langle u_z \rangle \text{ m/sec}$
0.00	-3.872	4.58	-0.211	9.66	-0.437
0.51	-3.628	5.09	-0.107	10.17	-0.485
1.02	-3.205	5.60	-0.081	10.68	-0.525
1.52	-2.773	6.10	-0.113	11.19	-0.553
2.03	-1.998	6.61	-0.177	11.70	-0.532
2.54	-1.493	7.63	-0.223	12.21	-0.343
3.05	-1.103	8.14	-0.29	12.72	-0.313
3.56	-0.723	8.65	-0.345		
4.06	-0.413	9.16	-0.39		
$\theta^*(8; 15.3; 0.25), Re_F = 24,300$					
ϵ, mm	$\langle f_\theta \rangle \text{ MHz}$	ϵ, mm	$\langle f_\theta \rangle \text{ MHz}$	ϵ, mm	$\langle f_\theta \rangle \text{ MHz}$
0.00	0.03	3.94	0.807	8.50	0.411
0.13	0.105	4.44	0.758	9.02	0.251
0.38	0.283	4.95	0.7		
0.89	0.624	5.46	0.647		
1.40	0.788	5.97	0.603		
1.91	0.846	6.48	0.538		
2.41	0.864	6.98	0.503		
2.92	0.862	7.49	0.471		
3.43	0.842	8.00	6.438		
$Z(19; 15.3; 0.25), Re_F = 24,300$					
ϵ, mm	$\langle u_z \rangle \text{ m/sec}$	ϵ, mm	$\langle u_z \rangle \text{ m/sec}$	ϵ, mm	$\langle u_z \rangle \text{ m/sec}$
0.00	-3.13	7.62	0.36	13.21	-0.09
0.51	-3.008	8.13	0.345	15.24	-0.202
1.02	-2.643	8.64	0.296	16.26	-0.238
2.03	-1.881	9.14	0.262	17.27	-0.271
3.05	-1.13	9.65	0.21	19.30	-0.311
4.06	-0.53	10.16	0.165	20.32	-0.33
5.08	-0.134	10.67	0.115	21.34	-0.233
6.10	0.185	11.18	0.073	21.84	-0.211
7.11	0.347	12.19	-0.012		

Table D.1 (cont'd).

$Z^*(20; 15.3; 0.25), Re_F = 24,300$					
ϵ, mm	$\langle u_z \rangle$ m/sec	ϵ, mm	$\langle u_z \rangle$ m/sec	ϵ, mm	$\langle u_z \rangle$ m/sec
0.00	-3.038	7.63	0.35	16.28	-0.211
0.51	-2.968	8.14	0.337	17.29	-0.244
1.53	-2.108	9.16	0.261	18.31	-0.276
2.54	-1.392	10.17	0.169	19.33	-0.308
3.56	-0.778	11.19	0.077	20.35	-0.341
4.58	-0.3	12.21	-0.003	20.85	-0.039
5.60	0.026	13.22	-0.062		
6.61	0.264	14.24	-0.117		
7.12	0.331	15.26	-0.174		
$\theta^*(20; 15.3; 0.25), Re_F = 24,300$					
ϵ, mm	$\langle f_\theta \rangle$ MHz	ϵ, mm	$\langle f_\theta \rangle$ MHz	ϵ, mm	$\langle f_\theta \rangle$ MHz
0.00	0.022	4.318	0.72	11.43	0.416
0.25	0.184	4.826	0.69	12.44	0.392
0.76	0.453	5.334	0.64	12.46	0.355
1.27	0.642	5.842	0.61	14.48	0.333
1.78	0.733	6.350	0.59		
2.29	0.77	7.366	0.54		
2.79	0.792	8.382	0.51		
3.30	0.782	9.398	0.47		
3.81	0.754	10.414	0.45		
$Z(31; 15.34; 0.25), Re_F = 24,400$					
ϵ, mm	$\langle u_z \rangle$ m/sec	ϵ, mm	$\langle u_z \rangle$ m/sec	ϵ, mm	$\langle u_z \rangle$ m/sec
-0.25	-1.948	7.37	0.315	17.02	0.011
0.25	-1.959	7.87	0.34	19.05	-0.033
0.76	-1.903	8.38	0.33	21.08	-0.094
1.27	-1.783	8.89	0.296	23.11	-0.144
2.29	-1.39	9.40	0.248	25.15	-0.176
3.31	-0.912	10.92	0.099	26.16	-0.193
4.32	-0.498	12.95	0.007	27.18	-0.088
5.33	-0.126	13.97	0.003		
6.35	0.149	14.99	0.014		

Table D.1 (cont'd).

$Z^*(32; 15.3; 0.25), Re_F = 24,400$					
ϵ, mm	$\langle u_z \rangle \text{ m/sec}$	ϵ, mm	$\langle u_z \rangle \text{ m/sec}$	ϵ, mm	$\langle u_z \rangle \text{ m/sec}$
0.00	-1.803	7.12	0.317	16.79	-0.003
0.51	-1.728	7.63	0.288	18.82	-0.05
1.02	-1.552	8.65	0.198	20.86	-0.107
2.03	-1.123	9.66	0.099	22.89	-0.155
3.05	-0.625	10.68	0.051	24.42	-0.117
4.07	-0.248	11.70	0.033	25.43	-0.077
5.09	0.087	12.72	0.041	25.94	-0.019
6.10	0.274	13.73	0.049		
6.61	0.311	14.75	0.038		
$\theta^*(32; 15.3; 0.25), Re_F = 24,300$					
ϵ, mm	$\langle f_\theta \rangle \text{ MHz}$	ϵ, mm	$\langle f_\theta \rangle \text{ MHz}$	ϵ, mm	$\langle f_\theta \rangle \text{ MHz}$
0.00	0.012	4.57	0.713	13.21	0.386
0.51	0.173	5.08	0.694	14.22	0.373
1.02	0.325	6.10	0.631	15.24	0.364
1.52	0.478	7.11	0.564	16.26	0.363
2.03	0.586	8.13	0.517	17.27	0.354
2.54	0.644	9.14	0.475	18.29	0.346
3.05	0.696	10.17	0.445	19.30	0.343
3.56	0.713	11.18	0.424	20.32	0.34
4.06	0.722	12.19	0.407	21.34	0.331
				22.35	0.328
$\theta^*(20; 18.6; 4), Re_F = 26,600$					
ϵ, mm	$\langle f_\theta \rangle \text{ MHz}$	ϵ, mm	$\langle f_\theta \rangle \text{ MHz}$	ϵ, mm	$\langle f_\theta \rangle \text{ MHz}$
0.00	-0.014	3.94	0.78	11.05	0.48
0.13	0.056	4.45	0.773	12.06	0.441
0.38	0.18	4.95	0.756	13.08	0.407
0.89	0.385	5.97	0.698	14.10	0.39
1.91	0.612	6.99	0.643	15.11	0.35
2.41	0.686	8.00	0.60	16.13	0.076
2.92	0.732	9.02	0.553		
3.43	0.77	10.03	0.516		

Table D.1 (cont'd.).

$Z^*(1; 15.3; 4), Re_F = 24,300$					
ϵ, mm	$\langle u_z \rangle$ m/sec	ϵ, mm	$\langle u_z \rangle$ m/sec	ϵ, mm	$\langle u_z \rangle$ m/sec
-7.121	-0.295	-2.543	-0.321	2.035	-0.061
-6.612	-0.642	-2.035	-0.229	2.543	-0.126
-6.104	-0.84	-1.526	-0.108	3.052	-0.251
-5.596	-0.799	-1.018	-0.068	3.561	-0.257
-5.087	-0.696	-0.509	-0.025	4.069	-0.138
-4.578	-0.596	0.0	-0.009	4.578	-0.086
-4.069	-0.501	0.509	-0.066		
-3.561	-0.442	1.018	-0.074		
-3.052	-0.408	1.526	-0.054		
$Z^*(2.5; 15.3; 4), Re_F = 24,300$					
ϵ, mm	$\langle u_z \rangle$ m/sec	ϵ, mm	$\langle u_z \rangle$ m/sec	ϵ, mm	$\langle u_z \rangle$ m/sec
-7.63	-0.383	-3.05	-0.077	1.53	-0.102
-7.12	-0.367	-2.54	-0.037	2.03	-0.094
-6.61	-0.278	-2.03	-0.005	2.54	-0.213
-6.10	-0.208	-1.53	-0.008	3.05	-0.341
-5.60	-0.074	-1.02	-0.03	3.56	-0.39
-5.09	0.071	-0.51	-0.111	4.07	-0.393
-4.58	0.125	0.00	0.175	4.58	-0.47
-4.07	0.062	0.51	-0.22	5.09	-0.502
-3.56	0.037	1.02	-0.164	5.60	-0.015
$Z(7; 15.4; 4), Re_F = 24,300$					
ϵ, mm	$\langle u_z \rangle$ m/sec	ϵ, mm	$\langle u_z \rangle$ m/sec	ϵ, mm	$\langle u_z \rangle$ m/sec
-2.79	0.177	1.27	-0.245	6.86	-0.043
-2.29	-0.016	1.78	-0.18	7.87	-0.17
-1.78	-0.152	2.28	-0.045	8.89	-0.274
-1.27	-0.252	2.79	0.143	9.91	-0.343
-0.76	-0.295	3.30	0.334	10.92	-0.038
-0.25	-0.319	3.81	0.461		
		4.32	0.477		
0.25	-0.319	4.83	0.397		
0.76	-0.295	5.84	0.169		

Table D.1 (cont'd.).

Z(8; 15.3; 4), $Re_F = 24,300$					
ϵ, mm	$\langle u_z \rangle \text{ m/sec}$	ϵ, mm	$\langle u_z \rangle \text{ m/sec}$	ϵ, mm	$\langle u_z \rangle \text{ m/sec}$
0.00	-0.356	4.58	0.343	9.16	-0.351
0.51	-0.336	5.09	0.237	9.66	-0.404
1.02	-0.3	5.60	0.15	10.17	-0.44
1.53	-0.21	6.10	0.037	10.68	-0.443
2.03	-0.68	6.61	-0.058	11.19	-0.226
2.54	0.127	7.12	-0.137	11.70	-0.019
3.05	0.315	7.63	-0.184		
3.56	0.433	8.14	-0.245		
4.07	0.421	8.65	-0.308		
$\theta(8; 15.3; 4), Re_F = 24,300$					
ϵ, mm	$\langle f_\theta \rangle \text{ MHz}$	ϵ, mm	$\langle f_\theta \rangle \text{ MHz}$	ϵ, mm	$\langle f_\theta \rangle \text{ MHz}$
0.00	0.058	4.19	0.7		
0.13	0.114	4.70	0.655		
0.63	0.294	5.21	0.614		
1.14	0.436	5.71	0.575		
1.65	0.545	6.73	0.499		
2.16	0.65	7.75	0.42		
2.67	0.715	8.76	0.231		
3.17	0.756	9.27	0.075		
3.68	0.75				
Z(19; 15.3; 4), $Re_F = 24,300$					
ϵ, mm	$\langle u_z \rangle \text{ m/sec}$	ϵ, mm	$\langle u_z \rangle \text{ m/sec}$	ϵ, mm	$\langle u_z \rangle \text{ m/sec}$
0.00	-0.487	4.32	0.68	11.43	0.128
0.25	-0.472	4.83	0.788	13.46	-0.024
0.76	-0.418	5.33	0.815	15.41	-0.013
1.27	-0.326	5.84	0.784	17.52	-0.229
1.78	-0.212	6.35	0.71	19.05	-0.266
2.29	-0.048	6.86	0.633	20.07	-0.283
2.79	0.109	7.37	0.564	21.08	-0.215
3.30	0.313	8.38	0.487	21.59	-0.106
3.81	0.512	9.40	0.338		

Table D.1 (cont'd.).

$Z^*(20; 15.3; 4), Re_F = 24,400$					
ϵ, mm	$\langle u_z \rangle$ m/sec	ϵ, mm	$\langle u_z \rangle$ m/sec	ϵ, mm	$\langle u_z \rangle$ m/sec
-20.09	-0.287	- 4.43	0.681	2.29	-0.051
-19.58	-0.35	- 3.81	0.39	3.37	0.336
-18.06	-0.267	- 2.80	0.033	4.32	0.675
-16.02	-0.196	- 1.78	-0.282	5.34	0.785
-13.99	-0.087	- 1.02	-0.434	6.87	0.597
-11.95	0.041	- 0.51	-0.478	8.90	0.327
- 9.92	0.2	0.00	-0.495	10.94	0.126
- 7.88	0.43	0.51	-0.46	12.97	-0.021
- 5.85	0.694	1.27	-0.346	15.00	-0.19
				17.04	-0.195
				19.07	-0.326
				20.09	-0.359
				21.11	-0.006
$\theta^*(20; 15.3; 4), Re_F = 24,300$					
ϵ, mm	$\langle f_\theta \rangle$ MHz	ϵ, mm	$\langle f_\theta \rangle$ MHz	ϵ, mm	$\langle f_\theta \rangle$ MHz
0.00	0.022	3.94	0.688	13.08	0.346
0.13	0.11	4.95	0.651	14.10	0.273
0.38	0.297	5.97	0.607	15.11	0.25
0.89	0.427	6.98	0.559	16.13	0.211
1.40	0.531	8.00	0.515		
1.90	0.61	9.02	0.482		
2.41	0.654	10.03	0.45		
2.92	0.688	11.05	0.413		
3.43	0.695	12.06	0.388		
$Z(31; 15.3; 4), Re_F = 24,200$					
ϵ, mm	$\langle u_z \rangle$ m/sec	ϵ, mm	$\langle u_z \rangle$ m/sec	ϵ, mm	$\langle u_z \rangle$ m/sec
0.00	-0.515	7.11	0.693	16.26	0.027
0.51	-0.497	8.13	0.522	18.29	-0.008
1.02	-0.437	9.14	0.377	20.32	-0.073
1.52	-0.352	10.16	0.213	22.35	-0.131
2.54	-0.206	11.18	0.126	24.38	-0.19
3.56	0.144	12.19	0.064	25.91	-0.224
4.57	0.492	13.21	0.027	26.92	-0.125
5.08	0.776	14.22	0.017	27.43	-0.051
6.10	0.807	15.24	0.03		

Table D.1 (cont'd.).

Z(32; 15.4; 4), $Re_F = 24,200$					
ϵ, mm	$\langle u_z \rangle \text{ m/sec}$	ϵ, mm	$\langle u_z \rangle \text{ m/sec}$	ϵ, mm	$\langle u_z \rangle \text{ m/sec}$
0.00	-0.515	5.60	0.791	18.82	-0.041
0.51	-0.476	7.12	0.521	20.85	-0.098
1.02	-0.404	9.16	0.199	22.89	-0.171
1.53	-0.263	10.17	0.096	24.42	-0.191
2.03	-0.103	12.21	0.004	25.43	-0.211
2.54	0.055	14.24	0.013	26.45	-0.12
3.05	0.232	15.26	0.023	26.96	-0.012
3.56	0.435	16.28	0.013		
4.58	0.736	17.29	-0.008		
$\theta(32; 15.3; 4), Re_F = 24,400$					
ϵ, mm	$\langle f_\theta \rangle \text{ MHz}$	ϵ, mm	$\langle f_\theta \rangle \text{ MHz}$	ϵ, mm	$\langle f_\theta \rangle \text{ MHz}$
0.00	0.0	4.19	0.787	12.32	0.404
0.13	0.054	4.70	0.702	13.33	0.39
0.63	0.238	5.21	0.683	14.35	0.378
1.14	0.401	6.22	0.635	15.37	0.365
1.65	0.507	7.24	0.584	16.38	0.358
2.16	0.589	8.25	0.537	17.4	0.35
2.67	0.64	9.27	0.495	18.41	0.346
3.17	0.675	10.29	0.457	19.43	0.334
3.68	0.701	11.30	0.428	20.45	0.329
				21.46	0.087
Z(34.2; 15.3; 4), $Re_F = 24,200$					
ϵ, mm	$\langle u_z \rangle \text{ m/sec}$	ϵ, mm	$\langle u_z \rangle \text{ m/sec}$	ϵ, mm	$\langle u_z \rangle \text{ m/sec}$
0.00	0.599	4.32	0.88	12.21	0.109
0.25	-0.573	4.58	0.922	14.24	0.103
0.76	-0.487	4.83	0.956	16.28	0.075
1.27	-0.35	5.09	0.953	18.31	0.022
1.78	-0.127	5.60	0.907	20.35	-0.052
2.29	0.085	6.10	0.799	22.38	-0.139
2.80	0.292	7.12	0.563	23.91	-0.204
3.31	0.523	8.14	0.367	24.92	-0.025
3.81	0.74	10.17	0.153	25.94	-0.328
				26.96	-0.021

Table D.1 (cont'd.).

$Z^*(20; 10.2; 4), Re_F = 20,000$					
ϵ, mm	$\langle u_z \rangle \text{ m/sec}$	ϵ, mm	$\langle u_z \rangle \text{ m/sec}$	ϵ, mm	$\langle u_z \rangle \text{ m/sec}$
-21.105	-0.024	- 6.61	0.476	4.58	0.592
-20.85	-0.021	- 4.58	0.625	6.61	0.384
-19.84	-0.273	- 3.05	0.258	8.65	0.187
-17.80	-0.213	- 2.03	-0.031	10.68	0.044
-16.79	-0.17	- 1.02	-0.274	12.72	-0.057
-14.75	-0.099	0.00	-0.431	14.75	-0.151
-12.72	-0.027	0.51	-0.427	16.79	-0.216
-10.68	0.099	1.02	-0.381	18.82	-0.285
- 8.65	0.245	2.54	0.187	19.84	-0.1
				20.34	-0.039
$\theta^*(20; 10.3; 4), Re_F = 20,100$					
ϵ, mm	$\langle f_\theta \rangle \text{ MHz}$	ϵ, mm	$\langle f_\theta \rangle \text{ MHz}$	ϵ, mm	$\langle f_\theta \rangle \text{ MHz}$
0.00	0.003	4.06	0.551	11.68	0.332
0.51	0.145	5.57	0.554	12.70	0.327
1.02	0.304	5.59	0.509	13.72	0.312
1.52	0.395	6.60	0.471	14.73	0.24
2.03	0.474	7.62	0.441	15.75	0.181
2.54	0.518	8.64	0.402		
3.05	0.542	9.65	0.379		
3.56	0.548	10.67	0.352		
$Z^*(20; 5.4; 4), Re_F = 14,500$					
ϵ, mm	$\langle u_z \rangle \text{ m/sec}$	ϵ, mm	$\langle u_z \rangle \text{ m/sec}$	ϵ, mm	$\langle u_z \rangle \text{ m/sec}$
-20.85	-0.011	- 4.07	0.401	6.61	0.352
-19.84	-0.193	- 3.05	0.274	8.65	0.196
-18.31	-0.174	- 2.03	-0.054	10.68	0.086
-16.28	-0.131	- 1.02	-0.163	12.72	-0.001
-14.24	-0.084	0.00	-0.29	14.75	-0.058
-12.21	-0.015	1.02	-0.173	16.79	-0.125
-10.17	-0.067	2.03	0.016	18.31	-0.181
- 8.14	0.179	3.05	0.228	19.33	-0.207
- 6.10	0.323	4.58	0.454	20.35	-0.072

Table D.1 (cont'd.).

$\theta^*(20; 5.1; 4), Re_F = 14,300$					
ϵ, mm	$\langle f_\theta \rangle$ MHz	ϵ, mm	$\langle f_\theta \rangle$ MHz	ϵ, mm	$\langle f_\theta \rangle$ MHz
0.00	-0.009	6.22	0.316	14.35	0.153
0.13	0.021	7.24	0.291	15.36	0.116
0.63	0.116	8.25	0.275		
1.14	0.226	9.27	0.262		
2.16	0.313	10.29	0.242		
3.17	0.354	11.30	0.227		
4.19	0.353	12.32	0.213		
5.21	0.336	13.33	0.16		
$Z^*(20; 2.2; 4), Re_F = 9,200$					
ϵ, mm	$\langle u_z \rangle$ m/sec	ϵ, mm	$\langle u_z \rangle$ m/sec	ϵ, mm	$\langle u_z \rangle$ m/sec
-20.346	-0.065	- 5.087	0.283	7.63	0.14
-19.838	-0.109	- 3.052	0.194	9.665	0.06
-18.820	-0.133	- 2.034	0.055	11.699	0.004
-17.295	-0.101	- 1.018	-0.056	13.734	-0.041
-15.260	-0.053	0	-0.13	15.768	-0.073
-13.225	-0.013	1.018	-0.075	17.803	-0.101
-11.19	0.026	2.035	0.036	18.82	-0.109
- 9.156	0.093	3.561	0.292	19.838	-0.131
- 7.121	0.178	5.596	0.23	20.855	-0.066
$Z^*(20; 15.4; 6.8), Re_F = 22,400$					
ϵ, mm	$\langle u_z \rangle$ m/sec	ϵ, mm	$\langle u_z \rangle$ m/sec	ϵ, mm	$\langle u_z \rangle$ m/sec
- 8.14	0.346	1.02	0.001	11.19	0.075
- 7.12	0.469	2.03	0.156	13.22	-0.047
- 6.10	0.592	3.05	0.447	15.26	-0.125
- 5.09	0.707	4.07	0.678	16.28	-0.166
- 4.07	0.631	5.09	0.775	17.29	-0.229
- 3.05	0.395	6.10	0.666	18.31	-0.28
- 2.03	0.178	7.12	0.46	19.33	-0.319
- 1.02	-0.021	8.14	0.345	20.35	-0.128
0.00	-0.077	9.156	0.251		

Table D.1 (cont'd.).

$Z(7; 15.3; \infty), Re_F = 24.100$					
ϵ, mm	$\langle u_z \rangle \text{ m/sec}$	ϵ, mm	$\langle u_z \rangle \text{ m/sec}$	ϵ, mm	$\langle u_z \rangle \text{ m/sec}$
- 0.25	0.445	4.32	0.556	8.89	-0.319
0.25	0.445	4.83	0.414	9.40	-0.359
0.76	0.515	5.33	0.186	9.91	-0.404
1.27	0.604	5.84	0.071	10.41	0.435
1.78	0.737	6.35	-0.004	10.92	-0.212
2.286	0.847	6.86	-0.116	11.43	-0.083
2.79	0.88	7.37	-0.161		
3.30	0.832	7.87	-0.235		
3.81	0.697	8.38	-0.283		
$Z^*(8; 15.3; \infty), Re_F = 24,100$					
ϵ, mm	$\langle u_z \rangle \text{ m/sec}$	ϵ, mm	$\langle u_z \rangle \text{ m/sec}$	ϵ, mm	$\langle u_z \rangle \text{ m/sec}$
-11.44	-0.072	-2.29	0.814	6.36	0.029
-10.43	-0.276	-1.27	0.564	7.37	-0.126
- 9.41	-0.198	-0.25	0.417	8.39	-0.25
- 8.39	-0.063	0.25	0.434	9.41	-0.363
- 7.37	0.08	1.27	0.617	10.43	-0.403
- 6.87	0.263	2.29	0.832	11.44	-0.184
- 5.34	0.546	3.30	0.802		
- 4.32	0.864	4.32	0.511		
- 3.30	0.99	5.34	0.217		
$\theta^*(8; 15.3; \infty), Re_F = 24,100$					
ϵ, mm	$\langle f_\theta \rangle \text{ MHz}$	ϵ, mm	$\langle f_\theta \rangle \text{ MHz}$	ϵ, mm	$\langle f_\theta \rangle \text{ MHz}$
0.00	0.008	4.32	0.672	9.40	0.305
0.25	0.101	4.83	0.64		
0.76	0.284	5.33	0.605		
1.27	0.385	5.84	0.573		
1.78	0.495	6.35	0.538		
2.29	0.591	6.86	0.5		
2.79	0.655	7.37	0.456		
3.30	0.684	7.87	0.438		
3.81	0.69	8.89	0.38		

Table D.1 (cont'd.).

$Z(19; 15.4; \infty), Re_F = 24,100$					
ϵ, mm	$\langle u_z \rangle$ m/sec	ϵ, mm	$\langle u_z \rangle$ m/sec	ϵ, mm	$\langle u_z \rangle$ m/sec
- 0.25	0.333	6.86	0.59	16.00	-0.163
0.25	0.334	7.87	0.449	17.02	-0.205
0.76	0.383	8.89	0.34	18.03	-0.239
1.78	0.514	9.91	0.227	19.05	-0.279
2.79	0.718	10.92	0.158	20.07	-0.294
3.81	0.881	11.94	0.037	20.57	-0.303
4.32	0.92	12.95	-0.023	21.08	-0.306
4.83	0.906	13.97	-0.094	21.59	-0.313
5.84	0.757	14.99	-0.143	22.10	-0.316
				22.61	-0.293
				23.11	-0.287
				23.62	-0.032
$Z^*(20; 15.4; \infty), Re_F = 24,100$					
ϵ, mm	$\langle u_z \rangle$ m/sec	ϵ, mm	$\langle u_z \rangle$ m/sec	ϵ, mm	$\langle u_z \rangle$ m/sec
-20.09	-0.01	- 5.34	0.847	8.90	0.277
-19.07	-0.293	- 4.32	0.931	10.94	0.094
-18.06	-0.28	- 2.80	0.734	12.97	-0.041
-16.53	-0.198	- 0.76	0.365	15.00	-0.153
-14.50	-0.08	0.25	0.329	17.04	-0.229
-12.46	0.05	1.78	0.589	19.07	-0.292
-10.43	0.216	3.81	0.871	20.09	-0.308
- 8.39	0.445	4.83	0.831	21.11	-0.203
- 6.36	0.763	6.87	0.525	21.62	-0.111
$\theta^*(20; 15.3; \infty), Re_F = 24,100$					
ϵ, mm	$\langle f_\theta \rangle$ MHz	ϵ, mm	$\langle f_\theta \rangle$ MHz	ϵ, mm	$\langle f_\theta \rangle$ MHz
0.00	-0.001	4.19	0.648	11.81	0.39
0.13	0.046	4.70	0.661	12.83	0.368
0.63	0.242	5.21	0.649	13.84	0.338
1.14	0.39	5.71	0.629	14.86	0.315
1.65	0.473	6.73	0.584	15.87	0.27
2.16	0.517	7.75	0.547		
2.67	0.556	8.76	0.482		
3.17	0.596	9.78	0.457		
3.68	0.632	10.79	0.426		

Table D.1 (cont'd.).

$Z(31; 15.4; \infty), Re_F = 24,100$					
ϵ, mm	$\langle u_z \rangle$ m/sec	ϵ, mm	$\langle u_z \rangle$ m/sec	ϵ, mm	$\langle u_z \rangle$ m/sec
0.0	0.236	7.62	0.51	16.76	0.021
1.02	0.281	8.64	0.366	17.78	-0.001
2.03	0.493	9.75	0.237	18.80	-0.032
3.05	0.745	10.67	0.127	19.81	-0.063
3.56	0.957	11.68	0.075	20.83	-0.095
4.06	1.011	12.70	0.03	21.84	-0.124
4.57	0.979	13.72	0.019	22.86	-0.154
5.59	0.915	14.73	0.026	23.88	-0.178
6.60	0.709	15.70	0.028	24.89	-0.195
				25.91	-0.198
				26.92	-0.176
				27.94	-0.11
$Z^*(32; 15.4; \infty), Re_F = 24,100$					
ϵ, mm	$\langle u_z \rangle$ m/sec	ϵ, mm	$\langle u_z \rangle$ m/sec	ϵ, mm	$\langle u_z \rangle$ m/sec
-9.66	0.217	5.09	0.912	22.89	-0.133
-7.63	0.448	7.12	0.514	23.91	-0.148
-5.60	0.847	9.16	0.222	24.92	-0.151
-3.56	1.032	11.19	0.07	25.94	-0.027
-1.53	0.554	13.22	0.027	26.45	-0.011
0.00	0.230	15.26	0.032		
1.02	0.287	17.29	-0.004		
2.54	0.656	19.33	-0.05		
4.07	0.959	21.36	-0.099		
$\theta^*(32; 15.3; \infty), Re_F = 24,100$					
ϵ, mm	$\langle f_\theta \rangle$ MHz	ϵ, mm	$\langle f_\theta \rangle$ MHz	ϵ, mm	$\langle f_\theta \rangle$ MHz
0.00	0.021	3.94	0.681	12.57	0.402
0.13	0.076	4.44	0.678	13.59	0.387
0.38	0.157	5.46	0.651	14.60	0.377
0.63	0.242	6.48	0.608	15.62	0.367
0.89	0.296	7.49	0.572	16.64	0.357
1.40	0.387	8.51	0.52	17.65	0.354
1.90	0.448	9.52	0.48	18.67	0.348
2.41	0.503	10.54	0.442	19.68	0.338
2.92	0.568	11.56	0.481	20.70	0.25

Table D.1 (cont'd.).

$Z^*(34.2; 15.3; \infty), Re_F = 24,100$					
ϵ, mm	$\langle u_z \rangle$ m/sec	ϵ, mm	$\langle u_z \rangle$ m/sec	ϵ, mm	$\langle u_z \rangle$ m/sec
-5.09	0.968	9.16	0.306	25.94	-0.279
-3.05	0.829	11.19	0.157	26.96	-0.08
-1.02	0.129	13.22	0.124	27.47	-0.02
0.00	0.032	15.26	0.092		
1.53	0.372	17.29	0.047		
3.05	0.924	19.33	-0.025		
4.07	1.203	21.36	-0.103		
5.09	1.151	23.40	-0.183		
7.12	0.642	24.92	-0.248		
$Z(34.6; 15.3; \infty), Re_F = 24,100$					
ϵ, mm	$\langle u_z \rangle$ m/sec	ϵ, mm	$\langle u_z \rangle$ m/sec	ϵ, mm	$\langle u_z \rangle$ m/sec
-3.05	0.856	3.56	1.138	8.14	0.353
-2.03	0.432	4.07	1.23	8.65	0.25
-1.02	0.124	4.58	1.225	9.16	0.176
-0.51	0.04	5.09	1.11	9.66	0.137
0.00	0.021	5.60	0.975	10.17	0.125
0.51	0.129	6.10	0.827	10.68	0.124
1.53	0.396	6.61	0.704	11.19	0.129
2.54	0.761	7.12	0.584	12.21	0.129
3.05	0.979	7.63	0.459	13.22	0.13
$\theta(20; 10.2; \infty), Re_F = 19,700$					
ϵ, mm	$\langle f_\theta \rangle$ MHz	ϵ, mm	$\langle f_\theta \rangle$ MHz	ϵ, mm	$\langle f_\theta \rangle$ MHz
0.00	-0.001	4.32	0.514	12.95	0.28
0.25	0.074	4.83	0.5	13.97	0.254
0.76	0.205	5.84	0.466	14.98	0.242
1.27	0.3	6.86	0.429	16.00	0.058
1.78	0.38	7.87	0.396		
2.28	0.433	8.89	0.371		
2.79	0.473	9.91	0.344		
3.30	0.513	10.92	0.321		
3.81	0.52	11.94	0.299		

Table D.1 (cont'd.).

$Z(20; 5.2; \infty), Re_F = 14,000$					
ϵ, mm	$\langle u_z \rangle \text{ m/sec}$	ϵ, mm	$\langle u_z \rangle \text{ m/sec}$	ϵ, mm	$\langle u_z \rangle \text{ m/sec}$
-21.87	-0.084	- 3.56	0.478	14.75	-0.096
-19.84	-0.169	- 1.53	0.276	16.79	-0.158
-17.80	-0.137	0.51	0.279	18.82	-0.191
-15.77	-0.094	2.54	0.473	20.85	-0.104
-13.73	-0.026	4.58	0.534	21.36	-0.019
-11.70	0.059	6.61	0.32		
- 9.66	0.185	8.65	0.176		
- 7.63	0.337	10.68	-0.063		
- 5.59	0.535	12.72	-0.024		
$\theta(20; 5.17; \infty), Re_F = 14,000$					
ϵ, mm	$\langle f_\theta \rangle \text{ MHz}$	ϵ, mm	$\langle f_\theta \rangle \text{ MHz}$	ϵ, mm	$\langle f_\theta \rangle \text{ MHz}$
0.00	0.012	4.19	0.332	12.83	0.198
0.13	0.024	4.70	0.328	13.84	0.184
0.63	0.139	5.71	0.314	14.86	0.17
1.14	0.196	6.73	0.295	15.87	0.141
1.65	0.247	7.75	0.278		
2.16	0.29	8.76	0.259		
2.67	0.307	9.78	0.244		
3.17	0.32	10.79	0.227		
3.68	0.327	11.81	0.209		

LIST OF REFERENCES

LIST OF REFERENCES

- Adrian, R.J., and Fingerson, L.M., 1981, TSI Short Course.
- Balakrishnan, C., and Gordon, R.J., 1971, "New Viscoelastic Phenomenon and Turbulent Drag Reduction," *Nature Phys. Sci.* 231, 25.
- Bedi, P.S., and Thew, M.T., 1973, "Localized Velocity and Turbulence Measurement in Turbulent Swirling Flows Using Laser Doppler Anemometry," *Opto-Electronics* 5, 9.
- Beenackers, Antonie A.C.M., 1978, "Aromatic Sulfonation in a Cyclone Reactor, A Stirred Cell, a Cocurrent Tube Reactor; Influence of Mass Transfer on Selectivity," *Int. Symp. on Chem. React. Eng.*, 5th, Houston, TX, March 13-15, published by Am. Chem. Soc., Washington, DC, 1978, 327.
- Benjamin, T.B., 1962, "Theory of the Vortex Breakdown Phenomenon," *J. Fluid Mech.* 14, 593.
- Bhattacharyya, P., 1980, "Theoretical Study of the Flow Field Inside a Hydrocyclone with Vortex Finder Diameter Greater than that of Apex Opening - I. Laminar Case," *Appl. Sci. Res.* 36, 197.
- Bhattacharyya, P., 1980, "Theoretical Study of the Flow Field Inside a Hydrocyclone with Vortex Finder Diameter Greater Than That of Apex Opening - II. Turbulent Case," *Appl. Sci. Res.* 36, 213.
- Binnie, A.M., 1957, "Experiments on the Slow Swirling Flow of a Viscous Liquid Through a Tube," *Quart. J. Mech. and Appl. Math* 10, 276.
- Binnie, A.M., and Harris, D.P., 1950, "The Application of Boundary-Layer Theory to Swirling Liquid Flow Through a Nozzle," *Quart. J. Mech. and Applied Math.*, Vol. III, part 1, 89.
- Binnie, A.J., and Teare, J.D., 1956, "Experiments on the Flow of Swirling Water Through a Pressure Nozzle and an Open Trumpet," *Proc. Roy. Soc. A* 325, 78.
- Bloor, M.I.G., and Ingham, D.B., 1976, "Boundary Layer Flows on the Side Walls of Conical Cyclones," *Trans. Inst. Chem. Eng.* 54, 276.

- Bird, R.B., Stewart, W.E., and Lightfoot, E.N., 1960, Transport Phenomena, John Wiley and Sons, Inc.
- Bican, A.F., 1982, "Refraction Correction for LDA Measurements in Flows with Curved Optical Boundaries," TSI Quarterly 8, Issue 2, 10.
- Bradley, D., 1965, The Hydrocyclone, Pergamon Press.
- Bradley, D., and Pulling, D.J., 1959, "Flow Patterns in the Hydraulic Cyclone and Their Interpretation in Terms of Performance," Trans. Inst. Chem. Eng. 37, 34.
- Boysan, F., Ayers, W.H., and Swithenbank, J., 1982, "A Fundamental Mathematical Modeling Approach to Cyclone Design," Trans. Inst. Chem. Eng. 60, 222.
- Cassidy, J.J., and Falvey, H.T., 1970, "Observations of Unsteady Flow Arising After Vortex Breakdown," J. Fluid Mech. 41, part 4, 727.
- Chanaud, R.C., 1965, "Observations of Oscillatory Motion in Certain Swirling Flows," J. Fluid Mech. 21, part 1, III.
- Chiou, C.S., and Gordon, R.J., 1976, "Vortex Inhibition: Velocity Profile Measurements," AIChE J 22, 947.
- Colman, D.A., and Thew, M.T., 1980, "Hydrocyclone to Give a Highly Concentrated Sample of a Lighter Dispersed Phase," p. 209 in Hydrocyclone, Int. Conf., Cambridge, England, BHRA Fluid Eng.
- Dabir, B., Wallace, L.B., and Petty, C.A., 1980, "The Effect of Drag Reducing Agents on the Centrifugal Efficiency of a 10 mm Hydrocyclone," I. Chem. E. Symposium Series No. 59, 5:911.
- Donaldson, C. Dup., 1956, "Solution of the Navier-Stokes Equations for Two and Three-Dimensional Vortices," Ph.D. Thesis, Princeton University.
- Donaldson, C. Dup., and Snedeker, R.S., 1962, "Experimental Investigation of the Structure of Vortices in Simple Cylindrical Vortex Chambers," Aero. Res. Ass. of Princeton, Inc. Rep. No. 47.
- Donaldson, C. Dup., and Sullivan, R.D., 1960, "Behaviour of Solutions of the Navier-Stokes Equations for a Complete Class of Three-Dimensional Viscous Vortices," Proc. 1960 Heat Transfer and Fluid Mech. Inst., p. 16, Stanford University Press.

- Durrani, T.S., and Greated, C.A., 1977, Laser Systems in Flow Measurement, Plenum Press.
- Durst, F., Melling, A., and Whitelaw, J.H., 1976, Principles and Practice of Laser-Doppler Anemometry, Academic Press.
- Escudier, M.P., Bornstein, J., and Zchnder, N., 1980, "Observations and LDA Measurements of Confined Turbulent Vortex Flow," J. Fluid Mech. 98, part 1, 49.
- Faler, J.H., and Leibovich, S., 1978, "An Experimental Map of the Internal Structure of a Vortex Breakdown," J. Fluid Mech. 68, part 2, 313.
- Fontein, F.J., 1961, "Separation by Cyclone According to Specific Gravity," Chap. 10 in Cyclone in Industry.
- Fontein, J.F., and Dijksman, C., 1953, in Proceeding of Symposium on Mineral Dressing (London: The Institution of Mining and Metallurgy).
- George, W.K., Jr., and Berman, N.S., 1973, "Doppler Ambiguity in Laser Doppler Velocimeter," Appl. Phys. Lett. 23, 222.
- George, W.K., and Lumley, J.L., 1973, "The Laser-Doppler Velocimeter and its Application to the Measurement of Turbulence," J. Fluid Mech. 60, 321.
- Grabek, E., Mierzwinski, S., Popiolek, Z., and Patasz, J., 1980, "Application of the Laser Doppler Anemometer to Industrial Problems," DISA Info. No. 25, 30.
- Greenspan, H.P., 1968, Theory of Rotating Fluids, Cambridge Press.
- Haas, D.A., Nurmi, E.O., Whatley, M.E., and Engel, J.R., 1957, "Midget Hydrocyclones Remove Micron Particles," Chem. Eng. Prog. 53, 203.
- Hall, M.G., 1966, "The Structure of Concentrated Vortex Cores," Progress in Aeronautical Sciences, 7, Pergamon Press.
- Harvey, J.K., 1962, "Some Observations of the Vortex Breakdown Phenomenon," J. Fluid Mech. 14, 585.
- Hayduk, W., and Neale, G., 1978, "Vortex Formation in Stirred Draining Vessels," Can. J. Chem. Eng. 56, October, 544.
- Katchalsky, A., and Eisenberg, H., 1951, "Molecular Weight of Polyacrylic and Polymethacrylic Acid," J. Polym. Sci. 6, No. 2, 145.

- Kelsall, D.F., 1952, "A Study of the Motion of Solid Particles in a Hydraulic Cyclone," Trans. Inst. Chem. Eng. 30, 87.
- Kelsall, D.F., 1953, "A Further Study of the Hydraulic Cyclone," Chem. Eng. Sci. 2, 254.
- Kim, O.K., Little, R.C., and Ting, R.Y., 1973, "Polymer Structural Effects in Turbulent Drag Reduction," AICHE Symposium Series, No. 130, Vol. 69, 39.
- Knowles, N.S.R., 1971, "Photographic Fluid Velocity Measurement in a Hydrocyclone," M. Eng. Thesis, Dept. of Chem. Eng., McMaster University, Hamilton, Ontario.
- Knowles, S.R., Woods, R.D., and Feuerstein, I.A., 1973, "The Velocity Distribution Within a Hydrocyclone Operating Without an Air Core," Can. J. Chem. Eng. 51, 263.
- Lewellen, W.S., 1965, "Linearized Vortex Flows," A.I.A.A. J. 3, No. 1, 91.
- Lewellen, W.S., 1971, "A Review of Confined Vortex Flows," N.A.S.A. Contractor Rep. No. 1772.
- Loader, A.J., and Thew, M.T., 1975, "Analysis and Characteristics of Turbulence in Confined Swirling Flow Studies with an LDA," Proc. LDA-Symposium, Copenhagen.
- Metzner, A.B., Uebler, E.A., and Chan Man Fong, C.F., 1969, "Converging Flows of Viscoelastic Materials," AICHE J. 15, No. 5, 750.
- Nissan, A.H., and Bresan, V.P., 1961, "Swirling Flow in Cylinders," AICHE J. 7, No. 4, 543.
- Nuttal, J.B., 1953, "Axial Flow in a Vortex," Nature 172, 582.
- Ohasi, H., and Maeda, S., 1958, "Motion of Water in a Hydraulic Cyclone," Chem. Eng. (Japan), 22, 200.
- Orloff, K.L., and Bossel, H.H., 1973, "Laser Doppler Velocity Measurements of Swirling Flows with Upstream Influence," N.A.S.A. Contractor Rep. No. 2284.
- Poole, J.B., and Doyle, D., 1968, Solid-Liquid Separation--A Review and a Bibliography, Chem. Publishing Company.
- Reischman, M.M., and Tiederman, W.G., 1975, "Laser-Doppler Anemometer Measurements in Drag-Reducing Cahnnel Flows," J. Fluid Mech. 70, 369.

- Rietema, K., 1961a-d, "Performance and Design of Hydrocyclones--I, II, III, IV," Chem. Eng. Sci. 15, 298, 303, 310, 320.
- Rietema, K., and Verver, C.G., 1961, Cyclone in Industry, Elsevier Publishing Company.
- Rosenzweig, M.L., Lewellen, W.S., and Ross, D.H., 1964, "Confined Vortex Flows with Boundary-Layer Interaction," A.I.A.A. J. 2, No. 12, 2127.
- Rosenzweig, M.L., Ross, D.H., and Lewellen, W.S., 1962, "On Secondary Flows in Jet-Driven Vortex Tubes," J. Aerosp. Sci. 29, 1142.
- Sarpkaya, T., 1971a, "On Stationary and Travelling Vortex Breakdowns," J. Fluid Mech. 45, part 3, 545.
- Sarpkaya, T., 1971b, "Vortex Breakdown in Swirling Conical Flows," A.I.A.A. J. 9, 1792.
- Sarpkaya, T., 1974, "Effect of the Adverse Pressure Gradient on Vortex Breakdown," A.I.A.A. J. 12, 602.
- Sears, F.W., and Zemansky, M.W., 1964, University Physics, Addison-Wesley Publishing Company.
- Seyer, F.A., and Metzner, A.B., 1969, "Turbulence Phenomena in Drag-Reducing Systems," AIChE J. 15, 426.
- Smith, J.L., 1962, "An Experimental Study of the Vortex in the Cyclone Separator," J. of Basic Eng. 84, 602.
- Som, S.K., and Mukherjee, S.G., 1980, "Theoretical and Experimental Investigations of the Formation of Air Core in a Swirl Spray Atomizing Nozzle," Appl. Sci. Res. 36,
- Squire, H.B., 1960, "Analysis of the Vortex Breakdown Phenomenon, Part I., Aero. Dept., Imperial Coll., Rep. No. 102.
- Stairmand, C.J., 1951, "The Design and Performance of Cyclone Separators," Trans. Inst. Chem. Eng. 29, 356.
- Sullivan, R.D., 1959, "A Two-Cell Vortex Solution of the Navier-Stokes Equations," J. Aerosp. Sci. 26, No. 11, 767.
- Svarovsky, L., 1977, Solid-Liquid Separation, Butterworths, London.
- Sylvester, N.D., and Tyler, J.S., 1970, "Dilute Solution Properties of Drag-Reducing Polymers," Ind. Eng. Chem. Prod. Res. Develop., Vol. 9, No. 4, 548.

- Taylor, G.I., 1950, "The Boundary Layer in the Converging Nozzle of a Swirl Atomizer," Quart. J. Mech. and Appl. Math, Vol. III, part 2, 129.
- Ter Linden, A.J., 1949, "Investigations into Cyclone Dust Collectors," Proc. Inst. Mech. Eng., 1960, 233.
- Thew, M.T., Silk, S.A., and Colman, D.A., 1980, "Determination and Use of Residence Time Distributions for Two Hydrocyclones," p. 225 in Hydrocyclones, Int'l. Conf., Cambridge, England, BHRA Fluid Eng.
- Thomas, G.E., 1982, "The Effect of Separan AP-30 on the Performance of a 10 mm Hydrocyclone," M.S. Thesis, Michigan State University.
- Ting, R.Y., 1974, "Cavitation Suppression by Polymer Additives: Concentration Effect and Implication on Drag Reduction," AICHE J. 20, 827.
- TSI, 1982a, "System 9100-3 General Purpose Helium-Neon LDV System Instruction Manual."
- TSI, 1982b, "Instruction Manual Model 1980 Counter Type Signal Processes for Laser Velocimeter."
- TSI, 1982c, "Model 9180 Frequency Shift System Instruction Manual."
- Virk, P.S., 1975, "Drag Reduction Fundamentals," AICHE J. 21, 625.
- Wallace, L.B., 1980, "The Effect of Polyacrylamide on the Performance of a Hydrocyclone," M.S. Thesis, Michigan State University.
- Wallace, L.B., Dabir, B., and Petty, C.A., 1980, "Preliminary Findings on the Effect of Polyacrylamide on Particle-Liquid Separation in Hydrocyclone," Chem. Eng. Commun. 7, 27.
- Wilks, G., 1968, "Swirling Flow Through a Convergent Funnel," J. Fluid Mech. 34, 575.
- Yeh, Y., and Cummins, H.Z., 1964, "Localized Fluid Flow Measurement, with He-Ne Laser Spectrometer," Appl. Phys. Lett. 4, 176.

MICHIGAN STATE UNIVERSITY LIBRARIES



3 1293 03195 9301